

Synthesis of carbon nanotubes supported iron catalysts for light olefins via Fischer-Tropsch synthesis

A Thesis Submitted to the
College of Graduate and Postdoctoral Studies
In Partial Fulfilment of the Requirements for the
Degree of Doctor of Philosophy
In the Department of Chemical and Biological Engineering
University of Saskatchewan
Saskatoon, Saskatchewan

By
Arash Yahyazadeh

Copyright Arash Yahyazadeh, January 2023, All rights reserved.
Unless otherwise noted, copyright of the material in this thesis belongs to the author

PERMISSION TO USE

In presenting this thesis in partial fulfillment of the requirements for a Doctor of Philosophy Degree from the University of Saskatchewan, I agree that the Libraries of this University may make this thesis freely available for inspection. I further agree that permission for copying of this thesis in any manner, in whole or in part, for scholarly purposes may be granted by Professor Ajay Kumar Dalai who supervised my thesis work or, in their absence, by the Head of the Department or the Dean of the College of Graduate Research and Studies in which my thesis work was done. It is understood that any copying or publication or use of this thesis or parts thereof for financial gain shall not be allowed without my written permission. It is also understood that due recognition shall be given to me and to the University of Saskatchewan in any scholarly use which may be made of any material in my thesis.

Requests for permission to copy or to make other uses of materials in this thesis in whole or parts shall be addressed to:

Head of the Department of Chemical and Biological Engineering

57 Campus Drive

University of Saskatchewan

Saskatoon, Saskatchewan S7N 5A9, Canada

Or

Dean

College of Graduate and Postdoctoral Studies

University of Saskatchewan

116 Thorvaldson Building, 110 Science Place

Saskatoon, Saskatchewan S7N 5C9, Canada.

ABSTRACT

Light olefins including ethylene, propylene and butylene are the basics of many chemical products. As the demand for light olefins is dramatically increased and oil resources are limited, it becomes desirable to produce light olefins from other resources such as syngas. Syngas could be obtained from alternative feedstocks such as methane, coal, biomass, and plastic wastes. Fischer-Tropsch (FT) synthesis involves conversion of syngas to hydrocarbons. FT products at high temperatures are mainly gasoline and light olefins. In FT catalytic reaction, iron is preferred due to its low cost, high selectivity towards olefins and flexibility in terms of use for different ratio of H_2 to CO in syngas feed. In this study, catalytic performance of iron catalyst was evaluated using molybdenum and potassium as promoters and carbon nanotubes (CNTs) as support. The study plan for this research was divided into four sub-objectives or phases.

In the first phase, catalytic chemical vapor deposition (CCVD) method was applied to synthesize CNTs using Fe/ $CaCO_3$ and acetylene as catalyst and hydrocarbon source, respectively. Applying response surface methodology, the optimum operating conditions were determined in CVD reactor for maximal yield and purity of CNTs. The effects of reaction time (30–60 min), reaction temperature (700–800 °C), and loading of the catalyst (10–30 wt% Fe) were investigated. 20Fe/CNTs-synthesized, 20Fe/CNTs-commercial, and 20Fe/ Al_2O_3 were analyzed in terms of physio-chemical properties and FTS catalytic performance. The catalytic performance of Fe-based catalysts was investigated using a fixed-bed reactor at 280 °C under 2.0 MPa. 20Fe/CNTs-synthesized exhibited a lower rate of water-gas-shift (WGS) reaction compared with 20Fe/CNTs-commercial, with C_2 - C_4 selectivity of 23.6% which is slightly less than that of its commercial counterpart. After 120 h time-on-stream under steady state condition, the higher activity was maintained by the 20Fe/CNTs-synthesized catalyst compared to the 20Fe/CNTs-Commercial and 20Fe/ Al_2O_3 catalysts.

Electronic structural promoters such as K and Mo improve olefins' selectivity and catalytic activity. Hence, in the second phase, CNTs synthesized by CCVD were used as support to obtain K- and/or Mo-promoted Fe/CNTs catalysts for light olefins' production in FTS. A two-level full factorial design was applied for K- and/or Mo-promoted Fe/CNTs catalyst to investigate the effects of synthesis conditions including Mo/K mass ratio, ultrasonic time, and iron loading on light olefins' yield. CO chemisorption and TEM revealed that molybdenum plays a significant role in metal dispersion, leaving structural defects on CNTs support.

Additionally, H₂-TPR confirmed that K as promoter facilitates reducibility of Fe/CNTs catalysts, which promoted CO conversion in FTS. Compared with the un-promoted Fe/CNTs catalysts, addition of molybdenum as a promoter increased light olefins' selectivity by 33.4%, while potassium led to an increase in CO conversion by 96.3%. The optimum formulation (0.5K5Mo10Fe/CNTs) obtained the olefins' yield of 35.5%.

In the third phase the kinetic study of FTS was performed over the optimum bimetallic promoted catalyst (0.5K5Mo10Fe/CNTs) in a fixed-bed reactor by collecting experimental data over a wide range of industrially relevant reaction conditions ($P = 0.68\text{--}4.13\text{ MPa}$, $T = 270\text{--}290\text{ }^{\circ}\text{C}$, $\text{H}_2/\text{CO} = 1$, $\text{GHSV} = 2000\text{ h}^{-1}$). Based on the adsorption of carbon monoxide and hydrogen, twenty-two possible mechanisms for monomer formation during Fischer-Tropsch synthesis were proposed in accordance with the Langmuir-Hinshelwood-Hougen-Watson (LHHW) and Eley-Rideal (ER) adsorption theories. Kinetic parameters such as activation energy, adsorption enthalpies of H₂ and CO were estimated to be 65.0, -13.0, and -54.0 kJ/mol, respectively. Based on the developed kinetic model, the effects of reaction temperature and pressure were assessed on FTS product distribution. In addition, the Anderson-Schulz-Flory model was applied to further assess the reliability of the best fit mechanistic model for a wide range of hydrocarbon products.

In the fourth phase, techno-economic analysis (TEA) and life cycle assessment (LCA) of light olefin production in Fischer-Tropsch synthesis reaction were investigated via different scenarios. Data from a lab-scale experiment using the optimum bimetallic promoted catalyst (0.5K5Mo10Fe/CNTs) were used to simulate a plant to produce 1 kg of ethylene/h. The economic feasibility of light olefins production was estimated based on a comprehensive cash flow analysis. The net rate of return (NRR) was calculated to 5.6%, 7.4%, and 18.2% for the base scenario (scenario 1), scenario 2 with wastewater treatment, and scenario 3 with wastewater treatment-separation unit, respectively, which means the project is profitable from an economic perspective. The GHG emissions performance was measured as 77.5 g CO_{2-eq} per MJ ethylene confirming the significant GHG emissions decrease compared to petroleum-based fuels production (3686 g CO_{2-eq} per MJ ethylene).

ACKNOWLEDGEMENTS

I would like to express my sincere appreciation to my Ph.D. supervisors, Dr. Ajay K. Dalai, and Dr. Lifeng Zhang, for their support and guidance during my Ph.D. studies. Their constant encouragement and mentorship ensured that I completed this thesis.

I would like to express my deepest appreciation to the members of my advisory committee: Dr. Mehdi Nemati, Dr. Jafar Soltan Mohammadzadeh, Dr. Catherine Niu, and Dr. Robert Scott for their constructive comments and suggestions they have given me throughout my doctorate program. Their valuable advice and suggestions helped me to improve the quality of my work.

I would like to extend my thanks to Mr. RLee Prokopishyn, Ms. Rosa Do Phuong, and Mrs. Jayasinghe Dushmanthi for their technical assistance in the laboratory. I am also grateful to Dr. Jianfeng Zhu (Saskatchewan Structural Sciences Center) for helping me with XRD analysis and Dr. Jason Maley (Saskatchewan Structural Sciences Center) for helping me with Raman Spectroscopy analysis.

I am grateful to the financial support of my research, from the Natural Sciences and Engineering Research Council of Canada (NSERC), BioFuel Net and Canada Research Chair (CRC) Program. The financial assistance of the Department of Chemical and Biological Engineering at the University of Saskatchewan (Graduate Teaching and Laboratory Assistantships) is greatly appreciated.

My sincere thanks go to the other members of Dr. Dalai's Catalysis and Chemical Reaction Engineering (CCRE) research group, especially Mr. Girish Kamath, Dr. Venu Borugadda, Dr. Philip. E. Boahene, Dr. Sundar Vedachalam, and Dr. Sonil Nanda for their assistance and advice at every stage of this work.

My special thanks also go to my supportive friends including Zahra Teimouri, Biswa Patra, Dr. Biswajit Saha, and Amin who supported me with endless love and words of encouragement during the adversity period of my life.

Special thanks to my wife Mrs. Somaye Seraj and my lovely family, Mr. Nadali Yahyazadeh, Mrs. Shahla Khatami, Mr. Hamed Yahyazadeh, and Mr. Ashkan Yahyazadeh for their constant support and motivation. I would like to express my sincere gratitude to my parents-in-law, Tuba and Khalil Seraj.

DEDICATION

To My Spouse, Somaye, for being a great source of love, motivation, inspiration, and patience. I wish I could find the appropriate words to adequately thank her for the candor and all the support she continues to provide.

Table of Contents

PERMISSION TO USE	I
ABSTRACT.....	II
ACKNOWLEDGEMENTS	IV
DEDICATION	V
LIST OF TABLES.....	X
LIST OF FIGURES	XII
LIST OF NOMENCLATURE AND SYMBOLS.....	XVI
GLOSSARY OF TERMS.....	XIX
CHAPTER 1: INTRODUCTION AND THESIS OUTLINE	1
1.1 FISCHER-TROPSCH.....	1
1.2 KNOWLEDGE GAPS	3
1.3 HYPOTHESES	3
1.4 RESEARCH OBJECTIVES.....	4
1.5 ORGANIZATION OF THE THESIS	5
CHAPTER 2: LITERATURE REVIEW	8
2.1 ABSTRACT	8
2.2 INTRODUCTION	9
2.3 SYNGAS PRODUCTION TECHNOLOGIES	11
2.4 FISCHER-TROPSCH SYNTHESIS FOR LIGHT OLEFINS FROM SYNGAS	13
2.5 CATALYSTS FOR FISCHER-TROPSCH TO LIGHT OLEFINS (FTO).....	14
2.5.1 Catalyst active metal effects	15
2.6 METAL SUPPORT INTERACTION EFFECTS.....	27
2.6.1 Carbon nanotubes supported catalysts	28
2.6.2 Alumina, silica, and titania supported catalysts	29
2.7 PROMOTION EFFECTS	30
2.8 CURRENT MECHANISM OF FISCHER-TROPSCH SYNTHESIS REACTION.....	36
2.9 TECHNO-ECONOMIC ANALYSIS	42
2.10 FISCHER-TROPSCH SYNTHESIS PLANTS; LIFECYCLE ASSESSMENT	47
2.11 CONCLUSIONS	49
CHAPTER 3: EXPERIMENTAL SECTION.....	51
3.1 MATERIALS SECTION	51
3.2 SYNTHESIS AND PREPARATION OF CNTs SUPPORT AND CORRESPONDING CATALYSTS.....	51
3.2.1 Synthesis of CNTs support via catalytic chemical vapor deposition method	51
3.2.2 Acid treatment of pristine CNTs support	52
3.2.3 Preparation of Fe catalyst supported on CNTs	52
3.2.4 Preparation of KMo-promoted Fe catalyst supported on CNTs	53
3.3 CHARACTERIZATION TECHNIQUES OF SUPPORT AND CATALYSTS.....	53

3.3.1 N ₂ -adsorption-desorption measurement	53
3.3.2 Wide-angle X-ray diffraction (XRD)	53
3.3.3 Scanning electron microscope (SEM)	53
3.3.4 Transmission electron microscopy (TEM)	53
3.3.5 Inductively coupled plasma optical emission spectroscopy (ICP-OES)	54
3.3.6 X-ray photoelectron spectroscopy (XPS)	54
3.3.7 Raman spectroscopy	54
3.3.8 Fourier transform infrared (FTIR) spectroscopy	54
3.3.9 H ₂ -temperature programmed reduction (H ₂ -TPR)	54
3.3.10 CO ₂ -temperature programmed desorption (CO ₂ -TPD)	55
3.3.11 CO-chemisorption	55
3.3.12 Thermogravimetric analysis (TGA)	55
3.3.13 Synchrotron-based X-ray absorption (XAS)	55
3.4 FISCHER-TROPSCH SYNTHESIS	55
3.5 PRODUCT SAMPLING AND COMPOSITION ANALYSES	58
3.5.1 Gas chromatography (GC) analysis	58
3.5.2 Simulated distillation (Sim-Dist) analysis	58
3.6 KINETICS STUDIES OF FISCHER-TROPSCH SYNTHESIS	58
CHAPTER 4: OPTIMIZATION OF CARBON NANOTUBE GROWTH VIA RESPONSE SURFACE METHODOLOGY FOR FISCHER-TROPSCH SYNTHESIS OVER FE/CNTS CATALYST	60
4.1 ABSTRACT	60
4.2 MATERIALS AND METHODS	61
4.2.1 Materials	61
4.2.2 Methodology	61
4.3 RESULTS AND DISCUSSION	62
4.3.1 CNTs production: optimization establishment and analysis	62
4.3.2 Characterization of CNTs support and corresponding catalysts	67
4.3.3 Catalytic performance of Fe-based catalysts in FTS	77
4.4 CONCLUSIONS	83
CHAPTER 5: OPTIMIZATION OF LIGHT OLEFINS' YIELD IN FISCHER- TROPSCH SYNTHESIS USING CARBON NANOTUBES SUPPORTED IRON CATALYST WITH POTASSIUM AND MOLYBDENUM PROMOTERS	84
5.1 ABSTRACT	84
5.2 MATERIALS AND METHODS	85
5.2.1 Materials	85
5.2.2 Methodology	85
5.3 RESULTS AND DISCUSSION	86
5.3.1 Optimization of catalyst synthesis conditions in FTS	86
5.3.2 Characterization	91
5.3.3 Fischer-Tropsch synthesis	104
5.4 CONCLUSIONS	108

CHAPTER 6: COMPREHENSIVE KINETIC STUDY FOR FISCHER-TROPSCH REACTION OVER KMOFE/CNTS NANI-STRUCTURED CATALYST.....	110
6.1 ABSTRACT	110
6.2 MATERIALS AND METHODS	111
6.2.1 Materials	111
6.2.2 Methodology	111
6.3 RESULTS AND DISCUSSION.....	115
6.3.1 Catalyst characterization	115
6.3.2 Comprehensive kinetic study	126
6.3.3 Effects of temperature and pressure on selectivity	138
6.3.4 Comparison of Anderson-Schulz-Flory distribution with the mechanistic model	140
6.4 CONCLUSIONS	143
CHAPTER 7: FISCHER-TROPSCH TO LIGHT OLEFINS OVER BIMETALLIC PROMOTED FE/CNTS NANOCATALYST: TECHNO-ECONOMIC AND LIFE-CYCLE ASSESSMENT.....	145
7.1 ABSTRACT	145
7.2 MATERIALS AND METHODS	146
7.2.1 FT synthesis process	146
7.2.2 Simulation of the FTO process	146
7.2.3 Techno-economic analysis	147
7.2.4 Life cycle assessment	147
7.2.5 Sensitivity analysis	149
7.2.6 Analysis of different scenarios	149
7.3 RESULTS AND DISCUSSION.....	151
7.3.1 Process simulation	151
7.3.2 The material and energy balances of the FTO	151
7.3.3 Fixed capital costs	153
7.3.4 Operating costs	153
7.3.5 Sale revenues	154
7.3.6 Net profit	154
7.3.7 Techno-economic analysis	155
7.3.8 Sensitivity analysis	158
7.3.9 Life cycle assessment	164
7.4 CONCLUSIONS	166
CHAPTER 8: CONCLUSIONS AND RECOMMENDATIONS.....	168
8.1 OVERALL PROJECT OVERVIEW AND CONCLUSIONS	168
8.2 RECOMMENDATIONS	169
REFERENCES.....	170
APPENDIX A: EXPERIMENTAL CALIBRATIONS	210

APPENDIX B: PERMISSIONS FROM PUBLISHERS.....	212
---	------------

List of Tables

Table 2.1: Different FTS plants and their capacity	11
Table 2.2: Different synthesis methods of Fe-based catalysts for FTO.	17
Table 2.3: Different synthesis methods of Co-based catalysts for FTO.....	20
Table 2.4: Techniques for investigating the basicity and reducibility of FTS catalysts.....	24
Table 2.5: Techniques for investigating the dispersion of active metal in catalysts.	26
Table 2.6: Light olefin selectivity of different Fe-based catalysts in FTO.	31
Table 2.7: Light olefin selectivity of different Co-based catalysts in FTO.....	35
Table 2.8: A summary of some kinetic studies predicating the FT reaction.	38
Table 2.9: Synchrotron methods employed in characterization of Fe and Co FTS catalysts.	42
Table 2.10: Techno-economic assessment of Fischer-Tropsch synthesis.	45
Table 2.11: Lifecycle assessment of Fischer-Tropsch synthesis.	48
Table 4.1: Process factors and their levels for CNTs production.	62
Table 4.2: Experimental design matrix with the value of responses.	62
Table 4.3: ANOVA for CNTs yield (CY) obtained by cubic polynomial model.	63
Table 4.4: ANOVA for CNTs graphitic structure (I_D/I_G) obtained by cubic polynomial model.....	65
Table 4.5: Textural properties of as-grown CNTs and corresponding catalysts.	69
Table 4.6: Quantitative results of H ₂ consumption for calcined catalysts obtained by H ₂ -TPR.....	76
Table 4.7: Selectivity and activity of Fe-based catalysts in Fischer-Tropsch synthesis.	79
Table 5.1: Factors and their levels considered in 2 ³ full factorial design.....	86
Table 5.2: 2-level full factorial design matrix with experimental response.	86
Table 5.3: Analysis of variance for olefins' yield obtained by 2-level full factorial model. .	87
Table 5.4: Monometallic promoted and un-promoted Fe/CNTs catalysts performance at 280 °C, 3.45 MPa, GHSV = 2000 h ⁻¹ , H ₂ /CO = 1, and TOS = 24 h.	90
Table 5.5: FTS results of the optimum KMoFe/CNTs catalyst in comparison with its monometallic promoted and un-promoted counterparts (280 °C, 3.45 MPa, GHSV = 2000 h ⁻¹ , H ₂ /CO = 1, and TOS = 24 h).	91
Table 5.6: Metal contents and textural properties of the synthesized CNTs support, fresh un-promoted and promoted Fe/CNTs catalysts.	93
Table 5.7: Average particle size of iron oxide for fresh and spent catalysts by XRD.	95
Table 5.8: H ₂ uptake by un-promoted and promoted Fe/CNTs catalysts.....	97
Table 5.9: Raman data for CNTs support, un-promoted, and promoted calcined catalysts..	99
Table 5.10: Raman data for un-promoted and promoted Fe/CNTs spent catalysts.....	100
Table 5.11: Basicity of the CNTs, un-promoted and promoted Fe/CNTs catalysts.....	101
Table 5.12: Catalytic performance of un-promoted and promoted Fe/CNTs catalysts in FTS (T = 280 °C, P = 3.45 MPa, H ₂ /CO = 1, GHSV = 2000 h ⁻¹ , and TOS = 24 h).	105
Table 5.13: Catalytic performance of un-promoted and promoted Fe/CNTs catalysts in FTS (T = 280 °C, P = 3.45 MPa, H ₂ /CO = 1, GHSV = 2000 h ⁻¹ , and TOS = 119 h).	108

Table 6.1: The experimental conditions and FTS results for kinetic study at $P_{\text{tot}} = 0.7\text{-}4.1$ MPa, $T = 270\text{-}290$ °C, $H_2/CO = 1$, and $GHSV = 2000$ h ⁻¹ in a fixed-bed reactor.	113
Table 6.2: Average particle size of iron oxide for the fresh and spent catalysts by XRD. .	116
Table 6.3: Physicochemical properties of the CNTs support and bimetallic promoted catalyst.	117
Table 6.4: Different mechanisms of monomer formation via elementary reactions for FTS.....	128
Table 6.5: CO consumption rate equations for different mechanisms.	132
Table 6.6: Kinetic parameters and their values for the FT-I kinetic model.	137
Table 6.7: Summary of several FTS kinetic studies on Fe catalysts compared with this study.....	138
Table 7.1: Midpoint method impact categories computed in the LCA.	149
Table 7.2: Summary of operating conditions for different unit operation.	151
Table 7.3: Summary of economic assumptions.....	156
Table 7.4: Equipment amplification factors and their percentages of the installation cost.	157
Table 7.5: Important assumptions for measuring the overall production costs of FT liquids.....	158
Table 7.6: The cost of facilities.	158
Table 7.7: Fixed capital investments.	158
Table 7.8: The number of operators required for the FTS.....	161
Table 7.9: Summary of economic analysis.....	162
Table 7.10: LCA results for the FT plant located in Canada for a basis of 1 kg ethylene. .	164
Table 7.11: Comparison of LCA studies on biofuels, FT liquid fuels, and olefins.....	166

List of Figures

Figure 1.1: Block diagram of this Ph.D. research program.....	5
Figure 2.1: Schematic of MTO process.....	10
Figure 2.2: Hydrocarbon feedstocks that can be transformed into syngas.....	12
Figure 2.3: Standard unit configuration of syngas for all reformer types..	12
Figure 2.4: Technologies for conversion of different feedstocks into light olefins.	14
Figure 2.5: Schematic of synthesis methods proposed for χ -Fe ₅ C ₂ phase catalyst.	19
Figure 2.6: Schematic of the mechanism proposed for C-C chain's initiation, propagation, and termination over HCP and FCC Co catalysts.....	23
Figure 2.7: CH ₄ selectivity and TOF for Co/SiO ₂ catalysts of different sizes in FTS.	26
Figure 2.8: Schematic of soldering metal-promoted iron catalyst for FTO.	34
Figure 2.9: Product distribution in FT synthesis with respect to the chain growth probability (α).	37
Figure 2.10: Schematic representation of olefins' isomerization and the corresponding paraffin.....	38
Figure 2.11: (a-c) The activity and selectivity measurements of the Co/TiO ₂ catalyst during 48 h using GC and operando XRD; (d-f) Operando XAS Co K-edge spectra of Co/TiO ₂ during FTS (P: 1.6 MPa, TOS: 48 h, H ₂ /CO: 1, T: 220 °C)...	40
Figure 2.12: Block flowsheet of Fischer-Tropsch to light olefins (left) and Fischer- Tropsch to liquids (right) with percentage cost of installed equipment.	44
Figure 3.1: Schematic of the CVD reactor for CNTs growth.....	52
Figure 3.2: Schematic representation of Fischer-Tropsch reaction setup.	57
Figure 4.1: Response surface plots of CNTs yield with the combined effects of (a) Reaction temperature and reaction time; (b) Reaction temperature and iron loading.....	64
Figure 4.2: Graphical prediction of optimum conditions maximizing CNTs yield.....	64
Figure 4.3: Response surface plots of I_D/I_G ratio with the combined effects of (a) Iron loading and reaction time; (b) Reaction temperature and iron loading.....	66
Figure 4.4: Graphical prediction of optimum conditions considering I_D/I_G ratio as response.....	66
Figure 4.5: Experimental and theoretically predicted values for optimization responses (a) CNTs yield; (b) I_D/I_G ratio.	67
Figure 4.6: XRD patterns of (a) As-grown CNTs and Acid-treated CNTs; (b) Fresh catalysts after calcination; (c) Used FTS catalysts at 280 °C for 24 h; (d) N ₂ adsorption-desorption isotherms.	68
Figure 4.7: SEM microphotographs of acid-treated CNTs.	70
Figure 4.8: TEM micrographs and corresponding histograms of particle size distribution for catalysts.	72
Figure 4.9: Raman spectra of the synthesized CNTs before and after acid-treatment.	73
Figure 4.10: FTIR spectra of commercial CNTs, as-grown CNTs, and acid-treated CNTs.	74
Figure 4.11: TGA profile of as-grown CNTs, acid-treated CNTs, and 20Fe/CNTs-Syn under nitrogen atmosphere.....	75
Figure 4.12: H ₂ temperature programed reduction profile for fresh catalysts.....	76

Figure 4.13: XPS spectra (a) C1s; (b) Fe2p; (c) O1s of the fresh calcined catalysts.	77
Figure 4.14: CO conversion for FTS catalysts (process conditions: T = 280 °C, P = 2 MPa, H ₂ /CO = 1, TOS = 24 h, GHSV = 2000 h ⁻¹). The deviation of experimental data from average data points was unbalanced.	78
Figure 4.15: Hydrocarbons produced by FTS catalysts (process conditions: T = 280 °C, P = 2 MPa, H ₂ /CO = 1, TOS = 24 h, GHSV = 2000 h ⁻¹).	80
Figure 4.16: (a) FTS liquid products; (b) Boiling point distribution for liquid products obtained by FTS catalysts.	81
Figure 4.17: CO conversion of 20Fe/CNTs-Syn, 20Fe/CNTs-Com, and 20Fe/Al ₂ O ₃ as a function of time-on-stream.	82
Figure 5.1: 2D contour and 3D surface plots of olefins' yield with simultaneous effects of (a,b) Mo/K mass ratio and iron loading; (c, d) Mo/K mass ratio and ultrasonic time.	89
Figure 5.2: Diagnostic plots (a) Predicted versus actual; (b) Residual versus predicted for olefins' yield as response.	89
Figure 5.3: (a) N ₂ adsorption-desorption isotherms of acid-treated CNTs and the prepared Fe/CNTs catalysts; (b) Pore size distribution of corresponding Fe/CNTs catalysts.	92
Figure 5.4: XRD spectra for the un-promoted and promoted Fe/CNTs calcined catalysts.	94
Figure 5.5: XRD spectra for the un-promoted and promoted Fe/CNTs spent catalysts.	94
Figure 5.6: TEM micrographs and particle size distribution histograms (a) 10Fe/CNTs; (b) 0.5K10Fe/CNTs; (c) 5Mo10Fe/CNTs; (d) 0.5K5Mo10Fe/CNTs.	96
Figure 5.7: H ₂ -TPR profiles of promoted and un-promoted Fe/CNTs catalysts.	97
Figure 5.8: Raman spectra of the CNTs support, un-promoted and promoted Fe/CNTs catalysts.	98
Figure 5.9: Raman spectroscopy of the un-promoted and promoted Fe/CNTs spent catalysts.	99
Figure 5.10: CO ₂ -TPD profiles of the CNTs, un-promoted and promoted Fe/CNTs catalysts.	101
Figure 5.11: (a) Wide XPS survey; (b) C1s; (c) Fe2p of the un-promoted and promoted fresh Fe/CNTs catalysts.	102
Figure 5.12: (a) Wide XPS survey; (b) C1s; (c) Fe2p of the un-promoted and promoted spent catalysts.	103
Figure 5.13: (a) TGA; (b) DTG thermograms of un-promoted and promoted fresh catalysts.	104
Figure 5.14: CO conversion as a function of TOS for unpromoted and promoted Fe/CNTs catalysts. Operating conditions: T = 280 °C, P = 3.45 MPa, H ₂ /CO = 1, GHSV = 2000 h ⁻¹ , and TOS = 119 h.	107
Figure 6.1: Schematic representation of Fischer-Tropsch reaction setup.	111
Figure 6.2: XRD pattern of synthesized CNTs with 0.5K5Mo10Fe/CNTs fresh and spent catalysts.	116
Figure 6.3: (a) Nitrogen adsorption-desorption isotherms; (b) Pore size distribution of CNTs support and 0.5K5Mo10Fe/CNTs fresh catalyst.	117

Figure 6.4: XPS spectra of 0.5K5Mo10Fe/CNTs calcined catalyst (a) Full-range scan; (b) Fe2p core level; (c) C1s core level; (d) Mo3d core level; (e) O1s core level.....	118
Figure 6.5: XPS spectra of 0.5K5Mo10Fe/CNTs spent catalyst (a) Full-range scan; (b) Fe2p core level; (c) C1s core level; (d) Mo3d core level; (e) O1s core level.	120
Figure 6.6: Fe K-edge XANES spectra for 0.5K5Mo10Fe/CNTs calcined and spent catalysts by means of fluorescence yield (FY).	122
Figure 6.7: Fe K-edge EXAFS spectra in R-space for 0.5K5Mo10Fe/CNTs calcined and spent catalysts by means of fluorescence yield (FY).	123
Figure 6.8: Mo L3-absorption edge EXAFS spectra in R-space for 0.5K5Mo10Fe/CNTs calcined and spent catalysts by means of fluorescence yield (FY).	124
Figure 6.9: (a,b) SEM and elemental mapping of the calcined catalyst; (c,d) TEM images of the calcined catalyst; (e,f) TEM images of the calcined and spent catalyst (0.5K5Mo10Fe/CNTs) with particle size distribution (PSD). PSDs of the catalysts (red boxes) were fitted by a sum of Gaussian functions (black line).	125
Figure 6.10: CO conversion as a function of the syngas flow rate at $T = 280\text{ }^{\circ}\text{C}$, $P = 4.1\text{ MPa}$, and $\text{GHSV} = 2000\text{ h}^{-1}$	126
Figure 6.11: CO conversion as a function particle size at $T = 280\text{ }^{\circ}\text{C}$, $P = 4.1\text{ MPa}$, and $\text{GHSV} = 2000\text{ h}^{-1}$	127
Figure 6.12: Comparison of the experimental and mechanistic CO consumption rates over 0.5K5Mo10Fe/CNTs catalyst in FTS.	136
Figure 6.13: The mechanistic CO consumption rates versus experimental CO consumption rates using 0.5K5Mo10Fe/CNTs catalyst in FTS.	136
Figure 6.14: Effects of FTS temperature on selectivity of hydrocarbons at $P = 4.1\text{ MPa}$ and $\text{H}_2/\text{CO} = 1$	140
Figure 6.15: Effects of FTS pressure on selectivity of hydrocarbons at $T = 280\text{ }^{\circ}\text{C}$ and $\text{H}_2/\text{CO} = 1$	140
Figure 6.16: Comparison between the mechanistic model and ASF model ($\alpha = 0.76$) at $T = 280\text{ }^{\circ}\text{C}$, $P = 4.1\text{ MPa}$ and $\text{H}_2/\text{CO} = 1$	143
Figure 7.1: Simplified block diagram of the FT system to produce light olefins (dotted boxes indicate scenarios).	148
Figure 7.2: FT simulation diagram for production of light olefins (scenario 1).	150
Figure 7.3: FT simulation diagram with wastewater treatment section (scenario 2).	150
Figure 7.4: FT simulation diagram with wastewater treatment and separation units (scenario 3).	150
Figure 7.5: (a-c) Mass and energy balances of the FT process for scenario 1-3.	152
Figure 7.6: (a-c) Sensitivity of operating cost for the scenarios; (d) Effects of syngas flow rate on capital expenditure.	160
Figure 7.7: Cost break-down of the operating expenditure for different scenarios.	160
Figure 7.8: <i>MIRR</i> of FT process in different cases as a function of syngas rate for 0.5K5Mo10Fe/CNTs catalyst (a): $\text{H}_2/\text{CO} = 1$; (b): $\text{H}_2/\text{CO} = 2$	162
Figure 7.9: The FT plant costs in different cases as a function of syngas rate for 0.5K5Mo10Fe/CNTs catalyst (a): $\text{H}_2/\text{CO} = 1$; (b): $\text{H}_2/\text{CO} = 2$	163

Figure 7.10: Impact of variations in plant capacity on (a) Profitability index; (b)	
Depreciation cost.....	163
Figure 7.11: Comparison of the LCA results of light olefins' production in different	
scenarios using 0.5K5Mo10Fe/CNTs catalyst.....	165

List of Nomenclature and Symbols

AGR	Acid-gas removal
ANOVA	Analysis of variance
AP	Acidification potential
ASF	Anderson-Schulz-Flory
BgTL	Biogas to liquid
BJH	Barret-Joyner-Halenda
BOP	Balance of plant
BPD	Barrel per day
BTL	Biomass-to-liquid
CCD	Central composite design
CCVD	Catalytic chemical vapor deposition
CEDnr	Cumulative non-renewable energy demand
CEPCI	Chemical engineering plant cost index
CTO	Coal-to-olefins
CVD	Chemical vapor deposition
CY	CNT yield
DAC	Direct air capture
DC	Direct cost
DCFR	Discounted cash flow rate of return
DME	Dimethyl ether
EP	Eutrophication potential
ER	Eley-Rideal
EXAFS	Extended X-ray absorption fine structure
FCI	Fixed capital investment
FTL	Fischer-Tropsch liquid
FTO	Fischer-Tropsch to olefins
FTS	Fischer-Tropsch synthesis
FU	Functional unit
GHG	Greenhouse gas
GHSV	Gas hourly space velocity
GWP	Global warming potential
IC	Indirect cost
IRR	Internal rate of return
LACCR	levelized annual capital charge rate
LCA	Life cycle analysis
LCIA	Life cycle impact assessment
LHHW	Langmuir-Hinshelwood-Hougen-Watson
MC	Maintenance cost
MIRR	Modified internal rate of return
MSP	Minimum selling price
MTO	Methanol to olefins
NPV	Net present value
NRR	Net return rate
OC	Operating cost
OCM	Oxidative coupling of methane
ODP	Ozone layer depletion potential
OTO	Oil-to-olefins

O&M	Operating and maintenance
PBP	Payback period
PEI	Potential environmental impacts
PI	Profitability index
R	Universal gas constant, 8.314 (J/mol K)
RDS	Rate determining step
SARE	Sale, administration, and research expenses
SC	Steam cracking
SR	Sale revenue
SXRMB	Soft X-ray microcharacterization beamline
TAC	Total annualized cost
TC	Total cost
TCI	Total capital investment
TDC	Total direct cost
TDIC	Total direct and indirect cost
TEA	Techno-economic analysis
TIC	Total indirect cost
TOC	Total operating cost
TPI	Total project investment
TPR	Total plant revenue
DCFR	Discounted cash flow rate of return
WC	Working capital
WGS	Water-gas shift
XANES	X-ray absorption near edge structure
XAS	X-ray absorption spectroscopy

List of Symbols

b_{CO}	Adsorption coefficient of CO (mol/min.g)
b_{H_2}	Adsorption coefficient of H ₂ (mol/min.g)
C_v	The concentration of free sites
E_a	Activation energy (kJ/mol)
F^0_{CO}	Molar inlet flow rate of CO (mol/min)
k	Rate constant of reaction (mol/g _{cat} .min)
$k_{ads,CO}$	Rate constant of adsorption of CO (mol/g _{cat} .min)
k_{ads,H_2}	Rate constant of adsorption of H ₂ (mol/g _{cat} .min)
$k_{des,CO}$	Rate constant of desorption of CO (mol/g _{cat} .min)
k_{des,H_2}	Rate constant of desorption of H ₂ (mol/g _{cat} .min)
P_{CO}	The pressure of CO (MPa)
P_{H_2}	The pressure of H ₂ (MPa)
r_{CO}	Rate of CO consumption (mol/g _{cat} .min)
W_i	The catalyst weight (g)
X_{CO}	The conversion of CO (% moles)

Greek Letters

θ_C	Surface occupied with carbon
θ_H	Surface occupied with hydrogen
θ_O	Surface occupied with oxygen
*	Unoccupied active sites

GLOSSARY OF TERMS

Net present value (NPV)

The final cumulative discounted cash flow value at project conclusion is called net present value.

Fixed Capital Investment (FCI) and Total Capital Investment (TCI)

Fixed capital Investment (FCI) is defined as the money spent on the required process equipment. FCI cannot be recovered easily as it is considered financially immobile. Working capital is the required money that is spent to bring the plant to a productive state. Working capital may not be lost and is partly returned to the investors at the end of the plant's life. Total capital investment (TCI) is calculated as the sum of FCI and working capital. TCI is considered to be the total amount of money that is spent by investors to build and operate a plant.

CHAPTER 1: Introduction and Thesis Outline

1.1 Fischer-Tropsch

The organization of the petroleum exporting countries (OPEC) has estimated the petroleum oil with increasing demand of 382 million barrels of oil equivalent per day (mboe/d) to be the main energy source up to 2040. Processing heavy petroleum oil with low API gravity to the light olefins including ethylene, propylene, butene, and butadiene are faced with many challenges. These challenges are related to impurities such as sulfur, asphaltene, nitrogen, and metals in heavy petroleum oil. On the other hand, the increased use of fossil fuels is one of the prime reasons for global warming leading to climate change. To achieve a balance between supply and demand, there are alternative technologies for light olefins production in addition to common techniques like steam cracking including steam catalytic cracking to olefin, synthesis gas to olefin and methanol to olefin (Alotaibi et al., 2018). The olefin production can be conducted via different intermediates including methanol, ethanol, and dimethyl ether through non-oil indirect routes of methanol to olefin (MTO), ethanol to olefin (ETO), dimethyl ether to olefin (DMTO) as well as the direct route of Fischer-Tropsch to olefin. Among them the Fischer-Tropsch to olefin as the heart of gas to liquid conversion processes is the only candidate for light olefin production without any intermediate steps (Di et al., 2019a).

FTS has been introduced as an established and reliable technology to produce synthetic hydrocarbons including methane, olefins, long chain alkanes, liquid fuels (diesel fuels and gasoline), as well as oxygenates like alcohols, aldehydes, ketones, and carboxylic acids directly from syngas. The complex chemistry of the FT process is attributed to a broad range of reactions occurring with two main groups of the desired products in the form of alkanes and alkenes. Fischer-Tropsch synthesis to olefins (FTO) including C_2 - C_4 alkenes is of great importance in modern chemical industries.

So far only Fe and Co catalysts have been proven economically feasible for FTS on industrial scales. Besides, Fe is an ideal FTS catalyst for converting H_2 -lean syngas derived from biomass and coal due to its high water-gas-shift activity producing more hydrogen. The major challenges faced in FTS are catalyst selectivity and activity which are affected by metal reactive sites, dispersion, and loading, as well as support and catalyst preparation method

(Zhang et al., 2003). It has been reported that Fe supported on alumina or silica forms mixed oxides, thus suggesting a strong metal-support interaction. These aluminates and silicates are difficult to reduce, and the active iron carbide phase is hindered as a result (Torres Galvis et al., 2012).

Carbon materials including activated carbon (AC) and carbon nanotubes (CNTs) were evaluated for FT catalyst support (Bahome et al., 2007; Chen et al., 2007; Pan et al., 2007). Carbon nanotubes were found to be a promising support for FT catalysts due to its surface chemical inertness, pore size distribution in the range of mesoporous to macroporous, and resistance to harsh acid/base medium (Serp et al., 2003). However, Fe catalysts supported on CNTs have suffered deactivation caused by metal site agglomerations (Abbaslou et al., 2009b). Structural promoters have shown a favorable performance for metal active site stabilization. Molybdenum can be highly dispersed on the support and its addition improves Fe dispersion (Malek Abbaslou et al., 2011). It is believed that catalytic performance of iron catalysts can be affected by encapsulation of iron nanoparticles inside of carbon nanotubes and promotion with bismuth in FTO (Gu et al., 2020a). It is also stated that carbon nanomaterial supported Fe catalysts are more likely to be selective to light olefins compared to common supports like alumina and silica (Torres Galvis et al., 2012). Given the weak metal-support interaction of carbon nanotubes and iron, high selectivity toward light olefins in FT reaction is suggested. It is of interest to study promoted iron catalysts supported on carbon nanotube for direct production of light olefins using syngas. Therefore, fabrication of carbon nanotubes supported iron catalysts, modification of the catalyst using suitable structural promoters and optimization of catalytic test for light olefins in FT synthesis are the focus in this research.

Response surface methodology and statistical techniques are employed to study influential parameters like syngas feed ratio, total pressure, and reaction temperature considering CO conversion and light olefins' selectivity as responses. Moreover, kinetic study helps to obtain a proper equation for CO consumption rate and reasonable mechanism. In FTS, due to various reaction pathways, prediction of reaction mechanisms is quite complicated. Furthermore, the FTS commercialization is mostly limited due to economically competitive energy markets (Rafati et al., 2017). Life cycle assessment (LCA) is a tool used to study the environmental impacts, energy consumptions, and GHG emissions of a product or process across the supply chain throughout its lifetime. In the U.S., fossil fuel combustion contributes 85% of the net

GHG emissions, and alternative sources of energy are being developed aiming to decrease the dependence on fossil fuels (Okeke et al., 2020a).

According to the literature, light olefins as the main building blocks for a variety of chemical industries can be produced via Fischer-Tropsch synthesis in the presence of Fe-based catalysts. The catalytic performance of Fe-based catalysts can be improved by implementing three different aspects as follow:

- 1- An effective catalyst preparation method with operating conditions being optimized.
- 2- Carbon nanotubes (CNTs) as support incorporating Fe particles inside the tubes thus enhancing catalyst stability.
- 3- Dual promoters e.g., KMo improving the yield of light olefins due to change in electronic properties of CNTs support.

The FT reactor design and techno-economic feasibility as well as environmental impacts of the process are crucial factors in commercialization of FT to light olefins plant.

1.2 Knowledge gaps

According to the literature review (Chapter 2) on production of light olefins via Fischer-Tropsch synthesis, the knowledge gaps were categorized as follow:

- While there are some literatures available on carbon materials supported FT catalysts, optimization of CNTs characteristics in a CCVD reactor for further use as FT catalyst supports is missing from the literature.
- Addition of molybdenum and potassium as promoters to CNT supported iron catalyst for FTS is rare in the literature.
- Kinetic study of the most active KMo-promoted Fe catalysts supported on CNTs for light olefins production via FT synthesis and their deactivation study are rare in the literature.
- There has not been any study on the techno-economic feasibility and life cycle analysis (LCA) of FT synthesis to light olefins with these catalysts.

1.3 Hypotheses

Based on the above-mentioned knowledge gaps, the hypotheses are listed as below:

- Optimization of CNTs characteristics such as the yield and graphite purity of CNTs in a CCVD reactor will provide high quality CNTs for FT catalyst support. It is postulated that

acid post treatment will enhance graphite purity while causing some defects on CNTs structure increasing the metal dispersion during impregnation for FT catalyst.

- High selectivity to light olefins in FT synthesis for Fe/CNTs catalyst can be achieved using Mo and K as promoters due to interaction of metals and carbon materials. It is hypothesized that these promoters will improve the reducibility of iron oxide while the activity of catalyst and selectivity to light olefins will increase considerably.
- Kinetic study of the most active KMo-promoted Fe catalysts supported on CNTs for FT to light olefins will predict the best fit kinetic model and the deviation from ASF distribution.
- It is hypothesized that the techno-economic analysis (TEA) and life cycle assessment (LCA) would help to ascertain the commercialization potential while evaluating the environmental impacts associated with FTO.

1.4 Research objectives

The main objective of this research is to synthesize CNTs with high yield and purity in a CCVD reactor for FT catalyst support. Fe catalyst supported on CNTs is evaluated for light olefins' production in FTS. Bimetallic KMo-promoted Fe/CNTs catalysts are formulated for maximizing the light olefins' yield. The FT reaction kinetics are studied over the most active KMo-promoted iron catalyst. Finally, the techno-economic analysis and life cycle assessment of the FT synthesis for light olefins are performed. The following sub-objectives are considered to support the overall research goals as follows:

- Optimization of CNTs characteristics in a CCVD reactor using Fe/CaCO₃ catalysts with high yield and high graphite purity from acetylene. Application of Fe/CNTs catalysts for light olefins' production through FTS.
- Formulation of bimetallic KMo-promoted Fe/CNTs catalysts for maximizing light olefin s' production through FTS.
- Kinetic study of the most active bimetallic KMo-promoted Fe/CNTs catalyst to develop a kinetic model for FT synthesis to light olefins as well as assessing the catalyst deactivation behavior.
- Applying techno-economic analysis and life cycle assessment to determine the techno-economic feasibility and environmental impacts associated with the process.

1.5 Organization of the thesis

Figure 1.1 summarizes the research of this Ph.D. program. This PhD thesis is structured in eight chapters based on the manuscript-style thesis guideline of the College of Graduate and Postdoctoral studies. The literature review presented in Chapter 2 has been published in the *Reactions* journal. The manuscripts described in Chapters 4, 5, and 6 were published in *Journal of Catalysis Today*, *Journal of Applied Catalysis A: General*, and the *Canadian Journal of Chemical Engineering*, respectively.

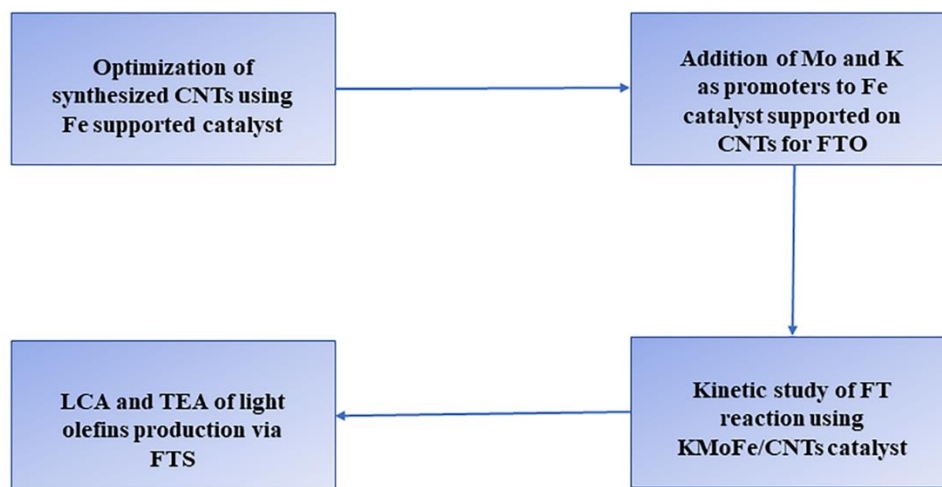


Figure 1.1: Block diagram of this Ph.D. research program.

Chapter 1 is organized as an introduction to the subject matter. Chapter 2 presents the most recent literature review on Fischer-Tropsch to light olefins (FTO) investigating the effects of active metals, promoters, and supports on the catalytic performance of FT catalysts. The experimental procedures conducted in this Ph.D. research are discussed in Chapter 3, including the chemicals and materials used, synthesis processes for CNTs support and corresponding catalysts, characterization techniques as well as FTS process. Following that, a brief description of subsequent chapters is provided to cover the research objectives and sub-objectives.

Chapter 4 describes FTS catalytic performance of Fe/CNTs supported catalyst under industrially relevant process conditions. CNTs were prepared through CCVD method using Fe/CaCO₃ and acetylene as catalyst and hydrocarbon source, respectively. Response surface methodology was adopted to specify the optimum process parameters maximizing CNTs yield and minimizing amorphous carbon structure in CNTs. The effects of CVD reaction time (30–

60 min), temperature (700–800 °C), and Fe catalyst loading (10–30 wt% Fe) were studied. Furthermore, the physio-chemical properties and FTS catalytic performance of the synthesized Fe/CNTs catalyst were compared with that of Fe catalysts supported on commercial CNTs and Al₂O₃.

Optimization of olefins' yield in FTS using bimetallic KMo-promoted Fe/CNTs catalyst is described in Chapter 5. A two-level full factorial design was applied for K- and/or Mo-promoted Fe/CNTs catalyst to investigate the effects of synthesis conditions including Mo/K mass ratio, ultrasonic time, and iron loading on light olefins' yield. Under industrially relevant conditions, a fixed-bed reactor was implemented to evaluate the activity, stability, and olefins' selectivity of the un-promoted and promoted iron catalysts. The catalysts were characterized in terms of iron particle size, CNTs structural defects, and iron oxidation state before and after FTS reactions.

The kinetic study of Fe-based FTS catalysts is essential for commercial process design, simulation, and optimization. However, the complex reaction networks during FTS make it quite challenging to model the kinetics and product selectivities. In Chapter 6, the kinetic study of FTS was performed over a potassium-molybdenum promoted iron catalyst in a fixed-bed reactor by collecting experimental data over a wide range of reaction conditions. This kinetic study was conducted to identify the best fit rate equation for FTS, as well as to determine the reaction rate constants using the multi-variable nonlinear regression method. In addition, the Anderson-Schulz-Flory model was applied to further assess the reliability of the best fit mechanistic model for a wide range of hydrocarbon products.

High energy demand and large capital costs have been the main drawbacks of FTS plants, which may challenge the economic viability of the FTS reaction. On the other hand, greenhouse gas (GHG) emissions and their destructive effects on climate change have become one of the critical environmental issues. Therefore, in Chapter 7, techno-economic analysis (TEA) and life cycle assessment (LCA) of FT to light olefins over KMo-promoted Fe/CNTs catalyst were investigated via different scenarios. Aspen plus simulation and OpenLCA software were used to analyze process economics and GHG emissions. A sensitivity analysis was also carried out regarding the effects of selectivity to light olefins and syngas feedstock rate on the economic aspect of the FT to olefins (FTO) using Aspen Plus simulation.

Finally, the overall conclusions and recommendations extracted from this Ph.D. research are provided in Chapter 8. The References section provides all references used in this study, and appropriate additional information including experimental calibrations and permissions from publishers are provided in Appendix A and Appendix B, respectively.

CHAPTER 2: Literature Review

The content of this chapter has been published in Reactions (Yahyazadeh et al., 2021) and a book chapter entitled “Conversion of syngas to olefins and green hydrocarbons through Fischer-Tropsch catalysis” (In Press). The permission to use the article in this thesis has been obtained from the MDPI as the journal holds the copyright as presented in Appendix B (Figure B.1).

Contribution of the Ph.D. Candidate

The manuscript was drafted by Arash Yahyazadeh with guidance, suggestions, and reviews provided by Dr. Ajay K. Dalai and Dr. Lifeng Zhang.

Contribution of this Chapter to Overall Ph.D. Research

This chapter gives an overview of FTS to produce light olefins as one the most important building blocks in chemical industry. The effects of metals, promoters and supports as the most influential parameters on the catalytic performance of catalysts were investigated. TEA and LCA of FTS plants were presented in terms of minimum fuel selling price and the potential for global environmental impacts, respectively, based on the most recent literature.

2.1 Abstract

Light olefins as one the most important building blocks in chemical industry can be produced via Fischer–Tropsch synthesis (FTS) from syngas. FT synthesis conducted at high temperature would lead to light paraffins, carbon dioxide, methane, and C₅₊ longer chain hydrocarbons. The present work focuses on providing a critical review on the light olefin production using Fischer–Tropsch synthesis. The effects of metals, promoters and supports as the most influential parameters on the catalytic performance of catalysts are discussed meticulously. Fe and Co as the main active metals in FT catalysts are investigated in terms of pore size, crystal size, and crystal phase for obtaining desirable light olefin selectivity. Larger pore size of Fe-based catalysts is suggested to increase olefin selectivity via suppressing 1-olefin readsorption and secondary reactions. Iron carbide as the most probable phase of Fe-based catalysts is proposed for light olefin generation via FTS. Smaller crystal size of Co active metal leads to higher olefin selectivity. The hexagonal close-packed (HCP) structure of Co has higher FTS activity than face-centered cubic (FCC) structure. Transition from Co to Co₃C is mainly

proposed for formation of light olefins over Co-based catalysts. Moreover, various catalyst deactivation routes are reviewed. Additionally, techno-economic assessment of FTS plants in terms of different costs including capital expenditure and minimum fuel selling price are presented based on the most recent literature. Finally, the potential for global environmental impacts associated with FTS plants including atmospheric and toxicological impacts is considered via lifecycle assessment (LCA).

2.2 Introduction

Olefins including ethylene, propylene, and butylene are considered the most widely used petrochemical feedstocks used as chemical intermediates for production of solvents, polymers, plastics, fibers, and detergents. The demand for ethylene as one of the important derivatives of olefins is over 155 million tons annually. The common method for olefin production is steam cracking (SC) of hydrocarbons. The trend of ethylene production using thermal cracking had a growth rate of 4% between 2007 and 2012 (Sadrameli, 2015). The ethylene production in Canada is based on ethane as a feed through steam cracking at high temperatures. From 2000 to 2010, it was reported that propylene production declined while ethylene production increased (Amghizar et al., 2017a).

Heavy petroleum oil with low API gravity containing different impurities such as sulfur, nitrogen, and metals brings about many challenges during its processing to light olefins. Petroleum oil is estimated to be the main energy source up to 2040 based on the OPEC's World Oil Outlook in 2016, with the energy demand reaching 382 million barrels of oil equivalent per day (mboe/d). As olefin production depends on oil fractions and steam cracking, the increasing demand for light olefins can cause strain on crude oil resources (Alotaibi et al., 2018). The non-oil routes for olefin production can be categorized in four groups, namely methanol to olefin (MTO), ethanol to olefin (ETO), dimethyl ether to olefin (DMTO), and the Fischer–Tropsch synthesis (FTS), which was developed in 1922 (van der Laan and Beenackers, 1999).

The technologies including MTO and FTS use methane as a feedstock for higher hydrocarbon production in an indirect way, while oxidative coupling of methane (OCM) is a direct route for ethylene and higher hydrocarbons production using methane. The H_2/CO ratio in CO-rich syngas needs to be adjusted by water–gas shift (WGS) reactions to eliminate the CO level, while resulting in CO_2 emissions (Amghizar et al., 2017b). However, the adjustment

of H_2/CO ratio is not necessary for H_2 -rich syngas. Synthesis of an intermediate like methanol or dimethyl ether is the basis of MTO and dimethyl ether-to-olefin (DMTO) processes to produce light olefins indirectly, while Fischer–Tropsch to olefins process is based on a one-step reaction consuming synthesis gas without adjustment of H_2/CO ratio (Amghizar et al., 2017b). An MTO plant schematic is shown in Figure 2.1 where methanol is consumed in an MTO reactor and light olefins are separated within two stages of separation.

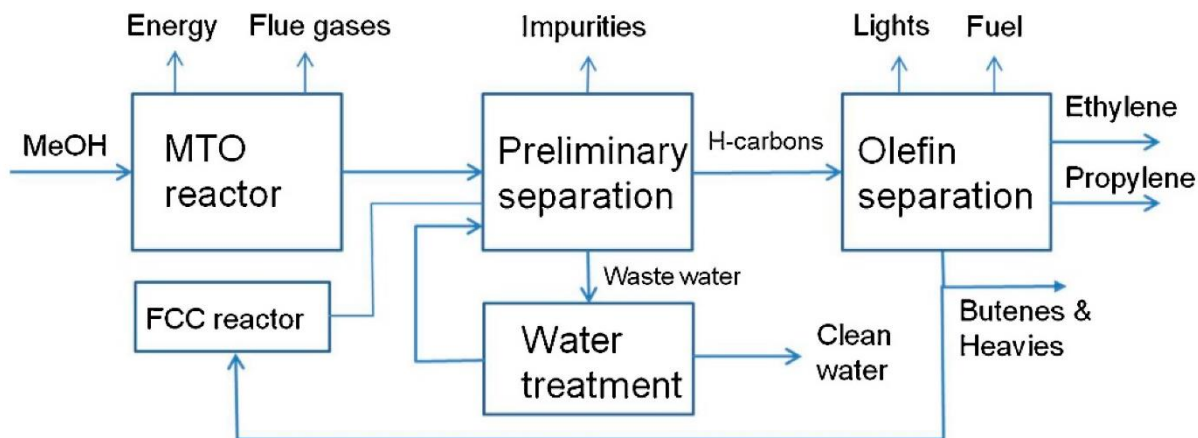


Figure 2.1: Schematic of MTO process. Reproduced with permission from (Dimian and Bildea, 2018).

Coal, natural gas, and biomass are the main source of synthesis gas for olefins production. Coal and biomass are converted to syngas via gasification, while the conversion of natural gas to syngas is carried out through steam reforming. The established FTS plants presented in Table 2.1 show a tendency toward natural gas compared to coal over the years (Ail and Dasappa, 2016). FTS provides two advantages compared to MTO. The lower cost of olefin production in FTS involves a one step process. Additionally, a wide range of raw materials can be used as feedstocks in FTS, with less wastewater production throughout the process (Zafari et al., 2020). Oil resource depletion and high cost of exploration has led scientists to develop alternative feedstocks for the olefins production. Biomass and waste streams including solid plastic waste or municipal waste are good candidates for future use in olefins production, indicating that FTS can be regarded as an environmentally friendly and economical process for light olefins production (Di et al., 2019b).

Table 2.1: Different FTS plants and their capacity (Ail and Dasappa, 2016; Lewis, 2013).

Company	Carbon source	Capacity (b/d)	Commissioning date
Sasol	Coal	2500	1955
Sasol	Coal	85,000	1980
Sasol	Coal	85,000	1982
MossGas	Natural gas	30,000	1992
Shell	Natural gas	12,500	1993
Sasol/Qatar Petroleum	Natural gas	34,000	2006
Sasol Chevron	Natural gas	34,000	2007
Shell	Natural gas	140,000	2009
Sasol/USA	Natural gas	96,000	2018
Sasol/Canada	Natural gas	96,000	2020

So far only iron and cobalt catalysts have been proven economically feasible on an industrial scale for FTS. However, iron possessing high water–gas-shift (WGS) activity compared to cobalt, can be an ideal catalyst for FTS. Selectivity is the most important challenge in the FTS process. In this process, the catalyst activity and selectivity are influenced by the nature and structure of support, nature of metal, reactive sites, metal dispersion, metal loading, and catalyst preparation method (Zhang et al., 2003). Moreover, the addition of promoting agents to catalysts significantly increases the activity and selectivity of catalysts toward a specific range of products, e.g., light olefins. Therefore, to optimize the selectivity of FTS to light olefins, conditions favoring high olefin to paraffin ratio should be achieved.

2.3 Syngas production technologies

The abundant supply of natural gas coupled with the increasing energy demand have prompted interest in GTL technologies for producing transportation fuels. Figure 2.2 shows different hydrocarbon feedstocks that can be converted into syngas via gasification, reforming, and reduction technologies. Three GTL processes were evaluated for various syngas technologies considering water generation and greenhouse gas (GHG) emissions by Gabriel et al (Gabriel et al., 2014). Heat and mass integration techniques, together with water and power production were used in this study to benchmark the process. The syngas production section as illustrated in Figure 2.3 consists of three technologies such as autothermal reforming (ATR),

partial oxidative reforming (PO_x), and steam methane reforming (SMR). ATR exhibited the best overall performance in terms of potential water production.

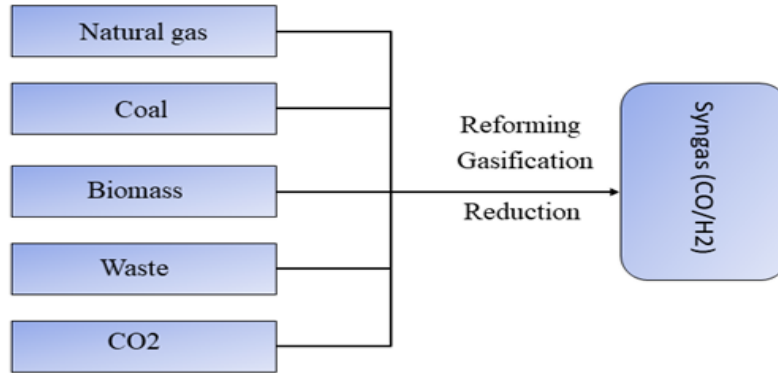


Figure 2.2: Hydrocarbon feedstocks that can be transformed into syngas. Reproduced with permission from (K. Cheng et al., 2017).

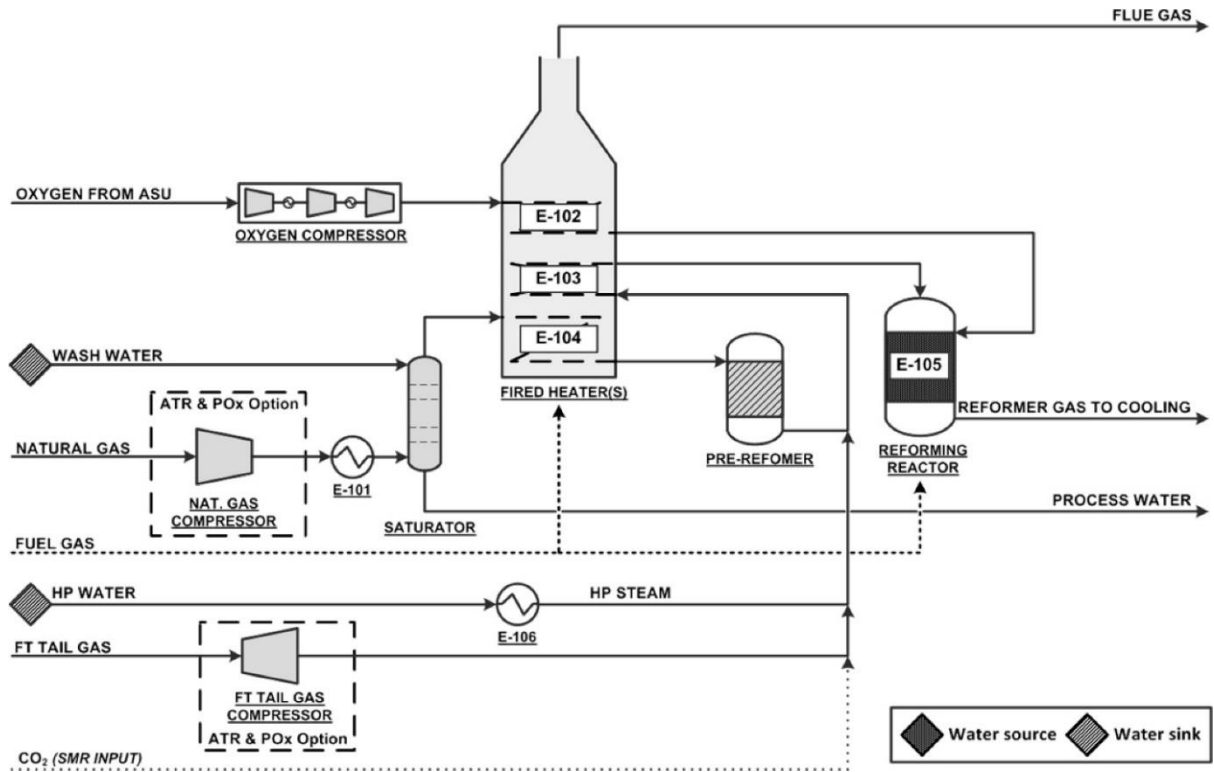


Figure 2.3: Standard unit configuration of syngas for all reformer types. Reproduced with permission from (Gabriel et al., 2014).

2.4 Fischer-Tropsch synthesis for light olefins from syngas

Light olefins including ethylene and propylene which are considered the key components of the chemical industry, can be derived from steam cracking (SC) of hydrocarbons (Amghizar et al., 2017b). Due to a comprehensive economic analysis carried out by Zhao et al. the conventional SC process is more economically attractive compared with other technologies (Zhao et al., 2021). Figure 2.4 summarizes different technologies for olefin production using feedstocks such as crude oil, natural gas, coal, and biomass. The cost of raw material was the main parameter influencing the total production cost (TPC) of different production methods (Gholami et al., 2021). In China due to large coal reserves, alternative technologies such as methanol-to-olefins (MTO) and methanol-to-propylene (MTP) have been developed to achieve lower production costs of olefins (Zhao et al., 2017). MTO and dimethyl ether to olefins (DTO) reactions have been compared in terms of products distributions and catalyst performance (Behbahani et al., 2014). The light olefins' selectivity of 77-78.5% was achieved at a reaction temperature ranging from 400 to 460 °C in the presence of a synthesized SAPO-34 catalyst during MTO reaction. The small and uniform catalyst crystals, with a high surface area and moderate acid sites in SAPO-34 catalyst enhanced the catalyst stability and selectivity to light olefins in MTO reaction. Although DTO and MTO reaction provide similar results in terms of kinetics and selectivities at higher temperatures, DTO reaction results in a lower fraction of C₅₊ compared with MTO reaction.

The oxidative coupling of methane (OCM) producing light olefins from natural gas can be improved using advanced catalysts and O₂ feeding (Spallina et al., 2017). The OCM process including catalytic oxidation of methane was compared with the conventional methods such as steam cracking and dehydration of ethanol for producing ethylene (Alkathiri et al., 2022). Although OCM can be an attractive method in the ethylene market, it requires a very high temperature for the reaction. The pinch analysis of the OCM process was performed to save a large amount of heating and cooling utilities at the optimal value of the minimum heat transfer temperature difference (ΔT_{\min}).

To prevent an imminent environmental collapse, FTS is a strategic technology for production of high value hydrocarbons, following a polymerization-like mechanism (Garona et al., 2021). The FTS process as a century-old technology uses iron or cobalt catalysts. Recently, the most influential factors in the catalytic performance of catalysts in FTS was

reviewed by Yahyazadeh et al. (Yahyazadeh et al., 2021). The decrease in the particle size of cobalt catalysts affects FTS selectivity toward lighter hydrocarbons such C₂-C₄. The most probable Fe phase for FT to light olefin is iron carbide including χ -Fe₅C₂, ϵ -Fe₂C, ϵ' -Fe_{2.2}C, and Fe₇C₃. The basicity of catalysts as well as phase transition during reducibility study is influenced by addition of alkali metal promoters e.g., Li, Na, and K. Catalyst deactivation in FTS is related to the type of support material, promoter, and synthesis method. It was reported that confinement of iron nanoparticles inside CNTs support protected metals from deactivation (Gu et al., 2019a). The sensitivity of cobalt to impurities is not negligible and promoted core-shell cobalt-based catalysts with an enhanced sintering resistance would be a promising option for FT to light olefins.

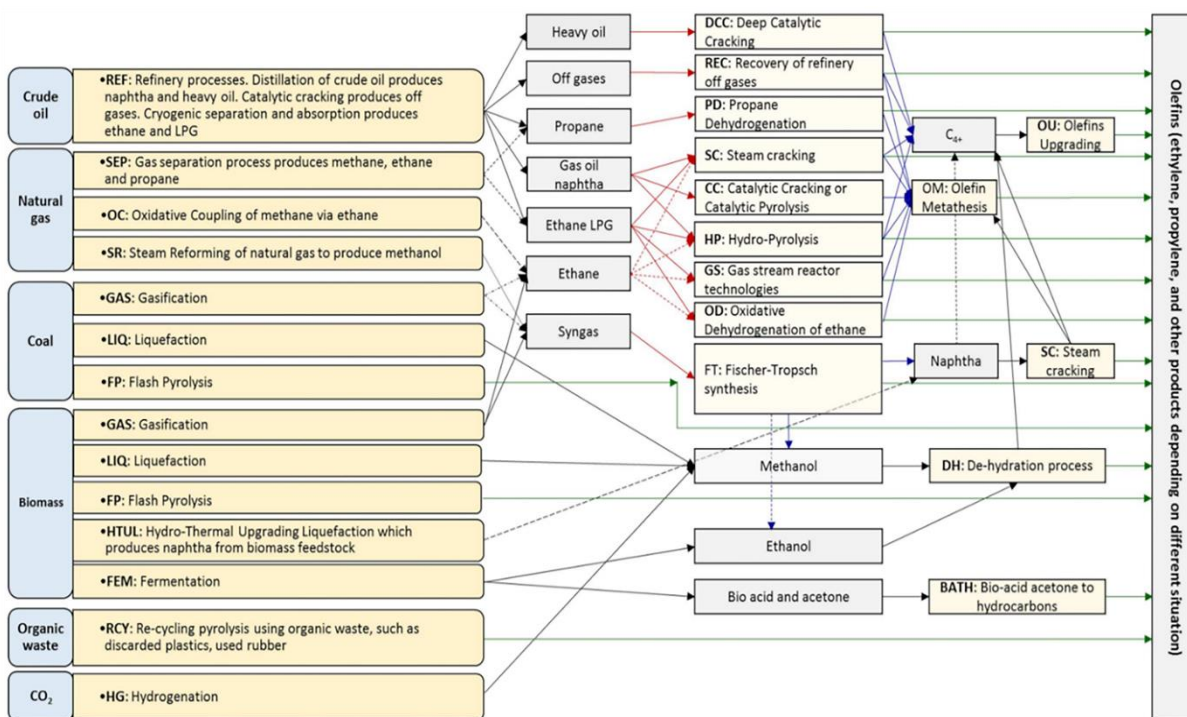


Figure 2.4: Technologies for conversion of different feedstocks into light olefins. Reproduced with permission from (Gholami et al., 2021).

2.5 Catalysts for Fischer-Tropsch to light olefins (FTO)

Generally, catalyst selectivity is based upon four factors including bond strength, coordination, ensemble, and template properties. The principle of bond strength is the electronic characteristics of the atoms involved. The number of possible reactions in the FTS

is influenced by bond strength varying from no chemisorption for weak bonds to slow desorption for strong bonds (Sachtler, 1981). Catalyst basicity, dispersion, active metals, and promoters as well as support interaction can influence the selectivity of FTS toward light olefins. Ponec et al. (Ponec, 1979) linked the olefins selectivity to electronic and geometric factors. Moreover, Biloen et al. (Biloen et al., 1983) asserted that whenever a molecule contacts the catalyst surface, the reactants react due to the chemistry and geometry of the catalyst active sites.

2.5.1 Catalyst active metal effects

Transition metals capable of syngas ($\text{H}_2 + \text{CO}$) adsorption and reducibility of metal oxides are used as FTS catalysts. Transition metals belonging to groups III-VI of the periodic table have tendency to form highly stable oxides that are difficult to be reduced in FTS, while they can be used for dissociative adsorption of CO. Additionally, some transition metals including Cu, Pd, Pt, and Ir have difficulty with CO dissociation resulting in high methanol selectivity in FTS. It is suggested that Fe, Co, Ni, and Ru are suitable transition metals for FTS, due to high rates of CO dissociation and subsequently high rate of chain growth (Teimouri et al., 2021). In some research, Rh was found to be suitable (Filot et al., 2015). However, it has been reported that Ru is not an economical catalyst due to its limited resources and high price. Nickel is observed to be selective to methane rather than the desired products. Therefore, Fe and Co are the most common metals for FTS catalyst (Jahangiri et al., 2014). Fe-based catalysts are more likely to tolerate sulfur impurities than Co. As a result, Fe catalysts are useful for biomass and coal. Moreover, Fe possesses a lower hydrogenation activity compared to Co, as a result, Fe provides higher selectivity toward olefins (Lødeng et al., 2018). Interestingly, there is a growing attention to molybdenum carbide as catalyst for catalytic reactions due to high activity for CO hydrogenation and dry reforming as well as its resistance to carbon deposition in comparison with Co- and Fe-based Fischer–Tropsch catalysts (A. Chernavskii et al., 2017).

Iron-based catalysts

Iron catalysts at lower temperatures are selective to paraffins, while by increasing temperature the selectivity changes toward olefins. Due to similarity of CO hydrogenation and iron carbide formation in terms of activation energy, the iron carbides are formed during the FTS process. Different format of iron carbides have been observed in FTS process (De Smit

and Weckhuysen, 2008). Table 2.2 shows a summary of iron-based catalysts for light olefin production via FTS. The nature and concentration of the promoters play a pivotal role in FTO catalysts and their selectivity. Galvis et al. (Galvis et al., 2013) studied the addition of sulfur plus sodium in low concentration to Fe/ α -Al₂O₃ catalyst with high C₂-C₄ olefins selectivity to improve the catalytic activity and decrease the methane production. Sodium addition caused a decrease in the methane selectivity due to the chain growth probability, while sulfur addition led to a higher olefin production (Galvis et al., 2013).

Various iron-based FTS catalysts along with catalyst synthesis methods and active phases are listed in Table 2.2. The most probable compounds in Fe-based catalysts are iron carbide, metallic Fe, and magnetite (Fe₃O₄). Identification of active phase in Fe catalyst is commonly performed by in situ magnetization measurement to obtain Curie temperature in which the first derivative of magnetization altering with temperature is plotted. Then, the active phase of catalysts will be identified based on the observed Curie temperature. Iron carbide can be in the form of ϵ -Fe₂C, ϵ' -Fe_{2.2}C, Hägg χ -Fe₅C₂, Fe₇C₃ or θ -Fe₃C. Active phases of Fe-based catalysts in FTS to light olefins have been mostly reported to be iron carbides in the form of Hägg χ -Fe₅C₂, ϵ -Fe₂C, ϵ' -Fe_{2.2}C, and Fe₇C₃. Carbides of ϵ -phase are stable below 250 °C, while Hägg carbide is stable in the range of 250-350 °C. Therefore, among iron carbides, χ -Fe₅C₂ is mostly known as active phase of typical FTS temperature (240-360 °C), with a Curie temperature between 205 °C and 238 °C (Cheng et al., 2015c). Fe₇C₃ is a carbide phase produced during CO-treatment of catalyst at moderate temperature and θ -Fe₃C is stable above 350 °C (Chang et al., 2018b).

Chang et al. (Chang et al., 2018b) investigated pretreatment of Fe/SiO₂ catalysts with CO, H₂, and syngas for FTO in the medium temperature range of nearly 260-300 °C and 2-3 MPa for H₂/CO = 2. They identified Fe₇C₃ and χ -Fe₅C₂ as active phases for CO-treated catalyst, while they reported ϵ -Fe₂C and χ -Fe₅C₂ as active phase composition for H₂-treatment. χ -Fe₅C₂ was the only carbide formed during syngas-treatment of the Fe/SiO₂ catalyst. Among these three carbide phases, the highest activity and the lowest methane selectivity belong to Fe₇C₃ and ϵ -Fe₂C for medium range of temperature in FTO. Jiang et al. (Feng Jiang et al., 2017) performed a series of experiments on Fe-based catalysts to control the catalytic activity, selectivity and deactivation in FTS process using different supports (γ -Al₂O₃, SiO₂, activated carbon (AC), anatase-TiO₂ and SiC) and promoters (K, Na and S).

Table 2.2: Different synthesis methods of Fe-based catalysts for FTO.

Active metal	Support	Promoter	Synthesis method	Active Phase	C ₂ -C ₄ Selectivity (%)	CO conversion (%)	Reference
Fe	CNTs	Mn/K	Impregnation	FeMn ₂ O ₄ before reduction	51.7	30.1	(Chen et al., 2018)
Fe	CNTs	Bi	Impregnation	Hägg χ -Fe ₅ C ₂ or ϵ -Fe ₂ C	60.9	10.0	(Gu et al., 2018a)
Fe	CNTs	Pb			57.7	18.6	
Fe	CNTs	Bi	Impregnation	χ -Fe ₅ C ₂	45-62.4	25.5-25.6	(Gu et al., 2019a)
Fe	CNTs	Pb/K			52.6-62	40.7-76.2	
Fe	CNTs	Mn/K	Impregnation	Hägg χ -Fe ₅ C ₂	50.3	22.7	(Wang et al., 2015)
Fe-Zn-Cu -	-	-	Co-precipitation	-	35	45	(Roe et al., 2017)
Fe	CNTs	K	Deposition-precipitation	-	42	16	
Fe	N-CNTs ^a	K	Impregnation	χ -Fe ₅ C ₂	54.6	14.4	(Lu et al., 2014a)
Fe	NMCs ^b	-	Ultrasonic-impregnation	Fe ₃ C ₂ and ϵ -Fe ₂ C	33.9	92.6	(Liu et al., 2018)
Fe-Cu	Graphite	-	Co-precipitation	Fe ₇ C ₃	37.8	44.9	(C. Li et al., 2016)
Fe	AC	K	Impregnation	χ -Fe ₅ C ₂ and ϵ -Fe _{2.2} C	21.7	48.9	(Feng Jiang et al., 2017)
Fe	CSiO ₂ ^c	K/S			51.7-26.5	11.8-32.2	
Fe	SiC	Na/S			51.4	10.3	
Fe	SiC	K			19.7	57.1	
Fe	TiO ₂	K			17.3	67.7	
Fe	mSiO ₂ ^d	-	Impregnation	χ -Fe ₅ C ₂ is dominant	12.8	15.4	(Cheng et al., 2015c)
Fe	SiO ₂	-		(Above 36%)	15.2	28.5	
Fe	SiO ₂ -CO ^e	-		Fe ₃ C and ϵ -Fe _{2.2} C	18.3	76.9	
Fe	SiO ₂ -H ₂ ^e	-		are low (less than 14%)	14.1	51.6	
Fe	SiO ₂ -E ^f	Mn	Impregnation	-	54.6	50.5	(Liu et al., 2015a)
Fe	SiO ₂	K	Impregnation	χ -Fe ₅ C ₂	10.1-18.7	23-29.9	(A. Chernavskii et al., 2017)
Fe-Cu	SiO ₂	K	Co-impregnation		15.2-18.1	33.9-34.3	
Fe	SiO ₂	Bi	Impregnation	χ -Fe ₅ C ₂	53	17	(V. V. Ordonsky et al., 2017)
Fe	SiO ₂	Pb	Impregnation		32	55	
Fe	SiO ₂ -GC ^g	-	Hydrothermal deposition	Hägg χ -Fe ₅ C ₂	12.9	40.6	(Ni et al., 2018)
Fe ₂ O ₃	SiO ₂	-			17.4	40.6	
Fe-Mn	SiO ₂	Cu	Co-precipitation, impregnation	Hägg χ -Fe ₅ C ₂	40.1	96.9	(Gong et al., 2020)
Fe	Si-CO ^e	-	Co-precipitation	Fe ₇ C ₃ , χ -Fe ₅ C ₂	30.8	50.8	(Chang et al., 2018a)
Fe	Si-H ₂ ^e	-		ϵ -Fe ₂ C, χ -Fe ₅ C ₂	15.0	33.1	
Fe	Si-Syngas ^e	-		χ -Fe ₅ C ₂	17.1	22.3	
Fe	α -Al ₂ O ₃	S/Na	Impregnation	-	50	66	(Galvis et al., 2013)
Fe-Ni	Al ₂ O ₃	K ₂ S	Co-precipitation	-	77.8	64.6	(Feyzi et al., 2014)
Fe	MgO-NS ^h	-	Impregnation	-	14.6	55.6	(LI et al., 2018)
Fe	MgO-NS	-	Deposition-precipitation		15.5	38.0	
Fe	MgO-NS	-	Ultrasonic impregnation		29.6	35.5	
Fe	MgOcub ^e	-	Ultrasonic impregnation		21.5	35.7	
Fe	MnO _x	Ag	Impregnation	χ -Fe ₅ C ₂	35.4	50.3	(Xu et al., 2018)
Fe	-	Na/S	Precipitation	-	66	30	(Botes et al., 2016)
Fe	-	-	Solvothermal	-	19.3	91.0	(Y. Zhang et al., 2015)
Fe	-	Na			23.3	93.2	
Fe	-	K			22.1	97.1	
Fe	-	Zn			18.1	98.3	

Fe	-	Zn/Na	Co-precipitation	-	42.7	97.16	(M. Zhao et al.,
Fe	-	Zn/K			37.19	5.02	2018a)
Fe	-	Zr	Co-precipitation	-	57	40.6	(Zhang et al., 2019)

^a Nitrogen-doped CNTs

^b Nitrogen-rich mesoporous carbon-supported Fe catalyst

^c Carbon-coated SiO₂

^d Mesoporous silica

^e Fe-Si calcined catalyst treated with CO, H₂, and syngas

^f Ethylene glycol pretreated silica support

^g Silica-graphitic carbon encapsulated iron

^h Nanosheet

It was concluded that the catalytic activity depends on the iron oxide reducibility which is related to the particle size-dependent carburization, promoter effects, interaction of iron with the support, and the particle size. The light olefin selectivity is increased beyond the limitation of the Schulz-Flory distribution using K, Na, and S. Finally, the reversible transformation of χ -Fe₅C₂ into Fe₃O₄ and K-induced carbon deposition were highlighted as the catalyst deactivation reasons (Feng Jiang et al., 2017). Li et al. (C. Li et al., 2016) synthesized K-promoted graphite supported catalysts during two stages including co-precipitation and incipient wetness impregnation. The FTS process was performed at 0.5 MPa and 300-330 °C using syngas (H₂/CO = 1) for 4 h. The potassium-promoted catalyst showed high activity and selectivity of liquid hydrocarbon. Subsequently, the iron electron density increased and potassium changed the iron crystallite morphology, while methane production went down (C. Li et al., 2016).

Feyzi et al. (Feyzi et al., 2014) utilized Fe-Ni/Al₂O₃ catalyst for production of light olefins using synthesis gas. They reported that the catalyst offers the highest selectivity toward C₂-C₄ olefins (77.8%) and the lowest selectivity with respect to methane (9.1%) and CO₂ (0.3%) at 340 °C, H₂/CO = 2, P = 0.1 MPa. Moreover, addition of K₂S into the catalyst increases the selectivity toward C₂-C₄ (Feyzi et al., 2014). Olefin selectivity is not affected by Fe particle size; however, it is reported that Fe nanoparticles less than 7-9 nm exhibit higher CH₄ selectivity compared to larger particles. Moreover, the smaller Fe nanoparticles lead to the lower chain growth probability. It was suggested that CH₄ formation is related to the corners and edge sites of catalyst crystals, which are enhanced by decreasing the particle size. In the case of olefins, terrace sites are proposed to improve olefin production.

Wang et al. (Wang et al., 2016) investigated an iron-catalyzed FTS process and promoter effects on light olefin selectivity. They reported Hägg iron carbide (χ -Fe₅C₂) as the dominant phase of iron catalyst used in Fischer-Tropsch reaction. It can be observed from Figure 2.5 that

there are three different synthesis methods for pure χ -Fe₅C₂ catalyst including wet-chemical method in the presence of bromide (Br), hydrothermal synthesis followed by thermal treatment method, and metal organic framework (MOF) mediated synthesis method. It was concluded that χ -Fe₅C₂ catalysts favor the synthesis of longer-chain hydrocarbons and alkanes. Moreover, the selectivity to C₂-C₄ can be improved using appropriate promoters (Wang et al., 2016).

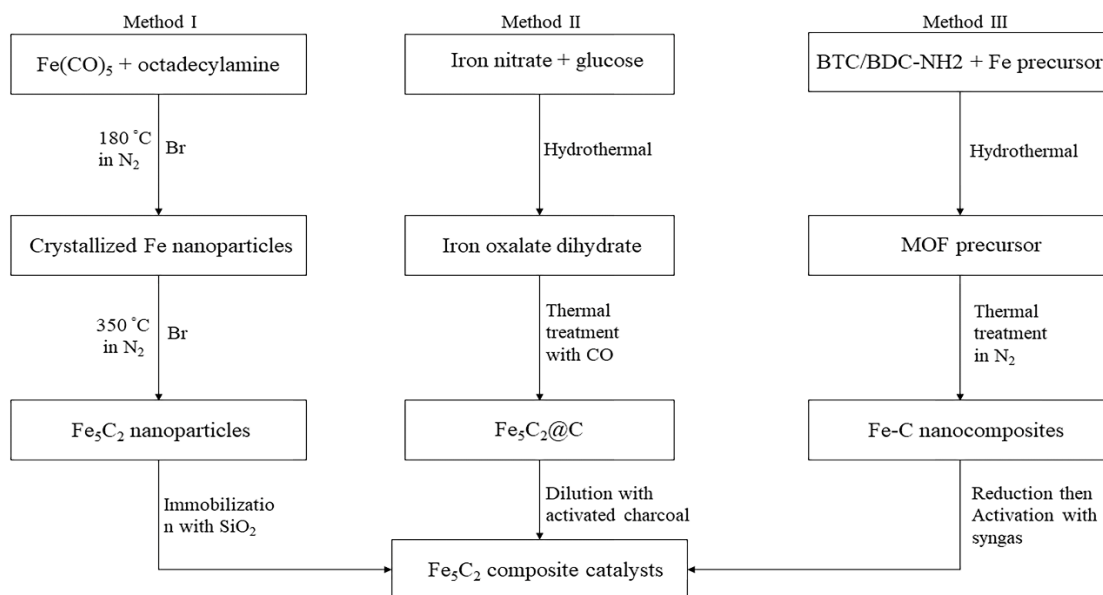


Figure 2.5: Schematic of synthesis methods proposed for χ -Fe₅C₂ phase catalyst. Reproduced with permission from (Wang et al., 2016).

The larger pore size of the support increases heavy hydrocarbon production and light olefin selectivity. It was reported that Fe-based catalysts (FeMn) with pore size in the order of 50-80 nm facilitated the diffusion of reactants and products while suppressing the secondary reactions of 1-olefins, thus resulted in higher selectivity toward light olefins (Liu et al., 2015a).

Cobalt-based catalysts

Cobalt-based catalysts for FTS have properties such as high catalytic activity, low WGS activity, and superior stability. Therefore, this group of catalysts require higher ratios of H₂/CO (2.0-2.2) compared to Fe-based catalyst (Sahir et al., 2019a). However, this type of catalyst is not selective to the light olefins for industrial application. The electron density and structure of cobalt catalysts are mainly influenced by metal-support interactions. The support acidity could lead to light hydrocarbons formation. The support porosity including average pore diameter, pore volume, and surface area could affect the cobalt dispersion and reducibility. Noble metals,

transition metal oxides, and some rare earth metal oxides are suggested as promoters for the cobalt oxide catalyst. In addition, the promoter affects the structure and dispersion of cobalt species, FT reaction rates, and product selectivity (Fu and Li, 2015). Table 2.3 shows some of support materials and promoters used for synthesis of Co-based catalysts using different synthesis methods.

Table 2.3: Different synthesis methods of Co-based catalysts for FTO.

Active metal	Support	Promoter	Synthesis method	C ₂ -C ₄ selectivity (%)	CO conversion (%)	Reference
Co	MHZSM 5 ^a	-	-	29.1	79.0	(Xing et al., 2015)
Co	HZSM 5	-	-	30.9	75.9	
Co	Al ₂ O ₃ /ZSM 5	La	Co-precipitation	24.1	20.7	(Ryu et al., 2015)
Co	γ-Al ₂ O ₃	Ru/La	Impregnation	11.2	45.8	(Sage et al., 2017)
Co	γ-Al ₂ O ₃ -PT ^b	Ru/La		15.9	43.7	
Co-Mn	γ-Al ₂ O ₃	-	Co-impregnation	8-11	20-45	(Pedersen et al., 2018)
Co	Al ₂ O ₃	-	Impregnation	44.8-50.4	9.5	(Nabaho et al., 2016)
Co	Al ₂ O ₃ +Pt/Al ₂ O ₃	Pt		46.2-59.2	13	
Co-Ni	mSiO ₂ ^c	-	Impregnation	26.8	19.7	(Sun et al., 2017c)
Co-Mn-Ce	SiO ₂	-	Impregnation	17.4	10.1	(Zohdi-Fasaei et al., 2017)
Co	Mn/SiO ₂	Zn/Ce	Impregnation	10-36	17-31.8	(Zafari et al., 2017)
Co	MnO _x	-	Co-precipitation	26.5-42.2	42.3-45.3	(W.-G. Zhou et al., 2015)
Co-Mn	-	-	Co-precipitation	50	2.5	(Z. Li et al., 2017)
Co-Mn	-	-	Co-precipitation	37.7	30	(Lin et al., 2019)
Co	TiO ₂	-	Deposition precipitation	10.6-20.9	27.5-33.1	(Phaahlamohlaka et al., 2018)
Co	TiO ₂ @mSiO ₂ ^c	-		5.2-21.7	17-46.1	
Co	TiO ₂ @mSiO ₂	Ru	Co-impregnation	12.1-23.3	31.6-58.9	(Hong et al., 2018)
Co	TiO ₂ -C ^d	Pt		5.4	28.6	
Co	TiO ₂ -P ^e	Pt	Impregnation	6.2-7.0	66.3	(Bertella et al., 2020)
Co	TiO ₂	-		32.3	24.3	
Co	TiO ₂	Ru	Impregnation	27.2-29.9	82.3-98.3	(Chen et al., 2019)
Co	C ^f	-		10.87-11.87	34.15-35.62	
Co-Mn	Al ₂ O ₃	-	Impregnation	14-28	21-37	(Zafari et al., 2020)
	GNS ^g	-		22-42	5.4-39.2	
Co-Mn	rGO ^h	-	Impregnation	25-53	20.5-33.2	(Zafari et al., 2019)
	GNS ⁱ	-		29.2	49	
Co	CNT	-	Impregnation	29.5-18.9	84-75	(Nakhaei Pour et al., 2017)
Co	CNT-800 ^j	-	Impregnation, Spark	8.1	14.9	(Chernyak et al., 2020)
Co	CNT-1000	-	plasma sintering	20.3	34.5	

^a Hierarchical HZSM-5 zeolite support

^b Acetylene pretreated catalyst

^c Mesoporous silica (mSiO₂)

^d Calcined CoPt/TiO₂

^e Plasma treated CoPt/TiO₂

^f Cobalt catalyst embedded in nanoporous carbon

^g Graphene nanosheet

^h Reduced graphene oxide

ⁱ Sintering temperature (800 and 1000 °C)

Concerning the decrease of long chain hydrocarbons (C_{25+}), Sage and co-workers (Sage et al., 2017) investigated the in-situ pre-treatment of Co/Ru/La catalysts using alumina support with acetylene pre-treatment (200 °C, 1 MPa, 4 h) in a fixed-bed reactor. It was suggested that the formation of carbidic and C_xH_y species on the catalysts can be related to acetylene dissociation and dehydrogenation. Methane TPH-MS revealed that acetylene decomposition causes formation of carbidic compounds. These carbidic compounds bring about a decrease in catalyst activity due to polymeric carbon onto the catalyst surface. Moreover, formation of these carbonaceous materials onto catalyst active sites was considered to alter the distribution of FTS products through affecting the 1-olefin secondary reactions. It was observed that the amount of heavy hydrocarbons significantly decreased (Sage et al., 2017).

Zhou et al. (W.-G. Zhou et al., 2015) evaluated the effects of 1,4-butanediol (BDO) as solvent using Co/MnO_x catalyst in the FTO reaction. It was observed that BDO as a solvent affected the light olefin selectivity (42.2 %) compared to the conventional Co/MnO_x catalyst (26.5 %). The main effect of BDO could be weakening the interaction of cobalt and support. So that the cobalt density of the surface or the number of cobalt atoms in the catalyst increases and the hydrogenation activity reduces. Co/MnO_x-BDO catalysts weaken the isomerization and hydrogenation reaction, thus forming more light olefins. This catalyst also decreases the methane selectivity, while doubling olefin/paraffin ratio (W.-G. Zhou et al., 2015).

Pedersen et al. (Pedersen et al., 2018) succeeded to synthesize CoMn/ γ -Al₂O₃ for light olefins production. Manganese enhanced the activity and selectivity toward light olefins and C_{5+} species. In addition, the selectivity to CH₄ decreased compared to the un-promoted Co catalyst. Mn was suggested to change the degree of reduction of Co₃O₄ particles together with a decrease in the cobalt surface area. Adding Mn to Co catalyst would lead to higher temperature peak in temperature programmed reduction (TPR) profiles and delayed reduction of Co₃O₄. Mn also inhibited hydrogenation activity due to the decrease in CH₃ and CH₄ formation (Pedersen et al., 2018).

Ryu et al. (Ryu et al., 2015) used Ru-, Pt- and La-promoted Co-Al₂O₃/ZSM-5 hybrid catalysts for the direct production of gasoline (C_5 - C_9) from syngas. Based upon NH₃-TPD, promoter addition affects the surface acidity of the catalyst and product distribution. The catalytic activity of the promoted Co-Al₂O₃/ZSM 5 catalyst was evaluated at 240 °C, 2 MPa and H₂/CO = 2 for 40 h in FTS process. Among catalysts, the Co-Al₂O₃-Pt/ZSM 5 showed the

highest conversion of 41.3 % while the olefin selectivity was just 17.9 %, which was related to the presence of fewer acidic sites (Ryu et al., 2015).

Liu et al. (Liu et al., 2019) investigated the mechanisms of CO activation, methane formation, and C-C coupling on three cobalt phases (Co, Co₂C, Co₃C) to find active site which affects the light olefins production in cobalt-catalyzed FTS reactions. It was found that the phase change from metallic Co into Co₃C increases the selectivity to light olefins, although Co₂C exhibits much lower activity and high selectivity to methane formation. The computational study was applied to indicate the dactive sites that affect the olefin production. It was believed that the reactions conducted at the Co/Co₃C interface is related to the formation and desorption of light olefins (Kitakami et al., 1997).

It is also discussed that Co catalyst deactivation is related to the carbide formation and carbon deposition (Tan et al., 2010). Xing et al. (Xing et al., 2015) used hierarchical HZSM-5 and conventional HZSM-5 zeolite supports for cobalt catalysts in FTS to evaluate the selectivity of the process. Changing the support pore size was found to influence the selectivity of products like isoparaffin, olefin and hydrocarbon (Xing et al., 2015).

According to the literature for Co₂C particle smaller than 7 nm, increasing the cobalt carbide particle size enhanced the intrinsic activity and light olefin selectivity (Dai et al., 2019). Bulk Co known as hexagonal close-packed (HCP) structure was the dominant phase for particle size larger than 40 nm; however, the metastable Co of face-centered cubic (FCC) structure was limited to particles smaller than 20 nm. Thermal phase transformation of HCP to FCC was observed at 400 °C. It was suggested that Co-based catalysts of HCP crystal phase are more likely to have higher FTS activity compared to FCC structure (Liu et al., 2017). Zhang et al. (Zhang et al., 2020) suggested CHO-insertion and carbide mechanism for the initial formation and growth of carbon chain over FCC and HCP Co facets. As it can be seen in Figure 2.6, initial formation of CH₂ is contributed to CO direct dissociation and hydrogenation on HCP Co, while in the case of FCC Co, CO hydrogen-assisted dissociation initiates formation of intermediates. It was also reported that the carbide mechanism on Co preferably suggested higher selectivity of C₂ hydrocarbons compared to CH₄ (Su et al., 2017).

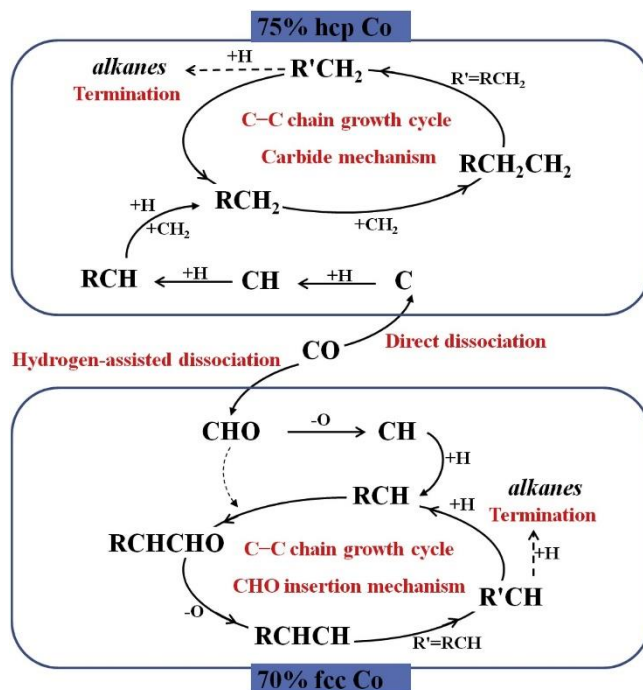


Figure 2.6: Schematic of the mechanism proposed for C-C chain initiation, propagation, and termination over HCP and FCC Co catalysts. Reproduced with permission from (Zhang et al., 2020).

Catalyst basicity effects

The basicity impacts the strength required for the hydrogenation of syngas on the transition metals such as Mn, Fe, Co, and Ni. The basicity and reducibility of catalysts can be evaluated by characterization techniques including CO_2 -temperature programmed desorption (CO_2 -TPD) and H_2 -temperature programmed reduction (H_2 -TPR), respectively. Table 2.4 illustrates the effects of nature of supports and active metals on the catalyst basicity, with CO_2 -desorption temperature being increased for strong basic sites. As can be seen in Table 2.4, the type and amount of alkali metal can influence phase transition in catalyst reduction, which is evaluated by H_2 -temperature programmed reduction.

Xiong et al. (Xiong et al., 2015) investigated the effects of alkali metal promoters such as Li, Na, and K on the catalytic performances of iron catalyst supported on carbon nanotubes in FTS in the absence of strong metal support. Results demonstrated that addition of alkali metal influenced the catalyst crystallite size, with the surface area being decreased. The basicity of the alkali metal increases in the order $Li < Na < K$. It was also reported that an increase in Na

and K loading increased the olefin/paraffin ratio and long-chain hydrocarbon formation (Xiong et al., 2015).

Table 2.4: Techniques for investigating the basicity and reducibility of FTS catalysts.

Catalyst	Technique	Note	Reference
Fe/MgO ^a	CO ₂ -TPD ^b	Surface basicity of catalyst based on desorption peaks: Moderate alkaline sites (Mg ²⁺ /O ²⁺) around 160-400 °C Strong basic sites (unsaturated O ²⁻) above 400 °C MgO nanosheet: Mg ²⁺ /O ²⁺ around 350 °C Unsaturated O ²⁻ nearly 600 °C For Fe/MgO-c-UI, the ratio of medium/strong basicity is higher than that of Fe/MgO-ns-UI	(LI et al., 2018)
Unmodified Fe ore K/Cu/iron ore Fe/Cu/K/SiO ₂ ^c	CO ₂ -TPD	CO ₂ adsorbed on the alkali surface: 22 µmol/g 100 µmol/g 129 µmol/g Iron ore-based catalysts contain Al ₂ O ₃ which is more acidic than SiO ₂	(Bae et al., 2019)
Alkali promoted Fe/SiO ₂	H ₂ -TPR ^d	Reducibility of catalysts based on alkali type: The First step reduction: The lower temperature peak: Fe ₂ O ₃ → Fe ₃ O ₄ The first step reduction temperature increase in the order of (J. Li et al., 2016) Li > Na > K > Rb > Cs Subsequent reduction: The higher temperature peaks: Fe ₃ O ₄ → FeO and FeO → α-Fe	(J. Li et al., 2016)
K/α-Fe ₂ O ₃	H ₂ -TPR	Reducibility of catalysts based on amount of alkali: The first reduction temperatures shift to higher temperature by increasing potassium levels. The second reduction temperatures decrease with increasing potassium.	(Niu et al., 2020)

^a Fe catalyst supported on MgO nanosheet (Fe/MgO-ns) and cubes (Fe/MgO-c) synthesized by ultrasonic impregnation (UI) method

^b CO₂-temperature programmed desorption

^c Precipitated Fe/Cu/K/SiO₂ catalyst

^d H₂-temperature programmed reduction

In another study, addition of alkali to the Fe/SiO₂ catalysts resulted in some changes in the reduction of catalyst due to strong interactions between alkali and iron metal. Potassium would lead to inhibition of the first reduction of iron oxide. However, it enhanced the metallic iron formation from FeO and activity of iron catalysts in FTS. Moreover, by increasing the alkali atomic number, the carbonization of catalysts enhanced (J. Li et al., 2016). Li et al. (J. Li et al., 2017) studied the effects of alkali metals as promoters on iron based FTS catalysts. They showed that Li and Na can penetrate to the catalyst surface. However, K, Rb, and Cs generally are not able to diffuse into the catalyst. By using alkali cations, the selectivity toward olefin and heavier hydrocarbons enhanced, while the selectivity toward methane and alkane decreased

at the same time. It is confirmed that Li diffused out of the catalyst, however, K is less movable in iron catalyst after FTS reactions. The main effect of alkalis was attributed to the surface adsorption, with CO adsorption and dissociation being improved (J. Li et al., 2017). MgO as both basic support and structural promoter in Fe-based catalyst can increase olefin to paraffin ratio by suppressing secondary hydrogenation reaction. Fe-based catalysts in the form of MgO nanosheet and MgO cube were prepared by incipient wetness impregnation, deposition-precipitation, and ultrasonic impregnation methods. It was reported that Fe/MgO nanosheet catalysts synthesized using ultrasonic impregnation method exhibited the strong basicity sites of MgO (Table 2.4). The as-mentioned catalyst enhanced dissociative adsorption of CO and demonstrated higher olefin selectivity of 29.6 % compared to the other catalysts (Li et al., 2018). CO₂-temperature programmed desorption is mainly used to investigate catalysts in terms of medium/strong basicity sites and CO₂ adsorption. It might be suggested that basicity of catalysts enhances olefin to paraffin ratio in FTS by suppressing secondary hydrogenation.

Catalyst dispersion effects

The decrease in metal particle diameter greatly affects the chemisorption behavior of both hydrogen and carbon monoxide, indicating the dispersion of catalyst active metal. Taking it into account, CO-chemisorption and H₂-temperature programmed desorption (H₂-TPD) in conjunction with O₂-titration are proved effective methods to determine active metal dispersion in catalysts. Table 2.5 illustrates active metal dispersion of different FTS catalysts for light olefin production.

Nakhaei Pour et al. (Nakhaei Pour et al., 2017) investigated the effects of using magnetized water in impregnation step of Co-based catalysts. They observed that the average particle size of impregnated Co nanoparticles decreased from 12.4 nm to 9.8 nm, while metal dispersion in H₂-TPD increased in the range of 8.2-10.8 %. They also reported that with increasing magnetized water, the selectivity toward higher hydrocarbon rose, however the selectivity of C₂-C₄ decreased from 29.5% to 18.9% (Nakhaei Pour et al., 2017).

Table 2.5: Techniques for investigating the dispersion of active metal in catalysts.

Catalyst	Technique	Dispersion (%)	C ₂ -C ₄ Selectivity (%)	Note	Reference
Co/TiO ₂	Pulse chemisorption	4.5-1.9	10.6-20.9	T _{Chemisorption} =350-450 °C	(Phaahlamohlaka et al., 2018)
Co/TiO ₂ @mSiO ₂ ^a		3.6-3.7	5.2-21.7	FTS (T=220-250 °C, P=1 MPa, H ₂ /CO=2, GHSV=800 mLg ⁻¹ h ⁻¹)	
CoRu/TiO ₂ @mSiO ₂		5.0-6.7	12.1-23.3		
Co/CNT	H ₂ -TPD	8.2-10.8	29.5-18.9	FTS (T=220 °C, P=2 MPa, H ₂ /CO=2, GHSV=40 mLg ⁻¹ h ⁻¹)	(Nakhaei Pour et al., 2017)
CoPt/TiO ₂ -C ^b	H ₂ -TPD O ₂ -titration	20.4	5.4	FTS (T=210 °C, P=1 MPa, H ₂ /CO=2, GHSV=4 SLg ⁻¹ h ⁻¹)	(Hong et al., 2018)
CoPt/TiO ₂ -P1 ^c		26.9	6.2		
CoPt/TiO ₂ -P4		73.7	7.0		
0CTAB-Co@C ^d	H ₂ -TPD	32.05	10.87	FTS (T=230 °C, P=2 MPa, H ₂ /CO=2, GHSV=6.75 SLg ⁻¹ h ⁻¹)	(Chen et al., 2019)
2CTAB-Co@C		20.07	11.87		
8CTAB-Co@C		38.51	11.27		

^a Mesoporous silica (mSiO₂), ^b Calcined CoPt/TiO₂, ^c Plasma treated CoPt/TiO₂ for 1 and 4 h, ^d Co catalyst embedded in nanoporous carbon with m(CTAB)/n(Co)= 0, 2, 8; Cetyltrimethyl ammoniumbromide (CTAB)

Wang et al. (Wang et al., 2012) investigated the effects of Co catalyst particle size on the turnover frequency (TOF) and CH₄ selectivity in FTS using a series of Co/SiO₂ model catalysts in the range of 1.4-10.5 nm. From Figure 2.7, it can be observed that the smaller Co particles (1.4-2.5 nm) lead to lower TOF and higher CH₄ selectivity (90 mol%) as compared to the larger Co particles (3.5-10.5 nm) with TOF and CH₄ selectivity being relatively constant (~72 mol%). The effects of Co particle size in the range of 1.4-2.5 nm was attributed to the oxidation of smaller Co particles in the presence of water vapor produced during reaction (Wang et al., 2012).

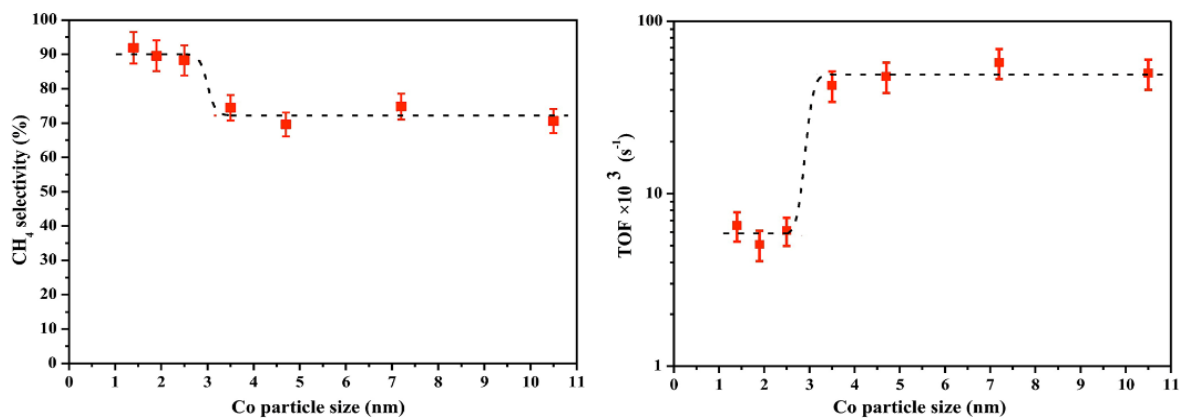


Figure 2.7: CH₄ selectivity and TOF for Co/SiO₂ catalysts of different sizes in FTS. Reproduced with permission from (Wang et al., 2012).

Phaahlamohlaka et al. (Phaahlamohlaka et al., 2018) reported the synthesis of a sinter resistant Co-based catalyst supported on TiO₂ encapsulated in a silica shell. Co/TiO₂ showed a decrease in dispersion after reduction at temperature between 350-450 °C, while the dispersion of active metal in the case of Co/TiO₂@SiO₂ catalyst remained constant after reduction. It was also reported that after reduction, Ru-promoted Co/TiO₂@SiO₂ catalyst exhibited an increased metal dispersion (Phaahlamohlaka et al., 2018).

A highly dispersed iron-based catalyst supported on macroporous silica was investigated by Liu et al. (Liu et al., 2016). The catalyst exhibited excellent catalytic activity in terms of olefin selectivity (46.2 %) as well as CO conversion (63.4 %) without any promoter. This can be attributed to high diffusion efficiency and high iron particle dispersion (Liu et al., 2016). In another study, CoPt catalyst on TiO₂ support was prepared by glow discharge plasma (GDP) method. It was reported that applying plasma treatment, the smaller size of cobalt particles with higher dispersion is achievable. It was suggested that the smaller size of particles resulted in the more surface active sites, while the activity of catalyst decreased significantly (Hong et al., 2018).

Gao et al. (Gao et al., 2016) implemented Fe-based catalysts for light olefins production in FTS reaction with Zn as promoter using microwave-hydrothermal and impregnation methods. They suggested that the dispersion of Zn directly affects the hydrogenation ability. In addition, Zn enhanced catalyst selectivity to lower olefins (38.1-40.9 %) and also improved the catalyst stability. The catalyst synthesized by the microwave-hydrothermal method showed high dispersion of Zn and Fe phases and low carbon deposition. They reported that the hydrogenation ability of the catalysts depends on the presence of Zn and its dispersion. Homogeneous dispersion of Zn over the catalyst, reduces the masking of iron active sites on the surface and leads to higher conversion (Gao et al., 2016). Chen et al. (Chen et al., 2019) synthesized cobalt catalysts embedded in nanoporous carbon via carbonization of metal-organic-framework (MOFs) precursor of CTAB-ZIF-67. H₂-TPD showed high Co dispersion and loading with increasing CTAB content (Chen et al., 2019). The selectivity to light olefins and CO conversion in FTS are improved by active metal dispersion.

2.6 Metal support interaction effects

Type of support has a profound effect on the performance of a catalyst. As discussed in section 2.4.1.3 and 2.4.1.4, the basicity and dispersion of support influence the catalytic

behavior of metals. Activated carbon, carbon nanotubes, alumina, silica, and titania are widely used as supports for FT catalysts.

Cho et al. (Cho et al., 2015) studied the support effect in Co/AlSBA-15 catalyst. They concluded that the increased C₂-C₄ selectivity was related to the formation of small cobalt particles with higher oxidation state, stronger metal-support interaction, and less aggregation of particles on the outer surfaces of the support, which suppressed heavy hydrocarbons formation. It was suggested that the larger the support pore diameter, the higher the formation rate of light olefins. The larger pore size of supports can also influence FTS product distribution via formation of the larger Co₃O₄ particles. In addition, formation of wax and water in the mesopores during the FTS process could affect the diffusion rate of both H₂ and CO on the cobalt active sites, with the diffusion rate of CO being higher than that of H₂ via wax-water emulsion layers. As a result, the selectivity of olefins increased (Cho et al., 2015).

In addition, Anderson et al. (Anderson et al., 1949) reported that increasing the diffusion rate of hydrogen into meso-macroporous catalysts would lead to an increase in H₂/CO ratio near active sites. Therefore, the selectivity tends to methane and light hydrocarbons (Anderson et al., 1949).

Cheng et al. (Cheng et al., 2015c) studied the effects of support pore size on silica supported iron catalysts in high-temperature Fischer-Tropsch synthesis. It was reported that larger pore size of silica supported iron catalyst offers higher olefin and C₅₊ selectivity due to easier iron carbidization (Cheng et al., 2015c).

2.6.1 Carbon nanotubes supported catalysts

Multi-walled carbon nanotubes (MWCNTs) are an attractive candidate for FTS due to their impressive mechanical features, high accessibility of active sites, and lack of micro-porosity eliminating intraparticle mass transfer (Yahyazadeh and Khoshandam, 2017). This type of carbon material possesses an inert surface and weak interaction with metal components, thus providing high dispersion of active metal sites with electron donor particles (Li et al., 2015). Carbon nanotubes (CNTs) and carbon nanofibers (CNFs) have been extensively used as catalyst supports due to their unique properties like large surface area, acceptable thermal and chemical stability as well as high electrical conductivity. CNTs and CNFs as support enhance the catalyst activity and selectivity in comparison with their common counterparts like activated carbon (AC), alumina and silica.

Lu et al. (Lu et al., 2014b) synthesized iron catalysts immobilized onto N-doped carbon nanotubes for FTS to light olefins. The catalysts exhibited super catalytic selectivity (46.7%), activity, and stability for production of lower olefins. This performance could be related to high dissociative CO adsorption, inhibition of secondary hydrogenation of lower olefins, and presence of active phase of χ -Fe₅C₂. Nitrogen leads to anchoring effect and intrinsic basicity of the N-doped CNTs support. This helps catalyst to avoid loss of active particles and basic sites during FTS process (Lu et al., 2014b).

Wang et al. (Wang et al., 2015) developed CNTs supported Fe catalysts using manganese and potassium as promoters via two different synthesis methods. Results illustrated the superiority of Fe/MnK-CNTs catalyst over FeMnK/CNTs in terms of activity and stability to light olefins. This can be due to small-sized and uniform nanoparticles, the weak metal-support interaction, uniform distribution of promoters, and more defects on support in the case of Fe/MnK-CNTs (Wang et al., 2015).

Roe et al. (Roe et al., 2017) investigated FTS using CNTs supported catalysts based on iron in both gas phase (GP-FTS) and supercritical hexane operating conditions (SC-FTS; T_C = 234 °C, P_C = 2.97 MPa). It is believed that the carbon-supported catalysts offer high activity, low CH₄ formation, and high selectivity toward olefins and oxygenates. A remarkable increase in the extraction of olefins under SC-FTS operation was observed due to improved heat management, thus reducing methanation and allowing intermediates to readsorb and continue propagation. It was suggested that the chain growth factor, CO conversion, and selectivity toward un-hydrogenated products could be enhanced under supercritical operation. It was also observed that potassium promoter leads to considerable production of aldehydes in the Fe-catalyzed FTS (Roe et al., 2017). Tables 2.6 and 2.7 provide a summary of different types of supports used in FTS.

2.6.2 Alumina, silica, and titania supported catalysts

Alumina as an inert support with high mechanical stability can be used to study the interaction between the promoters and iron active sites. To this end, Galvis et al. (Galvis et al., 2013) reported that the addition of low amounts of S and Na to the catalyst resulted in high C₂-C₄ olefins selectivity, increased catalyst activity, and reduced methane formation in FTS reactions. In addition, they concluded that addition of extra Na decreased the catalyst activity due to formation of more carbon deposition (Galvis et al., 2013).

For silica supports, dispersion of active sites on the support is a function of the distribution, concentration, and type of silanol groups on the surface of silica. Identified on the surface of silica, H-bonded silanol group was believed to form larger metal crystallites compared to the isolated silanol. Therefore, the higher concentration of isolated silanol groups on silica, the higher was the catalytic activity of the silica supported catalyst (Okoye-Chine et al., 2020). To study the effects of pore size on light olefins selectivity in FTS, Liu et al. (Liu et al., 2015a) used Fe-Mn catalysts on modified silica support. The XRD results showed the pretreatment of silica supports by ethylene glycol resulting in lower crystalline size of supported iron oxide. In addition, H₂-TPR profiles revealed that the silica support and small iron oxide particle (Fe₂O₃) had a strong interaction. Therefore, it was concluded that light olefin formation is related to iron or iron carbide particle size. It was reported that the smaller iron carbide particle would lead to more light olefins production, less prone to deactivation.

Chernavskii et al. (A. Chernavskii et al., 2017) studied silica supported iron catalysts with copper and potassium promotion for high temperature Fischer-Tropsch synthesis. It was reported that the ratio of olefin to paraffin was increased with potassium promotion. Consistent with previous research, alkali metals by electron donation would lead to higher rate of CO dissociation. At the same time, alkali ions suppressed secondary olefin hydrogenation and increase chain growth probability (A. Chernavskii et al., 2017).

In the case of titania supports, the metal active sites are difficult to reduce up to very high temperatures due to the strong metal-support interactions. Addition of manganese enhanced the selectivity of Fe or Co catalysts supported on TiO₂ toward lower olefins (Atashi et al., 2010). Atashi et al. (Atashi et al., 2010) studied the cobalt-manganese catalyst on titania support for hydrogenation of carbon monoxide to light olefins. It was reported that Mn promotion effects on Fe catalyst would lead to high olefin formation (See Tables 2.6 and 2.7).

2.7 Promotion effects

The nature of the promoters used in commercial application of FTS is not disclosed. Here promoters used to increase the olefin selectivity of Fe- and Co-based catalysts are presented in Table 2.6 for Fe-catalysts and Table 2.7 for Co-catalysts. The most widely used promoters for Fe-Based FTS catalysts includes K, Na, S, Zn, Mn, Zr, Bi, Pb, and Cu.

Table 2.6: Light olefin selectivity of different Fe-based catalysts in FTO.

Catalyst	Promoter	T (°C)	P (MPa)	GHSV (Lh ⁻¹ g ⁻¹)	H ₂ /CO	C ₂ -C ₄ selectivity (%)	CO conversion (%)	Reference
Fe/ α -Al ₂ O ₃	S/Na	340	2	3	1	50	60-66	(Galvis et al., 2013)
Fe/ α -Al ₂ O ₃ -H ^a	S	350	0.1	9	1	68	0.9	(X. Zhou et al., 2015)
Fe-Ni/Al ₂ O ₃	K ₂ S	340	0.1	3	2	77.8	64.6	(Feyzi et al., 2014)
Fe/CNTs	Mn/K	270	2	30	1	51.7	30.1	(Chen et al., 2018)
Fe/CNTs	Bi	350	0.1	3.4	1	60.9	10	(Gu et al., 2018a)
	Pb	350	0.1	3.4	1	57.7	18.6	
Fe/CNTs-Confined ^b	Bi,Pb/K	350	1	17	1	45-52.6	60.2-76.2	(Gu et al., 2019b)
	Bi,Pb/K	350	0.1	3.4	1	62.4-62	25.6-40.7	
Fe/CNTs	Mn/K	270	2	30	1	50.3	22.7	(Wang et al., 2015)
Fe/N-doped CNTs	-	300	0.1	4.2	1	46.7	14.4	(Lu et al., 2014b)
Fe/N-doped CNTs	K	300	0.1	4.2	1	54.6	16.5	
Fe/NMCs ^c	-	340	1	-	1	33.9	92.6	(Liu et al., 2018)
Fe/CNTs	K	270	2	18	1	42.2	28.8	(Duan et al., 2016)
Fe/CNF	Na/S	350	0.2	12-24	10	50	10	(Xie et al., 2016b)
Fe/AC	K	300	1	2.2	1.1	21.7	48.9	(Jiang et al., 2017)
Fe/CSiO ₂ ^d	K	300	1	2.2	1.1	26.5	32.2	
Fe/SiC	Na/S	300	0.2	2.2	1.1	51.4	10.3	
Fe/SiO ₂ -E ^e	Mn	300	1	-	1	54.6	50.5	(Liu et al., 2015a)
Fe/SiO ₂	Bi	350	0.1	3.4	1	53	17	(V. V Ordonsky et al., 2017)
	Pb	350	0.1	3.4	1	32	55	
Fe/MnO _x	Ag	340	1	7.4	1.1	35.4	50.3	(Xu et al., 2018)
		320	1	7.4	1.1	34.3	55	
Fe/MgO nanosheets	-	300	1	8	1	14.6-29.6	35.5-55.6	(LI et al., 2018)
Fe/MgO cubes	-	300	1	8	1	21.5	35.7	
Fe-Cu/Graphite	-	260	2	-	1.1	37.8	44.9	(C. Li et al., 2016)
Fe	Na/S	330	2	12.9	4	64.24	25	(Botes et al., 2016)
Fe	-	280	2	3	1	19.3	91	(Y. Zhang et al., 2015)
	Na, K	280	2	3	1	23.3-22.1	93.2-97.1	
	Zn, Mn	280	2	3	1	18.1-34.1	98.3-37.4	
Fe	Zn/Na	350	2	3	2.7	42.7	95.1	(M. Zhao et al., 2018a)
	Zn/K	350	2	3	2.7	37.2	95.02	
Fe	Zr	280	1	-	1	57	40.6	(Zhang et al., 2019)
Mo/ γ -Al ₂ O ₃	K	300	1	6	2	21.8	4.2	(T. Li et al., 2017)

^a Hierarchical α -Al₂O₃ support; ^b Iron nanoconfinement inside carbon nanotubes; ^c Nitrogen-rich mesoporous carbon-supported Fe catalyst; ^d Carbon-coated SiO₂; ^e Ethylene glycol pretreated catalyst

Duan et al. (Duan et al., 2016) studied the effects of potassium addition on Fe-CNT-supported catalyst for the FTO process. It is believed that potassium as a promoter causes more uniform and smaller iron particles, higher degree of iron carbidization, and more defects on carbon nanotubes. The high stability of catalyst is also related to more defects on CNTs acting as anchoring sites to stabilize iron nanoparticles. The additional potassium promoter in FeK catalysts is favorable for obtaining higher yields of lower olefins and fuels (Duan et al., 2016).

Sodium and sulfur are promoters for iron catalyst which suppress methane selectivity and increase C₂-C₄ products with maximum olefin content, respectively. Botes et al. (Botes et al., 2016) showed that maximum C₂-C₄ selectivity was achieved at high loadings of these promoters. However, for maximum CO conversion, lower promoter loading was required. Additionally, it was reported that an increase in promoter concentrations increased the activity without negative effects on selectivity (Botes et al., 2016).

Xie et al. (Xie et al., 2016b) studied the fundamentals of structure sensitivity and combination of Na-S promotional effects on Fe/CNF in FTS for light olefins. They implemented density functional theory (DFT) on H adsorption for a fundamental understanding of (Na-S) promotion effects on selectivity. The researchers reported that Na₂S is a better promoter than Na₂O because it increased the H adsorption strength on iron and reduced the adsorption of carbon, thus decreasing methane formation and increasing olefin selectivity (Xie et al., 2016b). Zhou et al. (X. Zhou et al., 2015) added sulfur to Fe/ α -Al₂O₃ catalysts to obtain highly efficient and carbon-deposit-resistant catalysts for FTO process. The promoted sulfur catalysts exhibited low selectivity toward CO₂ and CH₄ and more carbon deposition. The change in the type of carbon deposits from encapsulating carbon to fibrous carbon was related to the sulfur addition.

Zhang et al. (Y. Zhang et al., 2015) investigated promoted porous iron-based catalyst prepared through one-pot solvothermal method for FTS. They evaluated the effects of promoters (Na, K, Zn, and Mn) and pore size on CO conversion and formation of light olefins. For iron-based catalysts, alkali metal ions as a promoter donate electrons to the active surface and improve the basicity. They suggested Na as the optimal promoter in FT synthesis. The presence of Mn in the promoted Fe/Mn catalyst led to a rise in olefins formation (34.1 %) and a decrease in methane selectivity, while the resultant CO conversion was 37.4 % (Y. Zhang et al., 2015).

Addition of zinc promoter to iron catalyst leads to the dispersion of iron sites. Hence, the CO conversion increases, and the CO₂ selectivity declines. Zhao et al. (M. Zhao et al., 2018a) prepared the Zn-modified iron catalyst using co-precipitation method for production of light olefins from syngas. XRD patterns of calcined promoted iron catalysts revealed that Zn promoter had significant effects on the crystalline structure of iron oxides. In addition, the promoter avoided the sintering of α -Fe in the reduction process. They used Na⁺ and K⁺ as electronic promoters and demonstrated their positive effects on the selectivity and activity of iron catalysts for light olefins production (M. Zhao et al., 2018a).

Zhang et al. (Zhang et al., 2019) used Fe-Zr co-precipitated catalysts for the production of light olefins using syngas. The addition of Zr enhanced the turnover frequency (TOF) of the catalyst as well as its stability. It was suggested that Zr promotion facilitated the dispersion of active crystallites, by decreasing the iron oxide crystal size. Hence the specific surface area of the Zr-promoted Fe-based catalysts increased. Based on TPR profile, Zr promoted catalysts started to reduce at a higher temperature. Finally, it was reported that the surface zirconium species effectively suppressed the hydrogenation capacity of primary olefin products and increased the olefin/paraffin ratio (Zhang et al., 2019).

Xu et al. (Xu et al., 2018) studied the catalytic performance of iron oxide catalysts supported on Ag-doped mesoporous MnO_x for FTS process. It was observed that Ag promoter increased the activity of Fe/MnO_x catalyst for CO conversion and improved the selectivity to light olefins. The Ag promotion also increased the carburization of reduced metallic Fe into iron carbides at low reduction temperature. Moreover, Ag enhanced the reduction of the MnO_x as support and provided more O vacancies for adsorption of CO, enhancing both the activity by 1-5 times and the light olefins selectivity (Xu et al., 2018). Table 2.6 shows some Fe-based catalysts used in light olefins production through FTO.

Bi and Pb possessing melting temperatures ($T_{Pb} = 327\text{ }^{\circ}\text{C}$; $T_{Bi} = 271\text{ }^{\circ}\text{C}$) lower than that of FT process, provides promising contact with iron catalysts. In addition, Bi and Pb have several oxidation states, resulting in favorable oxidation-reduction cycle (V. V Ordonsky et al., 2017). These two promoters decrease the C₅₊ selectivity with the product distribution shifting to lighter hydrocarbons compared to alkali promoters (Gu et al., 2019a). It was reported that Bi- and Pb-promoted catalysts led to an increase in the selectivity to light olefins (60 %) at atmospheric pressure. It was found that the intrinsic activity of iron carbide active sites

enhanced in the presence of promoters, facilitating CO dissociation via oxygen removal (Figure 2.8). It should be noted that, Gu et al. (Gu et al., 2019a) in a similar study evaluated the CNT role as a support. They reported that the catalyst selectivity to light olefins enhanced significantly due to synergetic effects of iron nanoparticles inside carbon nanotubes promoted with Bi and Pb. Secondly, the iron reduction and carbidization under atmospheric pressure was facilitated using CNTs support (Gu et al., 2019a).

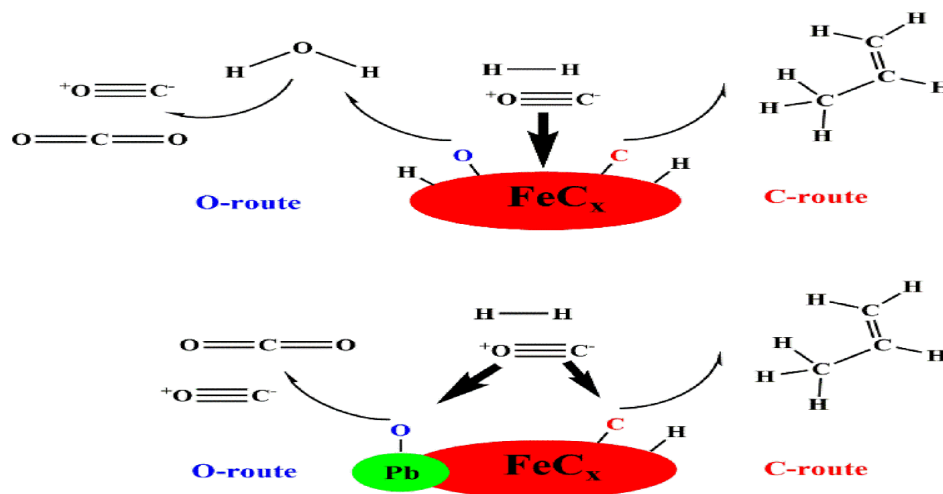


Figure 2.8: Schematic of soldering metal-promoted iron catalyst for FTO. Reproduced with permission from (V. V Ordonsky et al., 2017).

For cobalt catalysts based on oxide supports, the most commonly used promoters are noble metals, transition metal oxides, and some rare earth metal oxides. The most common promoters for Co-based FTS catalysts are listed in Table 2.7, and include Al, Pt, Mn, Zn, La, Ce, and Ru. The promoter favorably affects the structure and dispersion of cobalt species, FT reaction rates, and product selectivity. Considering Co-based catalysts, Nabaho et al. (Nabaho et al., 2016) studied promotion of platinum in cobalt-based FT catalysts. Pt promoters are more likely to improve the reducibility of the catalyst despite physical separation of promoter from active metal. The decoupling of hydrogen spillover effect was presented using a hybrid catalyst (i.e. mixture of Pt/Al₂O₃ + Co/Al₂O₃). The high hydrogenation effect happened at Pt promoter loadings greater than 0.1 % and CH₄ selectivity declines at low Pt loadings.

Zafari et al. (Zafari et al., 2017) reported the synergistic effects of Zn and Ce promoters on the performance of Co-Mn/SiO₂ catalyst in FTS for olefins synthesis. CeO₂ exhibited unique redox property with the ability to shift from reduced state (Ce³⁺) to oxidized state (Ce⁴⁺), which

significantly enhanced the reducibility of the catalyst. From the results, Zn and Ce promoters affected the surface area, pore volume, and pore size distribution, with surface area and pore volume being increased. In addition, promoters facilitated high dispersion of catalyst crystallites (Zafari et al., 2017).

Table 2.7: Light olefin selectivity of different Co-based catalysts in FTO.

Catalyst	Promoter	T (°C)	P (MPa)	GHSV (Lh ⁻¹ g ⁻¹)	H ₂ /CO	C ₂ -C ₄ selectivity (%)	CO conversion (%)	Reference
Co-Meso-HZSM 5 ^a	-	240	0.1	-	2	29.1	79	(Xing et al., 2015)
Co-HZSM 5	-	240	0.1	-	2	30.9	75.9	
Co/ γ -Al ₂ O ₃	Ru/La	220	2	4-6	2	11.2	45.8	(Sage et al., 2017)
Co/ γ -Al ₂ O ₃ -PT ^b	Ru/La	220	2	4-6	2	15.9	43.7	
Co/ γ -Al ₂ O ₃	Mn	240	0.5	-	2.1	8-11	20-45	(Pedersen et al., 2018)
Co-Al ₂ O ₃ /ZSM 5	La	240	2	4	2	24.1	20.7	(Ryu et al., 2015)
Co/MnO _x	-	240	1	2.5	2	26.5	45.3	(W.-G. Zhou et al., 2015)
Co/MnO _x -BDO ^c	-	240	1	2.5	2	42.2	42.3	
Co-Mn/SiO ₂	Zn/Ce	260	0.1	4.5	1	10-36	80-90	(Zafari et al., 2017)
Co/Al ₂ O ₃	-	220	2	144	2	44.8-50.4	9.5	(Nabaho et al., 2016)
Co/Al ₂ O ₃ +Pt/Al ₂ O ₃	Pt	220	2	144	2	46.2-59.2	13	
Co/TiO ₂	-	220-250	1	0.8	2	10.6-20.9	18.6-36.6	(Phaahlamohlaka et al., 2018)
Co/TiO ₂ @mSiO ₂ ^d	-	220-250	1	0.8	2	5.2-21.7	17-46.1	
Co/TiO ₂ @mSiO ₂	Ru	220-250	1	0.8	2	12.1-23.3	31.6-58.9	
Co/CNT	-	220	2	0.04	2	18.9-29.5	5-84	(Nakhaei Pour et al., 2017)
Co/CNT	-	240	2	5	2	8.1-20.3	34.5-66.7	(Chernyak et al., 2020)
CoPt/TiO ₂ -C ^e	-	210	1	4	2	5.4	19.9	(Hong et al., 2018)
CoPt/TiO ₂ -P1 ^f	-	210	1	4	2	6.2	48.2	
CoPt/TiO ₂ -P3	-	210	1	4	2	6.5	39.6	
0CTAB-Co@C ^g	-	230	2	6.75	2	10.87	35.62	(Chen et al., 2019)
2CTAB-Co@C	-	230	2	6.75	2	11.87	34.15	
4CTAB-Co@C	-	230	2	6.75	2	11.21	36.20	
8CTAB-Co@C	-	230	2	6.75	2	11.27	40.08	

^a Hierarchical HZSM-5 zeolite support; ^b Acetylene pretreated catalyst; ^c 1,4-Butanediol (BDO) was used as solvent for catalyst precursors; ^d Mesoporous silica (mSiO₂); ^e Calcined CoPt/TiO₂; ^f Plasma treated CoPt/TiO₂ for 1, 3, and 4 h; ^g Cobalt catalyst embedded in nanoporous carbon with m(CTAB)/n(Co)= 0, 2, 4, 8)

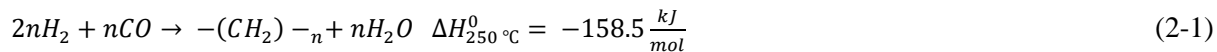
The effects of Mn, Ce, La, and Al on the final morphology of Co₂C nanoparticles as FTO catalyst were investigated (Z. Li et al., 2017). Mn as a typical electronic promoter formed a co-precipitated CoMn catalyst, provided higher CO surface coverage and enhanced both the

activity and olefin selectivity. It was reported that at a high reaction temperature (260 °C), Mn addition as a promoter led to decrease in methane selectivity and increase in the chain growth probability. The olefin selectivity of the promoted catalysts synthesized by impregnation were in the order: Co/Mn > Co/Ce > Co/La, which was similar to that of un-promoted Co₃O₄. Mn promotion altered the chemisorption of the reactants on the catalyst and increased dispersion of the active phase. It was concluded that the desired morphology is obtained by co-precipitation of the cobalt species and the Mn promoter in the presence of Na (Z. Li et al., 2017).

Li et al. (T. Li et al., 2017) evaluated the effects of potassium addition on catalytic performance of alumina supported carburized molybdenum catalyst for FTS. It was suggested that addition of potassium increased the interaction between molybdenum and alumina support. Moreover, the selectivity of light olefins and long chain hydrocarbons enhanced, while the reaction rate of FTS declined. The hydrogenation of olefins was avoided because of the increase in catalyst basicity.

2.8 Current mechanism of Fischer-Tropsch synthesis reaction

As described in Eq (2-1), the reactants (CO and H₂), adsorb and dissociate at the surface of the catalyst to form methylene and H₂O (Hassankiadeh et al., 2012).



Biomass is assumed as a feedstock gasified to generate synthesis gas for further conversion into transportation fuels and other longer chain hydrocarbons in the FT process. The kinetic studies of FT synthesis can be accomplished using empirical power law expressions considering rate-limiting steps. The Langmuir-Hinshelwood-Hougen-Watson (LHHW) rate theory has also been employed to describe the mechanism of FTS. The FTS kinetic has extensively been studied, and in most cases, the mole fractions of hydrocarbons (M_n) follow Anderson- Schultz-Flory (ASF) model as function of the carbon number (*n*) and chain growth probability (*α*):

$$M_n = (1 - \alpha)\alpha^{n-1} \quad (2-2)$$

Under an idealized circumstance, *α* reflects the catalyst ability to catalyze chain propagation as follows:

$$\ln\left(\frac{W_n}{n}\right) = n\ln\alpha + \text{constant} \quad (2-3)$$

where W_n refers to the mass fraction of species with chain length of n . There is a general agreement that the product distribution follows the ASF chain-length statistics. As for the lighter hydrocarbons (C_1 - C_4), the selectivity was predicted to be higher than α . However, as shown in Figure 2.9, higher selectivity of heavier products (C_{21+}) can be obtained at a larger chain growth probability value. For the ideal ASF model, the FTS product distribution based on carbon number is a function of the α value (K. Cheng et al., 2017).

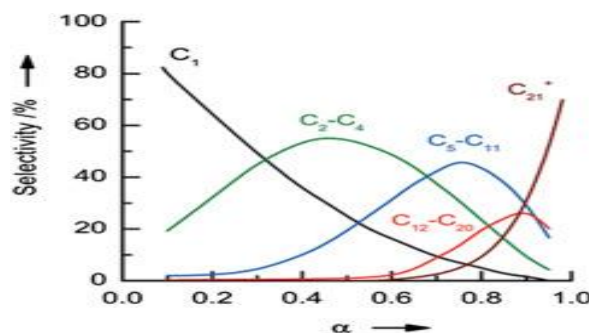


Figure 2.9: Product distribution in FT synthesis with respect to the chain growth probability (α). Reproduced with permission from (Y. Cheng et al., 2017).

In 2015, Förtsch et al. (Förtsch et al., 2015) studied an extension of the ideal ASF model to explain common deviations from experimental data for FTS reaction. It was also reported that a negative deviation can be found at C_2 together with an enhanced methane formation depending on the type of catalysts. The extended ASF model allows for significant data reduction to characterize product distributions in the components with a higher carbon number. Kinetic studies of FTS reaction using LHHW method are generally divided into two methods to provide quantitative information for syngas consumption rates and product distribution rates. The syngas consumption rate and the product (hydrocarbons) distribution rates can be estimated by lumped kinetics and the traditional ASF model, respectively (Méndez and Ancheyta, 2020).

A kinetic model describing FTS over Co/Al_2O_3 catalyst was introduced using CO-insertion mechanism (Bhatelia et al., 2014). It was found that 1-olefin re-adsorption phenomena provided an explanation for the observed deviation from a classical ASF distribution, with a linear chain length dependency for FTS over Co catalyst. On the other hand, the activation energy for the overall FTS was determined to be 99.15 kJ/mol, which was in close agreement with the range

reported for cobalt catalyst. Through catalytic-polymerization reactions, α -olefins and paraffins are formed on chain-growth sites as primary or secondary products (Figure 2.10). Dissociative desorption and CO_2 -hydrogenation reactions result in the formation of primary olefins. Furthermore, associative desorption reaction occurs on the surface of active metal phases to produce paraffins. Olefins isomerization can undergo secondary hydrogenation and lead to a higher conversion to the corresponding paraffin due to their carbon number (Panzone et al., 2020). For a comprehensive discussion on FTS mechanisms, a summary of major findings in the FT kinetic modeling is given in Table 2.8.

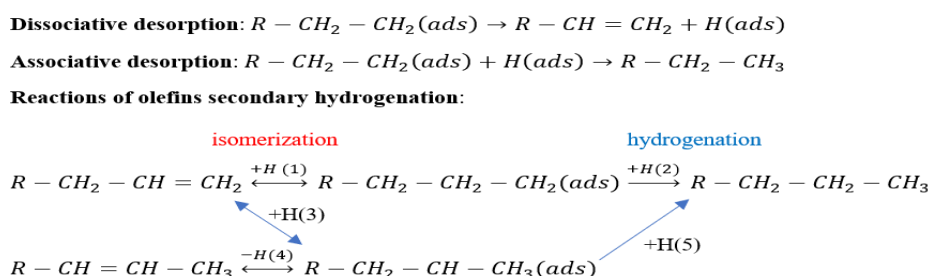


Figure 2.10: Schematic representation of olefins’ isomerization and the corresponding paraffin. Reproduced with permission from (Panzone et al., 2020).

Table 2.8: A summary of some kinetic studies predicating the FT reaction.

Catalyst	Reactor	Kinetic data acquisition conditions	Summary	Reference
Mn-Co/SiO ₂	Fixed-bed reactor	$-r_{CO} = \frac{abP_{CO}P_{H_2}}{(1 + bP_{CO})^2}$	The kinetics of FTS was reported as a function of Mn/Co ratio, temperature, and the partial pressures of H ₂ and CO	(Johnson et al., 2015)
Co-Mn/TiO ₂	Fixed-bed micro-reactor	$-r_{FT} = \frac{k_p b_{CO} P_{CO} P_{H_2}}{1 + b_{CO} P_{CO}}$	Non-linear regression method was used to obtain activation energies for optimal kinetic models	(Atashi et al., 2010)
Co-Ni/Al ₂ O ₃	Fixed-bed reactor	$-r_{FT} = \frac{k p_{CO} p_{H_2}}{(1 + a p_{CO} p_{H_2}^{0.5})^2}$	A kinetic model was established with LHHW adsorption theory by fitting the experimental data of the partial pressures with the kinetic equations	(Nikparsa et al., 2014)
Co-Ni/SiO ₂	Plug flow reactor	$r_{FT} = \frac{k p_{H_2}^{1/2} p_{CO}}{(1 + a p_{CO} + b p_{H_2}^{\frac{1}{2}} + c p_{H_2}^{1/2} p_{CO})^2}$	Different mechanisms according to LHHW indicates that model of CO insertion mechanism yields the most reasonable result	(Sun et al., 2016)
Co-Mn oxide	Fixed-bed reactor	$-r_{FT} = \frac{k P_{CO} P_{H_2}}{(1 + a P_{H_2}^{0.5} + b P_{CO} P_{H_2}^{0.5})^2}$	Based on carbide/ enolic mechanisms and LHHW approach, the activation energy for the best	(Mansouri et al., 2013)

			fitted model was found to be 80.63 kJ/mol.	
Fe-Ni-Ce	Fixed-bed micro reactor	$-r_{CO} = \frac{k_p b_{CO} P_{CO} (b_{H_2} P_{H_2})^2}{(1 + 2(b_{CO} P_{CO})^{0.5} + (b_{H_2} P_{H_2})^{0.5})^6}$	Levenberg-Marquardt (LM) algorithm was employed in obtaining the kinetic model and parameters	(Abbasi et al., 2019)
25%Co/Al ₂ O ₃	Continuously stirred tank reactor (CSTR)	$r_{FT} = \frac{0.0133 P_{CO}^{-0.31} P_{H_2}^{0.88}}{(1 - \frac{0.24 P_{H_2 O}}{P_{H_2}})}$	Addition of 10% water lowered CH ₄ rate during FTS on the unpromoted cobalt catalysts, while catalyst deactivation was observed slightly	(Ma et al., 2014)
Fe-Co-Mn/MgO	Fixed-bed reactor	$-r_{FT} = \frac{k_p (b_{H_2} P_{H_2}) (b_{CO} P_{CO})^{0.5}}{[1 + (b_{H_2} P_{H_2}) + 2(b_{CO} P_{CO})^{0.5}]^2}$	LHHW approach was used to obtain CO consumption rate equations based on eight mechanisms. The activation energy for the best fitted model, which was estimated from non-linear regression method, was 85 kJ mol ⁻¹	(Oliaei Torshizi et al., 2015)
Fe-Ni/Al ₂ O ₃	Fixed-bed micro reactor	$-r_{CO} = A \frac{P_{CO} P_{H_2}^{0.5}}{(1 + k_{CO} P_{CO} + k P_{H_2 O})^2}$	High apparent activation energies for hydrocarbon formation were consistent with the intraparticle mass transport limitations	(Sarkari et al., 2012)
K promoted precipitated iron	Microchannel reactor	$-r_{FT} = A \frac{P_{H_2} P_{CO}}{(1 + a P_{CO} + b P_{H_2} + c P_{H_2}^2 P_{H_2 O} P_{CO_2})^2}$	Eley-Rideal-type mechanism was determined to be the best fitting in both statistical and physical relevance	(Sun et al., 2017a)

FTS follows a polymerization mechanism via initiation, propagation, and termination, and in situ studies such as X-ray absorption spectroscopy (XAS) provide a better understanding of FTS catalyst at realistic conditions. Tsakoumis et al. (Tsakoumis et al., 2012) investigated the catalytic properties and performance of rhenium promoted and un-promoted cobalt-based catalysts using in situ X-ray absorption and diffraction experiments. The catalytic activities were evaluated in a fixed-bed reactor at 493 K, 1.8 MPa, H₂/CO = 2.1, and suggested the absence of bulk Co transformations at the initial FT catalyst deactivation. The addition of rhenium was observed to affect the transition from CoO to metallic Co.

The catalytic activity and carbide formation of the Co/TiO₂ catalyst for 48 h time-on-stream was studied using GC and operando XRD (Van Ravenhorst et al., 2021). Cobalt carbide formation, Co particle growth, and Co oxide formation were investigated to explain Co/TiO₂ catalyst deactivation. As shown in Figure 2.11, to gain fundamental insights into the FTS catalysts during deactivation, operando XRD and XAS measurements were performed, indicating the start of carbide formation (gray dotted line in Figure 2.11 a-c). More specifically,

the selectivity of the 10 wt% Co/TiO₂ catalyst changes from longer chain hydrocarbons to methane during 48 h time-on-stream. Operando XAS shows the corresponding Co K-edge XANES spectra (Figure 2.11 d) and magnitude of Fourier transform of the reference materials along with catalyst (Figure 2.11e,f). These synchrotron XAS spectra provide considerable change in Co pre-edge distinct which implies the metallic Co in the fresh reduced catalyst undergoing carbidization (Co₂C).

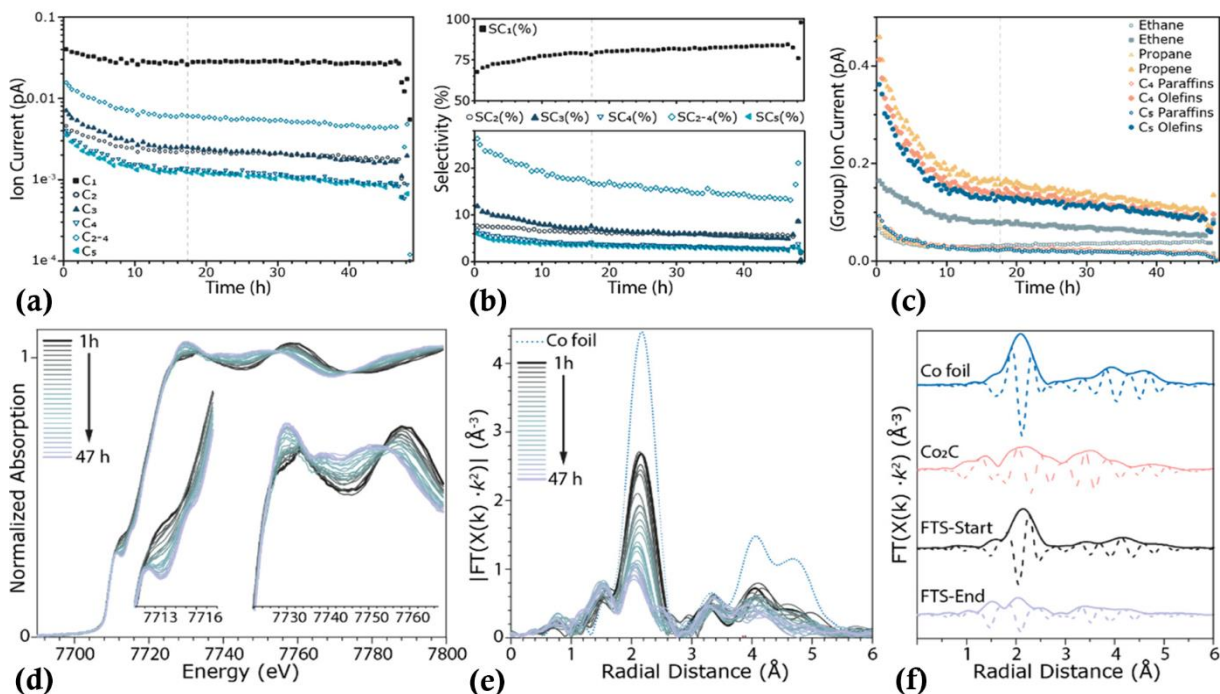


Figure 2.11: (a-c) The activity and selectivity measurements of the Co/TiO₂ catalyst during 48 h using GC and operando XRD; (d-f) Operando XAS Co K-edge spectra of Co/TiO₂ during FTS (P: 1.6 MPa, TOS: 48 h, H₂/CO: 1, T: 220 °C). Reproduced with permission from (Van Ravenhorst et al., 2021).

Considering reaction mechanism for iron catalysts, Peron et al. (Peron et al., 2021) prepared a series of promoted iron catalysts supported on amorphous SiO₂ through impregnation and mechanical mixing. The in-situ XANES spectra at the Sb K- and Sn K-absorption edges confirmed that the mechanism of the promotion with Sn can be different from that with Sb. Comparison with the reference XANES spectra provides a quantification of various Sb phases during the catalyst reduction.

Pena et al. (Peña et al., 2018) reported that carbon species on iron-based catalysts such as α -olefins from wax products during FTS may inhibit complete catalyst carburization. In situ XANES measurements demonstrated common features of Fe^0 and Fe_5C_2 phases. XRD analysis of the spent catalysts displayed Hägg carbide phase related to wax products. The sintering of Hägg carbide nanoparticles was enhanced by WGS reaction and formed stable complexes resistant towards hydrogenation during FTS. Different phases of iron such as FeO , Fe_5C_2 and Fe^0 were identified by a linear combination fitting (LCF) of the XANES. The interaction of carboxylate species with iron oxide sites can suppress iron catalyst carburization during FTS.

It was reported that Co_2C precursor can potentially allow modifying Co-based catalyst microstructural properties at the nanoparticle (NP) level (Tsakoumis et al., 2019). K-edge Co-XANES spectra confirmed that the reduced catalysts at different temperatures form hcp-rich metallic Co NPs, resembling bulk cobalt. According to the findings reported, FTS on hcp-Co NPs with lowest number of defects leads to the highest selectivity to C_{5+} and chain-growth probability due to stacking faults.

In another study by Bertella et al. (Bertella et al., 2020), in situ XAS was conducted to investigate Ru promotion effects on Co/TiO_2 FTS catalysts. According to in situ XAS measurements, a high loading of Ru (above 0.2 wt%) could partly cover the most active metallic Co catalysts, resulting in CoO_x species. It was suggested that Co^0 could donate partial electron charge to Ru^0 , with transformation of Co^0 to $\text{Co}^{\delta+}$. This electron donation at a high Ru concentration could promote an irreversible adsorption of surface oxygen obtained by dissociatively adsorbed CO on $\text{Co}^{\delta+}$. The influence of Ru loadings on the reduced CoRu/TiO_2 catalysts during FTS was assessed by EXAFS. The spectra for promoted catalysts showed a few changes in the Ru coordination environment, which is mainly attributed to a variation in Ru coordination number and the interaction between Ru and adsorbed species such as hydrogen and carbon adatoms. The higher the Ru content ($\gg 0.2$ wt%) was, the less noticeable changes in higher shells were. Table 2.9 shows a summary of notable studies using synchrotron analysis to understand the reaction mechanism in FTS. FTS reaction mechanism is still controversial due to different phases produced during the pretreatment of the catalysts and the complex reaction network.

Table 2.9: Synchrotron methods employed in characterization of Fe and Co FTS catalysts.

Catalyst	Synchrotron characterization techniques	Key findings	Reference
Co/TiO ₂	STXM-XAS	The structure-performance relationship between the Co valence state and the organic films obtained with the aid of C K-edge NEXAFS spectra	(Yao et al., 2018)
Co/TiO ₂ , Co/Al ₂ O ₃ , Co/SiO ₂ , Co/ZrO ₂	XAS, DRIFTS, XAS	The increase in activity measured for dried reduced versus dried calcined reduced catalysts is strongly related to hexagonal Co sites	(Mitchell et al., 2018)
Fe (110) single-crystal surface	In situ XPS	Iron carbides (octahedral and trigonal prismatic) in the active state of the catalyst confirmed that the CO insertion step is not involved in the FTS	(Shipilin et al., 2022)
Co/TiO ₂	XAS/X-PEEM	The oxygen vacancies as determined from the O K-edge spectra, prevent total reoxidation of Co nanoparticle in syngas and improves catalyst performance	(Qiu et al., 2022)
NaSFeMnO _x	XAS (XANES+EXAFS)	Promoters enhanced the formation of active species of Fe ₅ C ₂ and olefins by suppressing the oxidation state of Fe and enhancing formation of carbonized species	(Yang et al., 2022)
Fe-based	NEXAFS	In situ techniques were used to investigate the activation and carburization of iron oxide FTS catalysts	(Nielsen et al., 2020)

2.9 Techno-economic analysis

To be able to compare different studies like Biomass-to-Liquids (BTL) and combined processes, crude oil pricing is important. Moreover, local government policy for controlling greenhouse gas (GHG) reduction, land management, and types of feedstocks is of great importance (Y. Liu et al., 2020). Commercial companies such as Shell and Sasol use Gas-to-Liquids (GTL) and Coal-to-Liquids (CTL) for the production of synthetic fuels. Using bio-renewable sources like biomass is a viable option for fuel and chemical production instead of fossil-based materials in terms of carbon dioxide emission. The BTL process consists of various steps like transportation, gasification, Fisher-Tropsch synthesis, and upgrading the products (Martinelli et al., 2020).

Thai et al. (Do and Kim, 2020) used Aspen Plus to model and simulate the direct hydrogenation of carbon dioxide to light hydrocarbon. Criteria such as carbon element efficiency, environmental performance, and unit operation cost were studied. The techno-economic study of the FTS for liquid fuels production can be done by considering all mass and energy conversion of biomass to liquid (BTL).

Snehesh et al. (Snehesh et al., 2017) analyzed four different conversion scales ranging from 43% to 73% of FT reactors. They found electricity to be a major co-product in the BTL system, while a consistent and economic source of biomass is absolutely crucial. In addition, production of drop-in biofuel obtained from biogas using FTS was studied by Okeke et al. (Okeke and Mani, 2017). Aspen Plus simulation platform was applied to conduct a techno-economic assessment. As a result, it was suggested that a biogas to liquid (BgTL) plant has a potential for rapid commercialization and competition with traditional fossil-based liquid fuels in USA. The production cost of drop-in biofuel at target year of 2015 was reported at \$5.29 per gallon of gasoline (Okeke and Mani, 2017).

Liu et al. (Y. Liu et al., 2020) investigated the FT process for conversion of natural gas to light olefins. Based on the techno-economic analysis, the capital expenditure of the FeMnCuK-based FTO plant for treatment of 360 MT natural gas per day was \$170.8 MM. The cost of production for target year of 2012 was \$679/MT light olefins, which was ~\$2.25 per gallon of light olefins at target year of 2015 (assuming average density of 1.31 kg/m³ for C₂-C₄) (Y. Liu et al., 2020). A summary of equipment costs for each section of both processes together with their block flowsheet is shown in Figure 2.12 (Y. Liu et al., 2020; Okeke and Mani, 2017).

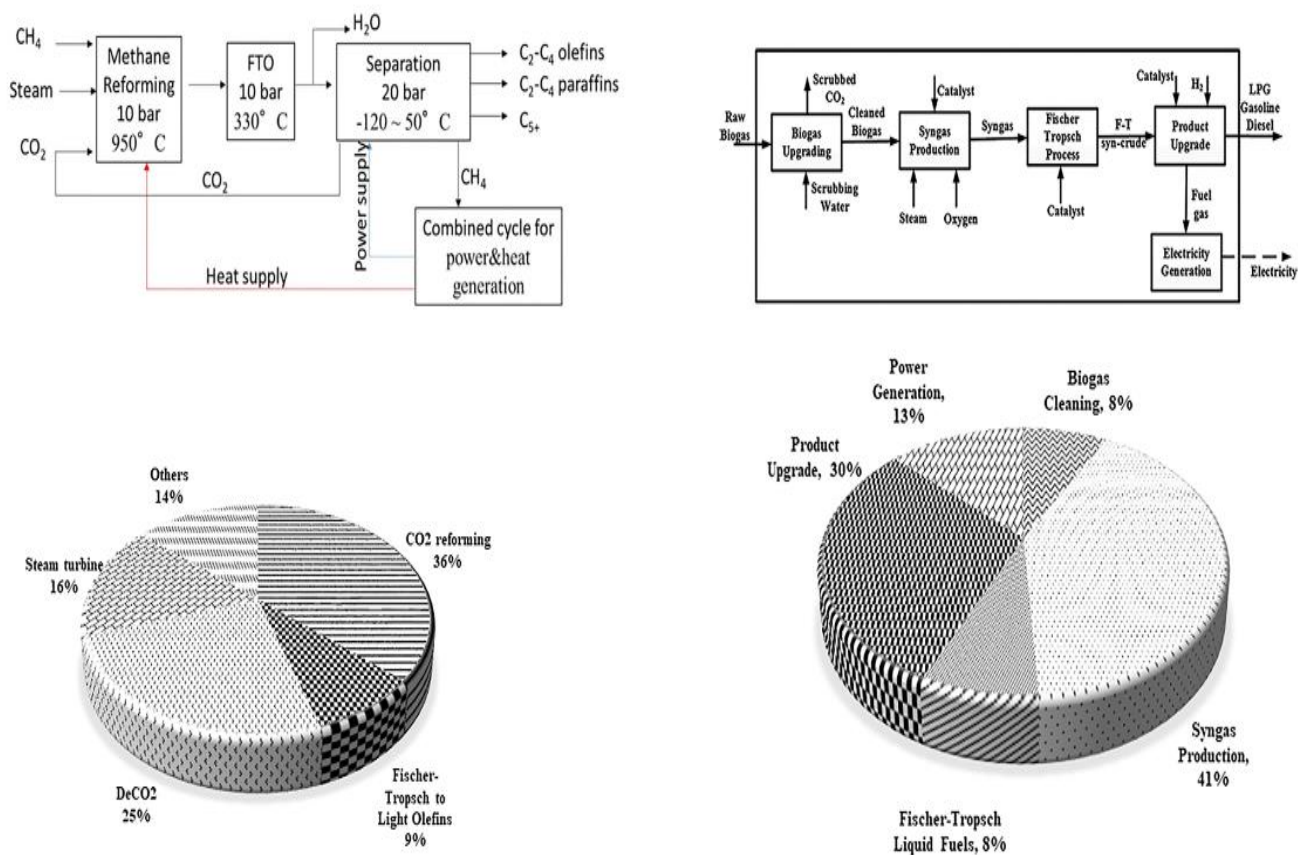


Figure 2.12: Block flowsheet of Fischer-Tropsch to light olefins (left) and Fischer-Tropsch to liquids (right) with percentage cost of installed equipment. Reproduced with permission from (Y. Liu et al., 2020; Okeke and Mani, 2017).

Applying techno-economic analysis, Fischer-Tropsch kinetics were investigated to develop process models and the effects of the paraffin-to-olefin ratio. It was concluded that co-processing natural gas and biomass not only improves the economic benefits of converting biomass-to-liquid fuels, but also facilitates flexibility in process integration (Sahir et al., 2019b). It was suggested that by optimizing FT kinetics and process integration strategies, the products can be controlled in terms of fuel ranges. Co-feeding natural gas and biomass, Rafati et al. (Rafati et al., 2017) studied the FTS process for production of liquid fuels. Although costs of liquid fuels reduced nearly 30% by co-feeding, production of FT biofuels at oil price of \$60/barrel is not economically feasible (Rafati et al., 2017).

The FTS has been studied widely in terms of economic feasibility and environmental impacts. Table 2.10 provides some of the studies on techno-economic assessment of FT plants

integrating with bioethanol, supercritical water reforming, electrolysis, direct methane to methanol, methanol-to-gasoline, and the Topsoe integrated gasoline synthesis technologies. The feedstock of these plants was mostly biomass, biogas, bio-oil, natural gas, renewable electrolytic H₂ and ethanol industry derived CO₂. Compared to the conventional FTS plants, these FT-based plants were environmentally friendly due to applying renewable resources, while in most cases the minimum fuel selling prices could not compete with the market prices, indicating the necessity of providing governmental subsidy and tax concessions or exemptions in FTS plants.

Table 2.10: Techno-economic assessment of Fischer-Tropsch synthesis.

Process-Catalyst	Notes	Reference
FTS-Bioethanol plant -Fe/CNT pellet catalyst	<ul style="list-style-type: none"> -Conversion of biomass-derived syngas to syncrude (biogasoline and biodiesel) -Reactant flow: 3305 kg syngas/h, product capacity: 1000 kg syncrude/h -Net annual profit: 5.2 MUSD/year, internal rate of return: 107.9% -Environmentally friendly process 	(Borugadda et al., 2020)
FTS -Fe and Co catalyst	<ul style="list-style-type: none"> -Conversion of biomass to FT liquids -Overall thermal efficiency of biomass to FT liquids considering electricity output was in the range of 41.3-45.5% for Fe- and Co-based catalyst. -Co-feeding of natural gas and biomass reduces costs of biomass pretreatment and gasification. -Co-feeding of natural gas and biomass reduces costs of FT liquids about 30% (from \$28.8 to \$19-\$20 per GJ of FT liquids). -Production of FT biofuels at oil price of \$60/barrel is not economically feasible. 	(Rafati et al., 2017)
LTFT and SCWR ^a -Not mentioned	<ul style="list-style-type: none"> -Integrating LTFT with SCWR of bio-oil aqueous phase to produce biofuels and electricity -Plant capacity: 60 t/h, feeding concentration: 25 wt%, return rate: 10% -FT liquids: 0.93€/kg diesel, 0.26€/kg jet fuel, 1.20€/kg gasoline -Electricity selling price: 0.17€/kWh -Decrease in selling price by increasing plant size (20-200 t/h) 	(Campanario and Gutiérrez Ortiz, 2017)
FTS and co-electrolysis ^b -Co catalyst	<ul style="list-style-type: none"> -Fuel production via Power-to-X process -Reduced numbers of reactors and heat exchanger compared to Power-to-X technologies^b -Overall energetic efficiency: 68% (62% considering heat losses) -Focus on valuable products like waxes favor economic feasibility -Capital expenditure of the plant: 194,000€/bpd which is higher than that of commercial plants e.g., Velocys (90,000€/bpd), Shell/Pearl (122,000€/bpd), and Sasol/Oryx (25,000-44,000 €/bpd) 	(Herz et al., 2018)

	-Availability and cost of renewable electricity affect the production cost	
FTS	-Conversion of lignite and woody biomass to jet fuel and electricity	
-Not mentioned	-Plant profitability is sensitive to biomass input fraction	
	-High moisture content of biomass (43%) causes energy penalty	(Kreutz et al., 2020)
	-Co-firing of lignite and biomass is less profitable than solely biomass	
	-Carbon-negative plants (only biomass input) are economically feasible at oil prices below \$100/bbl with carbon emission price above \$120/tonne CO _{2eq}	
	-Conversion of natural gas into liquid products	
	-Unit cost of DMTM process is sensitive to the methane recycle ratio	
	-Unit cost of FTS in MCR is less sensitive to the tailgas recycle ratios	
FTS and DMTM ^c	-Higher energy requirements compared to conventional GTL technologies ^d	(Santos et al., 2021)
-Co catalyst	-For internal rate of return (IRR) above 10%, tailgas recycle ratio has to be above 8% at CO conversion of 80%, while the minimum methane recycle ratio of 60% is required for profitability	
	-For profitability index (PI) >1, tailgas recycle ratio of 15% (at CO conversion of 80%) and minimum methane recycle ratio of 55% is required ^e	
FTS, MTG, TIGAS ^f	-Conversion of biomass to liquid hydrocarbon fuels via Biomass-to-liquid (BTL) process	
-Co catalyst	-Modelling of BTL systems for gasification of woody biomass	(Dimitriou et al., 2018)
	-Overall energy efficiency of BTL: 37.9-47.9% lower heating value (LHV)	
	-Production costs of BTL: 17.88-25.41€ per GJ of produced fuels	
	-BTL production costs is 8% higher than current market prices	
	-Conversion of H ₂ +CO ₂ to FT liquid fuels via electricity generated from renewable source	
	-CO ₂ and H ₂ are provided by ethanol plant and electrolysis, respectively.	
FTS	-H ₂ price (\$2/kg via electrolysis in 2020) has the largest impact on the minimum selling price of FT fuel (\$5.4-5.9/gal)	(Zang et al., 2021b)
-Barium zirconate-based perovskite-type catalyst	-Conversion of 223 metric ton H ₂ /day and 2387 metric ton CO ₂ /day into 351 metric ton/day of liquid FT fuel obtains overall energy efficiency of 57.5% LHV and 52.2% HHV ^g	
	-CO ₂ and H ₂ prices are required to be \$17.3/metric ton CO ₂ and \$0.8/kg H ₂ to be cost-competitive with petroleum diesel price of \$3.1/gal in 2050	
FTO ^h	-Conversion of natural gas into light olefins	
-FeMnCuK	-Capital expenditure of the FTO plant: 170.8 MM\$ for treatment of (360 MT/day and 18849 MMBtu/day) of natural gas	(Y. Liu et al., 2020)
-Fe ₂ O ₃	-Internal rate of return for FeMnCuK-based FTO plant: 20%	
	-The levelized production cost: \$679/MT in year 2012	
FTS	-Conversion of biogas to drop-in diesel fuel in biogas-to-liquid (BgTL) plant	
-Not mentioned	-Minimum selling price of the FT drop-in fuels: \$5.67/gal (feed capacity:2000 Nm ³ /h)	(Okeke and Mani, 2017)

	-Increasing feed capacity to 20000 Nm ³ /h reduces minimum selling price to \$2.06/gal	
FTS	-Co-conversion of natural gas and biomass to transportation fuels	
	-Hydrocracker increases the production of diesel and jet fuels	(Sahir et al., 2019b)
-	-Minimum fuel selling price: \$2.17-3.60 and \$2.47-3.47 per GGE ⁱ with and without hydrocracker, respectively	

^a Low-temperature Fischer-Tropsch and supercritical water reforming

^b Coupling of electrolysis and a chemical synthesis step; Power-to-Gas, Power-to-Fuel, Power-to-Chemicals

^c FTS in microchannel reactor (MCR) and Direct methane to methanol

^d Gas-to-liquid

^e Profitability index is the ratio of net present value to fixed capital investment (PI = NPV/FCI)

^f Methanol-to-gasoline (MTG) and the Topsoe integrated gasoline synthesis (TIGAS)

^g Higher heating value

^h FT synthesis to light olefins

ⁱ Gallon gasoline equivalent

2.10 Fischer-Tropsch synthesis plants; Lifecycle assessment

Due to the petroleum-based fuel with low oil price, many studies included system design, integration and optimization considering high value-added chemical. For instance, one solution to improve the production of C₂-C₄ olefins via catalytic performance is optimization of reaction conditions (Jiao et al., 2016). By doing a lifecycle assessment (LCA) of the economic, energy, and environmental aspects of the FT process, waste released, and raw material consumption can be reduced. Different potential for global atmospheric and toxicological impacts is evaluated via LCA (Huang et al., 2018). The potential for global atmospheric impact involves global warming, ozone depletion, acidification, and photochemical oxidation. Human toxicity potential by ingestion (HTPI), human toxicity potential by exposure (HTPE), terrestrial toxicity potential (TTP), and aquatic toxicity potential (ATP) are categorized as potentials for global toxicological impact (Borugadda et al., 2020). Calculating carbon and energy balances of 14 different FTS fuel production plants, LCA suggested that the cost of FTS diesel depends significantly on feedstock prices (Van Vliet et al., 2009). Coal to oil process via FTS consists of coal mining, washing, transportation, and FT synthesis. However, oil refinery contains crude oil extraction, oil transportation, and petroleum refining (Huang et al., 2018). Table 2.11 discusses some plants integrating FTS with biogas dry reforming, gasification, supercritical water reforming, and direct air capture technologies. These studies mostly focused on FT fuel production from renewable sources like biomass, solar- and wind-based electrolytic hydrogen, and CO₂ byproduct e.g., corn ethanol industry CO₂.

Table 2.11: Lifecycle assessment of Fischer-Tropsch synthesis.

Process	Notes	Reference
BDR ^a , FTS	<ul style="list-style-type: none"> -Conversion of biogas to liquid fuels -Functional unit of the LCA study is defined as 1 kg of synthetic biodiesel produced at plant -Lifecycle environmental profile of synthetic biodiesel is calculated and compared with conventional diesel -Evaluation of the plant in terms of global warming, cumulative non-renewable energy demand, ozone layer depletion, acidification, and eutrophication 	(Navas-Anguita et al., 2019)
LTFT HTFT ^b	<ul style="list-style-type: none"> -Conversion of coal to FT oil -Study focused on LCA of energy use, CO₂ emission and cost input of FTS from coal and its competitor -Mining and washing of coal, and oil production cause the energy input and CO₂ emission -The FTS plant from coal to oil is not beneficial compared to oil refinery pathway in terms of energy use and greenhouse gases emission 	(Huang et al., 2018)
Gasification FTS	<ul style="list-style-type: none"> -Conversion of biomass to FT jet fuel -Lifecycle includes the stages of biomass growth, collection, transportation, plant construction and demolition, production, product distribution, and consumption -Application of steam for heat supply (case1) and power generation (case2) -Cases1 and 2 are better than the commercial plant due to reduced nonrenewable resource consumption and pollutant emissions, while production costs increase. -The pollution mitigation benefit of case1 and 2 are small, the consumption of CO₂ is much less than in traditional processes -Case1 and 2 are sensitive to consumption of electricity and stalk, respectively 	(Li et al., 2019)
SCWR ^c LTFT HT ^c	<ul style="list-style-type: none"> -Production of biofuels via SCWR-LTFT and HT which process bio-oil aqueous phase and oil phase, respectively -Estimating the cradle-to-gate environmental impacts especially the global warming potential (GWP) -Hot water produced in the process is considered as a co-product to be used for district heating. The impact of catalyst is accounted for in the process to produce biofuels 	(Gutiérrez Ortiz et al., 2020)
FTS	<ul style="list-style-type: none"> -Conversion of H₂ and CO₂ into FT fuels -H₂ is provided by water electrolysis with electricity from solar, wind, and nuclear sources -CO₂ is provided by corm ethanol industry byproduct -investigation of greenhouse gas (GHG) emissions of FT fuel plant -Environmental impacts and GHG emissions of FT fuel plant are evaluated using GREET 2020 model^d -Energy efficiency of FT fuel production: 58% 	(Zang et al., 2021a)
FTS	<ul style="list-style-type: none"> -Conversion of miscanthus biomass to biogas via anaerobic digestion -Production of drop-in FT biodiesel by FTS -Focus on emission of CO₂, CH₄, and NO_x which contributes to global warming potential -Compared to commercial plants, the drop-in FT biodiesel reduces both GHG emissions (by 73%) and fossil fuel depletion (4.91 MJ/GGE), while potential of respiratory impacts, smog formation, acidification, and eutrophication is higher. 	(Okeke et al., 2020a)

	-Conversion of CO ₂ (obtained by DAC) and H ₂ (obtained by electrolysis) into FT biodiesel	
	-Evaluation of GHG emissions from the DAC-FTS to biodiesel plant	
DAC ^e , FTS	-The electricity emissions factor used in the process is relatively low	(C. M. Liu et al., 2020)
	-The biodiesel plant is suggested to be conducted in regions with very low grid emission factors	
	-The biodiesel is suggested to be co-located with a renewable energy facility	

^a Biogas dry reforming

^b Low-temperature and high-temperature Fischer-Tropsch synthesis

^c Supercritical water reforming and hydrotreating

^d Greenhouse gases, regulated emissions and energy use in transportation

^e Direct air capture system

2.11 Conclusions

Production of light olefins through Fischer-Tropsch synthesis using syngas as feedstock is an issue of great importance. Development of catalytic systems in terms of activity, selectivity, and stability is required to consider it feasible that light olefins can be produced on an industrial scale via FTO. Iron can be suggested as the promising metal for light olefin synthesis as it is more tolerant of sulfur contaminants present in hydrogen-deficient syngas obtained from biomass, inexpensive, and highly selective toward light olefins. Activity of Fe for water-gas-shift (WGS) reaction can compensate for H₂ deficiency in CO-rich syngas. Fe exists in different forms (χ -Fe₅C₂, ϵ -Fe₂C, ϵ' -Fe_{2.2}C, and Fe₇C₃) as iron carbide which is known to be the active phase in typical FTO process. Among these carbide phases, the highest activity and the lowest methane selectivity belong to Fe₇C₃ and ϵ -Fe₂C for medium range of temperature in FTO. Compared to Fe, Co-based catalysts exhibit high catalytic activity, low WGS activity, and superior stability. Due to low activity for WGS reaction, Co catalysts require higher ratios of H₂/CO in comparison with Fe-based catalyst. Formation of light olefins over Co-based catalysts is mainly attributed to the reactions taking place at the Co/Co₃C interface. In terms of crystal phase, hexagonal close-packed (HCP) structure of Co is believed to have higher FTO activity than face-centered cubic (FCC).

Selection of support, promoter, catalyst synthesis method, and process conditions can significantly affect the output. The support should be capable of providing desirable interaction with active metal and promoters. Promoters should be used cautiously to avoid catalyst poisoning. Basicity of catalysts can be improved by adding alkali metals enhancing syngas hydrogenation. Strong basicity sites would offer an enhanced dissociative adsorption of CO and higher olefin selectivity compared to medium basicity sites. Phase transition in catalyst

reducibility is also affected by adding alkali metals. That is to say, the low-temperature reduction would be inhibited, while high-temperature reductions will be enhanced by increasing alkali metal promoters. It is suggested that Fe-based catalysts possessing terrace or hierarchical sites with pores of molecular sieves are feasible to increase light olefin production during FTS. Surface modification of Fe catalysts supported on carbon materials with nitrogen-containing functionalities is also observed to increase light olefins selectivity in FTO.

Catalyst deactivation can be intensified by inadequate selection of the support, promoter, and synthesis method resulting in the catalyst poor structure. Fe particles as active metal require protection against re-oxidation, carbidization, carbon deposition, and sintering through designing a robust catalytic system specially by incorporating Fe particles within support porous network. Confinement of Fe nanoparticles inside carbon materials like carbon nanotubes would offer high dispersion of active metal within carbon nanotubes protecting metals from deactivation. Promoted core-shell Co-based catalysts with enhanced dispersion of active metals would also be another good candidate for Fischer-Tropsch to light olefins due to sintering resistance.

The economic, energy, and environmental aspects of the FTS process as well as carbon and energy balance of the process can be calculated applying a techno-economic and lifecycle analysis (TEA/LCA), thus suggesting a decrease in both the waste released and raw material consumption. Although the FTS-based plants are mostly environmentally friendly with pollutant emissions and nonrenewable source energy demand being reduced, the minimum biofuel selling price still cannot compete with the market prices of petroleum fuels. Therefore, it is necessary for governments to provide renewable FTS plants with governmental subsidy and tax concessions or exemptions, helping them to survive in the global market.

CHAPTER 3: Experimental Section

The details on the materials, methods of catalyst preparation, catalyst characterization, experimental study, as well as feed and products characterization are given below in detail.

3.1 Materials section

In this work, the chemicals utilized, their purity and suppliers are as follows: calcium carbonate 100%, Fisher Chemical FLC64500, Oakville, Canada; iron (III) nitrate nonahydrate 99+%, Thermo Fisher Scientific 202492500, Ottawa, Canada; aluminum oxide, Alfa Aesar AA4385530, Tewksbury, United States; commercial carbon nanotubes, Mknano Co. (M.K. IMPEX MWCNT-P0815, Ottawa, Canada); ammonium molybdate $((\text{NH}_4)_6\text{Mo}_7\text{O}_{24} \cdot 4\text{H}_2\text{O})$, Fisher Scientific, Hanover, PA); potassium nitrate (KNO_3 , Fisher Scientific, Hanover, PA); nitrogen (Ni-T), acetylene (AC 2.6 AA-A4), hydrogen (HY 5.0 UH-T), and syngas (COAR10H1ZC-AT) were purchased from Linde, Saskatoon, Canada Inc.

3.2 Synthesis and preparation of CNTs support and corresponding catalysts

3.2.1 Synthesis of CNTs support via catalytic chemical vapor deposition method

Carbon nanotubes were synthesized over Fe/CaCO_3 catalyst using acetylene as hydrocarbon source in a chemical vapor deposition (CVD) reactor (internal diameter: 1 in; effective length: 24 in). In each run, 0.19 g of the catalyst was uniformly distributed in an alumina boat and then was located at a 12 in distance from quartz reactor entrance. Figure 3.1 illustrates the experimental setup for CNTs growth where the catalyst boat was placed in the quartz reactor surrounded by a horizontal electric furnace (1740 W, 1200 °C maximum temperature). To avoid air flow to the reactor, the CVD system was purged of air by N_2 (30 mL/min), while heating at a rate of 10 °C/min. Once the set temperature was achieved (700-800 °C), hydrogen flow (100 mL/min) filled the reactor to reduce the metal oxides for 1 h. Subsequently, acetylene (20 mL/min) was fed to the reactor at the same temperature. The reaction continued for the desired reaction time of 30-60 min. After the reaction was completed, the CVD reactor was cooled down to room temperature by nitrogen flow. Finally, the CNTs yield was obtained by measuring the product weight inside the alumina boat according to the Equation (3-1) (Mohammed et al., 2017):

$$CNTs \text{ yield } (\%) = \frac{M_{Total} - M_{Catalyst}}{M_{Catalyst}} \times 100 \quad (3-1)$$

where M_{Total} and $M_{catalyst}$ represent the total mass of the carbon products and catalyst residue obtained by CCVD method and the initial mass of the calcined Fe/CaCO₃ catalyst, respectively.

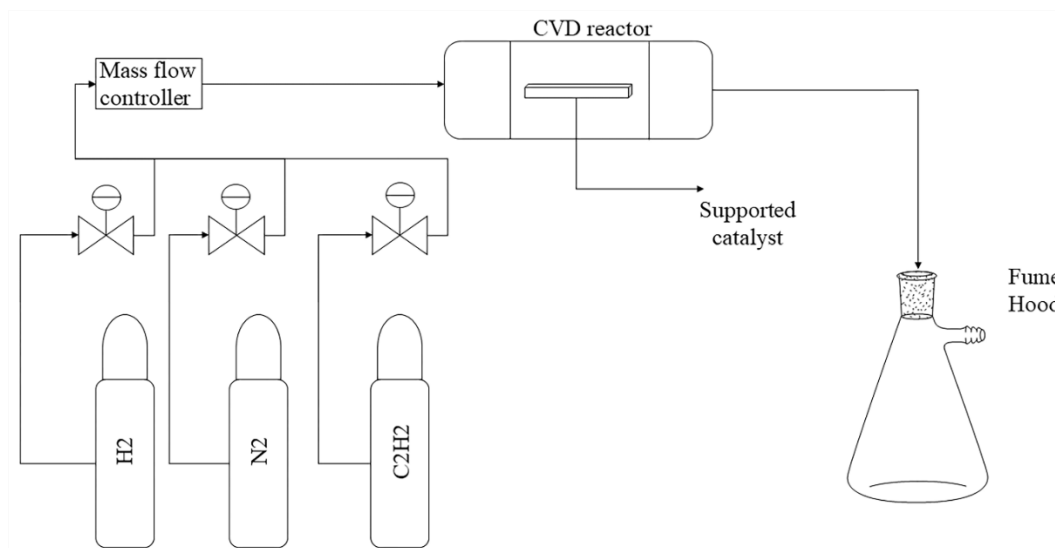


Figure 3.1: Schematic of the CVD reactor for CNTs growth.

3.2.2 Acid treatment of pristine CNTs support

Synthesized CNTs were treated in nitric acid at 110 °C as follows. 5 g of the synthesized CNTs were treated with 500 ml of 35 wt% of nitric acid and refluxed at 110 °C for 16 h. After vacuum filtration and washing with distilled water, CNTs were dried at 120 °C over night.

3.2.3 Preparation of Fe catalyst supported on CNTs

For preparation of Fe-based catalysts for FTS, acid-treatment of as-synthesized CNTs was conducted using nitric acid (30 wt%) at 110 °C for 16 h under reflux conditions. The nitric acid treatment removes Fe/CaCO₃ catalyst particles and enhances hydrophilicity of CNTs. Fe/CNTs catalyst was then prepared via ultrasonic-assisted wet impregnation method. To this, a desired amount of Fe (NO₃)₃·9H₂O was added to deionized water and mixed with acid-treated CNTs using ultrasonication. Subsequently, the impregnated Fe/CNTs catalyst was placed into an oven at 120 °C followed by calcination in air at 400 °C for 4 h.

3.2.4 Preparation of KMo-promoted Fe catalyst supported on CNTs

K and/or Mo-promoted Fe/CNTs catalysts were prepared using ultrasonic-assisted impregnation method with aqueous solutions of iron nitrate ($\text{Fe}(\text{NO}_3)_3 \cdot 9\text{H}_2\text{O}$, Fisher Scientific, Hanover, PA), ammonium molybdate ($(\text{NH}_4)_6\text{Mo}_7\text{O}_{24} \cdot 4\text{H}_2\text{O}$, Fisher Scientific, Hanover, PA) and potassium nitrate (KNO_3 , Fisher Scientific, Hanover, PA) followed by oven drying at 120 °C. Catalysts were calcined in air at 400 °C for 4 h, and labelled as xFeyMozK/CNT in which x, y, and z represent iron, molybdenum, and potassium loadings in wt.%, respectively.

3.3 Characterization techniques of support and catalysts

3.3.1 N₂-adsorption-desorption measurement

The textural properties of the CNTs support and corresponding catalysts were studied by N₂ adsorption-desorption at 77 K using Micromeritics ASAP 2020 Porosity Analyzer. Prior to vacuum degassing at 300 °C, the residual oil present in the samples was removed overnight at 315 °C. Then, degassing was performed at 200 °C under operating pressure of 500 μm Hg for 1.5 h.

3.3.2 Wide-angle X-ray diffraction (XRD)

A Bruker D8 Advance Series II X-Ray Powder Diffractometer (Bruker Corporation, Billerica, MA, USA) was employed to record the X-ray diffractograms of the samples via Cu K-α radiation source ($\lambda = 1.5406 \text{ \AA}$). The analyses were conducted at a voltage and current of 40 kV and 40 mA, respectively, with 2θ ranging from 5° to 80° at a scan rate of 2°/min.

3.3.3 Scanning electron microscope (SEM)

A Hitachi SU8010 field emission-scanning electron microscope (FE-SEM, Hitachi High-Technologies Corporation, Tokyo, Japan) was employed to study the surface morphology of CNTs support and corresponding catalysts at an accelerating voltage of 3 kV. Prior to FE-SEM imaging, the surface of samples were sputter coated with Au film (10 nm) by the sputtering unit (Quorum Q150T ES).

3.3.4 Transmission electron microscopy (TEM)

A transmission electron microscope (Philips CM20, 100 kV) was used to analyze the surface morphology of CNTs support and corresponding catalysts. For sample preparation, ultrasonic

irradiation was applied, providing a homogeneous suspension of the sample in ethanol. Thereafter, a droplet of the suspension onto a carbon-coated copper grid was analyzed by TEM.

3.3.5 Inductively coupled plasma optical emission spectroscopy (ICP-OES)

An inductively coupled plasma-optical emission spectrometry (ICP-OES, Varian VISTA-MPX) was used to determine the metal loadings in catalysts.

3.3.6 X-ray photoelectron spectroscopy (XPS)

The XPS analysis was conducted using a radiation (Al K- α monochromator; 1486.6 eV, 500 mm) obtained by Kratos AXIS Supra system (Manchester, UK) at Saskatchewan Structural Sciences Centre (SSSC), University of Saskatchewan. The operating voltage and current were 15 kV and 10 mA, respectively. Applying a pass energy of 20 eV with 0.05 eV steps, high resolution C1s, Fe2p, Mo3d, and O1s spectra were collected from six randomly selected positions of each sample. High resolution scans were performed using 0.05 eV steps with 20 eV pass energy and an emission current of 0.015 A.

3.3.7 Raman spectroscopy

The surface chemistry parameters of CNTs support and iron-based catalysts such as number of surface defects were measured using a Raman microscope (Invia Reflex, Reinshaw, UK) and a 514 nm laser.

3.3.8 Fourier transform infrared (FTIR) spectroscopy

The surface functional groups of CNTs before and after acid-treatment along with corresponding catalysts were investigated by FTIR. The analysis was conducted via a Bruker Vertex 70 FTIR spectrometer (Bruker Corporation, Billerica, MA, USA) equipped with an attenuated total reflection (ATR) diamond crystal as source of infrared spectra in the range of 4500-400 cm^{-1} .

3.3.9 H₂-temperature programmed reduction (H₂-TPR)

An Autosorb IQ (Quantachrome, USA) instrument was applied for H₂-TPR study. The desired amount of sample (10-30 mg) was loaded into a U-shaped quartz tube and located in the instrument. The sample was then heated up to 400 °C and held at that temperature for 0.5 h under He flow, removing moisture on the sample. Next, the sample was exposed to a H₂/N₂

(3% v/v) gas flow (30 mL/min) ramping from 25 °C to 650 °C, with heating rate being 10 °C/min.

3.3.10 CO₂-temperature programmed desorption (CO₂-TPD)

The carbon dioxide TPD was carried out via an Autosorb IQ (Quantachrome, USA) instrument. The desired amount of the sample (10-30 mg) was loaded in the U-shaped quartz tube, heated up to 150 °C under helium flow (50 mL/min) and held at that temperature for 30 min, removing the physically adsorbed CO₂. After cooling down to 50 °C, the TPD data were recorded by increasing the temperature in the range of 50 °C to 700 °C under He flow (50 mL/min), with heating rate being 10 °C/min.

3.3.11 CO-chemisorption

The Micromeritics ASAP 2020 Chemisorption system was used to determine the percentage of metal dispersion in the synthesized catalysts. The desired amount of catalyst was loaded in a U-shaped quartz tube and degassed at 150 °C for 1 h. The sample was then reduced under H₂ flow at 350 °C for 2 h. After cooling down to 35 °C, the chemisorption was conducted by passing CO pulses over the sample, measuring the total CO uptake at 35 °C. The metal dispersion was then related to the amount of CO adsorbed.

3.3.12 Thermogravimetric analysis (TGA)

The thermogravimetric analysis (TGA) was carried out using TGA-Q500 equipment (TA Instruments, USA). The sample was heated from room temperature to 650 °C under inert atmosphere (N₂, 60 mL/min) with heating rate of 10 °C/min and the weight loss was recorded.

3.3.13 Synchrotron-based X-ray absorption (XAS)

The X-ray absorption spectroscopy (XAS) was performed at Canadian Light Source, Saskatoon, Saskatchewan. The sample was dispersed on a conductive carbon tape in a glove box under inert atmosphere and then analyzed at soft X-ray microcharacterization beamline (SXRMB). The Fe K-edge absorption spectra were obtained in total electron yield. The XAS data was analyzed using Athena software.

3.4 Fischer-Tropsch synthesis

FTS experiments were carried out in a fixed-bed reactor ($D_i = 1.54$ cm, $L = 50$ cm). A mixture of calcined catalyst/silicon carbide (1/7 wt./wt.) was located in the reactor. After 18 h

of in-situ reduction under H₂ flow (30 mL/min) at 400 °C, the reactor was cooled down to 280 °C and the pressure increased to 3.45 MPa. Then, the synthesis gas (H₂/CO = 1) at a space velocity of 2000 cm³ (STP)/(h g) was fed into the fixed-bed reactor. The composition of the outlet gas stream was monitored by a gas chromatograph (Shimadzu GC-2014). CO conversion and product selectivity were measured during the time on stream (TOS = 24 h with 3 h intervals) using the following equations:

$$\text{Product Selectivity} = \frac{C_x}{\sum C_x} \times 100\% \quad (3-2)$$

$$\text{Conversion} = \frac{CO_{in} - CO_{out}}{CO_{in}} \times 100 \quad (3-3)$$

where CO_{in} and CO_{out} are moles of carbon monoxide at the inlet and outlet, respectively. In this case, C_x represents the mole of carbon in product x at the outlet. The carbon balance regarding this study obtained 100 ± 2%. Iron time yields (FTY, mol_{CO} /g_{Fe} s) were calculated as follow:

$$FTY = \frac{CO_{in} - CO_{out}}{M_{Fe}} \quad (3-4)$$

where M_{Fe} is the actual iron weight of the loaded catalysts (Zhipeng Tian et al., 2019a). Equation (3-5) determines the turnover frequency (TOF) as the surface-specific activity (Torshizi et al., 2021):

$$TOF = \frac{n_{CO}}{m_{cat} \times n_{Fe-surf}} \quad (3-5)$$

where n_{CO} represents the number of CO molecules (mole) transformed per second, n_{Fe-surf} stands for the number of surface iron atoms estimated by CO-chemisorption, and m_{cat} means the catalyst weight fed into the reactor. The metal dispersion is obtained from CO-chemisorption. Having the value of metal dispersion, TOF can be determined which is proportional to the number of active sites.

The experimental schematic of the FTS process is depicted in Figure 3.2. FTS experiments were carried out in a fixed-bed reactor (D_i = 1.54 cm, L = 50 cm). In each run, diluted catalyst (1.5 g catalyst and 7.5 g silicon carbide) was loaded in the tubular reactor and was reduced before the CO hydrogenation reaction. In-situ reduction was performed under pure hydrogen

at a flow rate of 30 mL/min at 400 °C for 18 h. After reduction at atmospheric pressure, the reactor operating parameters were shifted to the kinetic testing conditions with temperature and pressure in the range of 270-290 °C and 0.68-4.13 MPa, while H₂/CO and GHSV were maintained at 1 and 2000 h⁻¹, respectively.

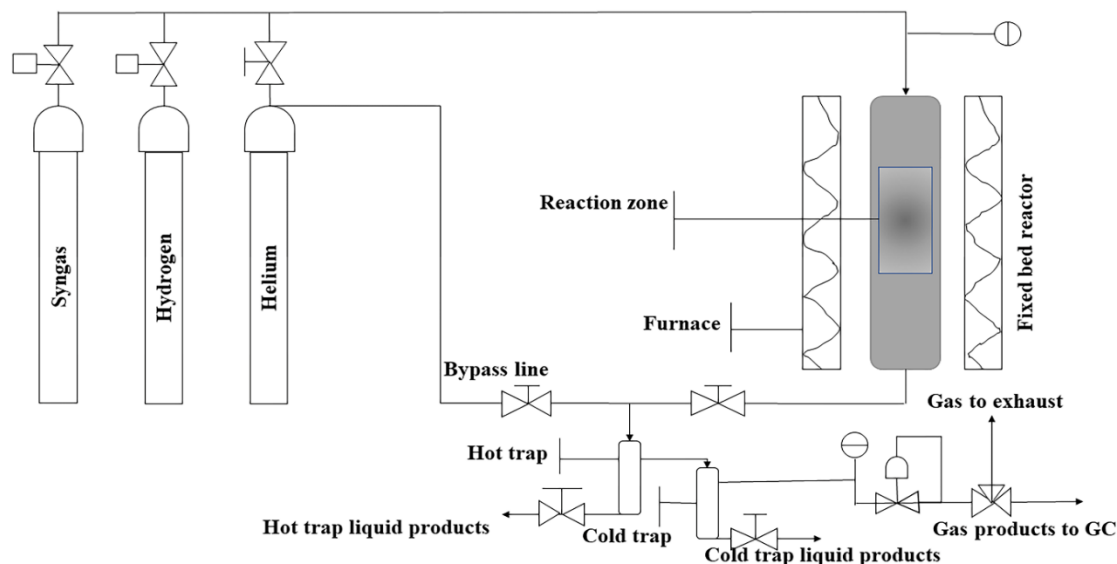


Figure 3.2: Schematic representation of Fischer-Tropsch reaction setup.

After reaching the desired reaction conditions, the compositions of the gaseous FT products were measured using an online gas chromatograph (Shimadzu-2014). The online GC was equipped with two thermal conductivity detectors (TCD) and one flame ionization detector (FID) for the analysis of CO, CO₂, CH₄, H₂, O₂, Ar, and hydrocarbon mixtures, respectively. Ma et al. (Ma et al., 2007) reported the oxygenate selectivity of less than 3 wt% for a Mo-promoted FeCuK/AC catalyst with 6 wt% Mo and 0.9 wt% K. In the kinetic study, the optimal formulation of the bimetallic promoted 0.5K5Mo10Fe/CNTs catalyst with 5 wt% Mo and 0.5 wt% K is fairly close to the Mo-FeCuK/AC reported by Ma et al. (Ma et al., 2007). Therefore, the value of oxygenate selectivity could be roughly negligible. Since the TCD-GC is not able to analyze water precisely, an oxygen balance determined the amount of water assuming that the contribution from oxygenates in the products was negligible (Sarkari et al., 2014; Lee et al., 2022).

3.5 Product sampling and composition analyses

3.5.1 Gas chromatography (GC) analysis

The gaseous products collected from FTS reactor were directly introduced into a Shimadzu GC-2014 by a gas autosampler. The helium gas as carrier was kept at 200 °C and 0.02 MPa, with flow rate of 110 mL/min and split ratio being 20.4:1. The GC was equipped with a Haysep Q packed column (L = 1.8 m, D_o = 3.17 mm) with molecular sieve 13X (L = 3.04 m, D_i = 3.17 mm), and capillary column made of CP-Al₂O₃/KCl (L = 25 m, D_i = 0.53 mm). The packed and capillary columns were connected to a thermal conductivity detector (TCD) and flame ionization detector (FID), respectively. In GC, the permanent gases (CO₂, CO, H₂, N₂, O₂) and hydrocarbons (alkanes: ethane, propane, butane and alkenes: ethylene, propylene, butene, and acetylene) were separated by packed and capillary columns, respectively.

3.5.2 Simulated distillation (Sim-Dist) analysis

The boiling point distribution of the obtained FT liquid products were estimated by simulated distillation (Sim-Dist) technique. The FT liquid sample was dissolved in CS₂ and introduced to a Varian CP-3800 GC. The analysis was conducted based on ASTM D-2887.

3.6 Kinetics studies of Fischer-Tropsch synthesis

The kinetic experiments were conducted under operating conditions with temperature and pressure in the range of 270-290 °C and 0.68-4.13 MPa, while H₂/CO and GHSV were maintained at 1 and 2000 h⁻¹, respectively. The plug flow pattern was considered for the gaseous feed stream and the consumption rate of CO in the feed was calculated as follows:

$$\frac{W_{cat}}{F_{CO}^0} = \int_{X_{CO,in}}^{X_{CO,out}} \frac{dX_{CO}}{-r_{CO}} = \frac{1}{(-r_{CO})_{avg}} \int_{X_{CO,in}}^{X_{CO,out}} dX_{CO} = \frac{X_{CO,out} - X_{CO,in}}{(-r_{CO})_{avg}} \quad (3-6)$$

$$(-r_{CO})_{avg} = \frac{F_{CO}^0 (x_{CO,out} - x_{CO,in})}{W_{cat}} \quad (3-7)$$

$$-r_{CO} = \frac{X_{CO} F_{CO}^0}{W_{cat}} \quad (3-8)$$

where F_{CO}^0 is the input flow rate of CO (mol/min) and W_{cat} is weight of the catalyst (g_{cat}). F_{CO}^0 was obtained as follows:

$$F_{CO}^0 = v_0 C_{CO} = \frac{v_0 P_{CO}}{RT} \quad (3-9)$$

The mass balance for the FTS reaction products is calculated as follow:

$$Mass\ balance = 1 - \left(\frac{|m_{C,in} - m_{C,out}|}{m_{C,in}} \right) \times 100 \quad (3-10)$$

where $m_{C,in}$ and $m_{C,out}$ denote the mass of input and output carbon (g), respectively. In the kinetics study, each experiment was performed in triplicate and the average values are reported. To evaluate catalyst activity, catalyst deactivation during the FTS reaction was controlled and kinetic data were reported with no deactivation.

CHAPTER 4: Optimization of Carbon Nanotube Growth via Response Surface Methodology for Fischer-Tropsch Synthesis over Fe/CNTs Catalyst

The content of this section has been published in *Catalysis Today* (Yahyazadeh et al., 2022a) and presented at the 71st Canadian Chemical Engineering Conference, Montreal, October 24-27, 2021.

Contribution of the PhD candidate:

Experiments were designed in consultation with Dr. Venu Babu Borugadda, (Postdoc member of the group) under the supervision of Dr. Ajay K. Dalai and executed by Arash Yahyazadeh. Material synthesis, catalysts characterization and data interpretation were performed by Arash Yahyazadeh. The manuscript was drafted by Arash Yahyazadeh with guidance, suggestions, and reviews provided by Dr. Venu Babu Borugadda and Dr. Ajay K. Dalai.

Contribution of this chapter to overall PhD research:

The first phase of the research is investigated in this chapter: Preparation, characterization, and optimization of carbon nanotubes using iron supported catalyst for Fischer-Tropsch Synthesis. This chapter is the basis of the following chapters.

4.1 Abstract

Light olefins such as ethylene, propylene, and butylene are key compounds in the chemical industry. Iron catalyst supported on carbon nanotubes (CNTs) is an appropriate candidate for light olefins production using synthesis gas in Fischer-Tropsch synthesis (FTS). The catalytic chemical vapor deposition (CCVD) method was applied to synthesize CNTs using Fe/CaCO₃ and acetylene as catalyst and hydrocarbon source, respectively. Applying response surface methodology, the optimum operating conditions were determined in CVD reactor for maximal yield and purity of CNTs. The effects of reaction time (30-60 min), reaction temperature (700-800 °C), and loading of the catalyst (10-30 wt% Fe) were investigated. The synthesized CNTs was characterized by Raman spectroscopy for its graphitic structure and purity. After acid-treatment of the synthesized CNTs, Fe/CNTs-synthesized catalyst was successfully fabricated by ultrasonic-assisted wet impregnation method. 20Fe/CNTs-synthesized, 20Fe/CNTs-commercial, and 20Fe/Al₂O₃ were analyzed in terms of physio-chemical properties and FTS

catalytic performance. Comparison of transmission electron microscopy (TEM) and CO-chemisorption results showed that the 20Fe/CNTs-synthesized catalyst reduces iron oxide agglomeration resulting in metal particles well-dispersed among the studied Fe-based catalysts. The catalytic performance of Fe-based catalysts was investigated using a fixed-bed reactor at 280 °C under 2.0 MPa. 20Fe/CNTs-synthesized exhibited a lower rate of water-gas-shift (WGS) reaction compared with 20Fe/CNTs-commercial, with C₂-C₄ selectivity of 23.6% which is slightly less than that of its commercial counterpart. Analysis of FTS liquid products revealed that the 20Fe/CNTs-synthesized catalyst provides liquid hydrocarbons in the range of C₈-C₁₈, while 20Fe/CNTs-commercial and 20Fe/Al₂O₃ obtained C₉-C₅₂ and C₁₀-C₂₀, respectively. After 120 h time on stream under steady state condition, higher activity had been maintained by the 20Fe/CNTs-synthesized catalyst compared to the 20Fe/CNTs-Commercial and 20Fe/Al₂O₃ catalysts.

4.2 Materials and methods

4.2.1 Materials

The chemicals utilized in this study, their purity and suppliers are as follows: calcium carbonate 100%, Fisher Chemical FLC64500, Canada; iron (III) nitrate nonahydrate 99+%, Thermo Fisher Scientific 202492500, Canada; aluminum oxide, Alfa Aesar AA4385530, United States; commercial carbon nanotubes, Mknano Co. (M.K. IMPEX MWCNT-P0815, Canada); nitrogen (Ni-T), acetylene (AC 2.6 AA-A4), hydrogen (HY 5.0 UH-T), and syngas (COAR10H1ZC-AT) were purchased from Linde Canada Inc. Preparation of CNTs support and corresponding Fe/CNTs catalyst are described in detail in sections 3.2.1 to 3.2.3 of chapter 3. The complimentary analytical techniques performed to characterize the CNTs support and calcined Fe/CNTs catalyst are provided in the previous chapter.

4.2.2 Methodology

In the case of catalyst preparation process with several variables, response surface methodology (RSM) was used for experimental design and data analysis (Nariyan et al., 2018). Data analysis and statistical design of the experiments were performed using Design Expert Software Version 7.0.0 (Stat-Ease, Inc., Minneapolis, USA). Optimization of carbon nanotubes production was aimed to achieve the optimum process conditions maximizing CNTs yield and minimizing CNTs I_D/I_G ratio. The D band is known as the disorder band and G band reflects

graphite structures. The decomposition reaction temperature, reaction time, and iron loading were considered as control factors. Table 4.1 represents the process factors and their levels.

Table 4.1: Process factors and their levels for CNTs production.

Variable	Range and Level				
	$-\alpha$	-1	0	1	α
Iron loading (wt%)	3.2	10	20	30	36.8
Reaction temperature ($^{\circ}\text{C}$)	665.9	700	750	800	834.1
Reaction time (min)	19.7	30	45	60	70.2

4.3 Results and discussion

4.3.1 CNTs production: optimization establishment and analysis

Central composite design (CCD) was employed to investigate the effects of influential factors on the synthesized CNTs as catalyst support (Mohammadian et al., 2018). A total of 20 runs were suggested by the software (Table 4.2).

Table 4.2: Experimental design matrix with the value of responses.

	Factor 1	Factor 2	Factor 3	Response 1	Response 2
Sample	Temperature $^{\circ}\text{C}$	Time (min)	Fe loading (wt%)	CNTs yield (%)	I_D/I_G ratio
1	-1	-1	-1	47.4	0.81
2	1	-1	-1	39.1	0.38
3	-1	1	-1	34.0	0.86
4	1	1	-1	23.7	0.57
5	-1	-1	1	18.0	0.65
6	1	-1	1	17.0	0.65
7	-1	1	1	9.7	0.63
8	1	1	1	6.1	1.94
9	-1.68	0	0	29.3	0.85
10	1.68	0	0	15.4	0.61
11	0	-1.68	0	35.0	0.82
12	0	1.68	0	14.9	0.93
13	0	0	-1.68	28.8	1.00
14	0	0	1.68	18.0	0.45
15	0	0	0	20	0.79
16	0	0	0	23.7	0.80
17	0	0	0	35.0	0.29
18	0	0	0	29.0	0.66
19	0	0	0	26.0	0.82
20	0	0	0	31.0	0.57

Analysis of variance (ANOVA) was applied to optimize the CNTs yield (CY) and CNTs I_D/I_G ratio. For CNTs yield (CY), cubic polynomial models fitted well with experimental data, providing acceptable R^2 -value of 0.94 (Table 4.3).

Table 4.3: ANOVA for CNTs yield (CY) obtained by cubic polynomial model.

Source	Sum of Squares	DF	Mean Square	F value	p-value Prob > F
Model	21.35	13	1.64	7.38	0.0110
A	1.11	1	1.11	4.98	0.067
B	2.11	1	2.11	9.50	0.021
C	0.63	1	0.63	2.84	0.143
AB	0.092	1	0.092	0.41	0.544
AC	0.086	1	0.086	0.39	0.556
BC	0.015	1	0.015	0.066	0.805
A ²	0.59	1	0.59	2.65	0.154
B ²	0.22	1	0.22	1.01	0.354
C ²	0.34	1	0.34	1.54	0.261
ABC	4.715E-3	1	4.715E-3	0.021	0.889
A ² B	5.635E-3	1	5.635E-3	0.025	0.878
A ² C	2.69	1	2.69	12.11	0.013
AB ²	0.072	1	0.072	0.33	0.589
Residual	1.33	6	0.22	-	-

Standard deviation = 0.47; Coefficient of variation % = 9.64

Predicted residual error of sum of squares (PRESS) = 2.91

$R^2 = 0.94$; R^2 (Predicted) = 0.87; R^2 (Adjusted) = 0.81; Adequate precision = 11.1

The regression equation based on cubic polynomial model estimating CNTs yield (CY) is presented as follow:

$$Sqrt(CY) = 5.22 - 0.44 \times A - 0.61 \times B - 0.33 \times C - 0.11 \times A \times B + 0.10 \times A \times C - 0.043 \times B \times C - 0.2 \times A^2 - 0.12 \times B^2 - 0.15 \times C^2 - 0.024 \times A \times B \times C - 0.041 \times A^2 \times B - 0.9 \times A^2 \times C + 0.15 \times A \times B^2 \quad (4-1)$$

where A, B, C, and CY stand for the reaction temperature, reaction time, iron loading in the catalyst, and carbon yield, respectively.

As it can be seen in Figure 4.1 (a,b), there is a notable increase in CNTs yield by decreasing reaction temperature from 800 °C to 700 °C which suggests catalyst deactivation and thermal degradation of CNTs at higher temperatures. Similarly, considering the thermogram of the as-grown CNTs (Figure 4.11) reveals that CNTs are thermally stable up to 600-750 °C (Matandabuzo and Ajibade, 2018). It should be noted that iron loading affects CNTs yield. In addition, it has been reported that multi-walled carbon nanotubes (MWCNTs) of uniform diameters are synthesized at low iron loading in catalyst synthesis (El-Ahwany et al., 2020).

From Figure 4.2 (a,b), catalyst with 10% iron loading exhibited the best performance for CNTs production, which is in agreement with previous studies (Liu et al., 2013). This can be attributed to synergistic interactions between CaCO_3 and iron phases in the chemical vapor deposition reaction. Additionally, it can be observed that maximum yield of CNTs is achieved at minimum reaction time of 30 min which might be related to sintering and agglomeration of catalyst active phase by increasing reaction time from 30 min to 60 min.

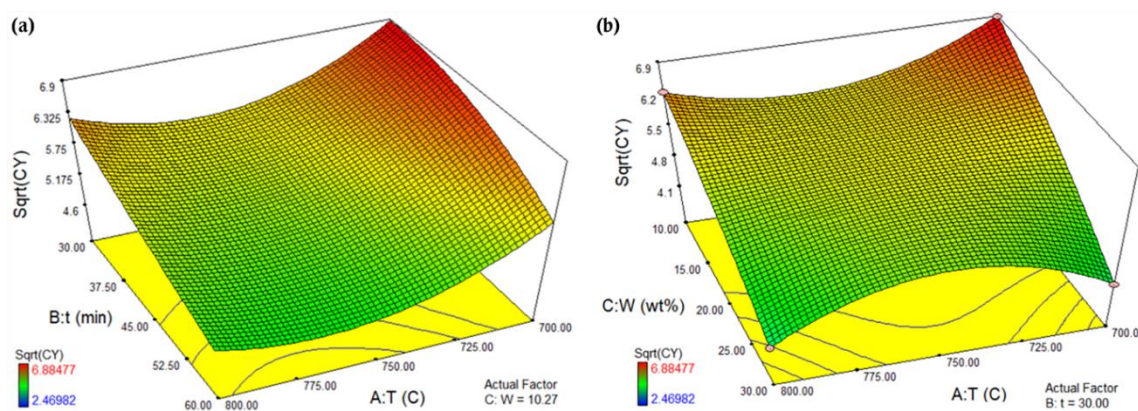


Figure 4.1: Response surface plots of CNTs yield with the combined effects of (a) Reaction temperature and reaction time; (b) Reaction temperature and iron loading.

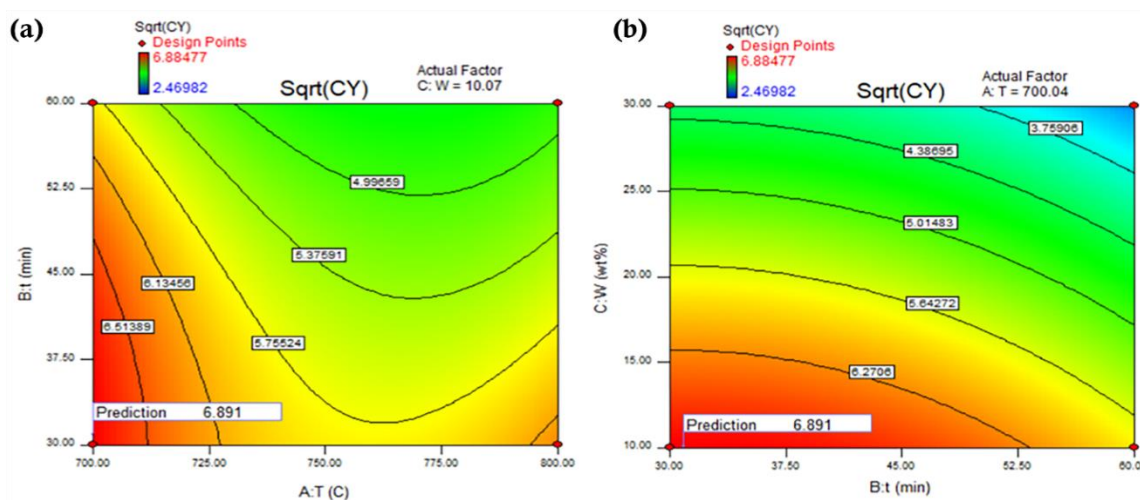


Figure 4.2: Graphical prediction of optimum conditions maximizing CNTs yield.

From Table 4.4, it can be suggested that iron loading and reaction temperature are the significant factors affecting CNTs graphitic structure (I_D/I_G). Considering the coefficient of

determination ($R^2 = 0.90$), the cubic polynomial model can successfully estimate CNTs graphitic structure (I_D/I_G) as follow:

$$I_D/I_G = 0.66 - 0.070 \times A + 0.032 \times B - 0.17 \times C + 0.18 \times A \times B + 0.25 \times A \times C + 0.13 \times B \times C + 0.032 \times A^2 + 0.083 \times B^2 + 0.030 \times C^2 + 0.15 \times A \times B \times C + 0.16 \times A^2 \times B + 0.32 \times A^2 \times C + 0.14 \times A \times B^2 \quad (4-2)$$

Table 4.4: ANOVA for CNTs graphitic structure (I_D/I_G) obtained by cubic polynomial model.

Source	Sum of Squares	DF	Mean Square	F value	p-value Prob > F
Model	1.90	13	0.15	4.22	0.043
A	0.028	1	0.028	0.80	0.404
B	5.725E-3	1	5.725E-3	0.17	0.698
C	0.15	1	0.15	4.44	0.079
AB	0.27	1	0.27	7.75	0.031
AC	0.51	1	0.51	14.69	0.008
BC	0.13	1	0.13	3.83	0.098
A ²	0.015	1	0.015	0.43	0.536
B ²	0.099	1	0.099	2.85	0.142
C ²	0.013	1	0.013	0.37	0.565
ABC	0.17	1	0.17	4.92	0.068
A ² B	0.081	1	0.081	2.33	0.177
A ² C	0.34	1	0.34	9.88	0.020
AB ²	0.068	1	0.068	1.95	0.212
Residual	0.21	6	0.035	-	-

Standard deviation = 0.19; Coefficient of variation % = 24.56

Predicted residual error of sum of squares (PRESS) = 0.81

$R^2 = 0.90$; R^2 (Predicted) = 0.62; R^2 (Adjusted) = 0.69; Adequate precision = 10.02

It has been reported that lower metal loading would enhance quality of single-walled carbon nanotubes (SWCNTs) with uniform diameters due to less agglomeration of the iron particles (Liu et al., 2013). Figure 4.3 demonstrates the cubic models' prediction of I_D/I_G ratio based on process parameters. From Figure 4.3, decreasing reaction time and iron loading to 30 min and 10 wt% produced high quality CNTs with minimum I_D/I_G ratio. It is worth noting that the hydrocarbon source (acetylene) can actively decompose at higher reaction temperatures (800 °C). Comparison of Figure 4.2 and Figure 4.4 revealed that increasing the reaction temperature in the range of 700-800 °C, the rate of CNTs production is faster than the rate of carbon atom deposition over the iron catalyst surface, thus decreasing both I_D/I_G ratio and CNTs yield. Figure 4.5 shows the predicted response versus actual values which confirms the acceptable correlation between the predicted and the observed values.

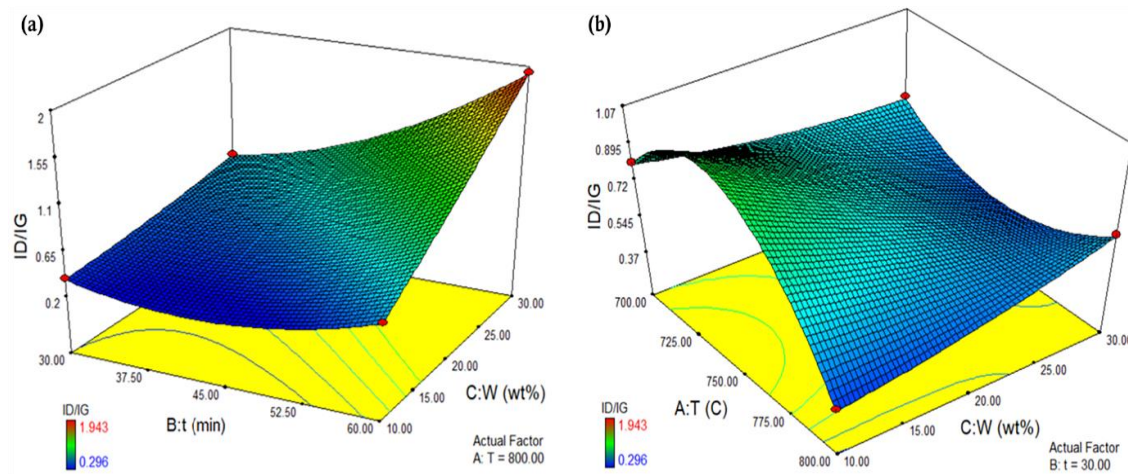


Figure 4.3: Response surface plots of I_D/I_G ratio with the combined effects of (a) Iron loading and reaction time; (b) Reaction temperature and iron loading.

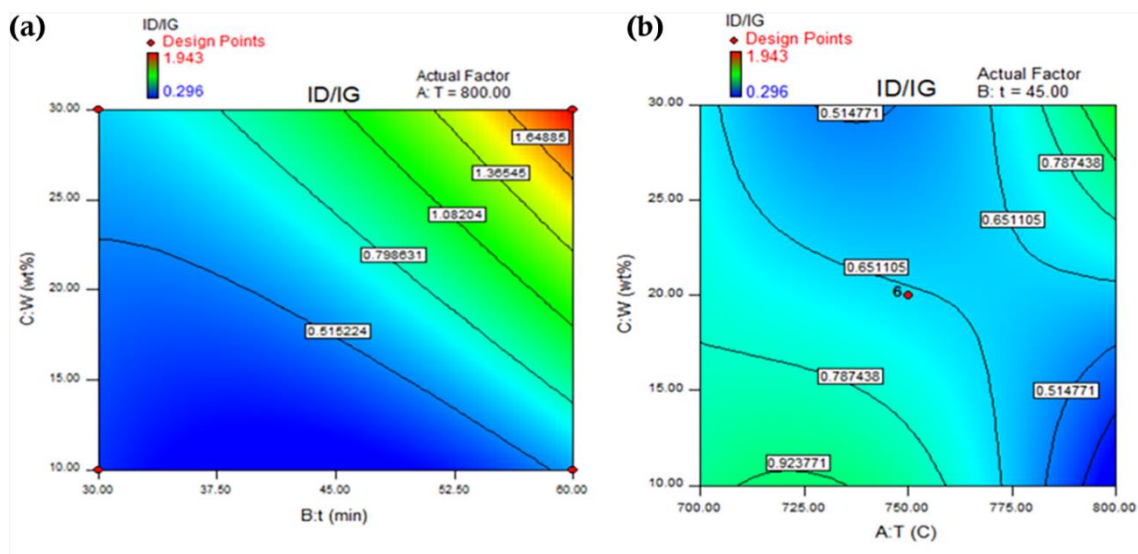


Figure 4.4: Graphical prediction of optimum conditions considering I_D/I_G ratio as response.

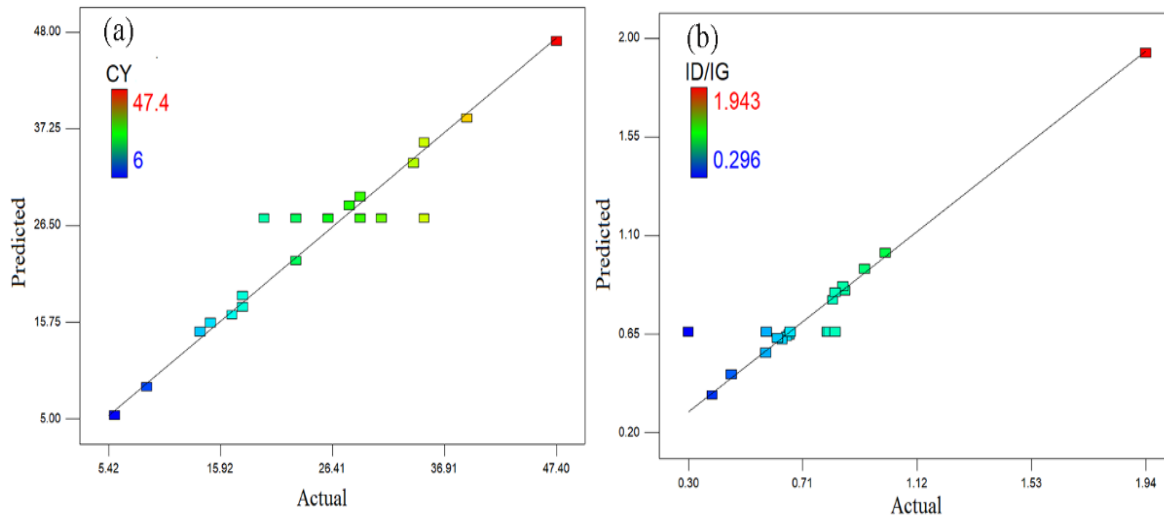


Figure 4.5: Experimental and theoretically predicted values for optimization responses (a) CNTs yield; (b) I_D/I_G ratio.

4.3.2 Characterization of CNTs support and corresponding catalysts

X-ray diffraction (XRD) analysis

Wide-angle X-ray diffraction (XRD) technique was applied to evaluate CNTs and corresponding catalysts in terms of different phases present and crystalline size. The XRD pattern of the as-grown and acid-treated CNTs is presented in Figure 4.6. The peaks at 26° and 42.76° can be well assigned to graphitic carbon in MWCNTs structure (Xiong et al., 2015). In the case of FeCaCO₃, the peak at 29.4° is contributed to CaCO₃ indicating the incomplete thermochemical conversion of CaCO₃ to CaO and CO₂ (Yoon et al., 2021). The diffraction peaks that appear at 23.06° , 35.96° , 39.42° , 43.16° , 47.48° , 48.5° , 57.4° and 64.62° can be indexed to cubic CaO (JCPDS No. 47-1743) (Guo et al., 2021). Surprisingly, there is no clear peak for iron and CaCO₃ in XRD pattern of as-grown CNTs, thus suggesting nanosized and highly dispersed iron particles over CaCO₃ that were potentially encapsulated within the wall of the CNTs (Bankole et al., 2018). As shown in Figure 4.6 (a), acid-treatment successfully removed FeCaCO₃ residues from CNTs backbone by removing peaks related to CaO in acid-treated CNTs spectrum (Guo et al., 2021).

From Figure 4.6 (b), diffraction peaks around 30.2° and 35.7° are attributed to Fe₃O₄ and Fe₂O₃-Fe₃O₄, respectively (Xiong et al., 2015). In addition, the peaks at 33.1° - 34.1° , 41.5° ,

53.9°, 54.6°, and 62.9° are assigned to Fe₂O₃ in the fresh catalysts (Xiong et al., 2015; Minett et al., 2014). In the case of 20Fe/CNTs-synthesized catalyst, the peak assigned to FeO was found at 60° (Tu et al., 2021). Moreover, the peaks at 2 θ of 26.1° and 43.3° match well with the graphite layers of CNTs (Figure 4.6(b)) (Karimifard and Alavi Moghaddam, 2016).

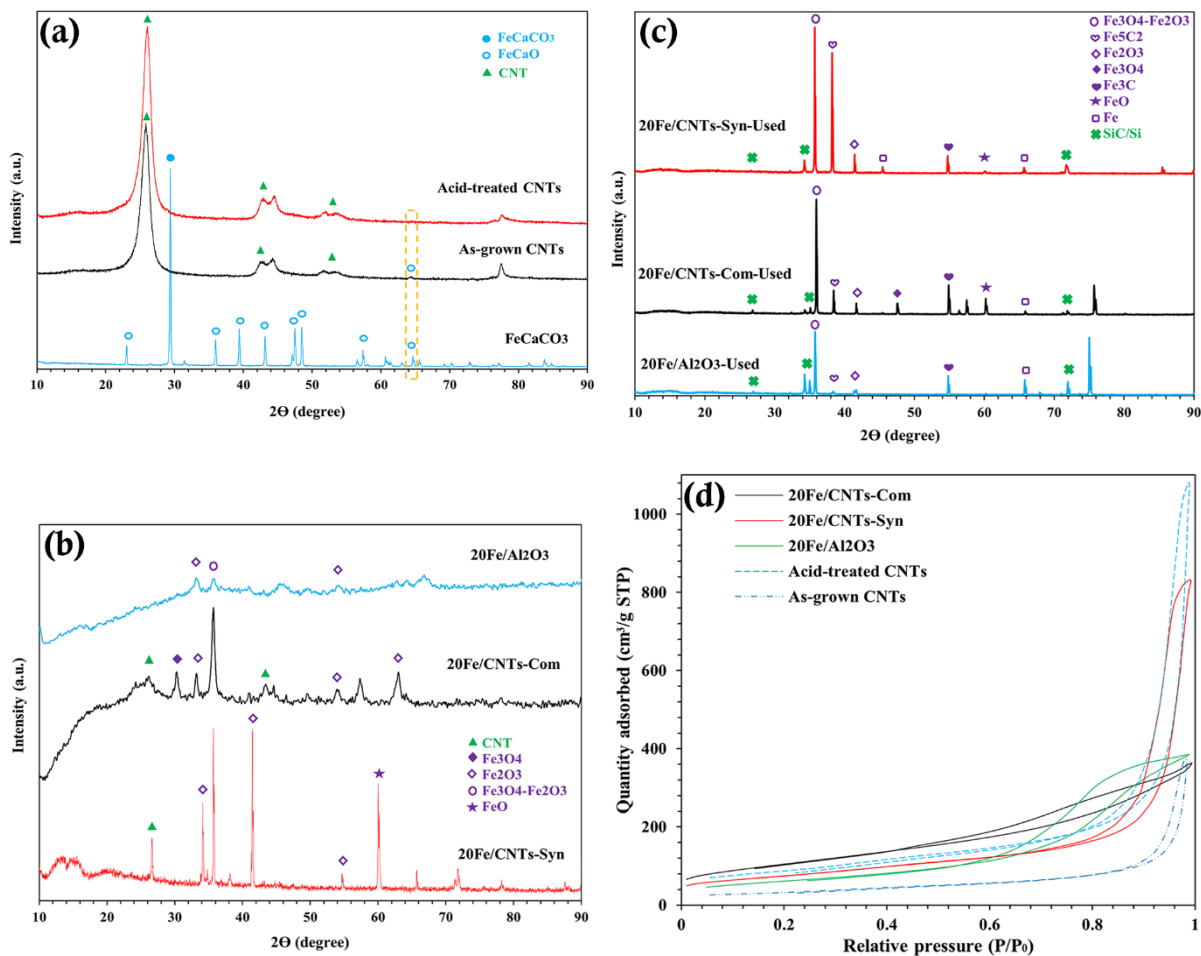


Figure 4.6: XRD patterns of (a) As-grown CNTs and Acid-treated CNTs; (b) Fresh catalysts after calcination; (c) Used FTS catalysts at 280 °C for 24 h; (d) N₂ adsorption-desorption isotherms.

The XRD pattern of the used Fe-based FTS catalysts shows the peaks assigned to different iron carbide structures such as Fe₅C₂ and Fe₃C in the range of 38.2°-38.5° and 54.7°-54.9°, respectively, which can directly be connected with high catalytic activity (Minett et al., 2014; Tu et al., 2021). From Figure 4.6 (c), it can be observed that different types of iron oxide are present in the used catalysts with diffraction peaks around 35.7°-35.9°, 41.4°-41.6°, 47.5°, and 59.8°-60.2° indicating Fe₂O₃-Fe₃O₄, Fe₂O₃, Fe₃O₄ and FeO, respectively (Minett et al., 2014;

Tu et al., 2021). It should be noted that the peaks at 45.2° and 65.4°-65.8° are attributed to atomic Fe in the used catalysts (Tavasoli et al., 2009). The presence of SiC residues observed at 26.4°-26.9°, 34.2°-35.1°, and 71.6°-71.9° resulted in disappearing of CNTs characteristic peaks in the used 20Fe/CNTs-synthesized and 20Fe/CNTs-commercial catalysts (Yoo et al., 2020).

Textural properties

The N₂ adsorption-desorption isotherms of as-grown CNTs, acid-treated CNTs, 20Fe/CNTs-Syn, 20Fe/CNTs-Com, and 20Fe/Al₂O₃ is depicted in Figure 4.6 (d). The N₂ adsorption-desorption hysteresis loop at relative pressure higher than $P/P_0 \geq 0.8$ shows type IV isotherm and mesoporous structure for 20Fe/CNTs-Syn catalyst. Table 4.5 summarizes textural properties of as-grown CNTs, acid-treated CNTs, commercial CNTs, 20Fe/CNTs-Syn, 20Fe/CNTs-Com, and 20Fe/Alumina catalysts. Initial acid-treatment increased the surface area of CNTs by 61%. It is related to removal of residual CaO which belongs to Fe/CaCO₃ catalyst. However, commercial CNTs exhibited a higher surface area of 450 m²/g compared with acid-treated synthesized CNTs (surface area: 309 m²/g). As shown in Table 4.5, nitric acid (30 wt%) increased pore volume and pore diameter in acid-treated synthesized CNTs by 65% and 10%, respectively, compared to as-grown CNTs. It can be related to acid-treatment resulting in tube disintegration, defect sites, and opening of tube tips. In the case of 20Fe/CNTs-Syn catalyst, iron loading onto acid-treated CNTs brings about iron accumulation in narrow capillaries, decreasing the surface area to 267 m²/g. After 20 wt% iron loading on the alumina and commercial CNTs the surface area dropped to 222 m²/g and 380 m²/g, respectively. Considering pore size of CNTs and corresponding catalysts, it can be concluded that these Fe-based catalysts are mesoporous (Wei et al., 2020).

Table 4.5: Textural properties of as-grown CNTs and corresponding catalysts.

Catalyst/support	BET surface area (m ² /g)	Pore volume (cm ³ /g)	Pore diameter (nm)	Metal dispersion (%) ^a
As-grown CNTs	118	0.58	17.3	-
Acid-treated CNTs	309	1.67	19.4	-
Commercial CNTs	450	0.87	6.6	-
20Fe/CNTs-Syn	267	1.29	17.4	4.8
20Fe/CNTs-Com	380	0.58	5.6	2.6
20Fe/Al ₂ O ₃	222	0.60	7.4	2.4

^a Obtained by CO-chemisorption method

CO-chemisorption

Metal dispersion in the Fe-based catalysts were measured using CO-chemisorption. The metal dispersion on 20Fe/CNTs-Syn, 20Fe/CNTs-Com, and 20Fe/Al₂O₃ catalysts are shown in Table 4.5. As it can be observed in Table 4.5, 20Fe/CNTs-Syn exhibited the highest metal dispersion compared with other catalysts, with Fe dispersion being 4.8%. This can be attributed to the enhanced support-metal interaction due to acid-treatment and ultrasonic treatment during catalyst preparation (Luo et al., 2020). Acid-treatment causes defect sites and functional groups on CNTs structure, leading to charge donation from carbon sites during Fe impregnation (Zhu et al., 2013). The defects left by acid-treatment on CNTs structure were confirmed by Raman spectroscopy. The higher dispersion of active metal would lead to increase in catalyst productivity due to less agglomeration or sintering in the FTS process (Lee et al., 2019).

Electron microscopy analyses of CNTs and calcined catalysts

Figure 4.7 shows scanning electron microscope (SEM) images of the acid-treated CNTs, which confirmed that acid-treatment successfully removed carbonaceous impurities from CNTs backbone. Acid-treatment is supposed to leave some defects onto CNTs wall, thus increasing the hydrophilicity of CNTs and metal loading via anchoring sites (De Menezes et al., 2018).

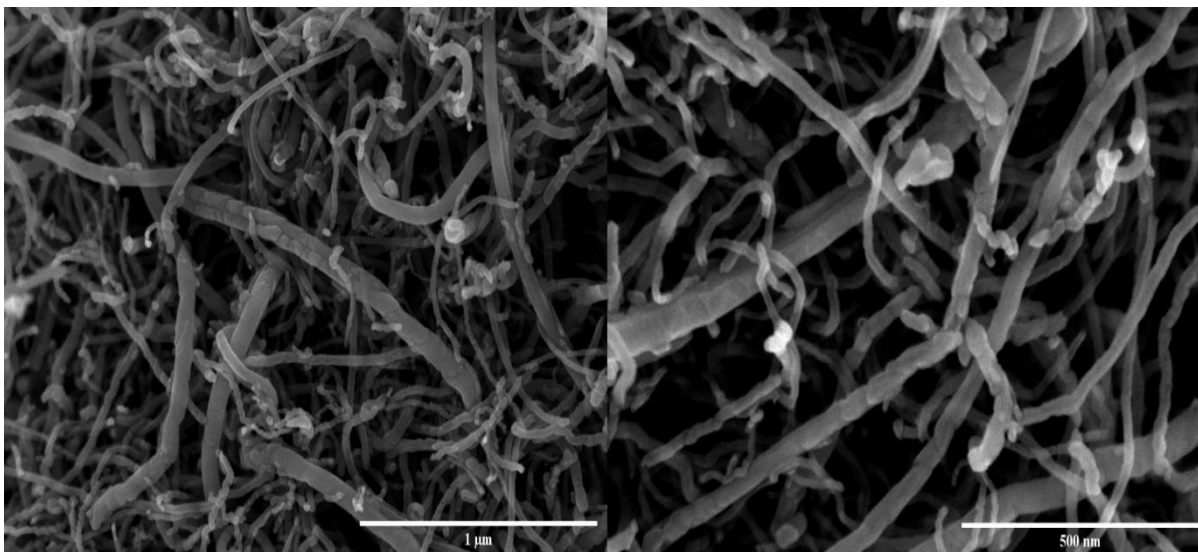


Figure 4.7: SEM microphotographs of acid-treated CNTs.

Moreover, transmission electron microscopy (TEM) was applied to study the Fe-based catalysts in terms of morphology and particle size distribution. TEM microphotographs of the calcined 20Fe/CNTs-Syn catalyst revealed that the ultrasonic-assisted wet impregnation method successfully provides iron loading on both internal and external wall of acid-treated CNTs. As it can be seen in Figure 4.8, there is low aggregation of iron on the external surface of the acid-treated CNTs, and iron particles penetrated inside the pores of CNTs. Moreover, the crystalline size of iron oxide in TEM images was measured using Gaussian analysis. From histograms of particle size distributions (PSDs), the average particle size of iron oxide for 20Fe/CNTs-Syn, 20Fe/CNTs-Com, and 20Fe/Al₂O₃ was 25, 13, and 40 nm, respectively.

The TEM images of 20Fe/Al₂O₃ and 20Fe/CNTs-Com illustrate that iron particles on alumina support tend to aggregate, while Fe particles become smaller (9-21 nm) with the introduction of commercial CNTs (Wu et al., 2019). 20Fe/CNTs-Syn resulted in a smaller Fe particles compared with 20Fe/Al₂O₃ which would lead to a higher catalyst activity and lower long chain alkanes (C₅₊) (Zhang et al., 2019). 20Fe/CNTs-Syn also possesses less Fe aggregates in comparison with 20Fe/CNTs-Com. It can be related to acid-treatment of the synthesized CNTs prior catalyst preparation resulting in penetration of iron nanoparticles inside of the acid-treated CNTs that is mainly because of pore opening and increasing hydrophilicity (Kazakova et al., 2018).

It should be noted that pore volume and pore diameter of 20Fe/CNTs-Syn are higher than those of 20Fe/CNTs-Com, which is expected to facilitate metal dispersion and mass transfer (Xie et al., 2017; Hwang et al., 2020). Based on TEM images, the aspect ratio of CNTs-Syn and CNTs-Com were determined 20 and 318, respectively. It has been reported that aspect ratio of CNTs is significantly affected by reaction temperature during CVD operation (Aliyu et al., 2017).

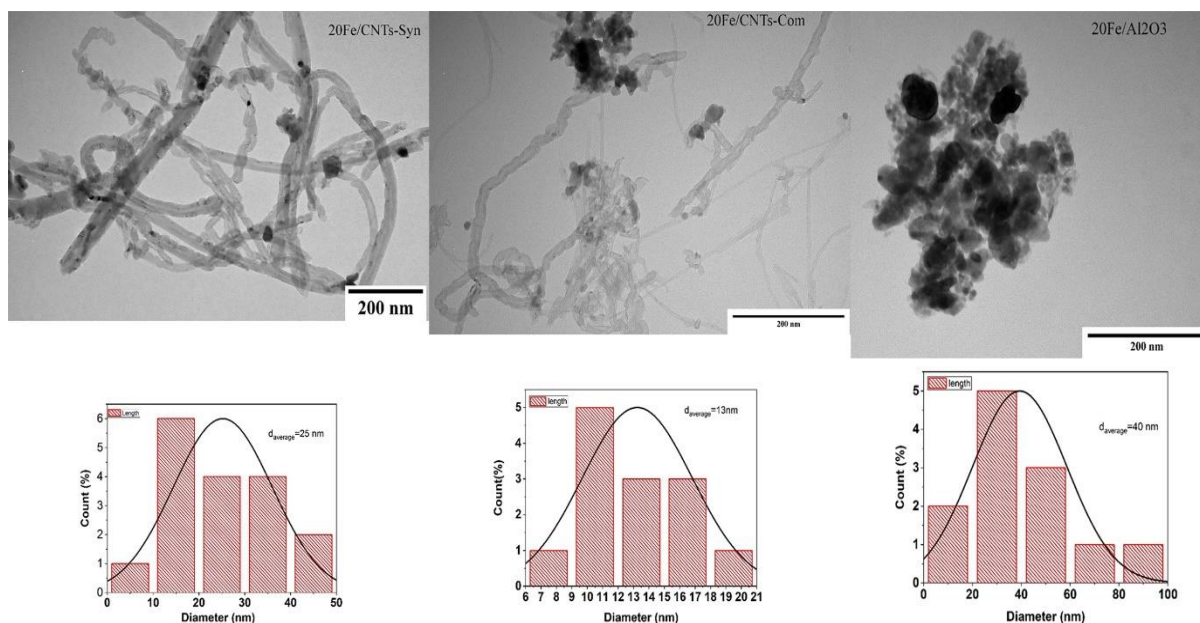


Figure 4.8: TEM micrographs and corresponding histograms of particle size distribution for catalysts.

Raman spectroscopy

Raman spectroscopy was used to study the synthesized CNTs before and after acid-treatment in terms of carbonaceous structure and quality. Moreover, Raman spectroscopy is a powerful method for providing information about metal impurities and amorphous carbon contents (Chernyak et al., 2017). From Figure 4.9, two characteristic peaks at 1350 cm^{-1} and 1590 cm^{-1} are attributed to D band and G band, respectively. The D mode shows the disorder characteristics of the synthesized CNTs and G band indicates the ordered graphite in CNTs structure (Fleming et al., 2019). The ratio of the D band to the G band (I_D/I_G) was selected as the optimization response to show the CNTs quality in terms of disorder or defects. Figure 4.9 demonstrates that acid-treatment decreases the I_D/I_G from 0.81 to 0.70 due to removal of amorphous carbon structure.

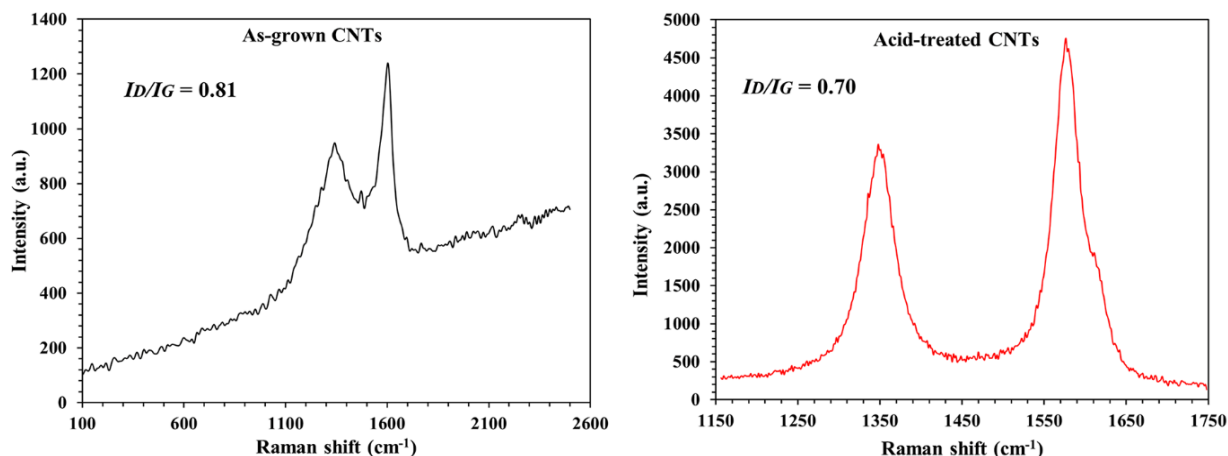


Figure 4.9: Raman spectra of the synthesized CNTs before and after acid-treatment.

Fourier-transform infrared (FTIR) spectroscopy

FTIR spectroscopy was employed to study the surface functional groups of the synthesized CNTs before and after acid-treatment. From Figure 4.10, the peaks in the range of 3743-3745 and 1236-1257 cm^{-1} are attributed to O-H and C-O-C stretching vibrations (T. Zhang et al., 2018; Peng et al., 2018). The peak appeared at 1533-1540 cm^{-1} can be related to C=C group, while the stretching vibration of carboxyl or carbonyl groups was observed at 1743-1749 cm^{-1} (Peng et al., 2018; Aziz et al., 2019). The peak at 1386 cm^{-1} assigned to H-C=O bond in acid-treated CNTs illustrates the effect of acid-treatment on multi-walled carbon nanotubes (Li et al., 2020). The peaks around 1452-1456 and 1647-1650 cm^{-1} are corresponded to methoxy (O-CH₃) group bending vibration and C=O group stretching vibration, respectively (Peng et al., 2018; Amiri et al., 2015). Comparison of FTIR spectra of as-grown CNTs and acid-treated CNTs confirmed the corresponding I_D/I_G ratio obtained by Raman spectroscopy indicating the defects and anchoring sites left on the CNTs wall after acid-treatment.

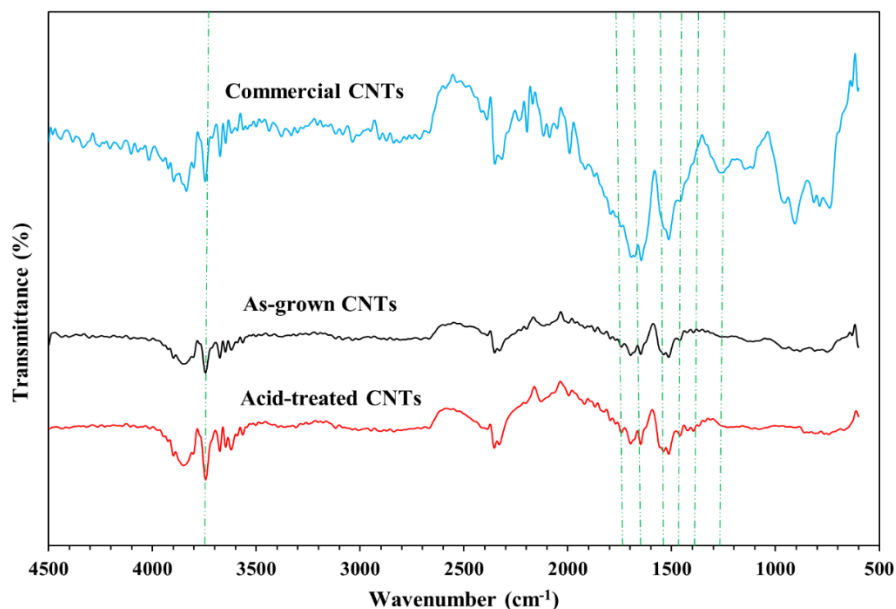


Figure 4.10: FTIR spectra of commercial CNTs, as-grown CNTs, and acid-treated CNTs.

Thermogravimetric analysis (TGA)

The thermal stability and purity of as-grown CNTs and acid-treated CNTs can be determined using thermogravimetric analysis (TGA). TGA profile (Figure 4.11) of the as-grown CNTs and acid-treated CNTs suggests thermal stability of MWCNTs up to 600 °C, with total weight loss being 0.8% and 2.1%, respectively (Behnam et al., 2019). It should be mentioned that acid-treatment resulted in the formation of defects and carboxyl functional groups at the surface of CNTs, thus reducing the solid residue from 99.2% to 97.9% in acid-treated CNTs (Behnam et al., 2019). The weight loss below 100 °C is assigned to water molecules physically adsorbed, while weight loss between 150 °C and 400 °C can be related to evolution of gaseous CO₂ (Atchudan et al., 2019). Additionally, the thermal decomposition of the calcined 20Fe/CNTs-Syn catalyst was investigated under nitrogen atmosphere. The thermogram of the calcined catalyst illustrated two weight loss regimes between 50 °C and 450 °C which confirmed the high thermal stability of the catalyst. The first weight loss below 100 °C is attributed to loss of unbound water and functional groups left on the surface of CNTs during acid-treatment (Farghali et al., 2017). The calcined 20Fe/CNTs-Syn catalyst showed a total weight loss of approximately 5% up to 600 °C.

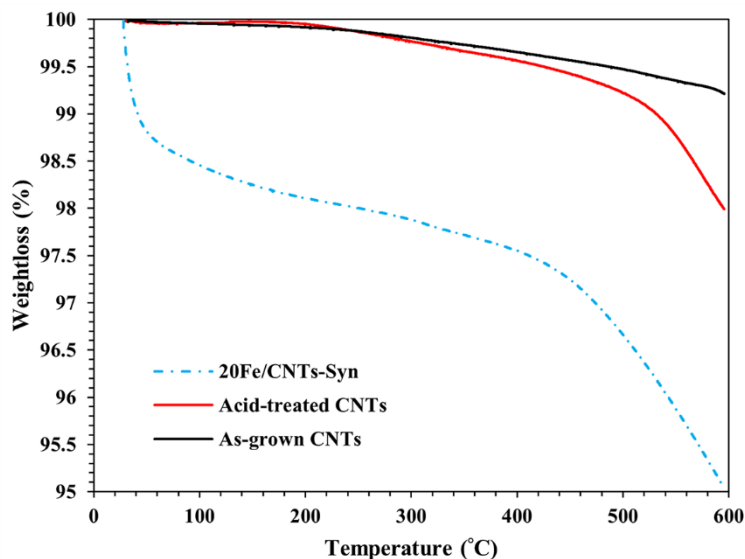


Figure 4.11: TGA profile of as-grown CNTs, acid-treated CNTs, and 20Fe/CNTs-Syn under nitrogen atmosphere.

H₂ temperature programmed reduction (H₂-TPR)

H₂-TPR analysis was applied to evaluate iron oxide reduction behavior in different Fe-based catalysts. From Figure 4.12 for the calcined FeCaCO₃ catalyst, the iron oxide reduction occurs below 700 °C, providing appropriate Fe catalyst for CNTs growth in CVD reactor. Figure 4.12 also shows the H₂-TPR profile for 20Fe/CNTs-Syn catalyst in which the first peak appears at nearly 396 °C representing the reduction of Fe₂O₃ to Fe₃O₄, and the second peak in the range of 500-550 °C attributed to the reduction of Fe₃O₄ to FeO followed by reduction of FeO to Fe (Badoga et al., 2020). 20Fe/CNTs-Com catalyst exhibits two distinct peaks at approximately 338 °C and 459 °C due to the reduction of Fe₂O₃ to metallic Fe in two steps. The reduction peaks for 20Fe/Al₂O₃ are observed at higher temperatures (nearly 375 °C and 545 °C) compared with 20Fe/CNTs-Com. It can be observed that the reducibility of 20Fe/CNTs-Syn is less than that of 20Fe/CNTs-Com which can be attributed to iron oxide particles incorporated inside the acid-treated CNTs on the one hand and larger iron oxide particle size (25 nm vs. 13 nm) on the other hand, resulting in iron oxide reduction at higher temperature. The reducibility of the Fe-based FTS catalysts is in the order of 20Fe/CNTs-Com > 20Fe/Al₂O₃ > 20Fe/CNTs-Syn. The amount of H₂ consumed during different reduction stages is summarized in Table 4.6.

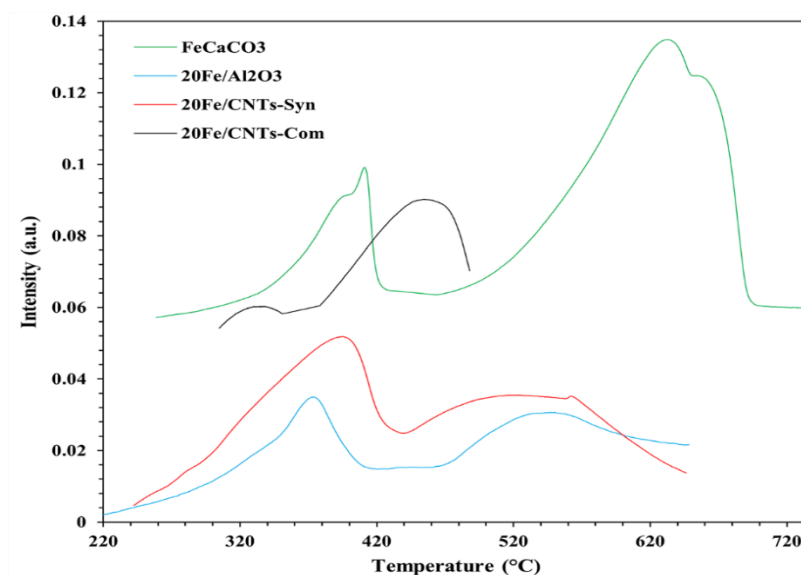


Figure 4.12: H₂ temperature programmed reduction profile for fresh catalysts.

Table 4.6: Quantitative results of H₂ consumption for calcined catalysts obtained by H₂-TPR.

Catalyst	Reaction temperature (°C)					H ₂ uptake (mmol/g)	
	Peak 1	Peak 2	Peak 3	Peak 4	Peak 5		
FeCaCO ₃	410	632	-	-	-	24.6	91.3
20Fe/Al ₂ O ₃	373	438	444	546	649	2.6	3.3
20Fe/CNTs-Syn	393	516	517	520	561	3.5	2.9
20Fe/CNTs-Com	375	632	-	-	-	0.8	2.9

X-ray photoelectron spectroscopy (XPS)

The surface composition and oxidation states of the fresh 20Fe/CNTs-Syn, 20Fe/CNTs-Com, and 20Fe/Al₂O₃ catalysts were studied by XPS analysis. Moreover, XPS can be used for determination of functional groups and structural defects on the surface of carbon nanotubes (Shen et al., 2018). The XPS survey was used to detect peaks related to carbon and oxygen over the binding energy ranges of 280-295 eV and 525-545 eV, respectively (Sezer and Koç, 2019). From Figure 4.13 (a), the peak at 284.4 eV is related to the graphitic network based on the deconvolution of the C1s photoemission (Sezer and Koç, 2019). Considering Fe2p XPS spectra in Figure 4.13 (b), the peaks in the range of 709.3-711.3 eV and 723-724.4 eV are assigned to Fe2p_{3/2} and Fe2p_{1/2} for Fe₃O₄ formation, respectively (Z. Zhang et al., 2018a). Additionally, Fe³⁺ satellite peak appeared at 718 eV (Zhou et al., 2017). XPS peaks observed at approximately 530 eV represent lattice O²⁻ in metal oxides (Zhou et al., 2017; Venugopalan et al., 2021).

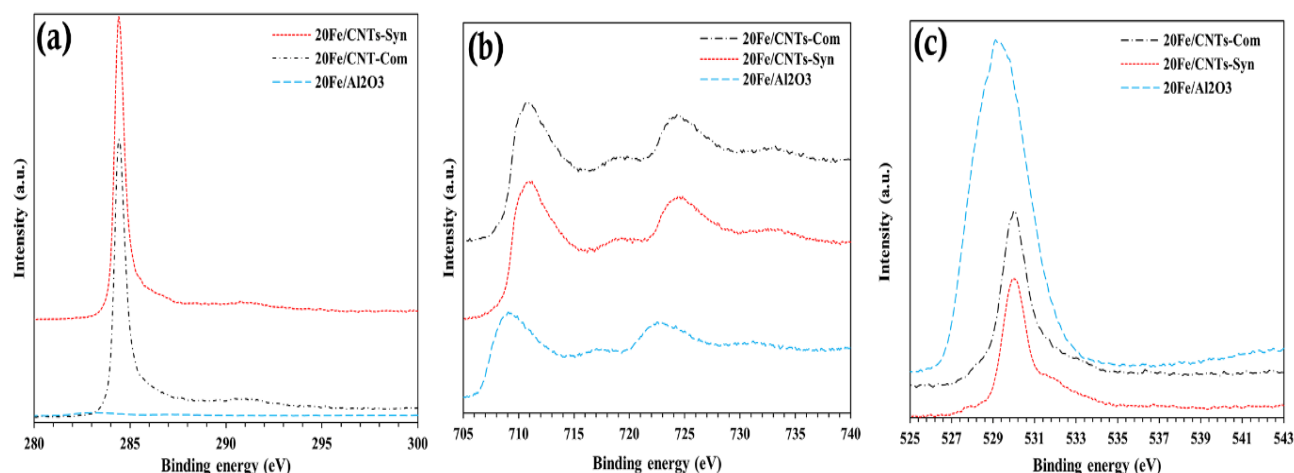


Figure 4.13: XPS spectra (a) C1s; (b) Fe2p; (c) O1s of the fresh calcined catalysts.

4.3.3 Catalytic performance of Fe-based catalysts in FTS

FTS reaction was conducted at 280 °C, 2 MPa, $H_2/CO = 1$, and GHSV = 2000 h⁻¹ for 24 h. The details of the FTS experiment as well as product sampling and composition analyses are described in sections 3.4 and 3.5, respectively. Figure 4.14 depicts the catalytic activity of the Fe-based catalysts in terms of CO conversion as a function of time on stream. It is generally believed that the catalytic activity of iron carbide as active phase of Fe-based catalysts originated from dissociative adsorption of CO molecules. CNT-based supports are supposed to enhance CO adsorption due to the large surface area and defects on the CNTs wall (Tian et al., 2019a). As can be seen from Figure 4.14, CO conversion for all Fe-based catalysts increased significantly within 8 h on stream. Afterward the catalysts conversion went up steadily until 24 h. CO conversion of 20Fe/CNTs-Com and 20Fe/CNTs-Syn catalyst is much more than that of 20Fe/Al₂O₃ catalyst which is likely due to larger surface area of 20Fe/CNTs-Com (380 m²/g) and 20Fe/CNTs-Syn (267 m²/g) compared with 20Fe/Al₂O₃ (221 m²/g), thus providing appropriate adsorption sites for CO molecules (Tian et al., 2019a).

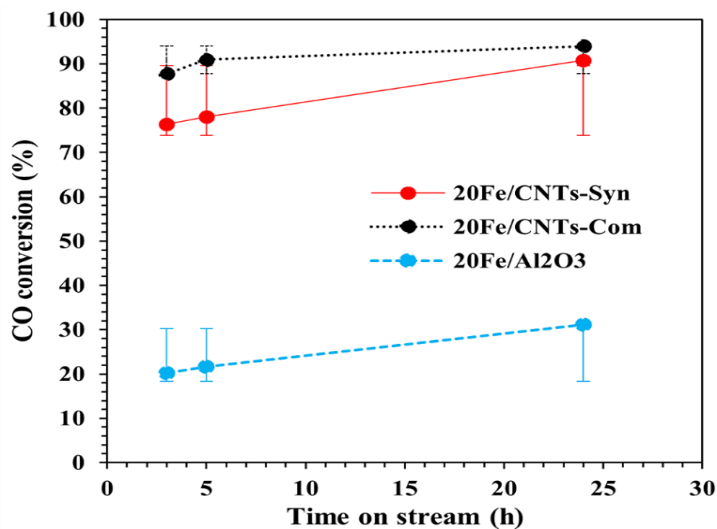


Figure 4.14: CO conversion for FTS catalysts (process conditions: $T = 280\text{ }^{\circ}\text{C}$, $P = 2\text{ MPa}$, $\text{H}_2/\text{CO} = 1$, $\text{TOS} = 24\text{ h}$, $\text{GHSV} = 2000\text{ h}^{-1}$).

Table 4.7 displays the catalytic activity and product selectivity for 20Fe/CNTs-Syn, 20Fe/CNTs-Com, and 20Fe/Al₂O₃ catalysts. Methane, light olefins (C₂-C₄), carbon dioxide, C₅⁺ hydrocarbons, and water were produced from syngas via FTS reaction over Fe-based catalysts. Considering the product selectivity for Fe-based catalysts, the selectivity to CH₄, CO₂, and C₂-C₄ for 20Fe/CNTs-Com (68.1%, 60.6%, and 26.1%) are more than the corresponding values for 20Fe/Al₂O₃ (17.3%, 28.8%, and 18.0%). The iron particle size has significant effects on light olefin selectivity. Decreasing the iron particle size would facilitate production of light hydrocarbons including methane. Furthermore, production of light olefins benefits from smaller iron particles (Liu et al., 2015b).

However, the trend for turn over frequency (TOF) is opposite, with $2.66 \times 10^{-3}\text{ s}^{-1}$ for 20Fe/Al₂O₃ and $0.67 \times 10^{-3}\text{ s}^{-1}$ for 20Fe/CNTs-Com. It is confirmed that lower TOF and higher methane selectivity for commercial CNTs support can be related to smaller iron oxide crystal size (Figure 4.8, iron oxide particle size: 13 nm) (Park et al., 2010). Based upon iron particle sizes in Figure 4.8, the TOF and C₅⁺ selectivity rises when the iron particle size increases from 13 nm for 20Fe/CNTs-Com to 40 nm for 20Fe/Al₂O₃ (Liu et al., 2017; Gu et al., 2020b). In the case of 20Fe/CNTs-Syn, CO conversion and light olefin selectivity are slightly less than those of commercial CNT-supported Fe catalyst. This is mainly due to larger pore diameter in synthesized CNTs support (Table 4.5, pore diameter: 17.4 nm) compared to commercial

counterpart (pore diameter: 5.6 nm) which causes larger iron oxide particles in 20Fe/CNTs-Syn (Figure 4.8, iron oxide particle size: 25 nm), thus reducing the contact area between iron carbide active sites and syngas during FTS reaction (Tian et al., 2019a).

FTY rate is defined as CO converted per total gram of iron per second, indicating the catalytic activity per gram of Fe which confirms the results of CO conversion for the studied catalysts (Tian et al., 2019a). The chain-growth probability (α) was measured based on Anderson-Schulz-Flory (ASF) (Iablokov and Kruse, 2019). From Table 4.7, as the value of α increased from 0.8 to 0.83, the production of C_{5+} rose and methane selectivity dropped (Zhang et al., 2010a). Table 4.7 also reveals that WGS reaction rate increases in the presence of CNTs as iron catalyst support. It has been suggested that high CO_2 selectivity is likely related to the increased water partial pressure at higher conversions which is confirmed in CNTs supports (Gavrilović et al., 2021).

Table 4.7: Selectivity and activity of Fe-based catalysts in Fischer-Tropsch synthesis.

Parameter	20Fe/CNTs-Syn	20Fe/CNTs-Com	20Fe/ Al_2O_3
CH_4 selectivity (%)	54.8 \pm 0.2	68.1 \pm 0.2	17.3 \pm 0.3
C_2 - C_4 selectivity (%)	23.6 \pm 0.1	26.1 \pm 0.2	18.0 \pm 0.1
C_{5+} selectivity (%)	21.6 \pm 0.3	5.8 \pm 0.5	64.6 \pm 0.2
CO_2 selectivity (%)	57.4 \pm 0.2	60.6 \pm 0.3	28.8 \pm 0.2
CO conversion (%)	90.4 \pm 0.4	94.2 \pm 0.3	30.8 \pm 0.4
$\frac{C_{2-4}}{C_{2-4}}$ ratio	0.20 \pm 0.01	0.20 \pm 0.01	0.32 \pm 0.02
Chain growth probability, α	0.83	0.80	0.83
FTY $10^{-4}(\frac{mol\ CO}{(g\ Fe)(s)})$	3.13	3.05	1.07
$R_{WGS}(\frac{g\ CO_2}{(g\ cat.)(h)})$	46.60	67.80	26.20
Apparent TOF $\times 10^3$ (s^{-1})	1.30	0.67	2.66

Operating conditions: T = 280 °C, P = 2 MPa, H_2/CO = 1, TOS = 24 h and GHSV = 2000 h^{-1} .

After collection of liquid products from hot and cold traps, the carbon number distribution of the products was identified by simulated distillation (SimDis). From Figure 4.15, 20Fe/CNTs-Syn obtained the lightest liquid product among the selected catalysts, with carbon

number between C₈ and C₁₈. However, liquid hydrocarbons of 20Fe/CNTs-Com and 20Fe/Al₂O₃ include C₉-C₅₂ and C₁₀-C₂₀, respectively.

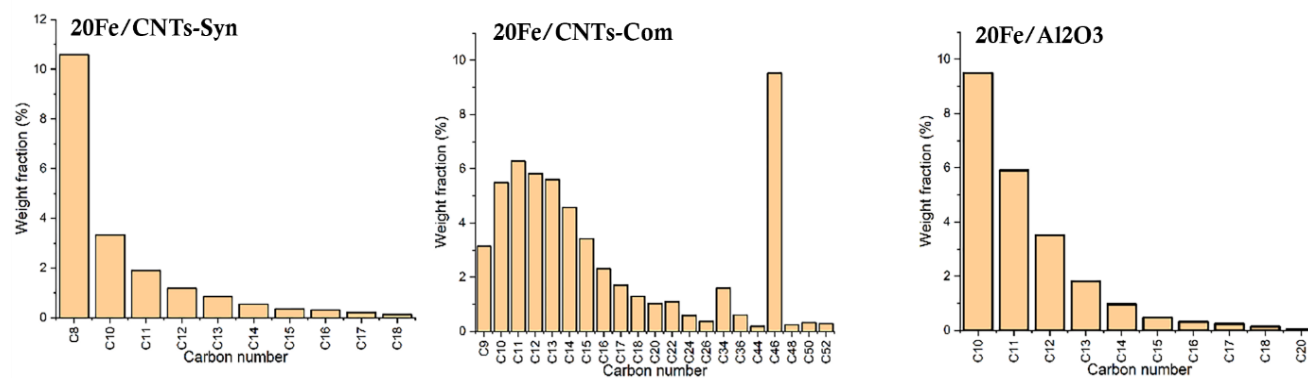


Figure 4.15: Hydrocarbons produced by FTS catalysts (process conditions: T = 280 °C, P = 2 MPa, H₂/CO = 1, TOS = 24 h, GHSV = 2000 h⁻¹).

Another outcome from the ASTM D6352 SimDis analysis is the boiling point distribution of liquid products for the selected catalysts during 24 h time-on-stream (Ra et al., 2021). As shown in Figure 4.16 (b), 92% and 78% of hydrocarbon fractions fall within the heavier products boiling point range (>300 °C) for 20Fe/CNTs-Com and 20Fe/Al₂O₃ catalysts, respectively. The result of liquid product boiling point confirmed carbon number distribution for the studied catalysts. In the case of liquid products, it might be suggested that synthesized CNTs having larger pore volume and pore size causes a faster ejection of liquid products which not only provides more available active sites for reaction but produces lighter liquid hydrocarbon compared with commercial CNTs (Figure 4.15 and Figure 4.16 (b)).

In addition, a larger pore volume of CNTs support improves dispersion of active iron (Zhang et al., 2010b). From Table 4.5, Fe dispersion of commercial CNTs support (2.6%) is less than that of synthesized CNTs (4.8%), indicating the effect of pore volume and pore diameter on Fe dispersion. In another perspective, the catalytic performance principally depends on iron phase composition rather than iron dispersion. From Figure 4.6 (c), the spent 20Fe/CNTs-Syn and 20Fe/CNTs-Com demonstrates higher proportion of Fe₅C₂ and Fe₃C, respectively. It was reported that the presence of iron carbide phase rich in carbon favored the production of long chain hydrocarbons (Saheli et al., 2021). In our study, Fe catalyst supported on synthesized CNTs has higher C₅₊ selectivity (21.6%) compared with its commercial counterpart (5.8%).

Additionally, composition of iron carbide and oxygen containing groups in CNTs affects interaction between the support and Fe species and thus, olefin selectivity in FTS (Zhang et al., 2010b). In Figure 4.6 (b,c), Fe catalyst supported on commercial CNTs exhibited higher contribution of Fe_3O_4 along with Fe_3C compared with synthesized CNTs possessing Fe_2O_3 - Fe_5C_2 , which was observed to improve C_2 - C_4 and C_{5+} selectivity in 20Fe/CNTs-Com and 20Fe/CNTs-Syn, respectively (Hwang et al., 2020).

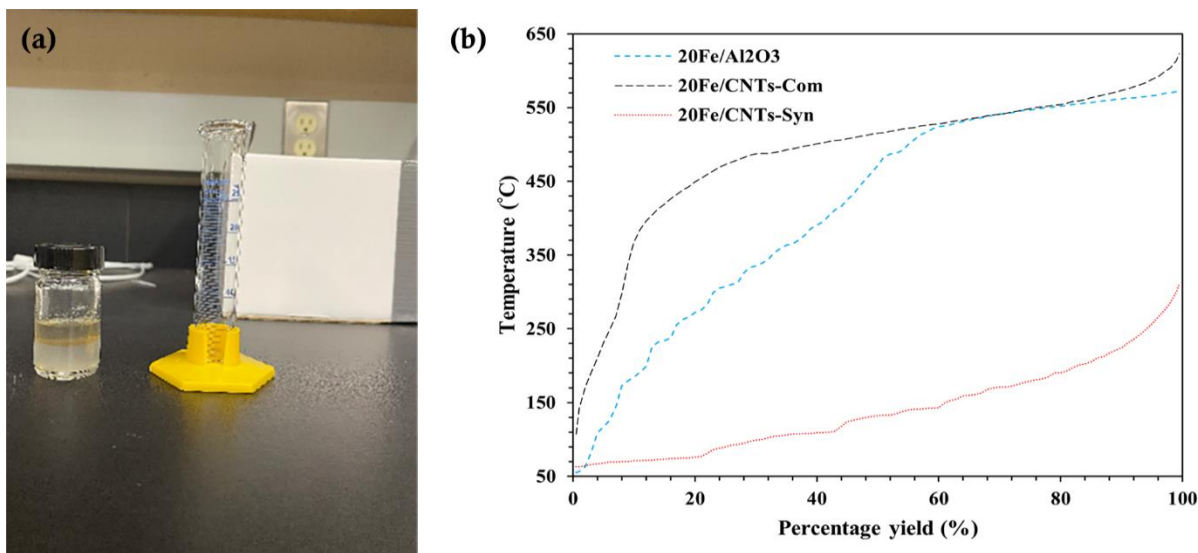


Figure 4.16: (a) FTS liquid products; (b) Boiling point distribution for liquid products obtained by FTS catalysts.

The time required to reach maximum CO conversion and steady state conditions for all studied catalysts can be observed in Figure 4.17. The difference in catalytic performance can be explained by the difference in distribution of iron phases formed during hydrogen pretreatment, which can cause mass transfer limitations (X. Zhao et al., 2018). The pore volume and pore diameter of supports also influence mass transport rate and catalyst activity. From Table 4.5, synthesized CNTs support exhibits larger pore volume and pore diameter ($V_p = 1.29 \text{ cm}^3/\text{g}$, $D_p = 17.4 \text{ nm}$) compared to those of commercial CNTs ($V_p = 0.58 \text{ cm}^3/\text{g}$, $D_p = 5.6 \text{ nm}$). As it was reported in previous researches, the higher the contribution of mesoporous volume, the lower the mass transport limitation (Hwang et al., 2020). From Table 4.7, CO conversion of 20Fe/CNTs-Syn reached its maximum (90.4%) after 24 h. Then the catalyst experienced deactivation and the activity decreased to as low as 81.7% after 120 h on stream. 20Fe/CNTs-Com and 20Fe/Al₂O₃ catalysts reached their highest activity after 24 h and 29 h with 94.2%

and 30.9% of CO conversion, respectively. Thereafter, catalytic activity of 20Fe/Al₂O₃ remained constant during the next 90 h.

As can be seen in Figure 4.17, there was a decrease in activity of 20Fe/CNTs-Com from 94.2% to 75.5% during the reaction period of 120 h. The higher stability of the 20Fe/CNTs-Syn compared to 20Fe/CNTs-Com may be attributed to the extent of mesopores and defects and/or the higher pore volume of the synthesized CNTs support compared with commercial one facilitating mass transfer. As discussed earlier, Raman spectroscopy (Figure 4.9) revealed that acid treatment at 110 °C could produce defects on the synthesized CNTs surface by removing Fe/CaCO₃ residue. The defects on the surface work as anchoring sites for stable iron particles on the supports surface (Malek Abbaslou et al., 2009; Cheng et al., 2014). The activity loss for iron nanoparticles supported on commercial CNTs was found to originate from severe sintering and carbon encapsulation of the iron carbide nanoparticles under reaction conditions (Chew et al., 2016; Ghofran Pakdel et al., 2019). While confinement of iron particles within the synthesized CNTs support modified the redox properties of encapsulated Fe oxides, and it led to a significant increase in Fe catalysts stability in FTS (Gu et al., 2018b).

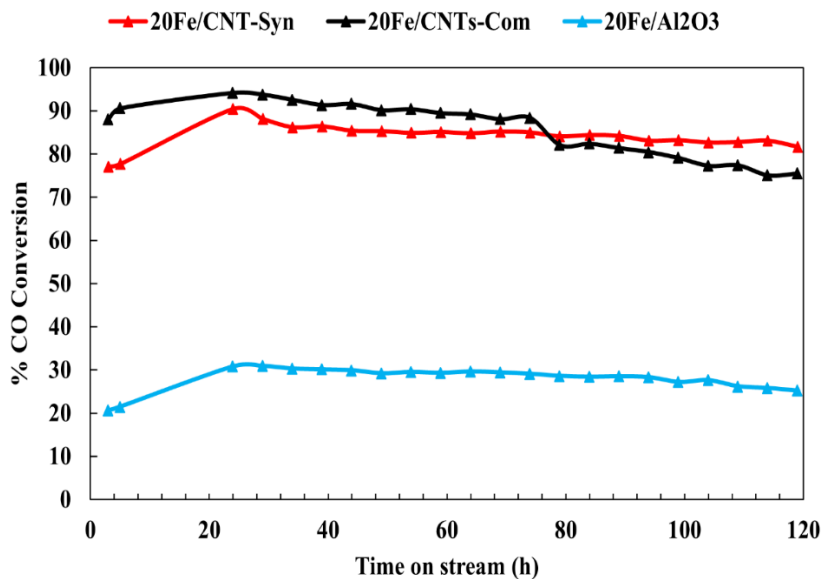


Figure 4.17: CO conversion of 20Fe/CNTs-Syn, 20Fe/CNTs-Com, and 20Fe/Al₂O₃ as a function of time-on-stream.

4.4 Conclusions

The approach of RSM was used to optimize the yield and quality of CNTs through CCVD process parameters. It was found that reaction temperature and reaction time have the most significant effects on CNTs growth. Applying 10Fe/CaCO₃ at minimum reaction temperature (700 °C) and minimum reaction time (30 min), maximum CNTs yield is achieved. However, based upon Raman spectroscopy results, the CNTs quality is not optimum at this condition ($I_D/I_G = 0.816$). The reaction temperature of 800 °C is suggested to obtain high quality CNTs with minimum I_D/I_G ratio, which is related to formation of graphitic carbon structure rather than amorphous carbon at elevated temperature. 20Fe/CNT-Syn, 20Fe/CNT-Com, and 20Fe/Al₂O₃ were assessed for FTS using syngas. The light olefin selectivity and CO conversion over 20Fe/CNTs-Syn were 23.6% and 90.4%, respectively, which is slightly less than that of 20Fe/CNT-Com. FTS liquid products of the studied Fe-based catalysts were analyzed via simulated distillation (ASTM D6352 SimDis) in terms of carbon number and boiling temperature. SimDis analysis evidenced that among the studied Fe-based catalysts, 20Fe/CNTs-Syn provides the highest amount of lighter hydrocarbons (C₈-C₁₈). Comparison of TEM and CO-chemisorption results revealed that the synthesized CNTs can alleviate the agglomeration of iron oxide particles and improve the dispersion of the iron oxide on the surface of catalyst. This might be related to acid-treatment of CNTs prior catalyst preparation resulting in some defects and anchoring sites on CNTs backbone. The oxygen-containing functional groups resulted in a higher intrinsic activity of 20Fe/CNT-Syn. It also shows a high and constant degree of CO conversion for a period of 120 h time on stream under industrially relevant conditions.

After finding the optimum conditions for CNTs production by CCVD method, it is utilized as support to obtain K and/or Mo-promoted Fe/CNTs catalysts for maximum light olefins' production in FTS. In the next phase, a fixed-bed reactor was employed to evaluate the activity, stability, and olefins' selectivity of the un-promoted and promoted iron catalysts supported on the synthesized CNTs.

CHAPTER 5: Optimization of Light Olefins' Yield in Fischer-Tropsch Synthesis using Carbon Nanotubes Supported Iron Catalyst with Potassium and Molybdenum Promoters

The content of this section has been published in Applied Catalysis A: General (Yahyazadeh et al., 2022b) and presented at the 26th Canadian Symposium on Catalysis Conference, Vancouver, May 15-18, 2022.

Contribution of the PhD candidate:

Experiments were designed in consultation with Dr. Venu Babu Borugadda, (Postdoc member of the group) under the supervision of Dr. Ajay K. Dalai and executed by Arash Yahyazadeh. Material synthesis, catalysts characterization and data interpretation were performed by Arash Yahyazadeh. The manuscript was drafted by Arash Yahyazadeh with guidance, suggestions, and reviews provided by Dr. Venu Babu Borugadda and Dr. Ajay K. Dalai.

Contribution of this chapter to overall PhD research:

The second phase of the research is investigated in this chapter: Addition of molybdenum and potassium as promoters to iron catalyst supported on CNTs for Fischer-Tropsch to light olefins. This chapter is the basis of the following chapters.

5.1 Abstract

Light olefins' (C_2 - C_4) production from syngas (H_2 +CO) through Fischer-Tropsch synthesis (FTS) benefits from Fe-based catalysts supported on carbon nanotubes (CNTs). A two-level full factorial design was applied for K and/or Mo-promoted Fe/CNTs catalyst to investigate the effects of synthesis conditions including Mo/K mass ratio, ultrasonic time, and iron loading on light olefins' yield. These catalysts were characterized to perform an in-depth study of Mo/K binary promoter effects on Fe/CNTs catalyst in Fischer-Tropsch to light olefins. CO chemisorption and TEM revealed that molybdenum plays a significant role in metal dispersion, leaving structural defects on CNTs support. Additionally, H_2 -TPR confirmed that K as promoter facilitates reducibility of Fe/CNTs catalysts, which promoted CO conversion in FTS. Compared with the un-promoted Fe/CNTs catalysts, addition of molybdenum as a promoter increased light olefins' selectivity by 33.4%, while potassium led to an increase in CO

conversion by 96.3%. The optimum formulation (0.5K5Mo10Fe/CNTs) obtained the olefins' yield of 35.5%.

5.2 Materials and methods

5.2.1 Materials

Preparation of CNTs support as well as corresponding unpromoted and promoted Fe/CNTs catalysts are described in sections 3.2.1 to 3.2.4 of Chapter 3. The complementary analytical techniques performed to characterize un-promoted and promoted Fe/CNTs catalysts are provided in Chapter 3.

5.2.2 Methodology

A two-level full factorial design was applied, and optimum catalyst synthesis conditions were obtained in terms of CO conversion and olefins' selectivity. Optimization was systematically carried out by varying the independent factors including promoters mass ratio (Mo/K; wt%/wt%), iron loading (Fe; wt%), and ultrasonic time (t; min). It is worth noting that ultrasonic time during wet impregnation was considered as a factor to investigate the effect of metal dispersion on catalyst performance. Table 5.1 represents the independent factors and their levels. Considering 3 center point replicates, a total of 11 experiments were proposed by 2-level full factorial design. All eleven catalysts were calcined at 400 °C for 4 h and used in FTS reactor at the same operating condition ($T = 280$ °C, $P = 3.45$ MPa, $GHSV = 2000$ h⁻¹, $H_2/CO = 1$, and TOS = 24 h). The details of FTS experiments as well as product sampling and composition analyses are described in sections 3.4 and 3.5, respectively.

The coefficient of determination (R^2) and R^2_{adj} were calculated as follows (Qin et al., 2011):

$$R^2 = 1 - \frac{SS_{Error}}{SS_{Total}} \quad (5-1)$$

$$R^2_{adj} = 1 - \frac{(1 - R^2)(n - 1)}{n - m - 1} \quad (5-2)$$

where SS_{Error} and SS_{Total} refer to the sum of the squares of the residuals and the total sum of squares, respectively. In Eq. (5-2), n and m are numbers of independent variables and the total number of variables, respectively. The value of R^2 and R^2_{adj} should be close to one. P-value lower than 0.05 was considered for 95% of a confidence interval (Torang et al., 2021).

Table 5.1: Factors and their levels considered in 2³ full factorial design.

	A: Promoters' mass ratio (Mo/K; wt%/ wt%) ^a	B: Iron loading (Fe; wt%)	C: Ultrasonic time (t; min)
Upper (+) level	10	30	18
Lower (-) level	0.25	10	6

^a Mo/K = 10; Mo = 5 wt% and K = 0.5 wt%, Mo/K = 0.25; Mo = 0.5 wt% and K = 2 wt%, Mo/K = 5.13; Mo = 3.8 wt% and K = 0.75 wt%

5.3 Results and discussion

5.3.1 Optimization of catalyst synthesis conditions in FTS

This optimization aims to investigate the effects of promoter's mass ratio, iron loading, and ultrasonic time on olefins' yield via full factorial design (Table 5.2). The analysis of variance (ANOVA) was applied to study the significance of the catalyst synthesis conditions (Table 5.3).

Table 5.2: 2-level full factorial design matrix with experimental response.

Run	A: Mo/K mass ratio (wt%/wt%)	B: Fe loading (wt%)	C: Ultrasonic time (min)	CO conversion (%)	C ₂ -C ₄ selectivity (%)	CO ₂ selectivity (%)	Response: Olefins' Yield= selectivity × conversion (%)
1	0.25	10	6	47.4	3.7	52.0	1.8
2	10	10	18	71.5	49.6	75.2	35.5
3	10	30	18	36.7	3.0	32.5	1.1
4	5.13	20	12	61.5	18.9	83.9	11.6
5	0.25	30	18	37.8	2.7	38.2	1.0
6	10	30	6	71.4	36.9	73.3	26.3
7	0.25	30	6	46.0	3.0	49.3	1.4
8	5.13	20	12	61.3	19.0	84.1	11.6
9	10	10	6	52.7	24.7	92.8	13.0
10	0.25	10	18	40.5	2.7	41.9	1.1
11	5.13	20	12	61.7	18.8	82.7	11.6

From Table 5.3, the promoter mass ratio (A) and iron loading (B) are the influential factors with p-value < 0.05. Additionally, the interaction between iron loading and ultrasonic time

(BC) was considered as a significant interaction. Considering olefins' yield as response, R^2 of 1-factor and 2-factor models were 0.522 and 0.777 respectively. For the one- and two-factor model, the model F-values are calculated to be 2.55 and 2.32, respectively, which implies that these models are insignificant relative to the noise. However, the 3-factor interaction (3FI) model fitted well with experimental data, providing acceptable R^2 of 0.996 (Table 5.3).

Table 5.3: Analysis of variance for olefins' yield obtained by 2-level full factorial model.

Source	Sum of Squares	DF	Mean Square	F Value	p-value
Model	1305.7	7	186.5	118.2	0.0012
A	624.3	1	624.3	395.6	0.0003
B	57.6	1	57.6	36.5	0.0091
C	1.8	1	1.8	1.1	0.3622
AB	53.0	1	53.0	33.6	0.0102
AC	0.4	1	0.4	0.2	0.6526
BC	280.7	1	280.7	177.9	0.0009
ABC	287.9	1	287.9	182.4	0.009
Residual	4.7	3	4.7		
Pure Error	1.3E-3	2	6.3E-4		
Cor Total	1310.4	10			

$R^2 = 0.9964$, Standard deviation = 1.26, Coefficient of variation % = 11.91, Adequate precision = 32.146

The regression equation estimating olefins' yield in terms of coded factors is shown as follow:

$$\text{Olefins yield (wt.\%)} = 10.55 + 8.83 \times A - 2.68 \times B - 0.48 \times C - 2.57 \times A \times B - 0.22 \times A \times C - 5.92 \times B \times C - 6.00 \times A \times B \times C \quad (5-3)$$

where A , B , and C stand for Mo/K mass ratio, iron loading (wt%), and ultrasonic time (min), respectively.

Figure 5.1 depicts the 2D-contour and 3D-surface plots of olefins' yield based on the binary interactions of AB and AC. In the case of carbon material supports, higher iron contents lead to larger crystallites of iron oxide. Increasing iron loading results in larger extent of aggregation of Fe nanoparticles in unpromoted iron catalyst. However, lowering iron loading results in smaller Fe nanoparticles in which carbon deposition was reported as the main reason for

deactivation over time for the unpromoted iron catalysts (Xie et al., 2016a). Based on the literature, the activation energy of CO conversion and intrinsic CO conversion activity drops with decreasing iron particle size. In case of iron particle size larger than 10 nm, the electronic effect including electron donation to iron is dominant, and the dispersion effect can be ignored. However, for iron particle size smaller than 10 nm, the electronic effect is not significant compared with the dispersion effects (Qin et al., 2011). Pour et al. studied stability of nano-structured Fe catalyst in FTS. They concluded that by reducing iron oxide particle size formation of inactive carbide phases and surface carbonaceous species like graphite are enhanced which leads to catalyst deactivation (Pour et al., 2010).

Ultrasonic time enhances iron dispersion and prevents formation of large inactive Fe aggregates by sintering. From Table 6, it is observed that 5Mo10Fe/CNTs shows the maximum iron dispersion (8.8%), while iron time yield (FTY) reached to a minimum of $0.0058 \text{ mol}_{\text{CO}} \text{ g}_{\text{Fe}}^{-1} \text{ s}^{-1}$ in 24 h. Increasing ultrasonic time above 18 min would lead to a decrease in FTY or CO converted in 1 s per gram Fe, thus lowering CO conversion. It can be suggested that the higher the ultrasonic time is, the lower the CO conversion will be. This is mainly related to suppressing iron oxide reduction and carburization (Qin et al., 2011). At the constant ultrasonic time (C = 18 min), maximum olefins' yield is achieved using 10 wt% iron loading and promoter's mass ratio of Mo/K = 10 (Figure 5.1 (a,b)). In addition, at constant iron loading (10 wt%), upper limits of ultrasonic time and Mo/K ratio resulted in the maximum olefins' yield (Figure 5.1 (c,d)). To maximize olefins' yield, the optimum synthesis conditions obtained at Mo/K mass ratio, Fe loading, and ultrasonic time of 10 wt%/wt%, 10 wt%, and 18 min, respectively corresponded to Run 2.

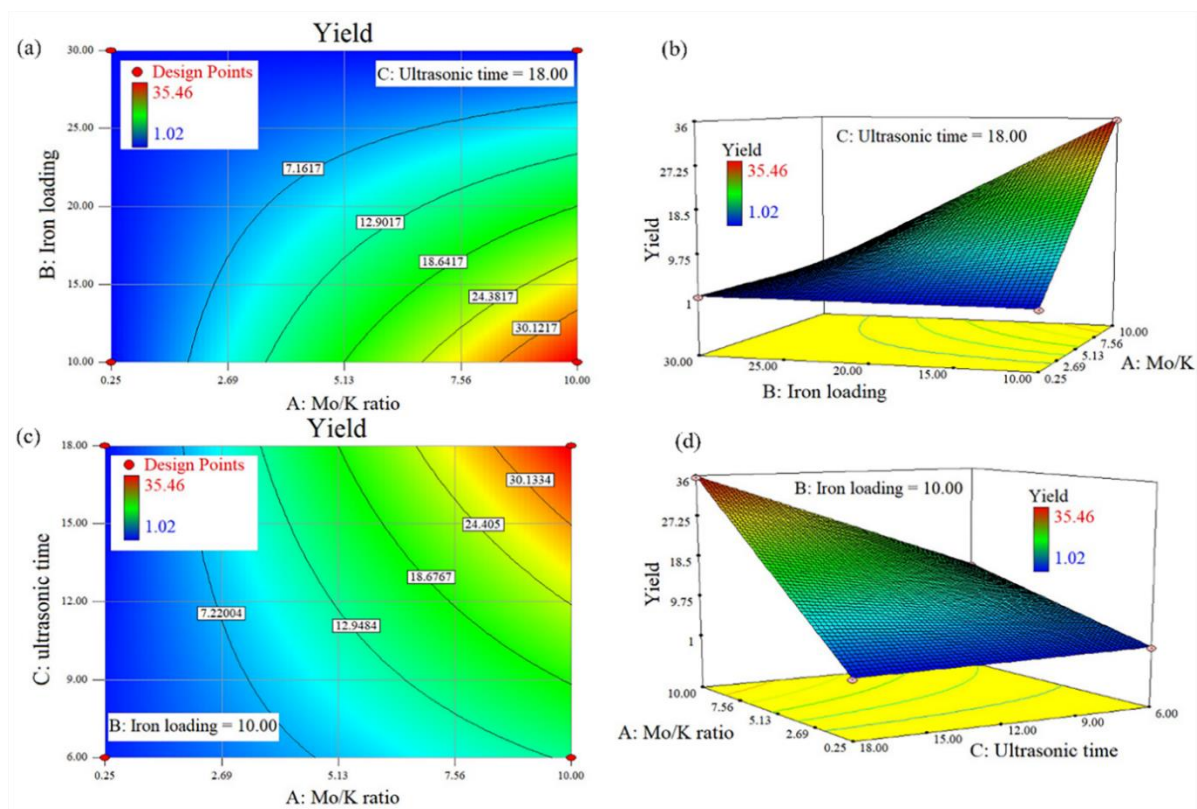


Figure 5.1: 2D contour and 3D surface plots of olefins' yield with simultaneous effects of (a,b) Mo/K mass ratio and iron loading; (c, d) Mo/K mass ratio and ultrasonic time.

The predicted results obtained by 3-FI model were plotted against both actual responses and residuals. Figure 5.2 confirmed that 3-FI model prediction of olefins' yield is in good agreement with experimental data.

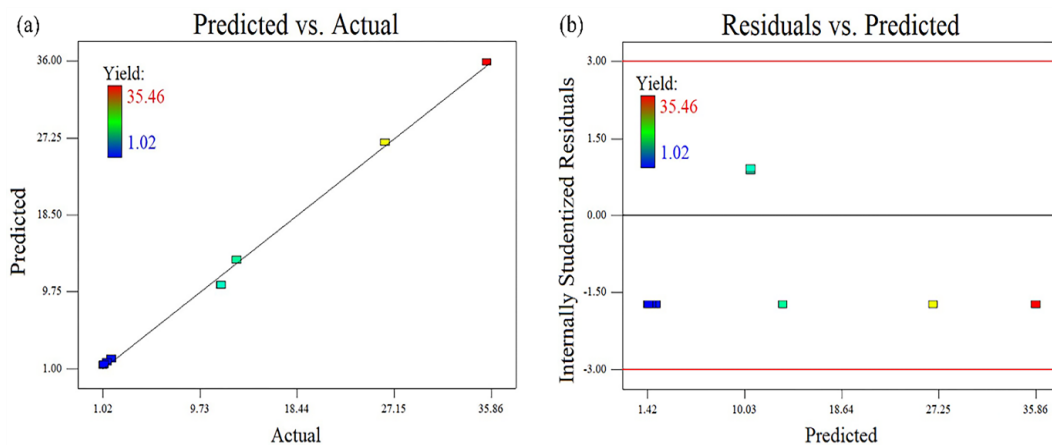


Figure 5.2: Diagnostic plots (a) Predicted versus actual; (b) Residual versus predicted for olefins' yield as response.

Based on the optimum synthesis conditions (Run 2) obtained by 2-level factorial design, the effects of molybdenum and potassium on Fe/CNTs catalyst were individually evaluated in FTS. To this purpose, a series of monometallic promoted and un-promoted Fe/CNTs catalysts were synthesized, and all catalysts were evaluated in terms of activity and product selectivity. Table 5.4 clearly indicates that molybdenum enhanced the olefins' selectivity, while potassium improved catalyst performance in terms of CO conversion. The un-promoted Fe/CNTs catalyst revealed a higher olefins' yield compared to K-promoted catalyst. However, in the case of Mo-promoted catalysts, olefins' selectivity was higher than that of un-promoted counterpart. Therefore, it was confirmed that the bimetallic promoted Fe/CNTs catalysts benefited from Mo and K simultaneously resulting in the maximum level of light olefins' yield.

Table 5.4: Monometallic promoted and un-promoted Fe/CNTs catalysts performance at 280 °C, 3.45 MPa, GHSV = 2000 h⁻¹, H₂/CO = 1, and TOS = 24 h.

Run	Mo (wt%)	K (wt%)	Fe (wt%)	Ultrasonic time (min)	CO conversion (%)	C ₂ -C ₄ selectivity (%)	CO ₂ selectivity (%)	Yield = olefins' selectivity × conversion (%)
1	5	-	10	18	60.2	26.9	62.2	16.19
2	-	2	10	18	95.9	2.8	52.7	2.68
3	0.5	-	10	18	62.2	32.7	65.6	20.33
4	-	0.75	10	18	96.1	2.4	52.1	2.30
5	3.8	-	10	18	80.7	33.4	68.2	26.95
6	-	0.5	10	18	96.3	2.8	52.3	2.69
7	-	-	10	18	90.3	15.4	59.7	13.90

Table 5.5 summarizes FTS results of the optimum synthesis conditions (Run 2) with its monometallic and un-promoted counterparts. These catalysts were characterized thoroughly to perform an in-depth study of Mo/K binary promoter effects on Fe/CNTs catalyst in Fischer-Tropsch to light olefins.

Table 5.5: FTS results of the optimum KMoFe/CNTs catalyst in comparison with its monometallic promoted and un-promoted counterparts (280 °C, 3.45 MPa, GHSV = 2000 h⁻¹, H₂/CO = 1, and TOS = 24 h).

Catalyst	Mo (wt%)	K (wt%)	Fe (wt%)	Ultrasonic time (min)	CO conversion (%)	C ₂ -C ₄ selectivity (%)	CO ₂ selectivity (%)	Yield = olefins' selectivity × conversion (%)
1	5	-	10	18	60.2	26.9	62.2	16.19
2	-	0.5	10	18	96.3	2.8	52.3	2.69
3	5	0.5	10	18	71.5	49.6	75.2	35.46
4	-	-	10	18	90.3	15.4	59.7	13.90

5.3.2 Characterization

Figure 5.3 demonstrates N₂ adsorption-desorption isotherms of the calcined catalysts compared to CNTs support. The pore structure of the CNTs support can be observed in all calcined catalysts. Likewise, the acid-treated mesoporous CNTs and all calcined catalysts exhibit Type IV isotherm. From Figure 5.3 (a), the decrease in BET surface area is in the order of 10Fe/CNTs < 0.5K10Fe/CNTs < 5Mo10Fe/CNTs < 0.5K5Mo10Fe/CNTs, which is related to pore filling with active metals such as iron, molybdenum, and potassium oxides (Badoga et al., 2017b). Barrett-Joyner-Halenda (BJH) desorption method was applied to obtain pore size distribution (PSD) curves of all catalysts (Figure 5.3(b)). From Table 5.6, K-promoted catalyst possess a wide range of pore distribution (~ 5-45 nm) which can be related to the disordered structure of mesoporous CNTs, while the PSD for Mo-promoted catalyst became narrower (~ 5-25 nm). The larger pore size of 0.5K10Fe/CNTs catalyst offers higher C₅₊ selectivity due to easier iron carbidization and carbon chain growth, which is confirmed by FTS results in Table 5.12 (Cheng et al., 2015c).

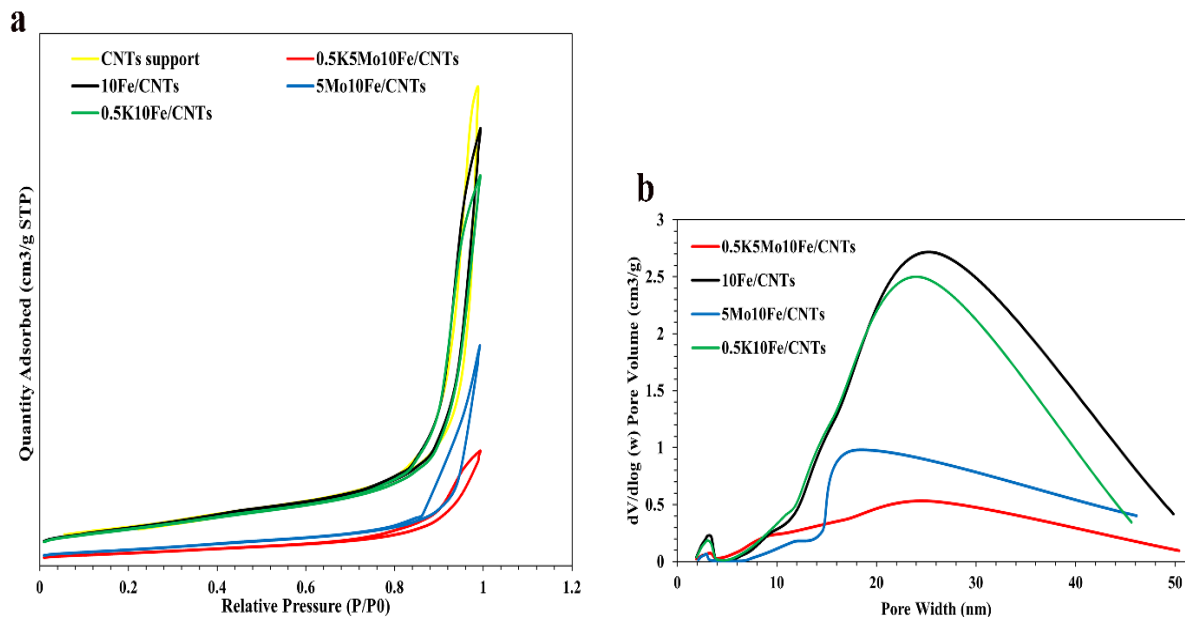


Figure 5.3: (a) N₂ adsorption-desorption isotherms of acid-treated CNTs and the prepared Fe/CNTs catalysts; (b) Pore size distribution of corresponding Fe/CNTs catalysts.

The textural properties of the acid-treated CNTs and calcined catalysts are shown in Table 5.6. It can be seen that impregnation caused a decrease in BET surface area and total pore volume. The sharpest decline in the effective surface area was observed in 0.5K5Mo10Fe/CNTs-Syn, with BET surface area being 103 m²/g. As it can be seen in Table 5.6, dispersion of iron species increased after addition of Mo promoter. Mo as a promoter resulted in a higher metal dispersion (8.8%), which confirms the narrower pore size distribution in Mo-promoted Fe/CNTs catalyst compared to potassium promoter (Figure 5.3(b)). It should be noted that average pore size in 5Mo10Fe/CNTs is less than that of 0.5K10Fe/CNTs indicating the larger metal oxide particle size in Mo-promoted iron catalyst compared to K-promoted one. Additionally, it may indicate more migration of metal species within carbon nanotubes in 5Mo10Fe/CNTs.

Table 5.6: Metal contents and textural properties of the synthesized CNTs support, fresh unpromoted and promoted Fe/CNTs catalysts.

Catalyst	Fe content (%) ^a	Mo content (%) ^a	K content (%) ^a	BET surface area (m ² /g) ^b	Total pore volume (cm ³ /g) ^c	Pore diameter (nm) ^c	Metal dispersion (%) ^d
CNTs-Syn	-	-	-	309	1.67	19.4	-
0.5K5Mo10Fe/CNTs-Syn	9.8	4.8	0.6	103	0.40	14.6	2.43
10Fe/CNTs-Syn	10.1	-	-	307	1.51	19.2	2.39
5Mo10Fe/CNTs-Syn	10.2	4.8	-	133	0.76	20.5	8.82
0.5K10Fe/CNTs-Syn	10.2	-	0.4	294	1.35	18.3	2.78

^a Determined by ICP analysis (error $\pm 0.4\%$), ^b Determined by BET method (error $\pm 3\%$), ^c Determined by BJH method (error $\pm 2.5\%$), ^d Determined by CO-chemisorption (error $\pm 1.5\%$)

XRD is an efficient tool to identify the crystallographic structure of the active metal present in heterogeneous catalysis. Hematite (α -Fe₂O₃) and magnetite (Fe₃O₄) are two forms of iron oxide that can be found in oxide catalysts (Figures 5.4 and 5.5). The diffraction peak at 26.3° corresponds to the (0 0 2) reflection of the synthesized CNTs. The peaks at 2 θ of 33.2°, 41°, 54°, and 63° are assignable to the standard hematite phase (α -Fe₂O₃, JCPDS 13-0534) (Alayat et al., 2018), while the peaks at 2 θ of 34° are attributed to the magnetite phase (Fe₃O₄, JCPDS 75-0449) for the spent catalysts (Gu et al., 2019b). The diffraction peaks between 30.2° and 35.7° are attributed to Fe₃O₄ and Fe₂O₃-Fe₃O₄, respectively (Xiong et al., 2015). The peak around 65.8° is assigned to atomic Fe in the catalysts (Tavasoli et al., 2009).

From Figure 5.4, additional peaks at 21° and 23° can be attributed to iron-molybdenum oxide (Fe₂Mo_xO_z) and reduced molybdenum oxide (MoO_{2.75}) in calcined catalysts (Ma et al., 2006). KO₂, K₂O, K₂CO₃, and KOH are more likely present in K-promoted catalyst compared to metal potassium. The diffraction patterns of the potassium promoter were not discernible, which is related to its low concentration and high dispersion within the catalyst except in 0.5K10Fe/CNTs calcined catalyst (Zhipeng Tian et al., 2019a). For iron catalysts, the rate of FTS reaction is influenced by the number and intrinsic reactivity of the iron carbide surface species. The extent of carbidization and iron carbide dispersion affect the concentration of iron carbide sites. Furthermore, observable phases in activated and spent catalysts are hematite, magnetite, and iron carbide (Fe₅C₂, Fe₃C, Fe₂C in Figure 5.5). It is suggested that iron oxide is finely dispersed on Mo-promoted catalysts due to the broad and small peaks at 2 θ = 33° (Figure 5.4).

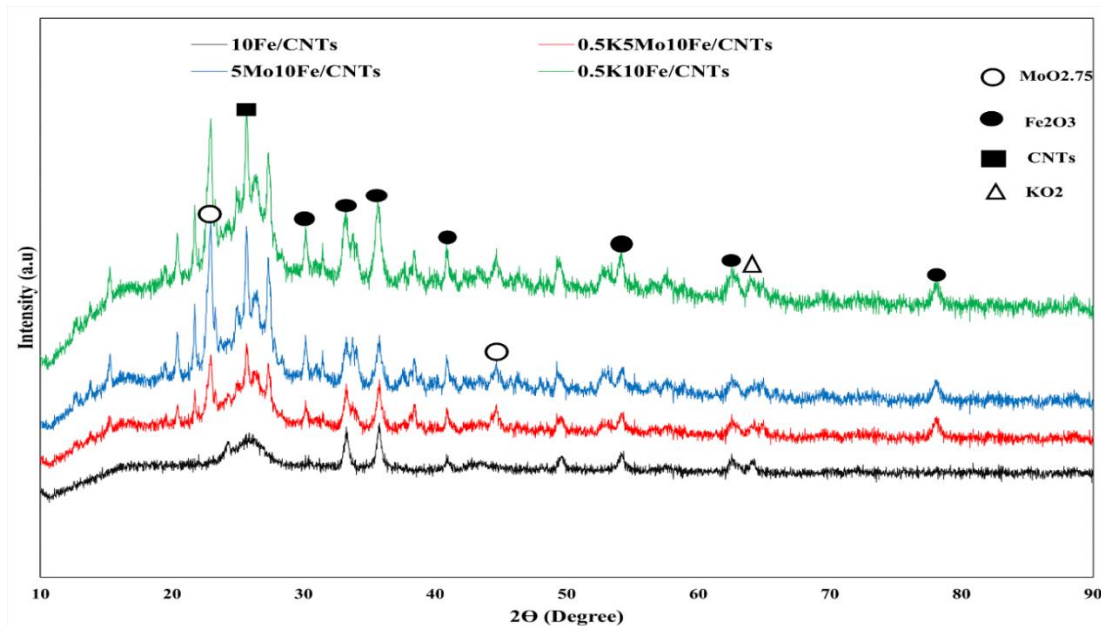


Figure 5.4: XRD spectra for the un-promoted and promoted Fe/CNTs calcined catalysts.

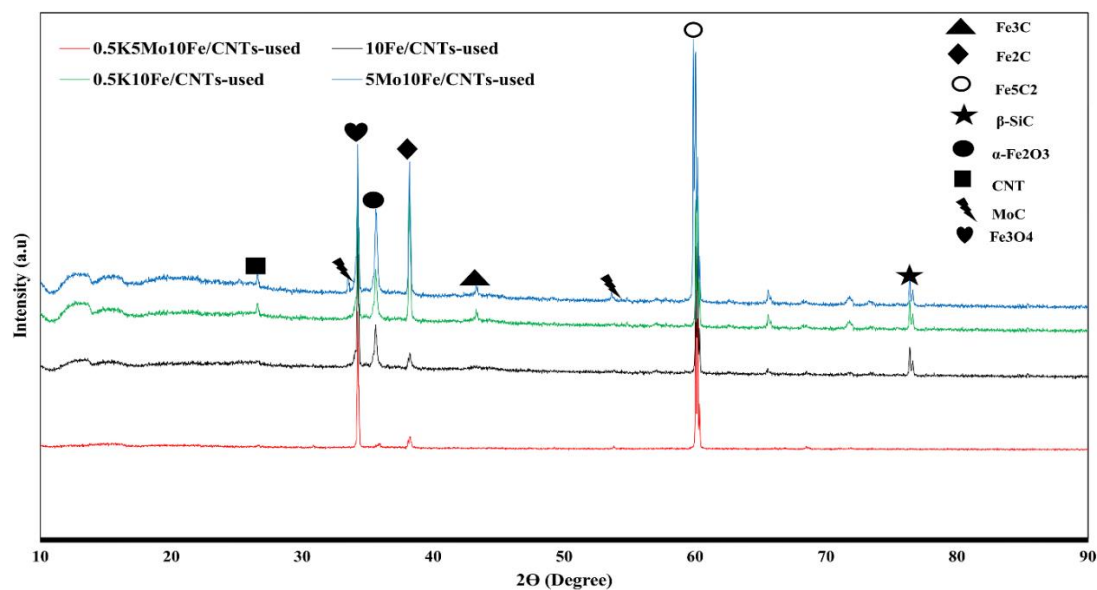


Figure 5.5: XRD spectra for the un-promoted and promoted Fe/CNTs spent catalysts.

Scherrer formula was used to measure the average Fe_2O_3 crystallite size of fresh and spent catalysts (Table 5.7). It has been suggested that the surface iron (II) oxide plays an important role during FTS through regulating the relative rates of CO hydrogenation and stabilizing the iron carbide catalyst. It has been also noted that difficulties with removal of the adsorbed

oxygen from the active iron carbides can be related to an irreversible oxidation in the presence of water (Thüne et al., 2012). It is obvious that addition of molybdenum to 10Fe/CNTs catalysts increased the average particle sizes in fresh catalysts (Tian et al., 2019b). However, the addition of 0.5 wt% potassium decreased iron oxide particle size slightly (30.0 nm) in calcined catalysts. After FTS reaction, the iron oxide particle size of 10Fe/CNTs increased due to gradual deactivation and agglomeration. However, the presence of molybdenum in spent 10Fe/CNTs catalysts resulted in a lower iron oxide particle size, confirming the increase in metal dispersion for Mo-promoted Fe/CNTs catalysts. It can be suggested that Mo strengthened the synergistic effect between iron carbides and Brönsted acid sites and enhanced the formation of light olefins by increasing metal dispersion and preventing iron oxide agglomeration.

Table 5.7: Average particle size of iron oxide for fresh and spent catalysts by XRD.

Catalyst	Fe ₂ O ₃ crystallite size (nm) (± 1)	
	Fresh	Spent
10Fe/CNTs-Syn	35.1	70.6
0.5K5Mo10Fe/CNTs-Syn	71.2	34.7
5Mo10Fe/CNTs-Syn	70.3	53.0
0.5K10Fe/CNTs-Syn	30.0	53.0

Acid treatment leads to CNTs cap opening, and these defects can serve as anchoring sites for the iron particles to attach or diffuse inside the CNTs during ultrasonic-assisted wet impregnation (Bora Ye et al., 2020). Iron particles are distributed on both inner and outer surfaces of CNTs (Setiabudi et al., 2018). Therefore, transmission electron microscopy (TEM) was employed to determine particle size distribution and morphological differences between promoted and un-promoted Fe/CNTs catalysts. TEM images for the calcined un-promoted and promoted Fe/CNTs catalysts are shown in Figure 5.6. CNT inner and outer diameters were between 3.8-7.7 nm and 12.3-18.2 nm, respectively. It can be observed that particle size distribution histograms of metal oxides in fresh catalysts are in good agreement with Fe₂O₃ crystallite size obtained by XRD (Table 5.7). Figure 5.6 (d) shows a desirable dispersion of metal species within carbon nanotubes due to the presence of binary promoter of Mo/K preventing metal particles from agglomeration.

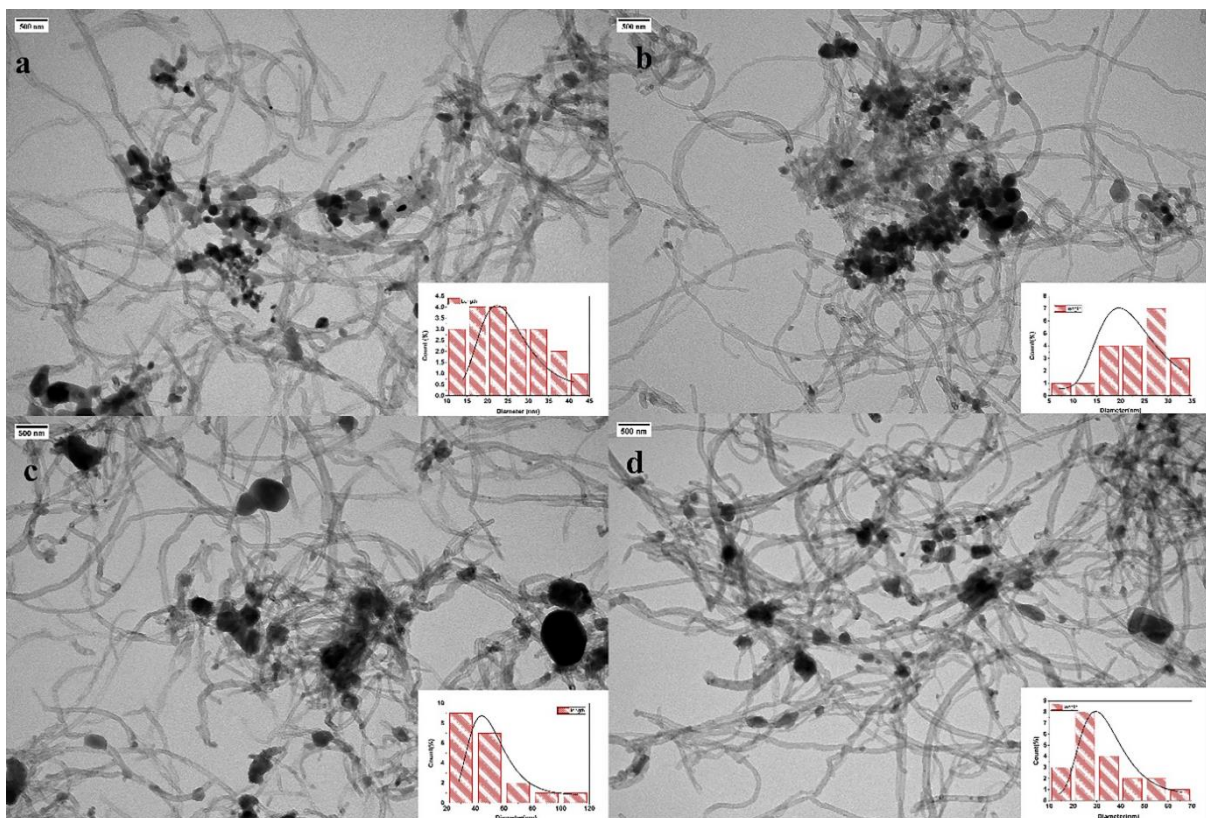


Figure 5.6: TEM micrographs and particle size distribution histograms (a) 10Fe/CNTs; (b) 0.5K10Fe/CNTs; (c) 5Mo10Fe/CNTs; (d) 0.5K5Mo10Fe/CNTs.

Figure 5.7 illustrates the H_2 -temperature programmed reduction (TPR) profile of un-promoted and promoted Fe/CNTs catalysts to understand the influence of promoters on iron-oxide reducibility. The peaks at a lower temperature represent Fe_2O_3 being reduced to Fe_3O_4 , while those at a higher temperature indicate Fe_3O_4 being reduced to FeO , which is then reduced to Fe . The iron oxide reduction peaks for 0.5K5Mo10Fe/CNTs catalysts appear at 455 °C and 539 °C, respectively. As indicated in the H_2 -TPR profiles, the addition of promoters increased the iron oxide reduction temperatures. The potassium promotion leads to a lower intensity of the H_2 -TPR peaks and probably corresponds to a lower extent of iron oxide reduction (Gu et al., 2021). The peak at a temperature higher than 650 °C can be assigned to the gasification of CNTs. The amounts of adsorbed H_2 are shown in Table 5.8 for un-promoted and promoted catalysts.

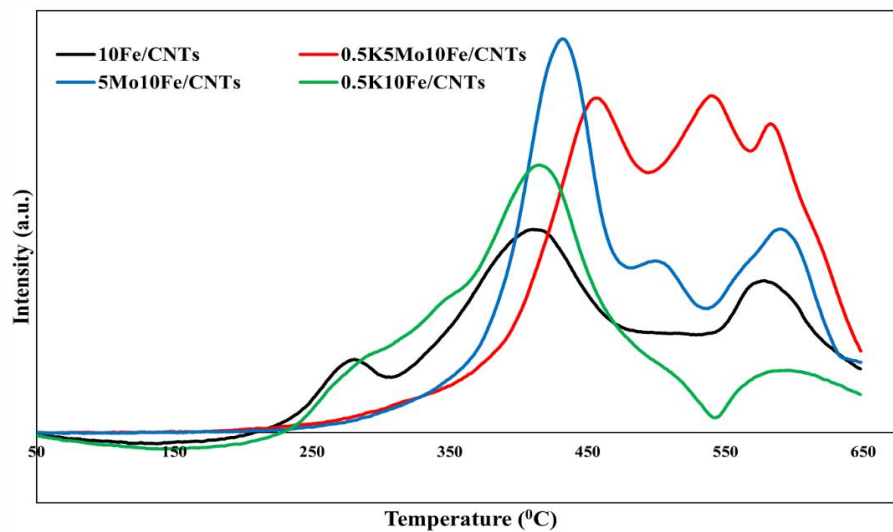


Figure 5.7: H₂-TPR profiles of promoted and un-promoted Fe/CNTs catalysts.

Table 5.8: H₂ uptake by un-promoted and promoted Fe/CNTs catalysts.

Catalyst	Reaction temperature (°C)					H ₂ uptake (mmol/g)				
	Peak 1	Peak 2	Peak 3	Peak 4	Peak 5					
10Fe/CNTs	280	409	511	513	576	0.1	5.4	0	0	0.9
0.5K10Fe/CNTs	-	414	-	-	-	2.8				
0.5K5Mo10Fe/CNTs	-	455	539	-	582	1.6	1.4		1.0	
5Mo10Fe/CNTs		431	498	-	589	2.3	0.9		1.2	

Raman spectroscopy was used to characterize the defects in CNTs, 10Fe/CNTs, 5Mo10Fe/CNTs, 0.5K10Fe/CNTs, and 0.5K5Mo10Fe/CNTs samples. From Figures 5.8 and 5.9, the Raman spectra are dominated by two vibration bands that are typical of carbonaceous material Raman vibrations: The D band at 1345 cm⁻¹ is assigned to amorphous or disordered carbon within structural defects. As a result of the sp² stretching vibration of graphitic structures, the G band at 1573 cm⁻¹ appears in graphitic samples. In Figure 5.8, the vibration bands at 993, 968, 818, and 775 cm⁻¹ correspond to ν (Mo=O) vibrations, while Mo-O-Mo vibrations appears at 350 cm⁻¹, and that of O-Mo-O is observed at 286 cm⁻¹ and 214 cm⁻¹ (Kazakov et al., 2020). Low intensity peaks at 200-700 cm⁻¹ can be detected in promoted and un-promoted fresh catalysts, corresponding to Fe species typical of α -Fe₂O₃ (Lama et al., 2018). Considering CNTs Raman spectra, the outer and inner diameter of the tubes is determined by

$d = 233.75/w_r$, where w_r is the radial breathing mode (RBM) frequency (cm^{-1}) and d is the tube diameter (nm) (Zhang and Jia, 2013). From Figure 5.8, the RBM frequency is approximately 118 cm^{-1} , and the calculated diameter is 2.0 nm, which is in good agreement with TEM images (Figure 5.6).

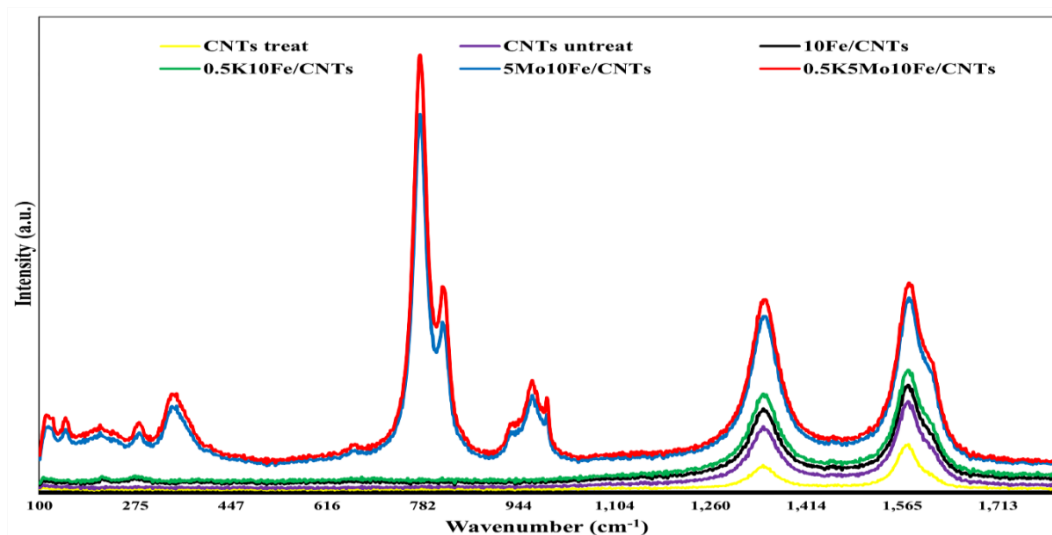


Figure 5.8: Raman spectra of the CNTs support, un-promoted and promoted Fe/CNTs catalysts.

The ratio of D band to G band (I_D/I_G) for CNTs before and after acid treatment together with its unpromoted and promoted Fe/CNTs fresh catalysts are shown in Table 5.9, where D indicates disordered graphitic lattice (i.e., graphene layer edge, A_{1g} symmetry), and greater I_D/I_G indicates more defects on the sample. In the case of 5Mo10Fe/CNTs fresh catalyst, the highest amount of metal dispersion (8.82%) was achieved by CO-chemisorption (Table 5.6), which can be attributed to the significant defects on CNT structure, thus resulting in the highest I_D/I_G of 3.23 in this sample (Table 5.9). The creation of a flawed CNT structure shortens the effective length of the CNT and produces orifices (Fellenberg et al., 2021). More flaws on CNTs, in theory, lead to a stronger metal-support interaction and hence a greater metal particle stability (Duan et al., 2016).

Table 5.9: Raman data for CNTs support, un-promoted, and promoted calcined catalysts.

Sample ID	Peak position (cm ⁻¹)		I_D/I_G
	D-band	G-band	
CNTs-treat.	1343	1576	0.56
CNTs-untreat.	1344	1576	0.89
10Fe/CNTs	1355	1576	0.92
5Mo10Fe/CNTs	1351	1528	3.23
0.5K10Fe/CNTs	1355	1576	0.89
0.5K5Mo10Fe/CNTs	1355	1576	1.02

Despite the existence of D-band and G-band peaks in the Raman pattern of spent catalysts (Figure 5.9), there are some characteristic peaks around 200-300 cm⁻¹ which can be assigned to the iron carbide (Fe₃C) (Wang et al., 2017). Table 5.10 represents the I_D/I_G ratio of the spent catalysts, which varied between 0.87 and 0.97. It should be noted that I_D/I_G of 5Mo10Fe/CNTs decreased from 3.23 to 0.87 after FTS process, which might be related to iron carbide species formation.

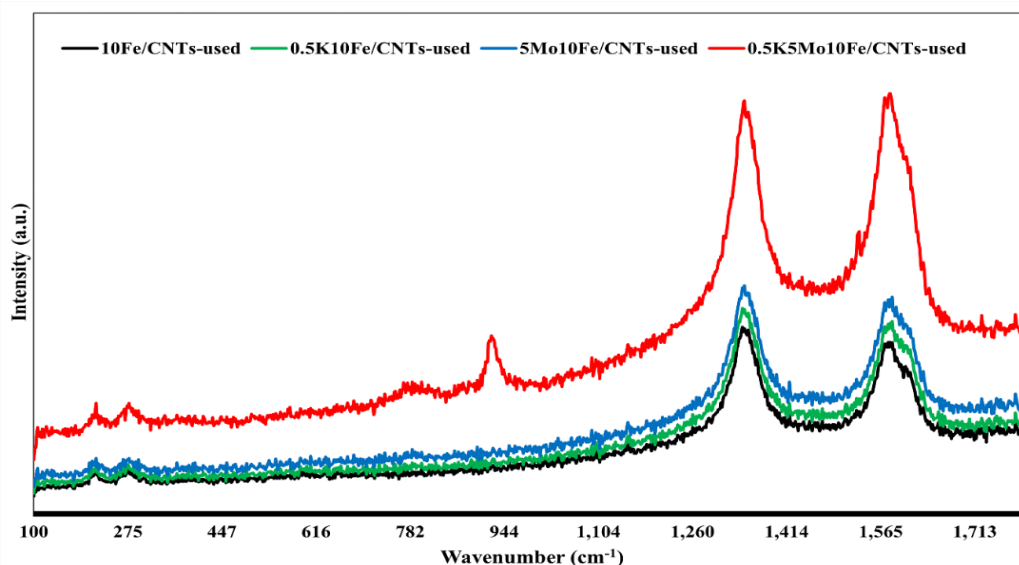
**Figure 5.9:** Raman spectroscopy of the un-promoted and promoted Fe/CNTs spent catalysts.

Table 5.10: Raman data for un-promoted and promoted Fe/CNTs spent catalysts.

Catalyst	Peak position (cm ⁻¹)		I _D /I _G
	D-band	G-band	
10Fe/CNTs	1330	1587	0.90
5Mo10Fe/CNTs	1351	1580	0.87
0.5K10Fe/CNTs	1334	1593	0.90
0.5K5Mo10Fe/CNTs	1330	1587	0.97

CO₂-TPD was used to investigate the effects of Mo and K promoters on the surface basicity of the catalysts. According to TPD profiles (Figure 5.10), addition of Mo as a promoter increased the surface basicity of the catalyst. The peaks at high temperatures (550-700 °C) correspond to desorption of chemically adsorbed CO₂ at strong primary sites (Gong et al., 2020). Peaks at temperatures ranging from 200 to 550 °C are attributed to moderately primary sites (T. Li et al., 2017). The amount of desorbed CO₂ represents the number of primary basic sites, and the higher the temperature of CO₂ desorption is, the stronger the strengths of basic sites are.

The CNTs support consists of moderate primary sites (Lu et al., 2014c). By adding K as a promoter, peaks shifted to lower temperatures, which decreased catalyst basicity. As indicated in Table 5.11, the total quantity of desorbed CO₂ over 10Fe/CNTs and 0.5K10Fe/CNTs (56 mmol/g) are less than that of 0.5K5Mo10Fe/CNTs (148 mmol/g) and 5Mo10Fe/CNTs (175 mmol/g). Comparison of CO₂-TPD results reveals that Mo can increase the number of primary adsorption sites on CNTs-supported iron catalysts. Similar effects has been reported for role of Mn in iron-manganese catalysts (Cheng et al., 2016). In addition, 5Mo10Fe/CNTs catalyst showed the highest CO₂ chemisorption which can be due to higher metal dispersion in Mo-promoted Fe/CNTs catalyst (Table 5.6). In practice, alkali metal ions are usually used to improve the surface basicity of iron catalysts, declining methane production and increasing light olefins' selectivity (Torres Galvis and de Jong, 2013). Nevertheless, alkali promoters exhibit gradual loss during operation, particularly in the presence of water. It has been reported that the basicity of the catalyst is favorable for light olefins' production, which is confirmed by FTS results (Table 5.12) (Gu et al., 2017).

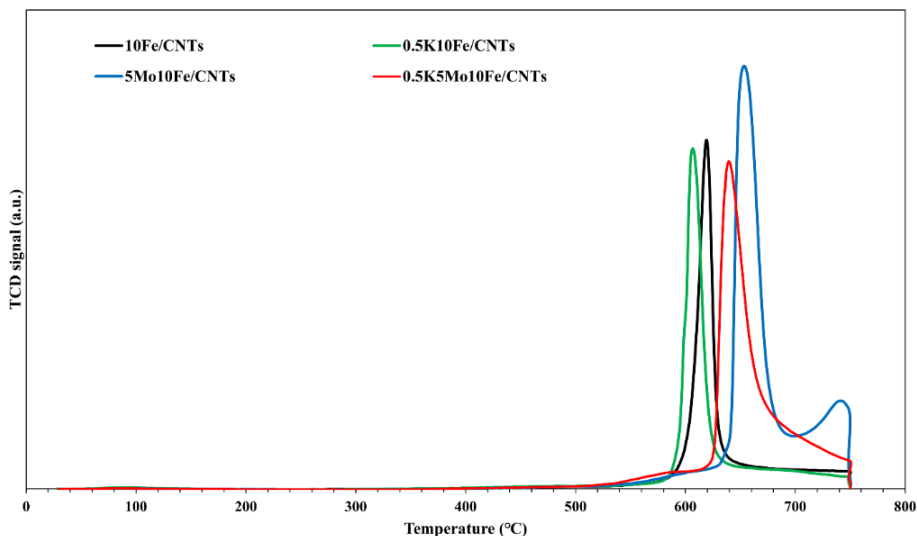


Figure 5.10: CO₂-TPD profiles of the CNTs, un-promoted and promoted Fe/CNTs catalysts.

From Table 5.11, the basicity of K-promoted catalyst is lower than Mo-promoted catalyst which leads to lower C₂-C₄ selectivity. The maximum level of CO₂ desorption which implies the highest basicity is observed in 5Mo10Fe/CNTs. From Table 5.9, 5Mo10Fe/CNTs also exhibits the maximum value of I_D/I_G (3.23). It has been reported that the highest degree of surface defects on the CNTs structure gives rise to maximum CO₂ release (Rinaldi et al., 2010). The large number of defects on 5Mo10Fe/CNTs catalyst facilitates the formation of iron carbide active phases and promotes light olefin selectivity, while lowering FTY (Z. Zhang et al., 2018b).

Table 5.11: Basicity of the CNTs, un-promoted and promoted Fe/CNTs catalysts.

Catalyst	CO ₂ desorption temperature (°C)		Total basicity (mmol CO ₂ g _{cat} ⁻¹)	
10Fe/CNTs	619		56	
0.5K10Fe/CNTs	606		56	
5Mo10Fe/CNTs	653	743	172	3
0.5K5Mo10Fe/CNTs	639		148	

The un-promoted and promoted Fe/CNTs catalysts before and after FTS reaction were characterized by XPS to determine chemical states and composition of Fe, Mo, and K species on the close vicinity of the surface. The XPS spectra were calibrated for the C1s peak at 284.8 eV. In the case of Fe2p, carbon enwrapped iron particles, causing a weak XPS response in the

Fe2p spectrum of spent catalysts (Jiang et al., 2015). The Fe2p high-resolution spectra show two regions around 710 and 723 eV, due to spin-orbit coupling leading to a splitting of the Fe2p_{3/2} and Fe2p_{1/2} transitions, respectively, with a shakeup satellite peak at 719.2 eV (Alayat et al., 2018). The form of the peaks together with the binding energies signify the presence of Fe³⁺ species. Peaks observed for Si2p and Si2s in spent catalysts are comparable to those observed for silica (BE (Si2p) = 101 eV) (Barreca et al., 2007). The XPS data approved the XRD patterns that depicted (α -Fe₂O₃) hematite phase in the un-promoted and promoted calcined catalysts. (Figure 5.11)

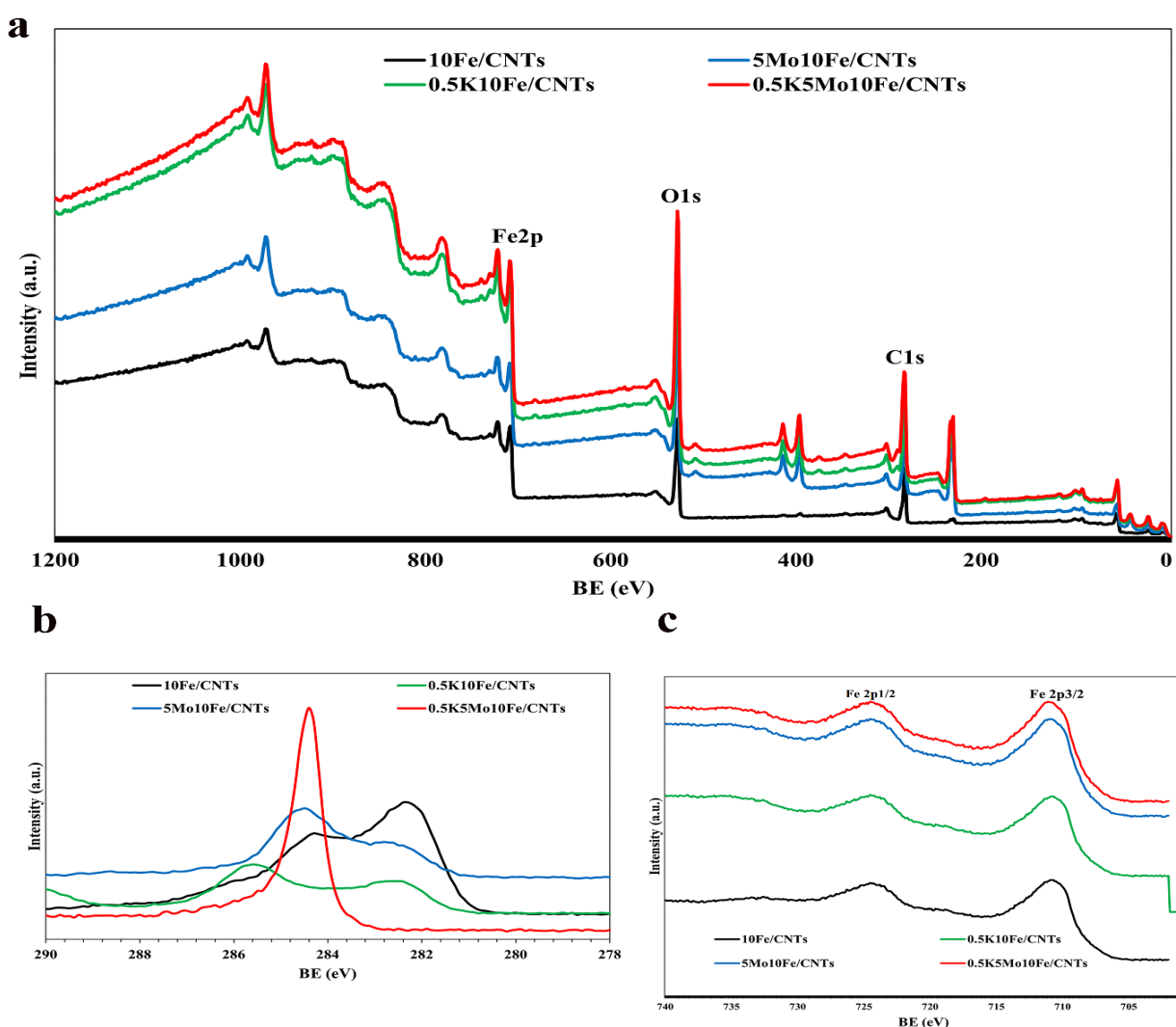


Figure 5.11: (a) Wide XPS survey; (b) C1s; (c) Fe2p of the un-promoted and promoted fresh Fe/CNTs catalysts.

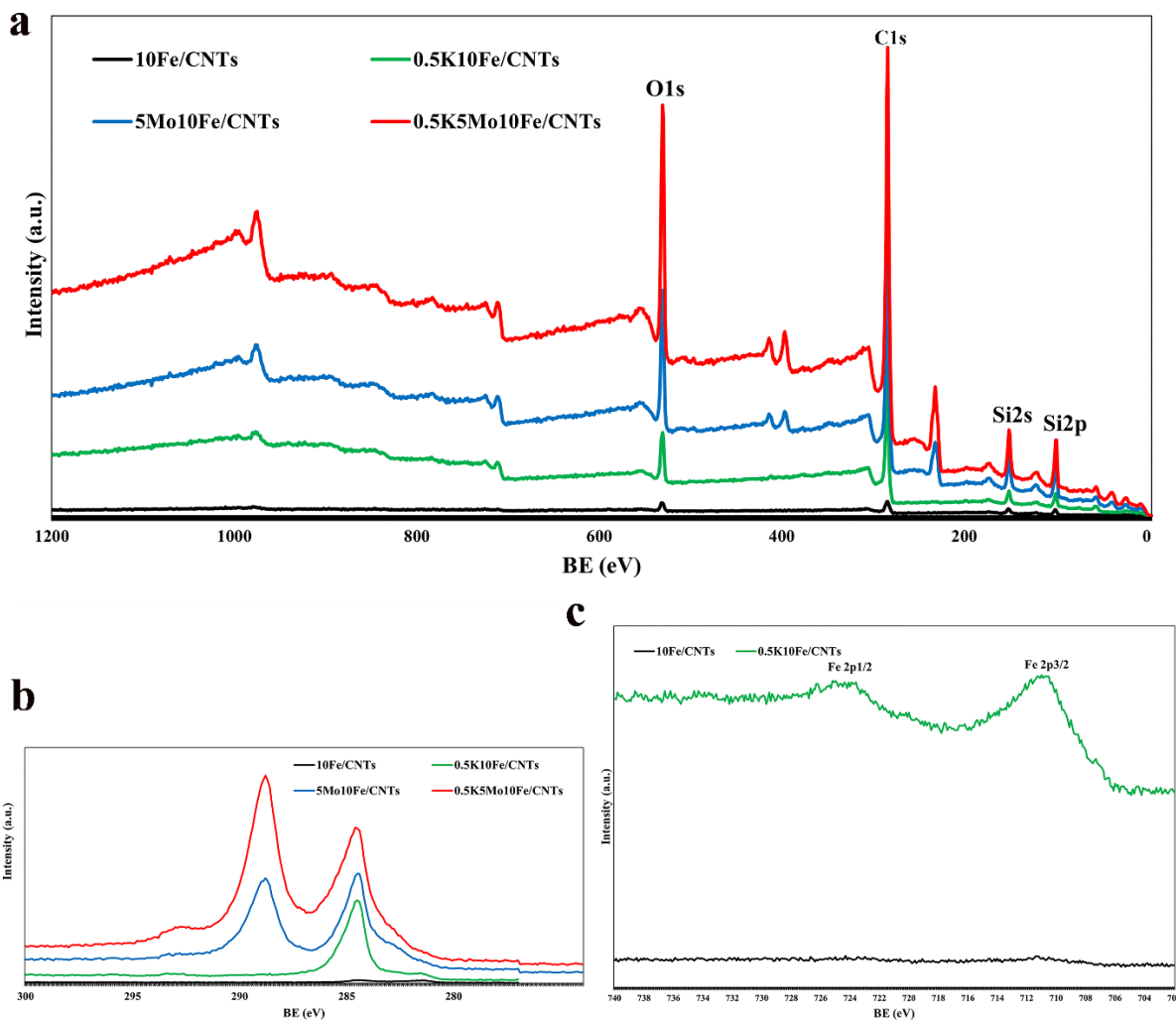


Figure 5.12: (a) Wide XPS survey; (b) C1s; (c) Fe2p of the un-promoted and promoted spent catalysts.

The Fe2p XPS spectrum of the 0.5K10Fe/CNTs catalyst (Figure 5.12 (c)) depicts a similar trend to that of Fe₃C/C catalyst with a shift of 0.5 eV toward lower binding energy. This indicates that adding potassium as a promoter would lead to iron carbide formation (Zhipeng Tian et al., 2019b). Promotion of iron catalysts with alkali metals leads to an increase in the chain length of hydrocarbon products or decrease in production of CH₄. In addition, increase in WGS activity or CO₂ selectivity occurs owing to alkali ions added to iron catalysts (Barrios et al., 2020).

Thermal properties of the calcined Fe/CNTs catalysts were studied applying TGA/DTG under a nitrogen atmosphere (Figure 5.13). 10Fe/CNTs catalyst (Figure 5.13 (a)) showed a total

weight loss of 5 wt% up to 600 °C, while 0.5K5Mo10Fe/CNTs catalyst exhibited a greater weight loss of nearly 11 wt%. Above 400 °C, the weight loss can be related to incomplete calcination and loss of graphitic carbon or CNTs, which corresponded to the DTG exothermic peak at 550 °C (Figure 5.13 (b)). The initial endothermic peaks in the range of 55-100 °C were observed in all catalysts, indicating the loss of adsorbed moisture and dehydration of iron oxyhydroxide (FeOOH) formed by ambient moisture (Peron et al., 2021).

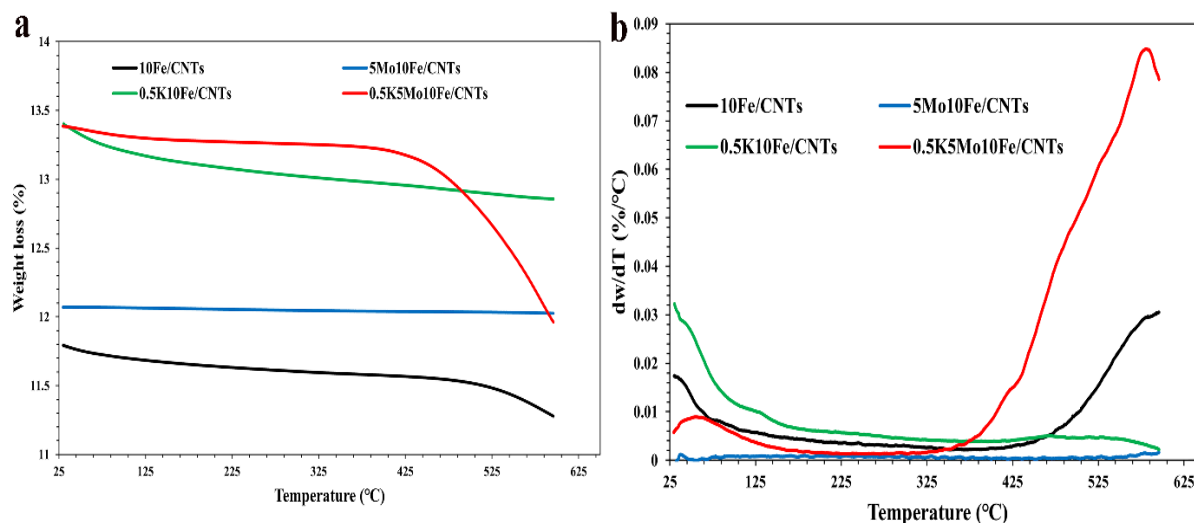


Figure 5.13: (a) TGA; (b) DTG thermograms of un-promoted and promoted fresh catalysts.

5.3.3 Fischer-Tropsch synthesis

As shown in Table 5.12, the catalytic performance data was acquired for 24 h of time-on-stream (TOS) and reached stable condition. Interestingly, potassium-promoted iron catalysts show the maximum CO conversion (96.3%) and FTY (0.01002 mol_{CO}/g_{FeS}). 5Mo10Fe/CNTs catalysts show the maximum iron dispersion (8.8%), while iron time yield (FTY) and CO conversion reached to a minimum of 0.0058 mol_{CO}/g_{FeS} and 60.2% in 24 h, respectively. This is mainly related to suppressing iron oxide reduction and carburization (Qin et al., 2011). The FTY and apparent TOF for Mo-promoted iron catalysts decreased with increasing Fe₅C₂ particle size compared to the un-promoted iron catalyst (Torres Galvis et al., 2012). Comparison of 10Fe/CNTs and 0.5K10Fe/CNTs catalytic performance revealed that promotion with potassium increases olefin to paraffin ratio (2.0 to 2.3), while decreases light olefins selectivity (15.4 to 2.8) (Cheng et al., 2015a).

It has been reported that the higher catalytic activity of 0.5K10Fe/CNTs is related to the positive effect of potassium on the formation of iron carbides. The presence of specific content of potassium enhances the adsorption of syngas on 0.5K10F/CNTs catalyst surface due to the higher rate of electron transfer among iron active sites (Tian et al., 2017). It can be proposed that K in 0.5K10Fe/CNTs catalyst controls the rate of iron carbide formation. It has also been suggested that high potassium content leads to accumulation of carbon on the iron catalyst surface and deactivation (Schulz, 2014). From the literature, TPR/XANES/EXAFS analyses have confirmed that potassium could promote the rate of carburization of Fe/CNTs catalyst. By adding alkali metals, due to an increase in the coverage of dissociatively adsorbed CO the carburization rate increases. From EXAFS Fourier transform magnitude spectra, the reduction/carburization of magnetite to form iron carbides occurs at relatively lower temperatures for potassium promoted Fe catalyst compared with the unpromoted catalyst. Carburized iron-based FTS catalysts are mixtures of Hägg and ϵ -carbides besides Fe_3O_4 . Due to the lower carburization temperature, ϵ -carbide presents as a higher fraction for K-promoted iron catalyst (Ribeiro et al., 2010).

Table 5.12: Catalytic performance of un-promoted and promoted Fe/CNTs catalysts in FTS (T = 280 °C, P = 3.45 MPa, $\text{H}_2/\text{CO} = 1$, GHSV = 2000 h^{-1} , and TOS = 24 h).

Catalysts	FTY $\times 10^{-4}$ ($\text{molCO}_{\text{gFe}}^{-1}\text{s}^{-1}$)	Apparent TOF $\times 10^3$ (s^{-1})	CO conversion (%)	CO ₂ selectivity (%)	Hydrocarbon selectivity (%)				$\text{C}_{2-4}^-/\text{C}_{2-4}^0$
					CH ₄	C_{2-4}^-	C_{2-4}^0	C_5^+	
10Fe/CNTs	92.8	0.85	90.3	59.7	72.0	15.4	7.7	4.8	2.00
5Mo10Fe/CNTs	58.0	0.15	60.2	62.2	56.6	26.9	14.3	2.2	1.88
0.5K10Fe/CNTs	100.2	0.80	96.3	52.3	17.6	2.8	1.2	78.4	2.33
0.5K5Mo10Fe/CNTs	78.7	0.75	71.5	75.2	34.7	49.6	14.3	1.4	3.46

It can be observed that among all promoted and unpromoted catalysts, 0.5K10Fe/CNTs shows the minimum CO₂ selectivity of 52.3% (Table 5.12 in 24 h) and 58.2% (Table 5.13 in 119 h). High carbon dioxide selectivity confirms that catalysts could be functional in direct dissociation of CO which releases O atoms as CO₂, or significantly active products in WGS (Liu et al., 2021). It is noticed that 10Fe/CNTs possesses the highest TOF which is $8.5 \times 10^{-4} \text{ s}^{-1}$, suggesting the electronic effects of K and Mo depend on the intrinsic activity of iron carbide

surface sites. Moreover, the presence of bimetallic promoter Mo/K changes the product selectivity toward light olefins compared with the un-promoted catalyst. For 0.5K5Mo10Fe/CNTs catalyst, the selectivity to methane decreases from 72.0% to 34.7%, while the olefin-to-paraffin (O/P) ratio increases from 2.0 to 3.46. In 5Mo10Fe/CNTs at a carbon monoxide conversion of 60.2%, the light olefins' selectivity reaches 26.9%.

The objective of using structural promoters such as molybdenum is to improve iron dispersion, light olefin selectivity, extent of iron carbidization, and FTS reaction rates. From the literature, it is seen that potassium increases CO dissociation by preserving the carbide phase, which is active for FTS. It is also seen that Mo inhibits the iron active phase formation, which leads to low FTS activity (Martínez del Monte et al., 2019).

In our study, applying potassium (0.5K10Fe/CNTs) led to a lower iron dispersion (2.78%) compared with molybdenum promoted catalyst of 5Mo10Fe/CNTs (8.82%). Figure 5.14 depicts the variations of CO conversion as a function of TOS on monometallic, bimetallic promoted, and unpromoted iron catalysts. According to Figure 5.14, the activity of the 0.5K5Mo10Fe/CNTs catalyst reached its maximum value of 71.5% after 24 h. Afterwards, syngas conversion drops to 60.7% at TOS of 119 h. It can be observed that the CO conversion rate of 5Mo10Fe/CNTs catalyst is lower than 0.5K10Fe/CNTs and 10Fe/CNTs catalysts. The effects of potassium loading on the deactivation of unpromoted, and K-promoted iron catalysts have been investigated. It has been reported by increasing potassium loading, the deactivation rate passes through a minimum.

In addition, by decreasing potassium loading, iron carbides significantly tend to oxidize with TOS which confirms potassium effect on the carburization rates of Fe catalysts. Unpromoted iron catalyst depicted a gradual decrease in the CO conversion with the reaction time. Addition of K slightly increased FTY from $92.8 \times 10^{-4} \text{ mol}_{\text{CO}} \text{ g}_{\text{Fe}}^{-1} \text{ s}^{-1}$ in 10Fe/CNTs to $100.2 \times 10^{-4} \text{ mol}_{\text{CO}} \text{ g}_{\text{Fe}}^{-1} \text{ s}^{-1}$ in 0.5K10Fe/CNTs (Table 5.12). The catalytic performance and deactivation behavior of the 0.5K10Fe/CNTs is similar to the unpromoted iron catalyst (Peron et al., 2021). However, K-promoted iron catalyst (0.5K10Fe/CNTs) results in a slight improvement of the stability in comparison with 10Fe/CNTs. This is mainly related to the formation of Fe_3O_4 and reducing χ - Fe_5C_2 phase with increasing TOS and, increase in stability with potassium loading up to 0.5% (Pendyala et al., 2014). It is suggested that K suppresses H_2 adsorption owing to donating electrons to iron oxide and increasing the electronic charge of metallic atoms. Thus, K promotes

the chain growth reaction and retards the hydrogenation reaction during FTS process. It is also reported that addition of potassium suppressed the oxidation of iron carbides and improved the stability (Wan et al., 2008).

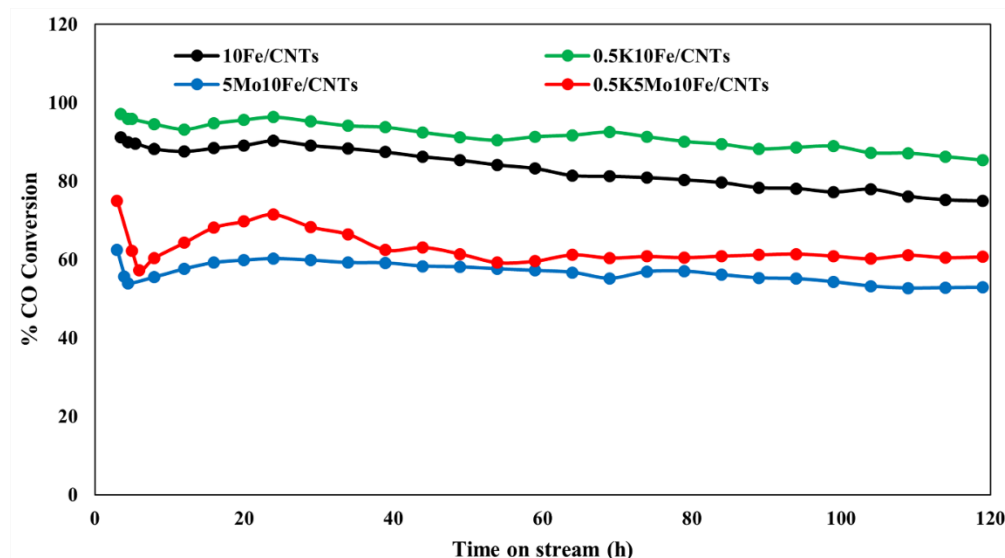


Figure 5.14: CO conversion as a function of TOS for unpromoted and promoted Fe/CNTs catalysts. Operating conditions: $T = 280\text{ }^{\circ}\text{C}$, $P = 3.45\text{ MPa}$, $\text{H}_2/\text{CO} = 1$, $\text{GHSV} = 2000\text{ h}^{-1}$, and $\text{TOS} = 119\text{ h}$.

The promoted and unpromoted Fe/CNTs catalysts were subjected to a 119 h test to evaluate the stability of these catalysts in FTS. As shown in Table 5.13, apparent TOF of all studied catalysts increased after 119 h on stream compared with that of 24 h. From Table 5.13, potassium as a promoter increased the activity of 10Fe/CNTs catalysts from 74.9% to 85.3%. Addition of Mo to the iron catalyst (5Mo10Fe/CNTs) led to a lower activity compared to the unpromoted iron catalyst (10Fe/CNTs). Regarding to H_2 -TPR results (Figure 5.7), addition of molybdenum increases reduction temperatures compared to 10Fe/CNTs resulting in a lower availability of Fe active sites. Moreover, due to high content of molybdenum and partial coverage of Fe active sites, the activity of 5Mo10Fe/CNTs (52.9%) is lower than that of the unpromoted iron catalyst (74.9%) at 119 h (Malek Abbaslou et al., 2011). Likewise, Li et al. reported the average particle sizes of iron oxide reduced by increasing Mo loading which led to FTS activity decline. By increasing Mo loading, dispersion was enhanced, while reduction of hematite to α -Fe was hindered due to the coverage effect of molybdenum. They concluded that high molybdenum loading resulted in the strong interaction between iron and molybdenum which decreased the intrinsic activity of iron active sites (L. Li et al., 2017).

From Table 5.7, the increase in iron particle sizes of the unpromoted catalyst (10Fe/CNTs) shows metal sintering, which is one of the deactivation mechanisms (Gu et al., 2019a). However, Mo-promoted catalysts exhibited a reduction in iron particle sizes. For Mo-promoted catalysts, based on Raman spectroscopy results (Table 5.9), CNTs support demonstrates maximum defect structures, which act as anchoring sites to stabilize Fe nanoparticles against sintering (Duan et al., 2016). In bimetallic promoted Fe/CNTs catalysts, potassium promotion appears to boost CO conversion, while Mo leads to a higher light olefins' selectivity, which finally enhanced light olefins' yield even further. Table 5.13 reveals that it is not possible to have high light olefins' selectivity and high CO conversion concurrently in a catalyst.

Table 5.13: Catalytic performance of un-promoted and promoted Fe/CNTs catalysts in FTS (T = 280 °C, P = 3.45 MPa, H₂/CO = 1, GHSV = 2000 h⁻¹, and TOS = 119 h).

Catalysts	FTY ×10 ⁻⁴ (mol _{CO} g _{Fe} ⁻¹ s ⁻¹)	Apparent TOF×10 ³ (s ⁻¹)	CO conversion (%)	CO ₂ selectivity (%)	Hydrocarbon selectivity (%)				C ₂₋₄ ⁼ /C ₂₋₄ ⁰
					CH ₄	C ₂₋₄ ⁼	C ₂₋₄ ⁰	C ₅ ⁺	
10Fe/CNTs	96.2	2.17	74.9	67.3	75.2	17.2	4.5	3.1	3.82
5Mo10Fe/CNTs	68.2	4.18	52.9	60.3	29.1	37.5	18.3	15.1	2.04
0.5K10Fe/CNTs	109.7	2.13	85.3	58.2	28.3	12.7	4.8	54.2	2.64
0.5K5Mo10Fe/CNTs	78.2	1.74	60.7	71.2	27.1	51.2	13.4	8.3	3.82

5.4 Conclusions

In this study, the effects of potassium and molybdenum as promoters for CNTs supported iron catalysts was investigated in FTS. Applying two-level full factorial design, the promoter mass ratio and iron loading were identified as significant factors. Compared with the monometallic promoted Fe/CNTs catalysts, 0.5K5Mo10Fe/CNTs prepared under the optimum synthesis conditions resulted in the highest olefins' yield. Addition of potassium increases CO conversion, while molybdenum enhances the selectivity to light olefins. Molybdenum as a promoter left structural defects on carbon nanotubes, thus increasing iron dispersion (8.8 %), reduction temperature, and CO₂-desorption temperature in Mo-promoted Fe/CNTs catalysts. Implementing Raman spectroscopy, CO-chemisorption, and H₂-TPR, and CO₂-TPD clearly confirmed our hypothesis.

Moreover, CNT mesoporous structure and FTS active phase of Fe_3C were observed in N_2 adsorption-desorption isotherms and X-ray diffractograms of Fe/CNTs calcined and spent catalysts, respectively. Iron oxide particle size measurements for calcined and spent Fe/CNTs catalysts showed that bimetallic promoters Mo/K helped prevent sintering and agglomeration. Additionally, C1s peak in XPS spectra enhanced by Mo, which might be a sign of molybdenum carbide phase present in spent Mo-promoted Fe/CNTs catalysts. Therefore, molybdenum carbide phase would lower stability of Mo-promoted catalysts due to its atomic size and its interactions with CNTs support. Likewise, FTY and TOF values decrease in the presence of Mo as a promoter, even though adding Mo increases light olefins' selectivity and sintering resistance compared to the un-promoted iron catalyst. Comparison between unpromoted and promoted catalysts revealed that the addition of 0.5 wt% K led to a more stable catalyst.

After finding the most active KMo-promoted Fe/CNTs catalyst formulation, in the next phase kinetic study is conducted to identify the best-fit rate equation for FTS over a wide range of reaction conditions using the optimal KMo-promoted Fe/CNTs catalyst.

CHAPTER 6: Comprehensive Kinetic Study for Fischer-Tropsch Reaction over KMoFe/CNTs Nano-structured Catalyst

The content of this section is submitted to The Canadian Journal of Chemical Engineering, and it was presented at the Canadian Chemical Engineering Conference, Vancouver, October 23-26, 2022.

Contribution of the PhD candidate:

Experiments were designed in consultation with Dr. Philip Boahene, (Postdoc member of the group) and Mr. Tolu Emiola-Sadiq (Ph.D. student of the group) under the supervision of Dr. Ajay K. Dalai and Dr. Lifeng Zhang and executed by Arash Yahyazadeh. Material synthesis, catalysts characterization and data interpretation were performed by Arash Yahyazadeh. The manuscript was drafted by Arash Yahyazadeh with guidance, suggestions, and reviews provided by Dr. Philip Boahene and Dr. Ajay K. Dalai.

Contribution of this chapter to overall PhD research:

The third phase of the research is investigated in this chapter: Kinetic study for Fischer-Tropsch reaction over KMoFe/CNTs nano-structured catalyst. This chapter is the basis of the following chapters.

6.1 Abstract

The kinetics of Fischer-Tropsch (FT) reaction was evaluated through detailed experimentation with KMo bimetallic promoted Fe catalyst supported on carbon nanotubes (CNTs). The kinetic tests were conducted in a fixed-bed reactor under operating conditions ($P = 0.7\text{--}4.1$ MPa, $T = 270\text{--}290$ °C, $H_2/CO = 1$, $GHSV = 2000$ h⁻¹). The present study aimed to investigate the mechanism prevailing in CO activation and rate equation for CO consumption during FT reactions over 0.5K5Mo10Fe/CNTs catalyst. To evaluate the synergistic effects of Fe, Mo, and K phases on the catalyst activity, both fresh and spent catalysts were thoroughly characterized using XRD, XPS, SEM-EDS, XANES, and EXAFS to ascertain the different phases (active sites) present and relevant interactions. Based on the adsorption of carbon monoxide and hydrogen, twenty-two possible mechanisms for monomer formation were proposed for Fischer-Tropsch synthesis in accordance with the Langmuir-Hinshelwood-Hougen-Watson (LHHW) and Eley-Rideal (ER) adsorption theories. The best fit kinetic model

was identified through a multi-variable nonlinear regression analysis. The selected mechanistic model was based on carbide formation approach, where H₂-assisted adsorption of CO was considered for the derivation. Kinetic parameters such as activation energy, adsorption enthalpies of H₂ and CO were estimated to be 65.0, -13.0, and -54.0 kJ/mol, respectively. Based on the developed kinetic model, the effects of reaction temperature and pressure were assessed on FTS product distribution. Additionally, the kinetic model was further compared with the typical Anderson-Schulz-Flory model, suggesting the effects of water-gas-shift and the existence of additional formation pathway such as secondary re-adsorption of olefins for heavier hydrocarbons.

6.2 Materials and methods

6.2.1 Materials

Preparation of the optimal nanocatalyst (0.5%K5%Mo10%Fe/CNTs) used in this phase is presented in section 3.2.4 (Yahyazadeh et al., 2022b). Diverse complementary analytical techniques performed to characterize 0.5K5Mo10Fe/CNTs catalyst are provided in detail in Chapter 3.

6.2.2 Methodology

The experimental schematic of the FTS process is depicted in Figure 6.1. FTS experiment, product sampling, composition analyses, and kinetic studies are described in sections 3.4 to 3.6.

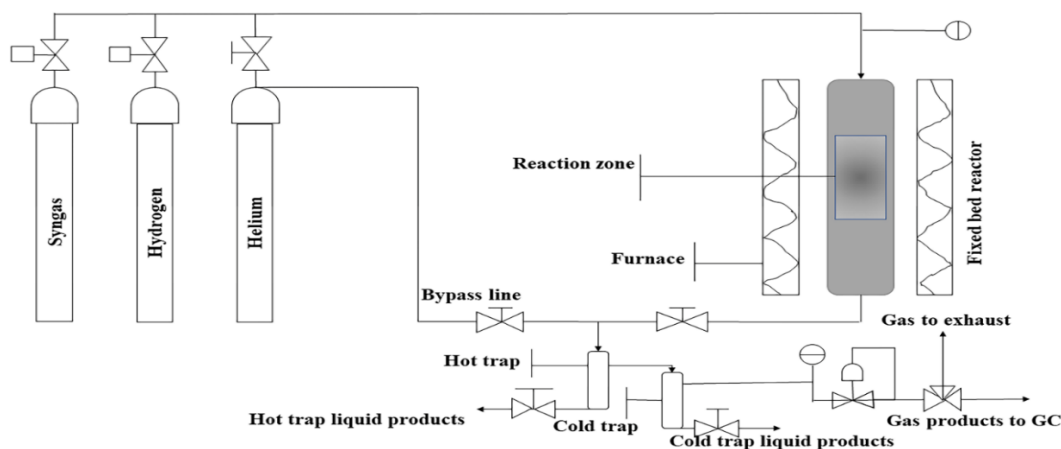


Figure 6.1: Schematic representation of Fischer-Tropsch reaction setup.

The plug flow pattern was considered for the gaseous feed stream and the experimental CO consumption rate was calculated as follows:

$$\frac{W_{cat}}{F_{CO}^0} = \int_{X_{CO,in}}^{X_{CO,out}} \frac{dX_{CO}}{-r_{CO}} = \frac{1}{(-r_{CO})_{avg}} \int_{X_{CO,in}}^{X_{CO,out}} dX_{CO} = \frac{X_{CO,out} - X_{CO,in}}{(-r_{CO})_{avg}} \quad (6-1)$$

$$(-r_{CO})_{avg} = \frac{F_{CO}^0 (x_{CO,out} - x_{CO,in})}{W_{cat}} \quad (6-2)$$

$$-r_{CO} = \frac{X_{CO} F_{CO}^0}{W_{cat}} \quad (6-3)$$

where F_{CO}^0 is the input flow rate of CO (mol/min) and W_{cat} is weight of the catalyst (g_{cat}). It should be noted that the CO conversion was less than 30 mol% for most of the experimental data points (Table 6.1), which could be a reasonable assumption for considering $(-r_{CO})_{avg}$ as a constant over the entire length of the reactor. F_{CO}^0 was obtained as follows:

$$F_{CO}^0 = v_0 C_{CO} = \frac{v_0 P_{CO}}{RT} \quad (6-4)$$

The mass balance for the FTS reaction products is calculated as follow:

$$Mass\ balance = 1 - \left(\frac{m_{C,in} - m_{C,out}}{m_{C,in}} \right) \times 100 \quad (6-5)$$

where $m_{C,in}$ and $m_{C,out}$ denote the mass of input and output carbon (g), respectively.

In the kinetics study, each experiment was performed in triplicate and the average values are reported. To evaluate catalyst activity, catalyst deactivation during the FTS reaction was controlled and kinetic tests reported for a safe period with no deactivation. Regarding our previous optimization study in Chapter 5, the highest yield of light olefins was obtained 35.5% using the optimal bimetallic promoted 0.5K5Mo10Fe/CNTs catalyst at $T = 280^\circ C$, $P_{tot} = 3.4$ MPa, $GHSV = 2000\ h^{-1}$, and $H_2/CO = 1$ for time-on-stream of 24 h (Yahyazadeh et al., 2022b). Therefore, the range of operating conditions for kinetic study were selected based on the optimal catalyst performance. Since the olefin content decreases with the increase in H_2/CO feed ratio (Todic et al., 2016), the H_2/CO feed ratio was considered as a constant value. Fischer-Tropsch synthesis is sensitive to the reaction temperature. As temperature increases the syngas conversion decreases (Øyen et al., 2022). Moreover, the rates of methanation and hydrocarbon chain termination tend to be slower at lower FTS reaction temperature compared to the rate of

CO dissociation (Van Santen et al., 2011). Hence, the kinetic tests were performed in the limited range of temperature (270-290 °C). Table 6.1 shows the experimental data obtained by variation of temperature and pressure within 15 experiments for kinetic study. The kinetic testing conditions are in the following ranges: Temperature = 270-290 °C, pressure = 0.7-4.1 MPa, $H_2/CO = 1$ and GHSV = 2000 h^{-1} .

Table 6.1: The experimental conditions and FTS results for kinetic study at $P_{tot} = 0.7-4.1$ MPa, $T = 270-290$ °C, $H_2/CO = 1$, and GHSV = 2000 h^{-1} in a fixed-bed reactor.

Test no	T (°C)	P_{tot} (MPa)	H_2/CO	P_{CO} (MPa)	P_{H_2} (MPa)	F^0_{CO} (mol/min)	r_{CO} (mol/min g_{cat})	CO conversion (mol%)	Mass balance (%)
1	270	4.1	1	1.1	1.4	0.00484	0.000969288	30.92	98.34
2	275	4.1	1	1.2	1.5	0.00535	0.000892887	25.10	99.12
3	280	4.1	1	1.1	1.4	0.00485	0.000906304	28.73	92.35
4	280	3.8	1	1.0	1.2	0.00436	0.000814502	28.91	97.62
5	280	3.4	1	1.3	1.4	0.00574	0.000689306	18.43	91.45
6	280	3.1	1	1.3	1.4	0.00587	0.000744275	19.75	94.57
7	280	2.8	1	1.3	1.2	0.00544	0.000544521	15.38	90.43
8	280	2.4	1	1.1	1.1	0.00498	0.000564441	17.97	90.11
9	280	2.1	1	1.0	1.0	0.00440	0.000558117	19.38	93.56
10	280	1.7	1	0.9	0.8	0.00374	0.000549474	22.61	92.46
11	280	1.4	1	0.7	0.7	0.00314	0.000503094	24.09	97.72
12	280	1.0	1	0.6	0.5	0.00238	0.000476914	30.39	99.29
13	280	0.7	1	0.4	0.4	0.00160	0.000470613	44.48	99.12
14	285	4.1	1	0.9	1.2	0.00372	0.001324656	53.32	96.25
15	290	4.1	1	0.8	1.2	0.00332	0.001285232	57.97	95.28

For kinetic study, the variation in the superficial velocity and the density of the gas mixture were not taken into consideration in the suggested model. However, Mendez et al. (Miroliaei et al., 2012) investigated the significance of gas density and superficial gas velocity in axial and radial directions for a fixed-bed FTS reactor. The process variables such as density and surface velocity affect the product distribution in FTS (Miroliaei et al., 2012). The estimation of the kinetic parameters through the best-fit model was determined by a multi variable non-

linear regression method, using the Levenberg-Marquardt (LM) algorithm. Typically, the cost functional minimization is the basis of non-linear regression of tracer kinetics models:

$$S(v) = \sum_{i=1}^N (y(i) - S_b(i, v))^2 = \|y - S_b\|_2^2 \quad (6-6)$$

where N and $y = [y(1), \dots, y(N)]^T$ refer to the number of curve points and the measured data. For estimating the optimum $\theta = (f; D_p; D_t)$, the LM algorithm is a common method approximating the Hessian of $S_b(\theta)$. Description of this algorithm is beyond the scope of the present study (Fusco et al., 2015).

The objective function used to optimize the parameters of the kinetic model is as follow:

$$SSR = \sum_{i=0}^{N_{exp}} (r_{i,CO}^{exp} - r_{i,CO}^{mod})^2 \quad (6-7)$$

where N_{exp} corresponds to the total number of experiments. In addition, $r_{i,CO}^{exp}$ and $r_{i,CO}^{mod}$ were assigned to the experimental and calculated CO conversion rates, respectively, considering the corresponding kinetic model in the i^{th} data point.

Three statistical functions including R^2 , $RMSD$ and $MARR$ were employed to estimate the accuracy of the fitted model relative to the experimental data. The R^2 value, known as the nonlinear correlation coefficient using the quantity of variance, was obtained as follows:

$$\sigma = \frac{1}{N_{exp}} \left(\sum_{i,CO}^{N_{exp}} r_{i,CO}^{exp} \right) \quad (6-8)$$

$$R^2 = 1 - \frac{\sum_{i=1}^{N_{exp}} (r_{i,CO}^{exp} - r_{i,CO}^{mod})^2}{\sum_{i=1}^{N_{exp}} (r_{i,CO}^{exp} - \sigma)^2} \quad (6-9)$$

To show the differences between the experimental and the calculated consumption rate of CO, the root mean square deviation ($RMSD$) was used:

$$RMSD = \frac{1}{N_{exp}} \left(\sum_{i=1}^{N_{exp}} (r_{i,CO}^{exp} - r_{i,CO}^{mod})^2 \right)^{1/2} \quad (6-10)$$

The accuracy of different rate models by considering the experimental consumption rates of CO was obtained via mean absolute relative residual ($MARR$) as follows:

$$MARR = \sum_{i=1}^{N_{\text{exp}}} \left| \frac{r_{i,CO}^{\text{exp}} - r_{i,CO}^{\text{mod}}}{r_{i,CO}^{\text{exp}}} \right| \times \frac{1}{N_{\text{exp}}} \times 100 \quad (6-11)$$

6.3 Results and discussion

6.3.1 Catalyst characterization

Considering the kinetics of FTS reaction, it is important to correlate the CO consumption to CO adsorption and $-\text{CH}_2$ -polymerization mechanism. Different active sites of the catalyst are directly related to these effects. The XRD patterns of the calcined and spent KMoFe/CNTs catalysts show iron metal phases (Fe_2O_3) around $2\theta = 40.9^\circ$ (Figure 6.2). The weak peaks attributed to iron oxides suggest high Fe dispersion in calcined and spent catalysts (Cheng et al., 2015b). The two diffraction patterns around $2\theta = 25.8^\circ, 42.4^\circ, 44.3^\circ$, and 77.5° correspond to graphite crystallites related to the lattice plane (0 0 2), (1 0 0), (1 0 1), and (1 1 0), respectively (Kumar et al., 2021). The calcined and spent catalysts display the diffraction peaks at $2\theta = 44^\circ$ which are attributed to $\chi\text{-Fe}_5\text{C}_2$ or $\varepsilon\text{-Fe}_2\text{C}$ (Peron et al., 2021). Iron molybdenum oxide ($\text{Fe}_2(\text{MoO}_4)_3$) peaks reported as the mixture of hematite and molybdenum trioxide can be detected at $2\theta = 13.7^\circ, 15.3^\circ, 20.4^\circ$, and 21.7° (Alayat et al., 2018). MoO_3 and $\text{K}_2\text{Mo}_4\text{O}_{13}$ (potassium molybdenum oxide) peaks were detected at $2\theta = 12.7^\circ, 46.2^\circ, 49.2^\circ, 52.8^\circ, 64.8^\circ, 69.3^\circ$, and $2\theta = 19.4^\circ, 22.9^\circ, 23.3^\circ, 24.9^\circ, 25.6^\circ, 26.5^\circ, 27.3^\circ, 30.2^\circ, 37.5^\circ$, and 38.4° , respectively; thereby, confirming the promoters' presence in the calcined catalyst.

Crystallite phase of molybdenum species did not show a sharp peak in the calcined catalyst even at 5 wt% of molybdenum loading due to the amorphous structure of the molybdenum species (Abbaslou et al., 2011). In the spent catalyst, the diffraction peaks at $2\theta = 34.2^\circ$ and 38.0° correspond to the Mo_2C crystal planes of (1 0 0) and (0 0 2), which indicate the existence of characteristic hexagonal close packed structure of molybdenum carbide (Stalin et al., 2018). Iron oxide in two phases (Fe_3O_4 and FeO) can be observed at $2\theta = 53.7^\circ$ and 60.0° , respectively, in the XRD pattern of the spent catalyst, suggesting the reduction of iron oxide in the catalysts.

The Debye-Scherrer equation was used to measure the average Fe_2O_3 crystallite size of fresh and spent bimetallic promoted catalysts (Table 6.2). From Table 6.2, the average Fe_2O_3 crystallite size in fresh and spent states were 71.2 nm and 34.7 nm, respectively. A structural promoter has been reported to prevent the sintering of $\alpha\text{-Fe}$ during reduction (M. Zhao et al.,

2018b). Due to overlapping of several XRD peaks of iron carbide, measuring the size of crystallites using Debye-Scherrer equation can be underestimated (Peron et al., 2021).

Table 6.2: Average particle size of iron oxide for the fresh and spent catalysts by XRD.

Catalyst	Fe ₂ O ₃ crystallite size (nm)	
	Fresh	Spent
0.5K5Mo10Fe/CNTs	71.2 ± 1	34.7 ± 1

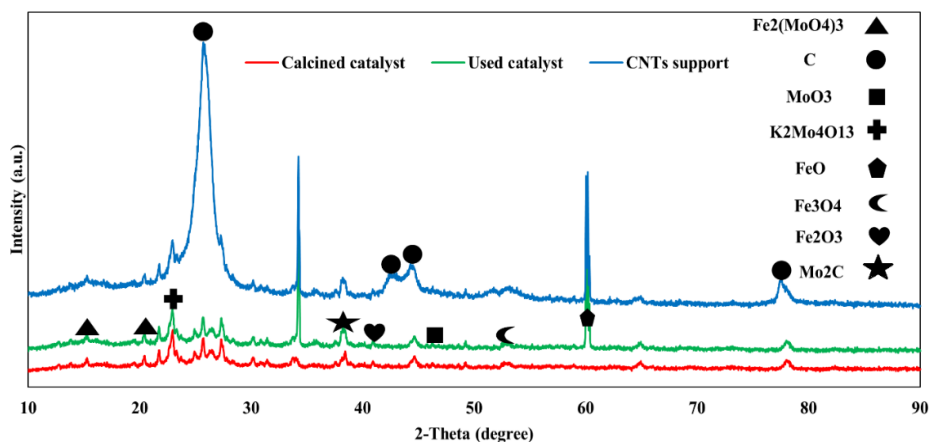


Figure 6.2: XRD pattern of synthesized CNTs with 0.5K5Mo10Fe/CNTs fresh and spent catalysts.

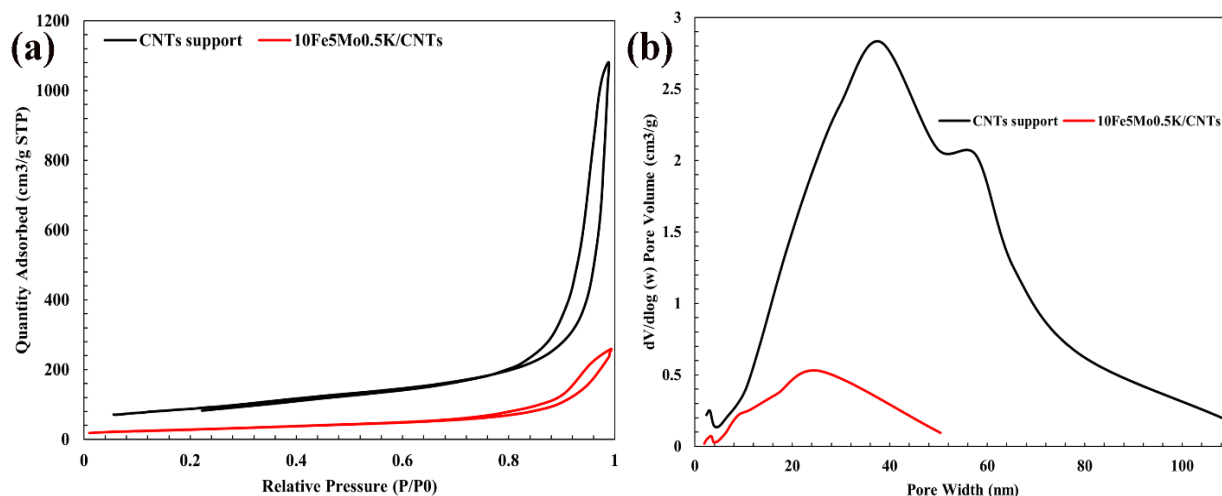
Table 6.3 summarized the physicochemical properties of the support and catalyst used in FTS to produce olefins. The surface area, pore volume and pore diameter of CNTs are 309 m²/g, 1.67 cm³/g and 19.4 nm, respectively. The decrease in surface area and pore diameter of catalyst indicates occupancy of the pore structure of the support due to the metal loadings. Figure 6.3 shows the nitrogen adsorption-desorption isotherms and the BJH desorption pore size distribution plots for both the support (CNTs) and the 0.5K5Mo10Fe/CNTs catalyst. Based on the IUPAC classification for materials, all isotherms correspond to type IV pattern with an H₃-type hysteresis loop, which is typical of mesoporous materials, with a significant volume increase at higher relative pressure in range of $P/P_0 \geq 0.8$. The slight change observed in the shape of the catalyst isotherm compared to that of the pristine CNTs support, suggests a modification in the structure of the carbon support due to metal nanocatalyst incorporation (Díaz et al., 2014).

Table 6.3: Physicochemical properties of the CNTs support and bimetallic promoted catalyst.

Catalyst	Fe content (%) ^a	Mo content (%) ^a	K content (%) ^a	BET surface area (m ² /g) ^b	Total pore volume (cm ³ /g) ^c	Pore diameter (nm) ^c	Metal dispersion (%) ^d
CNTs-Syn	-	-	-	309	1.67	19.4	-
0.5K5Mo10Fe/CNTs-Syn	9.8	4.8	0.6	103	0.40	14.6	2.43

^a Determined by ICP analysis (error $\pm 0.4\%$), ^b Determined by BET method (error $\pm 3\%$), ^c Determined by BJH method (error $\pm 2.5\%$), ^d Determined by CO-chemisorption (error $\pm 1.5\%$)

According to the results presented in Table 6.3, the total pore volume of 0.5K5Mo10Fe/CNTs catalyst decreased after the addition of metal. The decrease in pore volume can be explained by partial pore blockage by metal nanoparticles. The addition of active metals reduced the surface area of CNTs from 309 to 103 m²/g. A broad pore size distribution was observed for all materials, as predicted by BET isotherm analysis.

**Figure 6.3:** (a) Nitrogen adsorption-desorption isotherms; (b) Pore size distribution of CNTs support and 0.5K5Mo10Fe/CNTs fresh catalyst.

The oxidation states of metal species and the functionalized CNTs over calcined and spent 0.5K5Mo10Fe/CNTs catalysts were studied via XPS (Figures 6.4 and 6.5). In spite of weak intensity of the Fe 2p peak, Fe 2p_{3/2} and Fe 2p_{1/2} peaks at 711.5 and 725.1 eV, respectively, can be detected with a satellite peak around 720.8 eV, which corresponds to Fe₂O₃ phase (Huang et al., 2020). Iron carbide (Fe₅C₂) was detected in spent catalyst with a broad peak at a binding energy of 707.05 eV (Figure 6.5(b)) (Gu et al., 2018c). Iron oxide and iron carbide are present

simultaneously in the spent catalyst which can have an important effect on the light olefin selectivity.

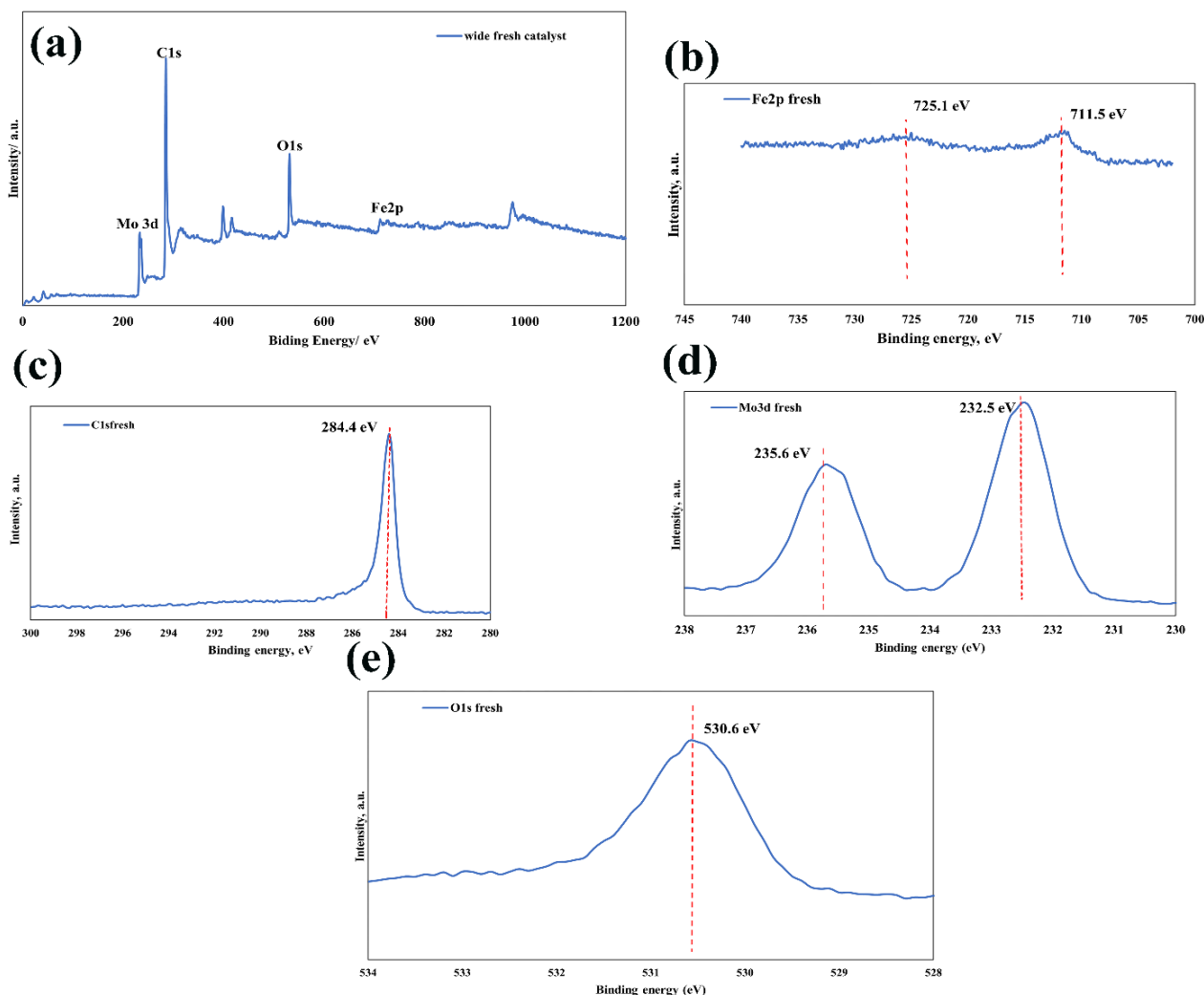


Figure 6.4: XPS spectra of 0.5K5Mo10Fe/CNTs calcined catalyst (a) Full-range scan; (b) Fe2p core level; (c) C1s core level; (d) Mo3d core level; (e) O1s core level.

The C1s XPS spectra of calcined and spent catalysts can be deconvoluted into a variety of components. The peaks at ~ 284 eV and 284.8 eV can be assigned to contributions from the sp^2 -hybridized graphitic surface carbon and defects in the graphitic framework (Oschatz et al., 2017). Interestingly, the peak at ~ 281 eV in the spent catalyst is classified as the metal carbide, indicating the primary intermediate product in the formation of carbon deposition (Zhou et al., 2019). The intensity of molybdenum carbide peaks in spent catalyst obviously increased, suggesting possible deactivation of catalyst. The Mo 3d spectra in calcined catalyst (Figure 6.4

(d)) can be mainly deconvoluted into two peaks, Mo 3d_{5/2} (235.6 eV) and Mo 3d_{5/2} (232.5 eV), illustrating the existence of Mo⁴⁺ in MoO₂ and Mo⁶⁺ in MoO₃ (Diao et al., 2022). The XRD analysis of the calcined catalyst also indicates the presence of MoO₃ phases. It is noted that a small peak at 229.05 eV is due to sulfur contamination, which is declined upon the hydrogen reduction (Toyoshima et al., 2021).

The XPS spectra of O1s for the calcined and spent catalysts are displayed in Figures 6.4 (e) and 6.5 (e). The O1s XPS spectra of the calcined catalyst (Figure 6.4(e)) contribute into two peaks at 532 and 530 eV, which could originate from O-C or O=C, respectively. It has been suggested that interaction between the lattice oxygen and the iron atoms leads to easy transfer of lattice oxygen atoms at low binding energy to the surface of the 0.5K5Mo10Fe/CNTs catalyst (Qu et al., 2014).

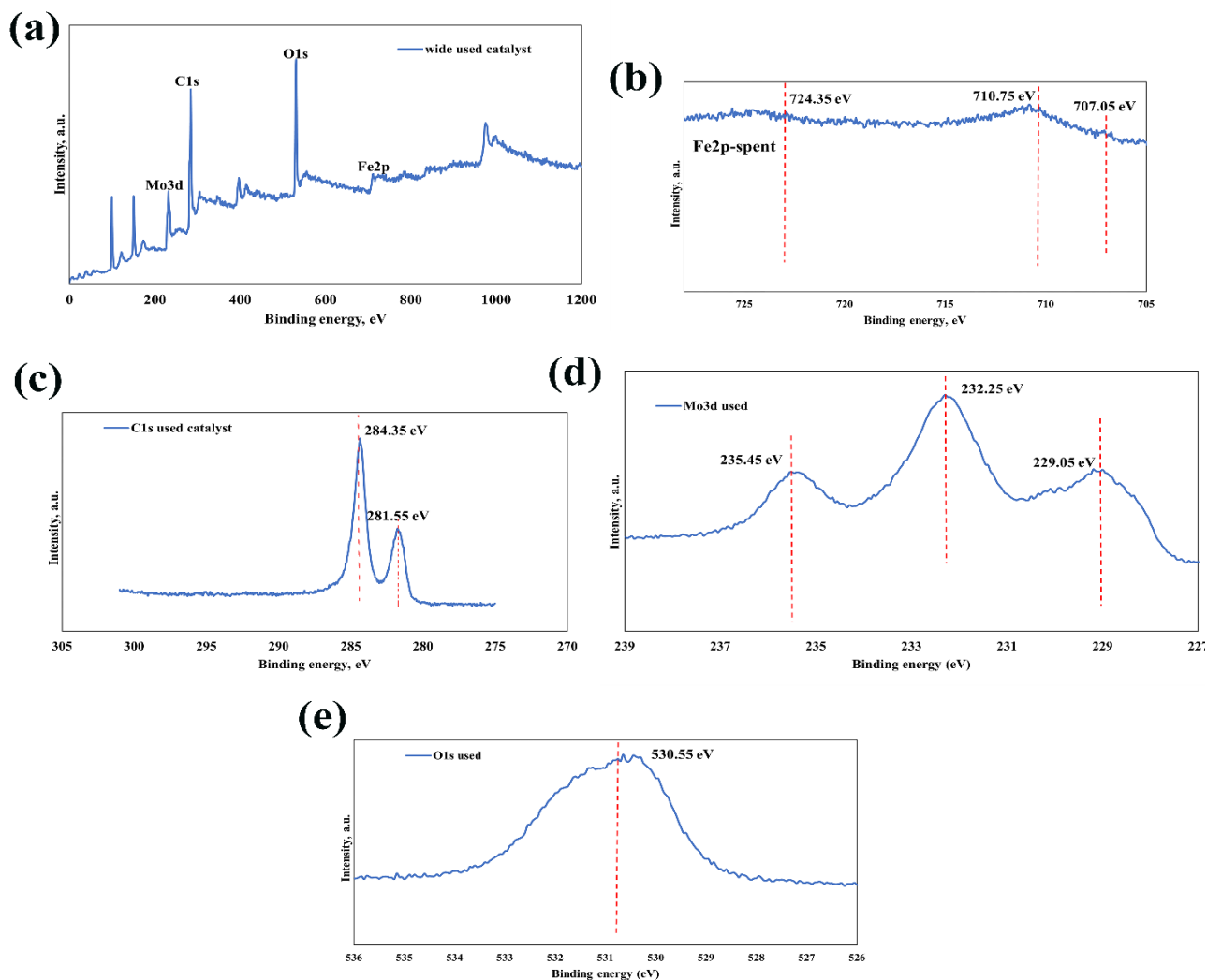


Figure 6.5: XPS spectra of 0.5K5Mo10Fe/CNTs spent catalyst (a) Full-range scan; (b) Fe2p core level; (c) C1s core level; (d) Mo3d core level; (e) O1s core level.

To gain insight into the interaction of supported metal oxide catalysts in heterogeneous catalytic systems, it is important to understand the molecular structure of the surface metal oxide. XANES measurement provides significant information regarding the molecular structure of metal oxide species on the surface of support materials. Owing to the metal interaction, XANES provides information about the symmetry around the molybdenum atom regarding the electronic state of the X-ray absorbing atom and its surroundings at the Mo L3-edge (absorption energy ~ 2500 eV) (Boahene et al., 2022).

In the Fe K-edge XANES spectra of the calcined bimetallic promoted iron catalysts (Figure 6.6), the edge energy resembles the Fe_2O_3 standard (7132 eV), which indicates that Fe_2O_3 is the dominant species after calcination. An electronic transition from 1s to 4p is responsible for the intense peak at ~7132 eV which is a characteristic of $\alpha\text{-Fe}_2\text{O}_3$, indicating a higher oxidation state and is consistent with the XPS results (Cao et al., 2013). The XRD pattern of the calcined catalyst confirmed this result (Figure 6.2). From the Fe K-edge of the calcined 0.5K5Mo10Fe/CNTs, peaks at ~7113 eV, ~7131 eV, and 7137 eV are similar to those of the reference $\text{Fe}_2(\text{MoO}_4)_3$ which is also confirmed by the XRD result (Stehle et al., 2021). After the FTS reaction for 24 h, the absorption edge of the spent catalyst shifts toward lower energy (7130 eV), indicating a reduction of oxidation state of Fe_2O_3 . Differences between Fe foil structure and FeKMo/CNTs catalysts are due to the structural disorder of highly dispersed iron species (Sadykov et al., 2021). There is a similarity between the Fe foil and the Fe K-edge for spent catalysts, which indicates the reduction of Fe (Badoga et al., 2020).

Moreover, most peaks of spent iron-based catalysts were in conformity with Fe_3O_4 , indicating both Fe (II) and Fe (III) phases existed in spent catalysts. Compared to Fe (III), Fe (II) has fewer electrons in its 3d atomic orbital, and the pre-edge peak corresponds to a transition of 1s→3d orbitals. Thus, the low intensity of the pre-edge peak of 0.5K5Mo10Fe/CNTs spent catalyst indicates that the number of electrons of 0.5K5Mo10Fe/CNTs spent catalyst in atomic orbital 3d is less than that of Fe_3O_4 . As a result, the amount of Fe_3O_4 in 0.5K5Mo10Fe/CNTs spent catalyst decreased with more Fe(II) compared with Fe(III) (Lai et al., 2021).

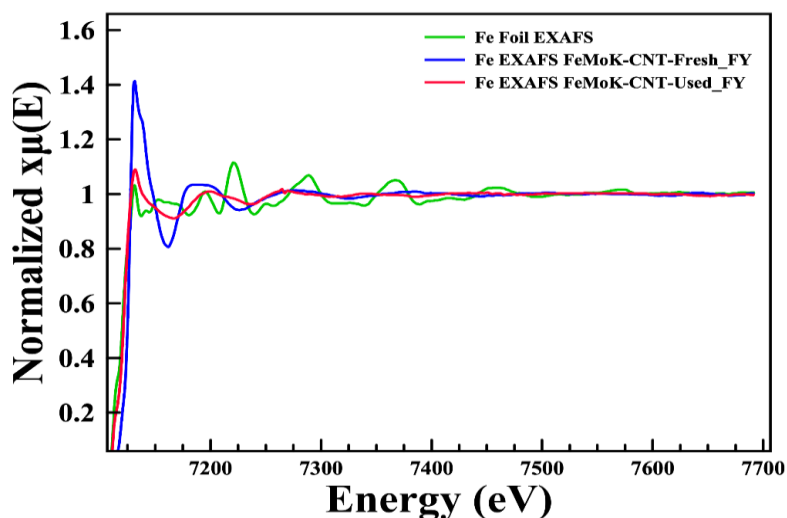


Figure 6.6: Fe K-edge XANES spectra for 0.5K5Mo10Fe/CNTs calcined and spent catalysts by means of fluorescence yield (FY).

Figure 6.7 illustrates the R-space EXAFS results for the Fe K-edge of calcined and spent catalysts. Calcined catalyst exhibits five distinct scattering peaks (1.54, 2.69, 3.10, 3.52, and 3.94 Å), which correspond to α -Fe₂O₃ or γ -Fe₂O₃. The peak at 1.54 Å represents the Fe-O bonding, whereas the peak at 2.69 Å corresponds to the Fe-Fe bond. The bond distance of the Fe-O is shorter than the corresponding bond length in the Fe-Fe, which suggests that the iron oxide particles are smaller (Feng et al., 2020). Together with the XRD pattern, this result indicates that the calcined catalyst has been highly dispersed. As for the 0.5K5Mo10Fe/CNTs spent catalyst, the contributions from 1.59 and 2.80 Å are due to unreduced iron oxide. Nevertheless, the shape and broadening of the peak at 1.59 Å suggests that different iron oxide and iron carbide species coexist, as both Fe-C and Fe-O bonds are relevant to this peak.

It is worth noting that, due to the reduction degree and the content of iron carbides, differences in other peaks have been observed for the spent catalyst which can be identified by the XRD analysis (Chang et al., 2018a). From Figure 6.7, the first sharp peak indicates Fe-Fe for Fe foil and Fe-O for the fresh catalyst. The spent catalyst exhibited both peaks observed for Fe foil and Fe-O (Ma et al., 2019).

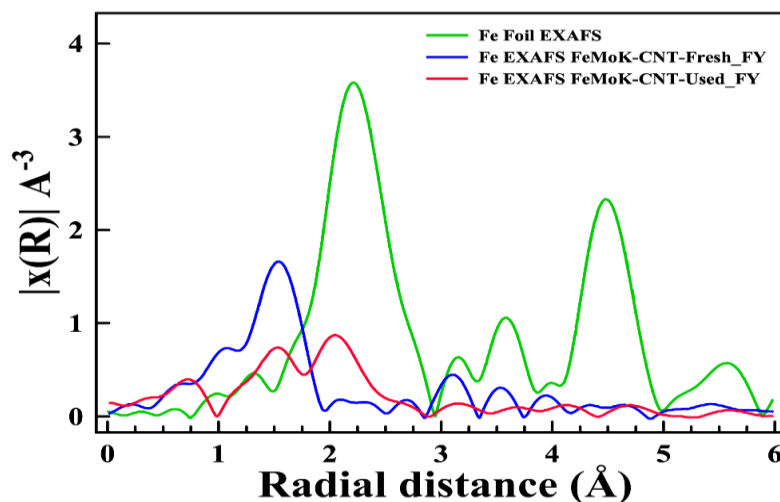


Figure 6.7: Fe K-edge EXAFS spectra in R-space for 0.5K5Mo10Fe/CNTs calcined and spent catalysts by means of fluorescence yield (FY).

To confirm the interaction between Mo and Fe, Mo L-edge XANES spectra of both calcined and spent 0.5K5Mo10Fe/CNTs catalysts were recorded (Figure 6.8). The low amount of Mo loading together with incorporation inside CNTs structure leads to disappearance of Mo_3C in Mo L3-absorption edge EXAFS spectra in R space. Given the valence state of the molybdenum and its electron configuration, the peak near 1.6 Å can be attributed to the chemical interaction between the molybdenum carbide and iron nanoparticles supported on CNTs in the form of Mo-O (K. Zhang et al., 2015).

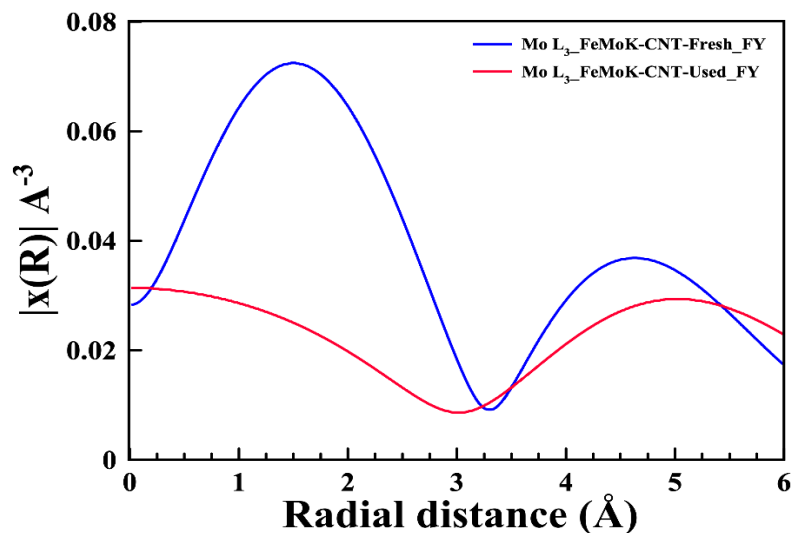


Figure 6.8: Mo L₃-absorption edge EXAFS spectra in R-space for 0.5K5Mo10Fe/CNTs calcined and spent catalysts by means of fluorescence yield (FY).

Iron, molybdenum, and potassium impregnation on CNTs support was qualitatively confirmed through the SEM-EDS and elemental mapping images (Figure 6.9 (a,b)). Figure 6.9 (c,d) shows TEM images of the fresh bimetallic promoted iron catalysts. It is evident that some of the iron oxide particles were effectively dispersed and immobilized on the CNTs support, which could be the result of the CNTs having a high surface area (X. Zhou et al., 2015). However, the clusters above 200 nm can be observed in the fresh promoted catalyst (Figure 6.9 (e)). Mo, K, and Fe were homogenously distributed in the calcined catalyst, as shown in the elemental mapping (Figure 6.9 (b)).

The particle size distribution histograms of iron active sites in the calcined and spent states are shown in Figure 6.9 (e,f). The average Fe active site particle size of the calcined and spent promoted catalysts were 65.1 nm and 32.5 nm, respectively. Regarding Table 6.3 the metal dispersion for the fresh promoted iron catalyst was measured at 2.43%. The iron crystallite size obtained by Debye-Scherrer equation (Table 6.2) for the calcined and spent catalyst were 71.2 nm and 34.7 nm, confirming the TEM histograms of the iron active sites. Comparison of the iron particle sizes in the fresh and spent promoted catalysts reveals that CNTs anchoring sites immobilized the iron particles preventing them from excessive sintering upon reaction (Chew et al., 2016).

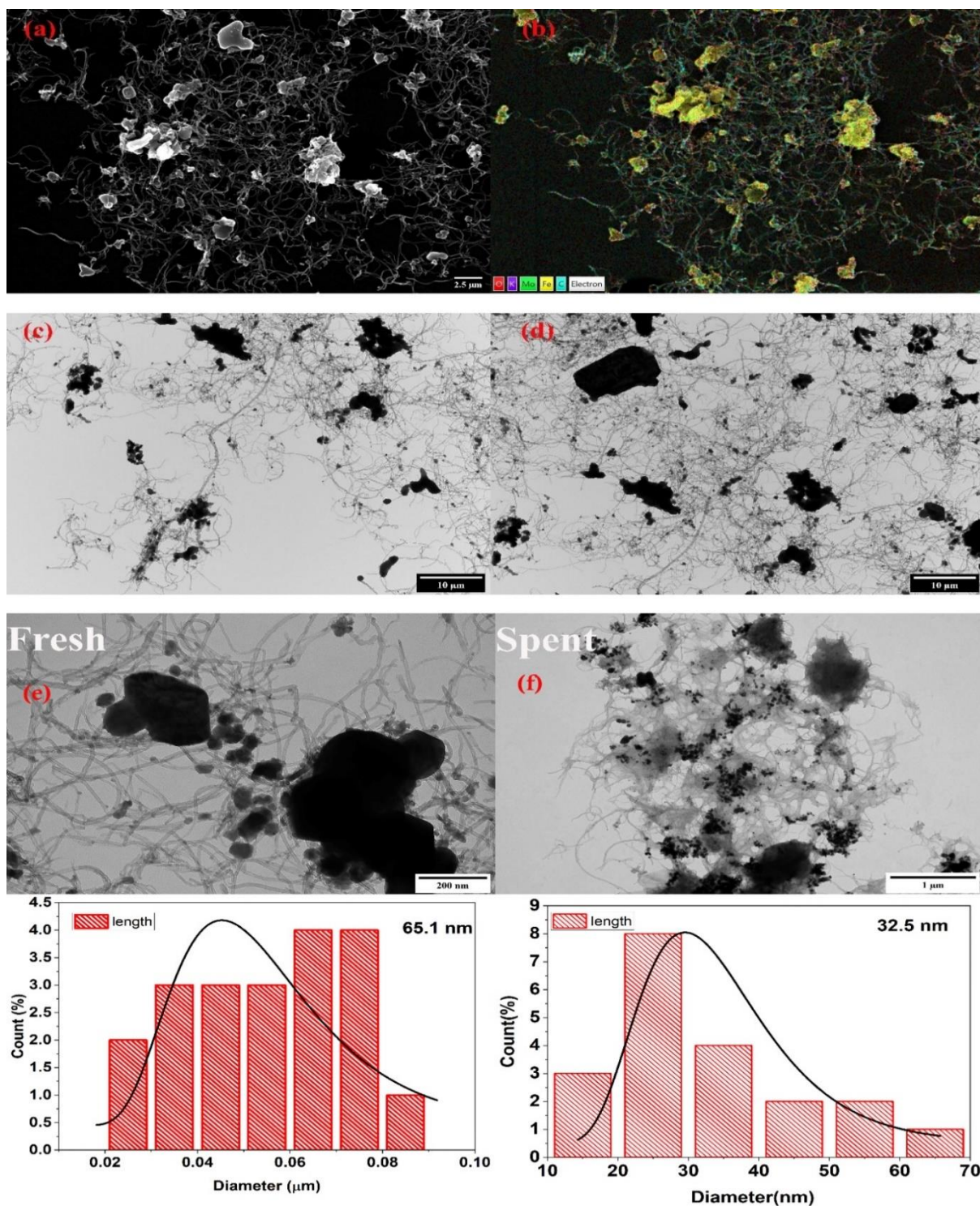


Figure 6.9: (a,b) SEM and elemental mapping of the calcined catalyst; (c,d) TEM images of the calcined catalyst; (e,f) TEM images of the calcined and spent catalyst (0.5K5Mo10Fe/CNTs) with particle size distribution (PSD). PSDs of the catalysts (red boxes) were fitted by a sum of Gaussian functions (black line).

6.3.2 Comprehensive kinetic study

Mass transfer limitation

To study the intrinsic kinetics of FTS, the data must be calculated in the absence of mass transfer restrictions due to their effect on the overall reaction rate. Therefore, they must be ascertained and eliminated before the development of the kinetics study (Eshraghi et al., 2020). Prior to kinetic study, the effects of pore and film mass-transfer resistances were evaluated and eliminated by changing process conditions. To control the external transport resistances, the syngas flow rate was changed with a corresponding change in the catalyst loading, so that a constant GHSV was achieved. Since the resultant CO conversion corresponding to the same GHSV at different flow rates are almost the same (Figure 6.10), it can be concluded that over the range of interested operating conditions, the film resistance is not significant.

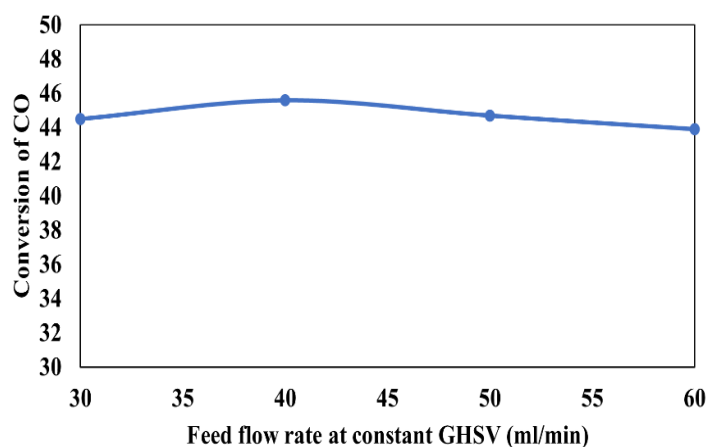


Figure 6.10: CO conversion as a function of the syngas flow rate at $T = 280\text{ }^{\circ}\text{C}$, $P = 4.1\text{ MPa}$, and $\text{GHSV} = 2000\text{ h}^{-1}$.

To investigate the internal diffusion resistance, 1.5 g of the bimetallic promoted catalyst with different sizes, 0.2, 0.4, 0.6, 0.8, and 1.5 mm, was loaded under same operating conditions (Eshraghi et al., 2020). As depicted in Figure 6.11, no pore diffusion was evident for particle size lower than 0.6 mm. Therefore, 0.6 mm was selected as the catalyst particle size for kinetic study. Hence, under the operating conditions used, the internal and external mass-transfer limitations were not significant. Additionally, Eshraghi et al. (Eshraghi et al., 2020) investigated the effects of Fe-based catalyst particle size on the diffusion limitation by measuring the Thiele modulus (ϕ) and effectiveness factor (η). It was suggested that for particle

size below 0.7 mm, the diffusion limitation was negligible due to $\phi < 0.4$ and $\eta = 0.99$. Moreover, gas-solid interphase heat resistance was not considered due to sufficiently small reactor diameter (Hazemann et al., 2020).

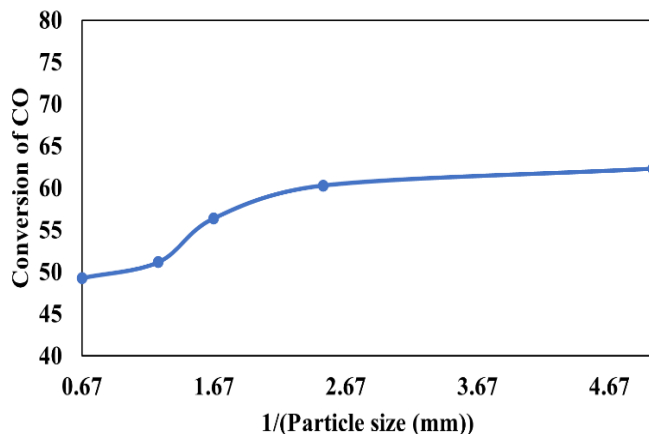


Figure 6.11: CO conversion as a function particle size at $T = 280\text{ }^{\circ}\text{C}$, $P = 4.1\text{ MPa}$, and $\text{GHSV} = 2000\text{ h}^{-1}$.

Kinetic study

To demonstrate the mechanism and rate of reaction, the kinetics of the FTS reaction was investigated by derivation of the rate equation based on mechanistic assumptions. The CO consumption rate depends on CO, H_2 and/or H_2O gas phase concentrations. FTS is a surface polymerization reaction involving reaction between the reagents (CO and H_2), which occurs on the surface of the catalyst. In the first step, reagents form an initiator followed by the formation of FTS products via polymerization condition. Considering three main steps including initiation, propagation, and chain termination, three mechanisms of carbide formation, CO insertion and hydroxycarbene mechanisms are suggested as the main polymerization schemes (Mahmoudi et al., 2017). It is necessary to describe the reaction mechanism to obtain kinetic models. Based on the LHHW and ER adsorption theories, monomer formation for the FT reaction mechanistic schemes have been outlined. Table 6.4 shows 22 different mechanisms based on elementary reactions for FTS.

Table 6.4: Different mechanisms of monomer formation via elementary reactions for FTS.

Model	No	Elementary reactions
FT-I	1	$CO + 2^* \leftrightarrow C^* + O^*$
	2	$H_2 + 2^* \leftrightarrow 2H^*$
	3	$C^* + 4H^* \leftrightarrow CH_2^* + 2H^*$
FT-II	1	$H_2 + * \leftrightarrow H_2^*$
	2	$CO + H_2^* \leftrightarrow CHOH^*$
	3	$CHOH^* + H_2 \leftrightarrow CH_3OH^*$
	4	$CH_3OH^* \leftrightarrow CH_2^* + H_2O$
FT-III	1	$H_2 + * \leftrightarrow H_2^*$
	2	$CO + 2H_2^* \leftrightarrow CH_3OH^*$
	3	$CH_3OH^* \leftrightarrow CH_2^* + H_2O$
FT-IV	1	$H_2 + 2^* \leftrightarrow 2H^*$
	2	$CO + H^* \leftrightarrow COH^*$
	3	$COH^* + H^* \leftrightarrow CH_2OH^* + *$
	4	$CH_2OH^* + H^* \leftrightarrow CH_3OH^* + *$
	5	$CH_3OH^* \leftrightarrow CH_2^* + H_2O$
FT-V	1	$H_2 + 2^* \leftrightarrow 2H^*$
	2	$CO + 2H^* \leftrightarrow CHOH^* + *$
	3	$CHOH^* + H_2 \leftrightarrow CH_3OH^*$
	4	$CH_3OH^* \leftrightarrow CH_2^* + H_2O$
FT-VI	1	$H_2 + 2^* \leftrightarrow 2H^*$
	2	$CO + 4H^* \leftrightarrow CH_3OH^*$
	3	$CH_3OH^* \leftrightarrow CH_2^* + H_2O$
FT-VII	1	$CO + * \leftrightarrow CO^*$
	2	$CO^* + H_2 \leftrightarrow CHOH^*$
	3	$CHOH^* + H_2 \leftrightarrow CH_2^* + H_2O$
FT-VIII	1	$CO + * \leftrightarrow CO^*$
	2	$CO^* + 2H_2 \leftrightarrow CH_3OH^*$
	3	$CH_3OH^* \leftrightarrow CH_2^* + H_2O$
FT-IX	1	$CO + * \leftrightarrow CO^*$
	2	$H_2 + * \leftrightarrow H_2^*$
	3	$CO^* + H_2^* \leftrightarrow CH_2O^* + *$
	4	$CH_2O^* + H_2^* \leftrightarrow CH_3OH^* + *$
	5	$CH_3OH^* \leftrightarrow CH_2^* + H_2O$

FT-X	1	$CO + * \leftrightarrow CO^*$
	2	$H_2 + 2^* \leftrightarrow 2H^*$
	3	$CO^* + H^* \leftrightarrow CHO^* + *$
	4	$CHO^* + H^* \leftrightarrow CHOH^* + *$
	5	$CHOH^* + H^* \leftrightarrow CH_2OH^* + *$
	6	$CH_2OH^* + H^* \leftrightarrow CH_3OH^* + *$
	7	$CH_3OH^* \leftrightarrow CH_2^* + H_2O$
FT-XI	1	$CO + * \leftrightarrow CO^*$
	2	$H_2 + 2^* \leftrightarrow 2H^*$
	3	$CO^* + 2H^* \leftrightarrow CH_2O^* + *$
FT-XII	1	$CO + * \leftrightarrow CO^*$
	2	$H_2 + 2^* \leftrightarrow 2H^*$
	3	$CO^* + 4H^* \leftrightarrow CH_3OH^* + *$
	4	$CH_3OH^* \leftrightarrow CH_2^* + H_2O$
FT-XIII	1	$CO + * \leftrightarrow CO^*$
	2	$CO^* + * \leftrightarrow C^* + O^*$
	3	$C^* + O^* + H_2 \leftrightarrow CH_2^* + O^*$
	4	$CH_2^* + O^* + H_2 \leftrightarrow CH_3OH^* + *$
	5	$CH_3OH^* \leftrightarrow CH_2^* + H_2O$
FT-XIV	1	$CO + * \leftrightarrow CO^*$
	2	$CO^* + * \leftrightarrow C^* + O^*$
	3	$C^* + O^* + 2H_2 \leftrightarrow CH_3OH^* + *$
	4	$CH_3OH^* \leftrightarrow CH_2^* + H_2O$
FT-XV	1	$CO + 2^* \leftrightarrow C^* + O^*$
	2	$C^* + H_2 \leftrightarrow CH_2^* + *$
FT-XVI	1	$CO + 2^* \leftrightarrow C^* + O^*$
	2	$H_2 + * \leftrightarrow H_2^*$
	3	$C^* + O^* + H_2^* \leftrightarrow CH_2^* + O^* + *$
	4	$CH_2^* + O^* + H_2^* \leftrightarrow CH_3OH^* + 2^*$
	5	$CH_3OH^* \leftrightarrow CH_2^* + H_2O$
FT-XVII	1	$CO + 2^* \leftrightarrow C^* + O^*$
	2	$H_2 + * \leftrightarrow H_2^*$
	3	$C^* + H_2^* \leftrightarrow CH_2^* + *$
FT-XVIII	1	$CO + 2^* \leftrightarrow C^* + O^*$
	2	$H_2 + 2^* \leftrightarrow 2H^*$

	3	$C^* + O^* + H^* \leftrightarrow CH_2^*O + 2^*$
	4	$CH_2^*O + 2H^* \leftrightarrow CH_3OH^*$
	5	$CH_3OH^* \leftrightarrow CH_2^* + H_2O$
FT-XIX	1	$CO + 2^* \leftrightarrow C^* + O^*$
	2	$H_2 + 2^* \leftrightarrow 2H^*$
	3	$C^* + H^* \leftrightarrow CH^* + ^*$
	4	$CH^* + H^* \leftrightarrow CH_2^*$
FT-XX	1	$CO + 2^* \leftrightarrow C^* + O^*$
	2	$H_2 + 2^* \leftrightarrow 2H^*$
	3	$C^* + O^* + 2H^* \leftrightarrow CH_2^* + O^* + ^*$
	4	$CH_2^* + O^* + 2H^* \leftrightarrow CH_3OH^* + 2^*$
	5	$CH_3OH^* \leftrightarrow CH_2^* + H_2O$
FT-XXI	1	$CO + 2^* \leftrightarrow C^* + O^*$
	2	$H_2 + 2^* \leftrightarrow 2H^*$
	3	$C^* + 2H^* \leftrightarrow CH_2^* + ^*$
FT-XXII	1	$CO + 2^* \leftrightarrow C^* + O^*$
	2	$H_2 + 2^* \leftrightarrow 2H^*$
	3	$C^* + O^* + 4H^* \leftrightarrow CH_3OH^* + 2^*$
	4	$CH_3OH^* \leftrightarrow CH_2^* + H_2O$

To achieve the rate equation for CO consumption, one step was chosen as the rate determining step (RDS) and other steps were assumed to remain at equilibrium. FT-I model is based on the Langmuir-Hinshelwood-Hougen-Watson (LHHW) model and carbide mechanism. In this model, the reaction between carbon and hydrogen atoms adsorbing on the catalyst surface is considered as the RDS. Following is a definition of the rate equation:

$$C^* + 4H^* \leftrightarrow CH_2^* + 2H^* \quad (6-12)$$

$$-r_{CO-I} = k \cdot \theta_c \cdot \theta_H^4 \quad (6-13)$$

$$\theta_c \cdot \theta_o = b_{CO} \cdot P_{CO} \cdot C_V^2 \quad (6-14)$$

$$b_{CO} = \frac{k_{ads,CO}}{k_{des,CO}} \quad (6-15)$$

$$\theta_c = \theta_o = (b_{CO} \cdot P_{CO})^{0.5} C_V \quad (6-16)$$

wherein b_{CO} corresponds to the equilibrium constant of CO adsorption.



$$k_{ads,H_2} \cdot P_{H_2} \cdot C_V^2 - k_{des,H_2} \cdot \theta_H^2 = 0 \quad (6-18)$$

$$b_{H_2} = \frac{k_{ads,H_2}}{k_{des,H_2}} \quad (6-19)$$

$$\theta_H = (b_{H_2} P_{H_2})^{0.5} C_V \quad (6-20)$$

where b_{H_2} corresponds to the equilibrium constant of H₂ adsorption. In the case of a fixed total number of sites, the concentration of unoccupied active sites (C_V) is calculated based on the site balance:

$$C_V = 1 - \sum_{i=1}^n \theta_i \quad (6-21)$$

Accordingly, θ_i is considered the fraction of adsorption sites occupied by adsorbed species. The assumption is generally made that the oxygen, hydrogen, and carbon species occupy a significant proportion of all sites:

$$C_V + \theta_C + \theta_O + \theta_H = 1 \quad (6-22)$$

The fraction of free active sites is calculated by substituting Eqs. (6-16) and (6-18) into Eq. (6-22):

$$C_V = 1 - (\theta_C + \theta_O + \theta_H) = 1 - \left[2(b_{CO} P_{CO})^{0.5} C_V + (b_{H_2} P_{H_2})^{0.5} C_V \right] \quad (6-23)$$

$$C_V = \frac{1}{\left[1 + 2(b_{CO} P_{CO})^{0.5} + (b_{H_2} P_{H_2})^{0.5} \right]} \quad (6-24)$$

Thus, by substituting Eq. (6-24) in Eqs. (6-16) and (6-18) it can be concluded that the values of θ_C , θ_O , and θ_H are:

$$\theta_C = \theta_O = \frac{(b_{CO} P_{CO})^{0.5}}{\left[1 + 2(b_{CO} P_{CO})^{0.5} + (b_{H_2} P_{H_2})^{0.5} \right]} \quad (6-25)$$

$$\theta_H = \frac{(b_{H_2}P_{H_2})^{0.5}}{\left[1 + 2(b_{CO}P_{CO})^{0.5} + (b_{H_2}P_{H_2})^{0.5}\right]} \quad (6-26)$$

After substituting θ_C , θ_O , and θ_H (Eqs. (6-25) and (6-26)) into the rate equation (Eq. (6-13)), the final form of the rate equation is obtained as follows:

$$-r_{CO} = \frac{k_p \cdot (b_{CO}P_{CO})^{0.5} \cdot (b_{H_2}P_{H_2})^2}{(1 + 2(b_{CO}P_{CO})^{0.5} \cdot (b_{H_2}P_{H_2})^{0.5})^5} \quad (6-27)$$

where P_{H_2} and P_{CO} are the partial pressures of H_2 and CO with assumptions based on ideal gas. The rate equations for the other mechanisms in Table 6.4 were also calculated using the same approach (Table 6.5).

Table 6.5: CO consumption rate equations for different mechanisms.

Model	Rate equation	Equation
FT-I RDS3	$-r_{CO} = \frac{k_p (b_{CO}P_{CO})^{0.5} (b_{H_2}P_{H_2})^2}{(1 + 2(b_{CO}P_{CO})^{0.5} + (b_{H_2}P_{H_2})^{0.5})^5}$	(6-27)
FT-II RDS2	$-r_{CO} = \frac{k_p P_{CO} b_{H_2} P_{H_2}}{1 + b_{H_2} P_{H_2}}$	(6-28)
RDS1	$-r_{CO} = \frac{k_{H_2} b_{H_2} P_{H_2}}{1 + b_{H_2} P_{H_2}}$	(6-29)
FT-III RDS2	$-r_{CO} = \frac{k_p P_{CO} (P_{H_2} b_{H_2})^2}{(1 + b_{H_2} P_{H_2})^2}$	(6-30)
FT-IV RDS2	$-r_{CO} = \frac{k_p P_{CO} (b_{H_2} P_{H_2})^{0.5}}{1 + (b_{H_2} P_{H_2})^{0.5}}$	(6-31)
RDS1	$-r_{CO} = \frac{k_{H_2} b_{H_2} P_{H_2}}{(1 + (b_{H_2} P_{H_2})^{0.5})^2}$	(6-32)
FT-V RDS2	$-r_{CO} = \frac{k_p P_{CO} b_{H_2} P_{H_2}}{(1 + (b_{H_2} P_{H_2})^{0.5})^2}$	(6-33)
FT-VI RDS2	$-r_{CO} = \frac{k_p P_{CO} (b_{H_2} P_{H_2})^2}{(1 + (b_{H_2} P_{H_2})^{0.5})^4}$	(6-34)

FT-VII RDS2	$-r_{CO} = \frac{k_p b_{CO} P_{CO} P_{H_2}}{1 + (b_{CO} P_{CO})}$	(6-35)
RDS1	$-r_{CO} = \frac{k_{CO} b_{CO} P_{CO}}{1 + (b_{CO} P_{CO})}$	(6-36)
FT-VIII RDS2	$-r_{CO} = \frac{k_p b_{CO} P_{CO} P_{H_2}^2}{1 + b_{CO} P_{CO}}$	(6-37)
FT-IX RDS3	$-r_{CO} = \frac{k_p b_{CO} P_{CO} b_{H_2} P_{H_2}}{(1 + b_{CO} P_{CO} + b_{H_2} P_{H_2})^2}$	(6-38)
RDS1	$-r_{CO} = \frac{k_{CO} b_{CO} P_{CO}}{1 + b_{CO} P_{CO} + b_{H_2} P_{H_2}}$	(6-39)
RDS2	$-r_{CO} = \frac{k_{H_2} b_{H_2} P_{H_2}}{1 + b_{H_2} P_{H_2} + b_{CO} P_{CO}}$	(6-40)
RDS1,2	$-r_{CO} = \frac{k_{CO} b_{CO} P_{CO} + k_{H_2} b_{H_2} P_{H_2}}{1 + b_{CO} P_{CO} + b_{H_2} P_{H_2}}$	(6-41)
FT-X RDS3	$-r_{CO} = \frac{k_p b_{CO} P_{CO} (b_{H_2} P_{H_2})^{0.5}}{(1 + b_{CO} P_{CO} + (b_{H_2} P_{H_2})^{0.5})^2}$	(6-42)
RDS1	$-r_{CO} = \frac{k_{CO} b_{CO} P_{CO}}{1 + b_{CO} P_{CO} + (b_{H_2} P_{H_2})^{0.5}}$	(6-43)
RDS2	$-r_{CO} = \frac{k_{H_2} b_{H_2} P_{H_2}}{(1 + b_{CO} P_{CO} + (b_{H_2} P_{H_2})^{0.5})^2}$	(6-44)
RDS1,2	$-r_{CO} = \frac{k_{CO} b_{CO} P_{CO} + k_{H_2} b_{H_2} P_{H_2} (1 + b_{CO} P_{CO} + (b_{H_2} P_{H_2})^{0.5})}{(1 + b_{CO} P_{CO} + (b_{H_2} P_{H_2})^{0.5})^2}$	(6-45)
FT-XI RDS2	$-r_{CO} = \frac{k_p b_{CO} P_{CO} (b_{H_2} P_{H_2})}{(1 + b_{CO} P_{CO} + (b_{H_2} P_{H_2})^{0.5})^3}$	(6-46)
FT-XII RDS3	$-r_{CO} = \frac{k_p b_{CO} P_{CO} (b_{H_2} P_{H_2})^2}{(1 + b_{CO} P_{CO} + (b_{H_2} P_{H_2})^{0.5})^5}$	(6-47)
FT-XIII RDS3	$-r_{CO} = \frac{k_p b_{CO} P_{CO} P_{H_2}}{(1 + 2(b_{CO} P_{CO})^{0.5})^2}$	(6-48)
RDS1	$-r_{CO} = \frac{k_{CO} b_{CO} P_{CO}}{(1 + 2(b_{CO} P_{CO})^{0.5})^2}$	(6-49)

FT-XIV	$-r_{CO} = \frac{k_p b_{CO} P_{CO} P_{H_2}^2}{(1 + 2(b_{CO} P_{CO})^{0.5})^2}$	(6-50)
FT-XV RDS2	$-r_{CO} = \frac{k_p P_{H_2} (b_{CO} P_{CO})^{0.5}}{1 + 2(b_{CO} P_{CO})^{0.5}}$	(6-51)
FT-XVI RDS3	$-r_{CO} = \frac{k_p b_{CO} b_{H_2} P_{CO} P_{H_2}}{(1 + 2(b_{CO} P_{CO})^{0.5} + b_{H_2} P_{H_2})^3}$	(6-52)
RDS1	$-r_{CO} = \frac{k_{CO} b_{CO} P_{CO}}{(1 + 2(b_{CO} P_{CO})^{0.5} + (b_{H_2} P_{H_2}))^2}$	(6-53)
RDS2	$-r_{CO} = \frac{k_{H_2} b_{H_2} P_{H_2}}{1 + 2(b_{CO} P_{CO})^{0.5} + b_{H_2} P_{H_2}}$	(6-54)
RDS1,2	$-r_{CO} = \frac{k_{CO} b_{CO} P_{CO} + k_{H_2} b_{H_2} P_{H_2} (1 + 2(b_{CO} P_{CO})^{0.5} + b_{H_2} P_{H_2})}{(1 + 2(b_{CO} P_{CO})^{0.5} + b_{H_2} P_{H_2})^2}$	(6-55)
FT-XVII RDS3	$-r_{CO} = \frac{k_p b_{H_2} P_{H_2} (b_{CO} P_{CO})^{0.5}}{(1 + 2(b_{CO} P_{CO})^{0.5} + b_{H_2} P_{H_2})^2}$	(6-56)
FT-XVIII RDS3	$-r_{CO} = \frac{k_p b_{CO} P_{CO} (b_{H_2} P_{H_2})^{0.5}}{(1 + 2(b_{CO} P_{CO})^{0.5} + (b_{H_2} P_{H_2})^{0.5})^3}$	(6-57)
FT-XIX RDS3	$-r_{CO} = \frac{k_p (b_{CO} P_{CO})^{0.5} (b_{H_2} P_{H_2})^{0.5}}{(1 + 2(b_{CO} P_{CO})^{0.5} + (b_{H_2} P_{H_2})^{0.5})^2}$	(6-58)
FT-XX RDS3	$-r_{CO} = \frac{k_p b_{CO} P_{CO} (b_{H_2} P_{H_2})}{(1 + 2(b_{CO} P_{CO})^{0.5} + (b_{H_2} P_{H_2})^{0.5})^4}$	(6-59)
FT-XXI RDS3	$-r_{CO} = \frac{k_p (b_{CO} P_{CO})^{0.5} b_{H_2} P_{H_2}}{(1 + 2(b_{CO} P_{CO})^{0.5} + (b_{H_2} P_{H_2})^{0.5})^3}$	(6-60)
RDS1	$-r_{CO} = \frac{k_{CO} b_{CO} P_{CO}}{(1 + 2(b_{CO} P_{CO})^{0.5} + (b_{H_2} P_{H_2})^{0.5})^2}$	(6-61)
RDS2	$-r_{CO} = \frac{k_{H_2} b_{H_2} P_{H_2}}{(1 + 2(b_{CO} P_{CO})^{0.5} + (b_{H_2} P_{H_2})^{0.5})^2}$	(6-62)
RDS1,2	$-r_{CO} = \frac{k_{CO} b_{CO} P_{CO} + k_{H_2} b_{H_2} P_{H_2}}{(1 + 2(b_{CO} P_{CO})^{0.5} + (b_{H_2} P_{H_2})^{0.5})^2}$	(6-63)
FT-XXII RDS3	$-r_{CO} = \frac{k_p b_{CO} P_{CO} (b_{H_2} P_{H_2})^2}{(1 + 2(b_{CO} P_{CO})^{0.5} + (b_{H_2} P_{H_2})^{0.5})^6}$	(6-64)

In addition, kinetic (k_p) and adsorption (b_{CO} and b_{H2}) constants were determined using the Arrhenius (Eq. 6-65) and Van't Hoff (Eq. 6-66) laws, respectively.

$$K_p(T) = K_{0i} \exp\left(\frac{-E}{RT}\right) \quad (6-65)$$

$$b_j(T) = b_{0j} \exp\left(\frac{-\Delta H_j}{RT}\right) \quad (6-66)$$

Accordingly, the values of partial pressure of the reactants were fitted on the FT-I to FT-XXII rate equations (Eqs. 6-27 to 6-64) to estimate their kinetic parameters. Applying multi-variable nonlinear regression, each of the rate equations (Eqs. 6-27 to 6-64) together with Arrhenius (Eq. 6-65) and Van't Hoff (Eq. 6-66) equations were solved, and models' parameters were calculated. A kinetic model must obey physicochemical laws. Therefore, the parameters of the derived kinetic model must follow physicochemical limitations ($k_{0,i}$, $b_{0,i}$, $E_i > 0$ and $\Delta H_i < 0$) (Todic et al., 2013).

Statistical criteria such as R^2 , $RMSD$, σ , and $MARR$ were used to evaluate the precision of the kinetic models using Eqs. 6-8 to 6-11. The total number of experiments is given by N_{exp} . FT-I model based on the Langmuir-Hinshelwood-Hougen-Watson (LHHW) model and carbide mechanism obtained the best match with the experimental data compared to other mechanisms. As seen from Table 6.6, the value of R^2 for FT-I is close to unity while the $RMSD$ value is negligible which is acceptable. Figures 6.12 and 6.13 show a comparison between the mechanistic (Eq. 6-27) and experimental (Eq. 6-3) CO consumption rates obtained by 15 different experimental conditions (Table 6.1) for kinetic study.

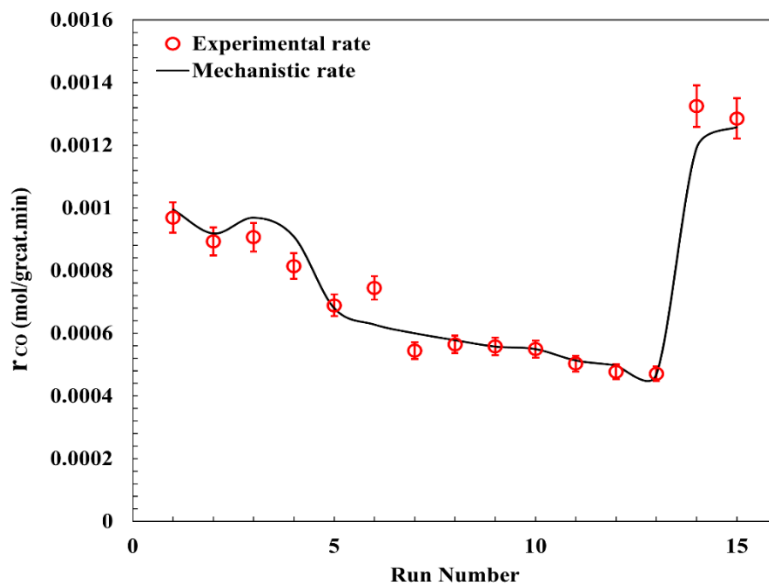


Figure 6.12: Comparison of the experimental and mechanistic CO consumption rates over 0.5K5Mo10Fe/CNTs catalyst in FTS.

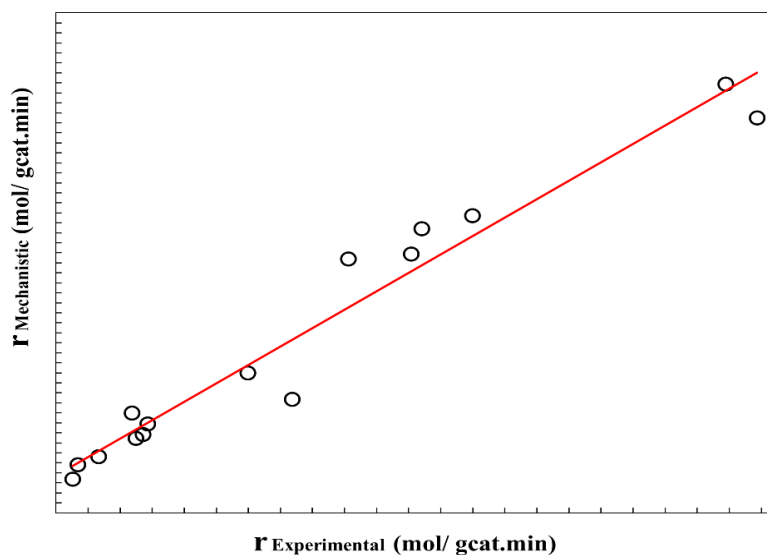


Figure 6.13: The mechanistic CO consumption rates versus experimental CO consumption rates using 0.5K5Mo10Fe/CNTs catalyst in FTS.

The results for experimental CO consumption rate fitted well with FT-I mechanistic model (Eq. 6-27) with $MARR < 16\%$. From Table 6.6, the FT-I model had an activation energy of 65.0 kJ/mol for the FT catalytic process. The corresponding activation energies for various catalysts in FTS have been reported in the range of 30 to 132 kJ/mol (Sarkari et al., 2014). Since the

physicochemical properties of the catalyst influence the adsorption of species in the reaction, the preparation method of the catalyst impacts the kinetic parameters using the LHHW kinetic models (Nikparsa et al., 2015). The value of activation energy demonstrates that the FT reactions are not limited by intraparticle diffusion resistances. In general, the mass diffusion limitations play a dominant role in enhancement of hydrocarbon selectivity through gas hourly space velocity (Sari et al., 2009). Carbon monoxide has a higher adsorption enthalpy than hydrogen because it adsorbs at the catalyst surface more strongly (Botes and Breman, 2006). Adsorption enthalpies for CO and H₂ ranged from -50 to -200 kJ/mol and -10 to -100 J/mol, respectively (Vannice, 1975). Table 6.7 summarized kinetic results of some studies compared with the present work. The results confirmed that the activation energy was close to those found in the literature.

Table 6.6: Kinetic parameters and their values for the FT-I kinetic model.

Parameter	Value	Dimension
k_0	4.61E+09	mol/min.g
E_a	65.00	kJ/mol
ΔH_{H_2}	-13.00	kJ/mol
ΔH_{CO}	-54.00	kJ/mol
b_{0,H_2}	1.72E-04	mol/min.g
$b_{0,CO}$	4.91	mol/min.g
R^2	9.53E-01	-
$RMSD$	1.68E-16	-
$MARR$ (%)	1.53E+01	-
σ	7.53 E-04	-
SSR	5.02E-08	-

Table 6.7: Summary of several FTS kinetic studies on Fe catalysts compared with this study.

Catalyst	Operating conditions	Kinetic equation	Kinetic parameters	Reference
Fe-Mn/Al ₂ O ₃	T= 240-270 °C, P= 0.1-1.2 MPa, GHSV= 4200-7000 h ⁻¹	$-r_{CO} = \frac{k_{FT} P_{CO} P_{H_2}}{P_{CO} + k_{H_2O} P_{H_2O}}$	E _a = 59.8 kJ/mol MARR= 19.39%	(Sarkari et al., 2014)
Fe-Cu/SiO ₂	T= 230-270 °C, P= 2 MPa, GHSV= 6000 h ⁻¹	$-r_{CO} = \frac{AP_{CO} P_{H_2}^{3/4}}{(1 + BP_{CO})^2}$	E _a = 83.0 kJ/mol MARR= 28.0%	(Sun et al., 2017b)
K/Fe-Cu-Mn-Al ₂ O ₃	T= 230-250 °C, P= 0.2-1 MPa, GHSV= 3000 h ⁻¹	$r_i = k_i \exp\left(-\frac{E_i}{RT}\right) P_{H_2}^{m_i} P_{CO}^{n_i}$	E _a = 52.0 kJ/mol MARR= 25.0%	(Park et al., 2014)
Fe-Co	T= 200-280 °C, P= 1-3 MPa, GHSV= 1800-6600 h ⁻¹	$r_{FT} = \frac{k P_{CO} P_{H_2}}{P_{H_2O} (1 + a P_{CO} + b P_{H_2}^2)^3}$	E _a = 94.8 kJ/mol MARR= 35.63%	(Sonal et al., 2017)
Fe-Ni/Al ₂ O ₃	T= 220-270 °C, P= 0.1-1.2 MPa, GHSV= 2100-7200 h ⁻¹	$-r_{CO} = A \frac{P_{H_2}^{0.5} P_{CO}}{(1 + k_{CO} P_{CO} + k_{H_2O} P_{H_2O})^2}$	E _a = 103.8 kJ/mol MARR= 13.26%	(Sarkari et al., 2012)
Fe-Co-Mn/MgO	T= 290-320 °C, P= 0.1-1 MPa, GHSV= 4500 h ⁻¹	$-r_{CO} = \frac{k b_{CO} P_{CO} P_{H_2}}{1 + b_{CO} P_{CO}}$	E _a = 82.5 kJ/mol MARR= 44.79%	(Arsalanfar et al., 2012)
KMoFe/CNTs	T= 270-290 °C, P= 0.7-4.1 MPa, GHSV= 2000 h ⁻¹	$-r_{CO} = \frac{k_p \cdot (b_{CO} P_{CO})^{0.5} \cdot (b_{H_2} P_{H_2})^2}{(1 + 2(b_{CO} \cdot P_{CO})^{0.5} \cdot (b_{H_2} \cdot P_{H_2})^{0.5})^5}$	E _a = 65.0 kJ/mol MARR= 15.3%	This study

6.3.3 Effects of temperature and pressure on selectivity

The process variables such as reaction temperature and pressure were investigated to determine the kinetics and selectivity of 0.5K5Mo10Fe/CNT nanocatalyst. Temperature is a critical process variable that significantly affects the kinetics and selectivity of FTS reaction. Under the same experimental conditions of H₂ /CO = 1, P = 4.1 MPa, and GHSV = 2000 h⁻¹, the effects of reaction temperature on the performance of the 0.5K5Mo10Fe/CNTs nanocatalyst were investigated (Figure 6.14). Considering FTS reactions being highly exothermic, a temperature increase can be detrimental for chain growth initiation and heavy hydrocarbon production (Bukur et al., 1997). In contrast, CO conversion deeply depends on reaction temperature, and increases with higher FTS temperatures, since lower temperatures may not provide enough energy for the catalyst to be activated for CO dissociation (De La Osa et al., 2011). It was reported that due to chain growth probability, olefins' content increases with increasing reaction temperature (Todic et al., 2016). Furthermore, owing to chain propagation, the increased reaction temperature facilitated the methane termination reaction as an

unfavorable by-products (Sun et al., 2017b). During the FTS reaction, total pressure plays an important role in hydrocarbon selectivity.

As shown in Figure 6.15, the effects of the total reaction pressure on the performance of the 0.5K5Mo10Fe/CNTs nanocatalyst for CO hydrogenation were investigated under the same operating conditions ($H_2/CO = 1$, GHSV = 2000 h^{-1} and $T = 280\text{ }^{\circ}C$). For iron catalysts, the methane selectivity is more affected by water-gas-shift activity and potassium promotion (Yang et al., 2014). Increasing the pressure and GHSV together leads to a decrease in methane selectivity while increasing C_{5+} selectivity (Riyahin et al., 2016). In Figure 6.15, as pressure increased the GHSV was constant (2000 h^{-1}). The selectivity of methane increased with an increase in pressure between 1.7 MPa and 3.7 MPa and then decreased. In our previous research, it was also found that in the presence of 0.5K5Mo10Fe/CNTs catalyst the methane selectivity decreased significantly compared with the unpromoted 10Fe/CNTs catalyst at the same operating conditions ($P = 3.5\text{ MPa}$ and GHSV = 2000 h^{-1}) (Yahyazadeh et al., 2022b). It was found that the promoters play a key role in the design of FTO catalysts and the decrease in methane selectivity was related to promoter effect (Galvis et al., 2013). CO and H_2 adsorption on the active sites increased by increasing pressure, which results in an increase in CO conversion due to increased extraction of the heavy hydrocarbons from the pores of the catalyst owing to the liquid-like density of the supercritical CO (Abbaslou et al., 2009a). Several steps are involved in the FTS reaction including series and parallel reactions, with each having a different activation energy. Each of these reactions can be affected by pressure or temperature based on the rate equation and the activation energy in the various steps of the reactions. Accordingly, temperature and pressure have different effects on selectivity.

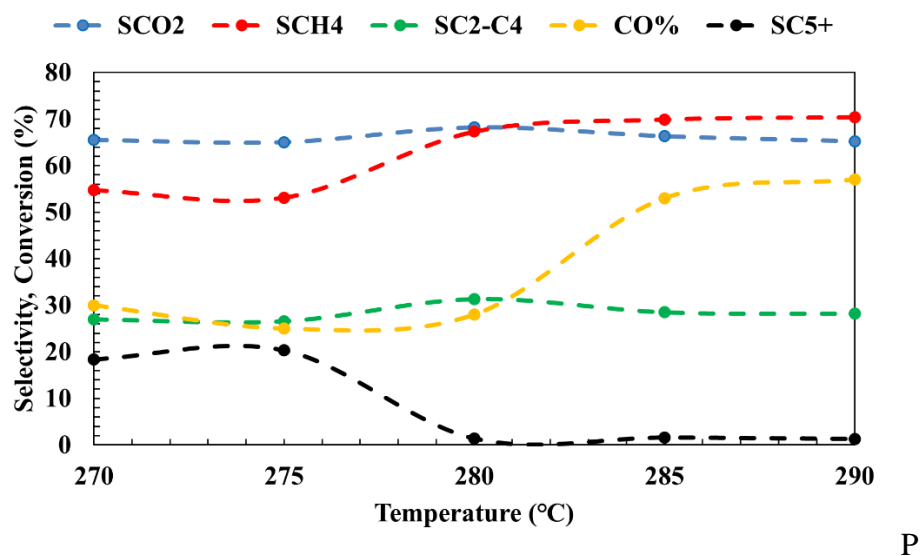


Figure 6.14: Effects of FTS temperature on selectivity of hydrocarbons at $P = 4.1$ MPa and $H_2/CO = 1$.

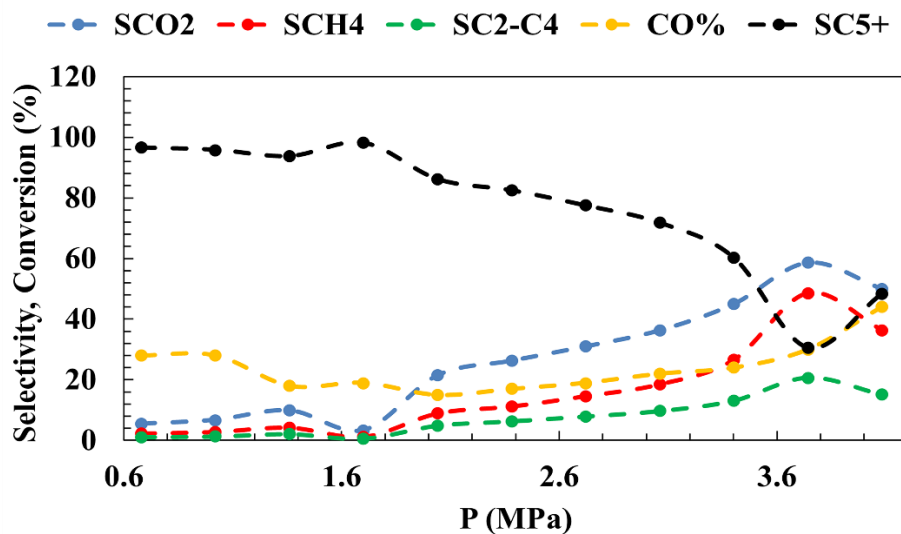


Figure 6.15: Effects of FTS pressure on selectivity of hydrocarbons at $T = 280$ °C and $H_2/CO = 1$

6.3.4 Comparison of Anderson-Schulz-Flory distribution with the mechanistic model

The developed kinetic model (Eq. 6-27) was compared with Anderson-Schulz-Flory (ASF) model. ASF is an established model for defining FT product distribution assumes a constant parameter known as 'chain growth probability' (α), which is a ratio between propagation and

termination. ASF model proposes the following relationship for the distribution of products during FT:

$$\ln\left(\frac{W_n}{n}\right) = n(\ln\alpha) + c \quad (6-67)$$

where W_n refers the mass fraction of hydrocarbons with n carbon atoms and c is a constant (Tavakoli et al., 2008). Experimentally, α value is determined by the slope of the line " $\ln(W_n/n)$ " versus " n ", which corresponds to " $\ln(\alpha)$ ". Accordingly, $\ln(W_n/n)$ was plotted versus n for the developed mechanistic model. A chain growth probability of 0.76 was found to be associated with the slope of this plot.

As seen in Figure 6.16, FTS product distribution over bimetallic promoted iron catalyst exhibited a good agreement with the ASF model ($R^2 = 0.95$). To determine the deviations from ASF model, the W_n values obtained by the mechanistic model were compared to those of the ASF model with a $\alpha = 0.76$. Figure 6.16 illustrates the deviation from ASF especially at higher carbon numbers. The deviation of the product distribution from the standard ASF plot suggested the possible presence of different chain initiation active sites (Vo et al., 2013). Additionally, re-adsorption of olefins causes a deviation from the ASF chain growth model. The longer the hydrocarbon chain on the Fischer-Tropsch catalyst sites, the more difficult is their diffusion through the catalyst pores, thus the possibility of re-adsorption increases (Simonetti et al., 2007). Secondary re-adsorption and reinsertion of 1-olefins in chain growth will change the chain growth probability, resulting in higher hydrocarbons or paraffins and a deviation from the typical ASF distribution. It will also reverse the original β -dehydrogenation process, decreasing the selectivity to light products and increasing α value (Bhatelia et al., 2014). Therefore, there might be alternative formation routes for heavier hydrocarbons in addition to or instead of the chain growth model.

Fe-based catalysts exhibit a lower activity for secondary reactions of olefins which negate the olefin readsorption of these catalysts for non-ASF distribution, thus suggesting an alternative theory based on chain length-dependent desorption of olefins. Similar ideas on the adsorptivity of higher hydrocarbon with increased chain length can be found in the literature (Todic et al., 2014). The non-ASF product distribution may be due to the appearance of an additional polymerization site on the catalyst surface located in the promoted iron-based

catalysts (Vo et al., 2013). According to a kinetic study by Todici et al. (Todici et al., 2017), the non-ASF change observed in α value with the carbon number was found to be justified by chain growth-dependent 1-olefin desorption concept. Furthermore, considering the secondary hydrogenation of 1-olefin to n-paraffin would change the slope of the n-paraffin formation rate versus carbon number, increasing the deviation from a ASF-type slope in C_{5+} range (Todici et al., 2017). The increase in ethane is due to secondary hydrogenation reactions (Van Der Laan and Beenackers, 1999). It was assumed that this phenomenon may have affected the model. However, the absence of any term that represents these effects in the developed model influenced their molar flow rates in such a way as to cause a deviation from the ASF model (Turan et al., 2022).

The deviation from ASF product distribution can be assigned to dissolution in liquid film on the catalyst surface and within the catalyst pores increasing the readsorption probability of alkenes and the resulting secondary reactions including hydrogenation, reinsertion, hydrogenolysis, and isomerization. Additionally, the readsorption of alkenes is carbon number-dependent and the following secondary reaction changes the FTS product distributions for heavier hydrocarbons (Qian et al., 2011). The deviation from ASF model could also be due to WGS reaction. Over iron-based catalysts, the FTS and WGS reactions occur on different active sites, whereas the rate of these reactions are influenced by the gas phase (Nakhaei Pour et al., 2013).

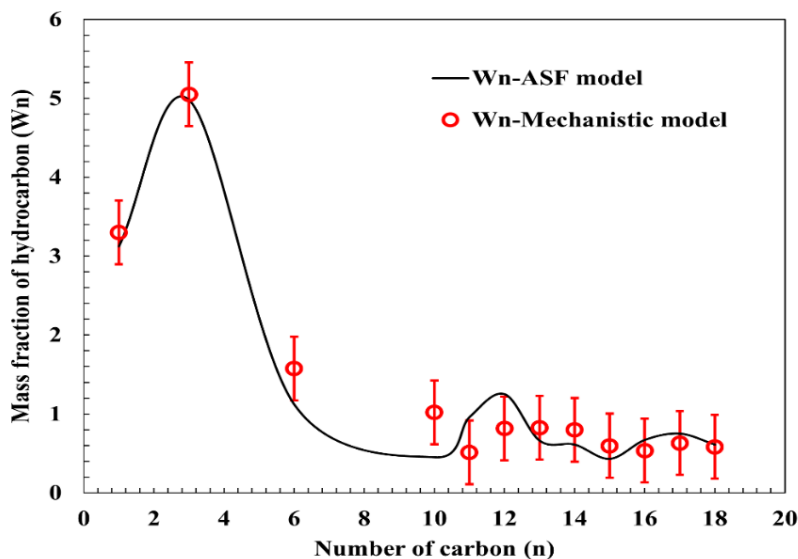


Figure 6.16: Comparison between the mechanistic model and ASF model ($\alpha=0.76$) at $T=280\text{ }^{\circ}\text{C}$, $P=4.1\text{ MPa}$ and $\text{H}_2/\text{CO}=1$.

6.4 Conclusions

FTS kinetics was investigated in a fixed-bed reactor using 0.5K5Mo10Fe/CNTs catalyst under a wide range of pressure (0.7-4.1 MPa) and temperature (270-290 $^{\circ}\text{C}$), with molar ratio of H_2/CO of 1 and GHSV of 2000 h^{-1} . XRD, SEM, EDS, XPS, and XAS techniques were used to characterize the bimetallic promoted nanocatalyst (0.5K5Mo10Fe/CNTs). A total of twenty-two mechanisms describing the adsorption characteristics of carbon monoxide and hydrogen using the LHW and ER adsorption theories were solved together with Arrhenius and Van't Hoff equations. Applying a non-linear regression (LM algorithm) and statistical criteria including R^2 , RMSD, and MARR tests, the optimal kinetic model for the FTS reaction over 0.5K5Mo10Fe/CNTs was achieved. FT-I mechanism provided the best match with experimental FTS data. From FT-I mechanism, carbon monoxide and hydrogen dissociatively adsorbed on the catalyst surface, and the reaction between adsorbed species was considered as the rate determining step.

Accordingly, kinetic parameters such as activation energy, CO adsorption enthalpy, and H_2 adsorption enthalpy were determined to be 65.0, -54.0, and -13.0 kJ/mol, respectively. In this case, the activation energy indicated a low mass transfer resistance in the catalyst and a lack of any diffusion limitations during FT reactions. Finally, the ASF model was compared with the

mechanistic kinetic model. The deviations observed especially at higher carbon numbers were attributed to the existence of additional reaction pathways including secondary re-adsorption of olefins and effects of WGS reaction.

The two-stages optimization of CNTs characteristics and light olefins production over KMo-promoted Fe/CNTs catalysts together with kinetics of the FT to light olefins (FTO) were studied. The next phase is dedicated to technoeconomic analysis (TEA) and life cycle assessment (LCA) of the FT to light olefins process using the most active catalyst (0.5K5Mo10Fe/CNTs).

CHAPTER 7: Fischer-Tropsch to Light Olefins over Bimetallic Promoted Fe/CNTs Nanocatalyst: Techno-Economic and Life-Cycle Assessment

The content of this section will be submitted for journal publication.

Contribution of the PhD candidate:

Experiments were designed in consultation with Dr. Philip Boahene, (Postdoc member of the group) under the supervision of Dr. Ajay K. Dalai and Dr. Lifeng Zhang and executed by Arash Yahyazadeh. Aspen plus simulation and OpenLCA were performed by Arash Yahyazadeh. The manuscript was drafted by Arash Yahyazadeh with guidance, suggestions, and reviews provided by Dr. Philip Boahene, and Dr. Ajay K. Dalai.

Contribution of this chapter to overall PhD research:

The fourth phase of the research is investigated in this chapter: The life cycle analysis and techno-economic evaluations employed to determine the environmental impacts associated during Fischer-Tropsch to olefins and the techno-economic feasibility of the process. This chapter is the basis of the following chapters.

7.1 Abstract

In this study, techno-economic analysis (TEA) and life cycle assessment (LCA) of light olefins' production through Fischer-Tropsch (FT) synthesis were investigated in different scenarios. Aspen plus simulation and openLCA software were used to study process economics and green-house gas (GHG) emissions. Experimental data from a fixed-bed reactor via bimetallic promoted Fe-based nanocatalyst (0.5K5Mo10Fe/CNTs) were used to simulate a plant to produce 1 kg of ethylene/h. The economic feasibility of light olefins' production was assessed via a detailed cash flow analysis. The net rate of return (*NRR*) calculated to 5.6%, 7.4%, and 18.2% for the base scenario (scenario 1), scenario 2 with wastewater treatment, and scenario 3 with wastewater treatment-separation unit, respectively, which means the project is economically profitable. From scenario 3, the minimum selling price of olefins is estimated to be 0.85 \$/kg, which was about 11% lower than that of scenario 1. The sensitivity analysis carried out on all scenarios depicted that the operating costs were affected significantly by the raw materials, operating labor cost, and utilities. Effects of syngas feedstock rate on the economic performance of the suggested scenarios were evaluated in terms of the modified

internal rate of return (*MIRR*) and total capital cost. A facility *MIRR* of 21.9% was obtained for scenario 3 and it was strongly influenced by syngas rate. The GHG emissions of scenario 1 was measured 77.5 g CO_{2-eq} per MJ ethylene confirming a significant drop in GHG emissions compared to petroleum-based FT fuel production.

7.2 Materials and methods

7.2.1 FT synthesis process

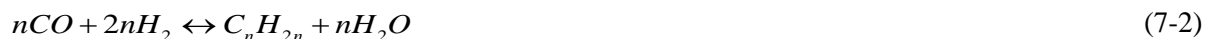
Preparation of the promoted nanocatalyst used in this study (0.5%K5%Mo10%Fe/CNTs) is described in section 3.2.4. FTS experiment, product sampling, and composition analyses are described in sections 3.4 to 3.5. Further, simulation studies were conducted considering syngas conversion (71.5%), C₂-C₄ product selectivity (49.6%), CO₂ product selectivity (75.2%), and methane product selectivity (34.7%) for 0.5K5Mo10Fe/CNTs catalyst (Yahyazadeh et al., 2022b).

7.2.2 Simulation of the FTO process

The FTO process was simulated using Aspen Plus software (version 12.0, AspenTech Corp.). Applying Peng-Robinson equation of state together with the Boston-Mathias alpha function, the thermodynamic calculations were performed. A three-phase separator was employed for water separation considering the nonrandom two-liquid thermodynamic equation for liquid-liquid-vapor mixtures. The heat loss and pressure drop in each unit during the FTO process were assumed negligible. For economic analysis, a steady state condition was considered. The Fischer-Tropsch process can be simulated using various flowsheets.

According to the guidelines obtained by Ulrich and Vasudevan (Ulrich and Vasudevan, 2004), an ASPEN-Plus flowsheet for the FTO process was developed to produce 1 kg of ethylene/h (Figures 7.1-7.3). Ulrich and Vasudevan approach was employed to design process components including reactors, distillation columns, adsorption columns, pumps, decanters, and compressors. A series of various reactions occurs to produce hydrocarbons through FTS. The most predominant step of FTS reactions is the monomer formation (-CH₂-), initiating the polymerization reactions thus producing longer oxygenated hydrocarbons, paraffins, and olefins. Considering Eq.s (7-1) and (7-2), the FTS reactions' stoichiometry can be derived (Trippe et al., 2013):





Eq.s (7-1) and (7-2) show the production of paraffins and olefins through exothermic reactions from syngas, respectively. The reaction enthalpies have been reported between 160 and 170 kJ/mol (Trippe et al., 2013). The water-gas shift (WGS) reaction is another predominant reaction for iron catalysts in FTS process.

7.2.3 Techno-economic analysis

TEA of FT process was carried out using Aspen Process Economic Analyzer (APEA) v12.0 on a 2021 US\$ pricing basis. The Icarus cost estimator was employed for sizing of the unit operation followed by mapping to the proper equipment in APEA to find the base equipment cost and installation cost. The Aspen Icarus Process Evaluator V12 (Bedford, MA, USA) was applied for equipment sizing as well as economic assessments. Implementing the chemical engineering plant cost index (CEPCI) of 628.2 for 2017, the cost estimation was carried out for syngas flow rates of 7000 kg/h resulting in 1 kg/h of ethylene. The fixed capital investment (FCI) was calculated based on Aspen data and CEPCI including equipment purchase price, installation, piping, electrical fittings, insulation, civil, overheads, contingencies as well as escalations. The method used to estimate total and fixed capital investments involved multiplying the sum of all equipment purchase prices by Lang factor ranging from 3 to 5, to obtain more accurate estimates (Tzanetis et al., 2017). The Lang factor is related to the type of process and starts from the costs of the equipment already installed (Gutiérrez Ortiz, 2020).

7.2.4 Life cycle assessment

Converting syngas into light olefins is considered the main function of the FTS plant in this LCA study. Therefore, 1 kg of ethylene produced at the biogas-to-liquid plant is the functional unit (FU) (Navas-Anguila et al., 2019b). Figure 7.1 depicts the FTS system boundaries, demonstrating each unit process in LCA. Applying a “cradle-to-gate” method, conversion of syngas to light olefins was covered, while all steps of the life cycle after the factory gate are neglected (Artz et al., 2018).

LCA represents a systematic method of assessing a process by considering the material and energy inputs for obtaining a product throughout its life cycle. The purpose of this analysis is to determine the areas contributing the majority of GHG emissions and to provide options to reduce emissions compared to conventional production methods using petroleum resources.

The LCA using cradle-to-grave approach requires system boundaries. Due to the limited amount of data, LCA provides policy makers with an opportunity to consider alternative scenarios that can be most beneficial for the environment (Tzanetis et al., 2017).

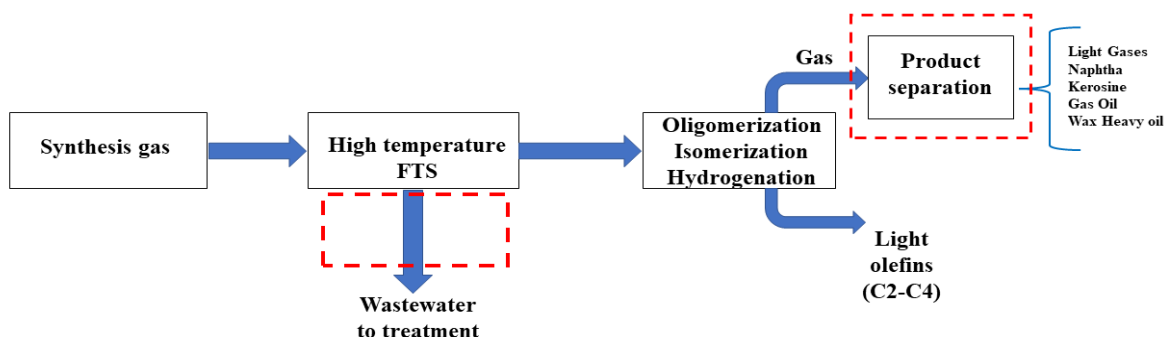


Figure 7.1: Simplified block diagram of the FT system to produce light olefins (dotted boxes indicate scenarios).

Any environmental impacts related to the input and output of the proposed FTO plant, and its upgrading was considered as potential environmental impacts (PEI). The life cycle analysis covered the potential environmental impacts such as acidification (AP), global warming (GWP), ozone layer depletion (ODP), cumulative non-renewable energy demand (CED_{nr}), and eutrophication (EP). CED_{nr} of fossil and nuclear was evaluated according to association of German engineers (VDI) guidelines while GWP was measured based on Intergovernmental Panel on Climate Change (IPCC). Other environmental impact categories were quantified based on the CML (Center of Environmental Science of Leiden University) methodology. These methods and categories are among the environmental profile of bioenergy systems (Navas-Anguita et al., 2019a). OpenLCA 1.11.0 software according to the CML 2015 impact assessment method with Ecoinvent 371 database was used for light olefins production using FTS. Resource consumptions and different emissions connected with environmental impact indicators were considered to estimate the life cycle impact categories. The functional unit assumed for performing life cycle impact assessment (LCIA) was considered 1 kg of ethylene production under different scenarios. According to the tool for reduction and assessment of chemicals and other environmental impacts (TRACI 2.1, v1.04) midpoint method presented in Table 7.1, LCIA categories and impact area were obtained.

Table 7.1: Midpoint method impact categories computed in the LCA.

Impact category	Abbreviation	Unit	Level of impact
Ozone depletion potential	ODP	Kg CFC-11-eq	Global
Global warming potential	GWP	Kg CO ₂ -eq	Global
Acidification potential	AP	Kg SO ₂ -eq	Reginal or National
Eutrophication potential	EP	Kg N-eq	Reginal or National
Carcinogenic potential	CP	CTUh	National
Non-carcinogenic potential	NCP	CTUh	National
Respiratory effects	RE	Kg PM _{2.5} -eq	Regional or National
Ecotoxicity potential	ETP	CTUe	National
Fossil fuel depletion	FFD	MJ surplus	Global

7.2.5 Sensitivity analysis

Plant economics is affected by factors including production capacity, capital cost, minimum selling price as well as feedstock cost. Applying a sensitivity analysis can be beneficial to determine the effects of factors' variation on plant economics. Accordingly, syngas flow rate changed between 2000 kg/h and 10000 kg/h to evaluate its effects on capital cost and other economic indicators for each scenario. The following factors were evaluated: raw materials, utilities, overhead, maintenance cost, operating charges, and operating labor cost. Canada's ecoENERGY for Biofuels Plant which presents different operating incentives, allowed an average internal rate of return (IRR) of 20% (Li et al., 2018). Therefore, the sensitivity analysis of net present value (NPV) was performed considering an upper limit of 20% for operating scales.

7.2.6 Analysis of different scenarios

Scenarios 1-3 were analyzed to provide an in-depth study of the environmental effects associated with light olefins production via FTS. The scenarios were considered (1) FTS without wastewater treatment and separation units (scenario 1, Figure 7.2), (2) FTS with wastewater treatment unit (scenario 2, Figure 7.3), and (3) FTS with wastewater treatment and separation sections (scenario 3, Figure 7.4). In B5 unit, the FT products were separated into three different forms of gas, heavy hydrocarbons, and wastewater. The wastewater stream was then introduced into a treatment unit (B6-9) to remove the residual hydrocarbons. In unit B10-11, FT gas products were separated to achieve pure olefins. The amount of water formation

during FTS compared to the liquid products were not significant. Therefore, this wastewater treatment section was added to the scenarios rather than the main process. Addition of the gas recycle stream in all scenarios can improve the economics when the process is optimized for maximum light olefins production (Rafati et al., 2017). In all scenarios off-gas was recycled and reused for heat and electricity generation.

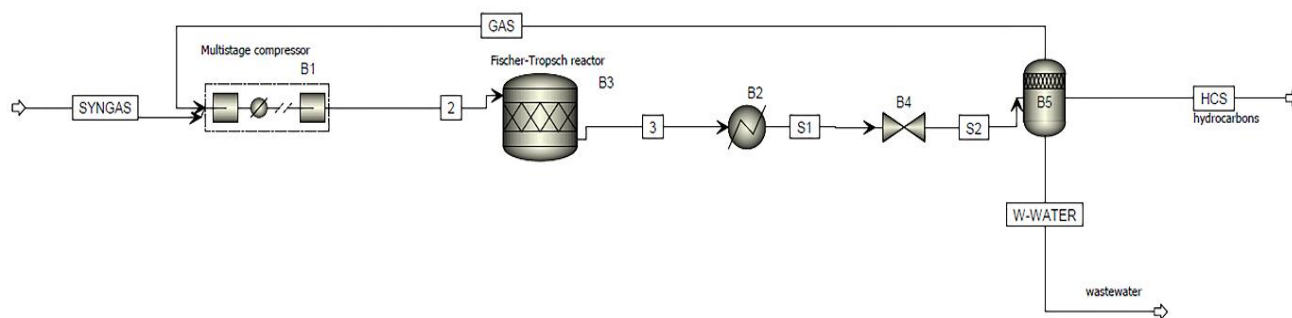


Figure 7.2: FT simulation diagram for production of light olefins (scenario 1).

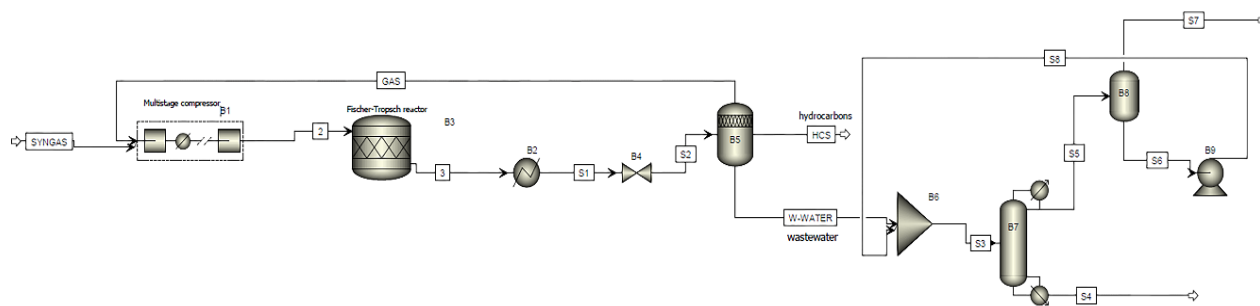


Figure 7.3: FT simulation diagram with wastewater treatment section (scenario 2).

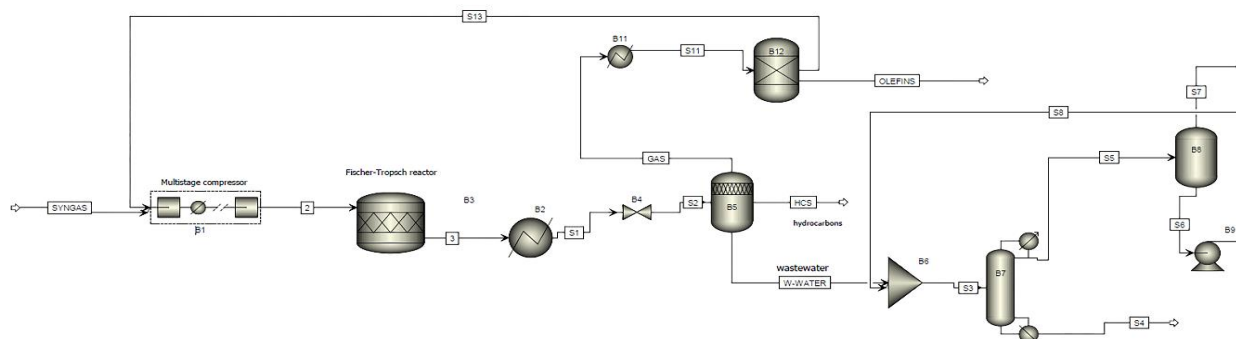


Figure 7.4: FT simulation diagram with wastewater treatment and separation units (scenario 3).

7.3 Results and discussion

7.3.1 Process simulation

The CO conversion and C₂-C₄ selectivity of 0.5K5Mo10Fe/CNTs catalyst reached 71.5% and 49.6%, respectively, under optimal operating conditions (T = 280 °C, P = 4 MPa, and GHSV = 2000 h⁻¹). In the simulation, the pure syngas with H₂/CO of 1 was assumed to be available at the desired temperature and pressure. The FTS tail gases were assumed as a mixture of unreacted syngas and humid gaseous hydrocarbons. Iron catalysts have shown a remarkable performance for H₂-lean syngas (H₂/CO ratio = 0.8–1.5) because of the high activity for WGS, providing more hydrogen for FTS reaction (Badoga et al., 2017a). Liquid hydrocarbons derived from FTS reactor often contained considerable amounts of water (834 kg/h). The residual water can be separated from liquid hydrocarbon by decantation or separator unit (Figures 7.2-7.4). This liquid hydrocarbon stream is a mixture of light to heavy species that can be used as fuel for automobiles. To separate liquid hydrocarbons into gasoline (C₅-C₁₂) and diesel fuels (C₁₃-C₂₀), a distillation column in scenario 3 was designed. Since no waxes (C₂₄₊) were produced by bimetallic promoted Fe/CNTs catalyst, the hydrocracking unit was not required. Table 7.2 describes the components of each unit in detail.

Table 7.2: Summary of operating conditions for different unit operation.

Unit operation	Aspen Plus block	Input conditions
Syngas compressor	MCompr	<ul style="list-style-type: none"> Three isentropic stages, intercooling at 50 °C and P= 2.6 MPa
Absorption unit	RadFrac	<ul style="list-style-type: none"> Eight stages
FT preheater unit	HeatX	<ul style="list-style-type: none"> Temperature difference of hot inlet and cold outlet = 10 °C
FT reaction unit	RStoic	<ul style="list-style-type: none"> T =280 °C, ΔP = -0.05 MPa Cooling water as utility ASF model for reaction conversions
Distillation tower	RadFrac	<ul style="list-style-type: none"> 10 stages, P =0.1 MPa with molar reflux ratio of 0.2 Kettle reboiler T(condenser) = 40 °C with cooling water

7.3.2 The material and energy balances of the FTO

Figure 7.5 depicts the simulation of FT plant of scenarios 1-3 using the bimetallic promoted 0.5K5Mo10Fe/CNTs catalyst, providing the detailed materials and energy balances in the

design. As shown in Figure 7.5, the boxes and lines depict the units and material or energy flow, respectively.

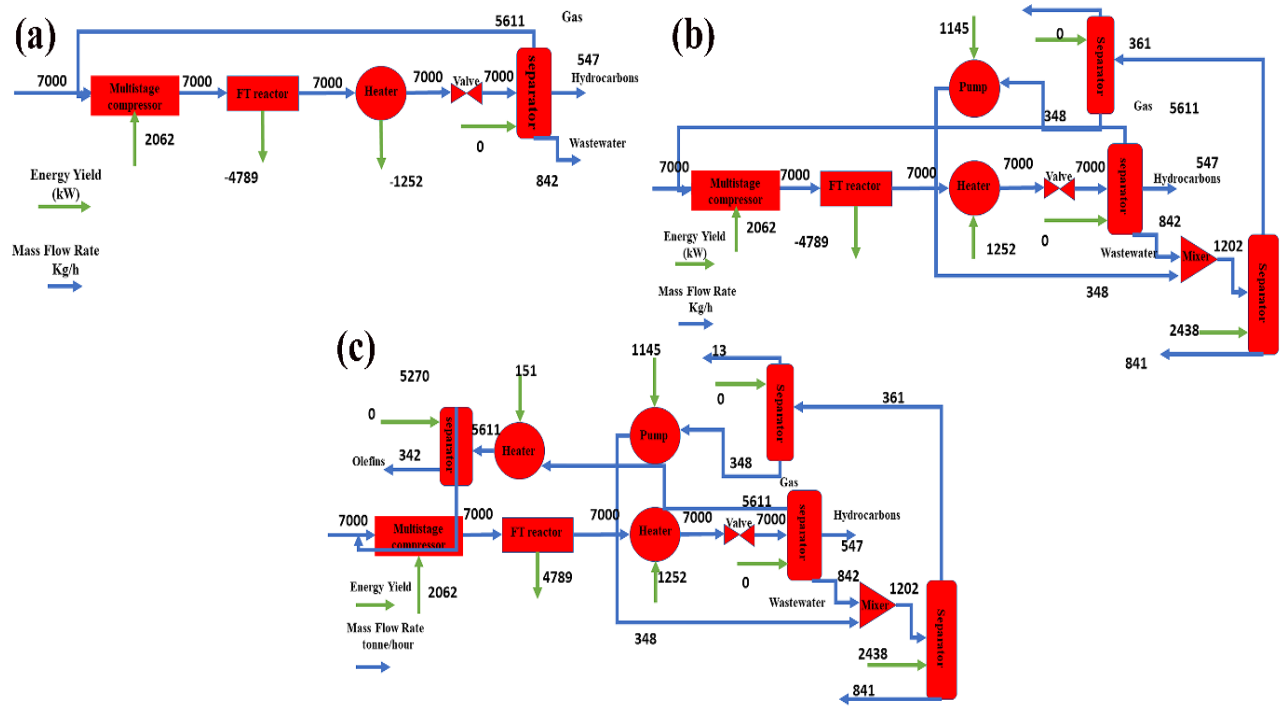


Figure 7.5: (a-c) Mass and energy balances of the FT process for scenario 1-3.

The energy conservation law was established to provide the energy balance as follow:

$$\sum_{in} m_{in} h_{in} = \sum_{out} m_{out} h_{out} + H_{loss} \quad (7-3)$$

where m_{in} , h_{in} , m_{out} , and h_{out} represent the input and output of mass flows and enthalpies, respectively. Excluding the heat transfer between the system and surroundings, H_{loss} is considered zero. The total electricity input (W_{tot}) in FT is calculated as follow:

$$W_{tot} = W_{CP} + W_{pump} - W_{EX} \quad (7-4)$$

In this case, W_{CP} represents the compressor's work, while W_{pump} stands for the pump duty. The electricity consumption for scenario 1, 2, and 3 ($W_{CP} + W_{pump}$) are 2238 KW, 2320 KW, and 2340 KW, respectively.

In general, Eq. (7-5) and (7-6) can be used to determine the net energy efficiency (η_E) and carbon efficiency (η_{Carb}).

$$\eta_E = H_{prod} / (H_{feed} + W_{tot}) \times 100\% \quad (7-5)$$

$$\eta_{Carb} = Carb_{prod} / Carb_{feed} \times 100\% \quad (7-6)$$

where H_{prod} , H_{feed} , and W_{tot} reflect the product energy, total feedstock energy, and electricity, respectively. $Carb_{prod}$ and $Carb_{feed}$ represent carbon in the product and feedstock, respectively. η_E values for 0.5K5Mo10Fe/CNTs catalyst is 62.2%, and η_{Carb} is 90.1%.

7.3.3 Fixed capital costs

Fixed capital costs are comprised of direct costs (DC) including costs of equipment and installation, as well as indirect costs (IC) such as spare part, engineering, startup, royalty, and contingency costs. IC s was estimated nearly 32% of the DC s (Baliban et al., 2013).

$$FCI = DC + IC \quad (7-7)$$

Table 7.6 provides the FT plant facility costs. The DC for common units (heat exchangers, distillation towers, and compressors) were estimated using the Aspen Process Economic Analyzer in Aspen Plus 12.0 software, while that of specific units (FT reactor, boiler, and separator) were determined using capital cost data (Table 7.2) as follow:

$$DC = (1 + BOP)C_o \left(\frac{S_r}{S_o} \right)^{sf} \quad (7-8)$$

where C_o refers to the base cost and BOP is the balance of plant including site and utility preparation (20%). S_r , S_o , and S_f stand for the actual capacity, base capacity, and scale factor, respectively.

7.3.4 Operating costs

The costs associated with fuel, electricity, steam, coolant, and refrigerants are categorized as operating costs (OC). The OC excluding feedstock cost was calculated as follows:

$$OC = \cos t_{elec} + \cos t_{steam} + \cos t_{fuel} + \cos t_{water} + \cos t_{refrigerant} + \cos t_{CO_2 \text{ TS\&M}} - \cos t_{elec-generation} \quad (7-9)$$

According to the results of the process simulation, the total amount of electricity consumed in the process was calculated.

7.3.5 Sale revenues

The working period of the FTO process was considered 330 days per year, with the remaining days dedicated to maintenance and refreshment. Diesel and gasoline prices changed over time. From 2014 to 2022, the price of diesel reduced from US\$942/MT to US\$609/MT. The price of light olefins e.g., ethylene also reduced from US\$1380/MT in 2014 to US\$500/MT by 2015, as the crude oil price decreased (C. Zhang et al., 2015).

7.3.6 Net profit

The gross profit, net gross profit as well as net annual earnings were calculated as follow:

$$\text{Gross profit} = SR - OC - MC \quad (7-10)$$

$$\text{Net gross profit} = \text{gross profit} - SARE \quad (7-11)$$

$$\text{Net annual earnings} = \text{net gross profit} \times (1 - \text{tax rate}) \quad (7-12)$$

where *SR*, *OC*, and *MC* stand for the sale revenue, operating cost, and maintenance cost (2% of the total cost). *SARE* reflects the sale administration and research expenses (10% of the net gross profit). In addition, the tax rate was assumed 40%. In this case, the equity ratio, debt ratio, and interest rate were taken 45%, 55%, and 14%, respectively, with a 10-year repayment period. The plant construction period was estimated as three years, with fixed capital distribution of 10%, 60%, and 30% in the first, second, and third year, respectively. The plant lifetime was considered 20 years. The annual cash flow was calculated as below:

$$\text{Cash flow}_i = \text{net annual earnings}_i + \text{depreciation credit}_i + \text{fixed capital cost}_i \quad (7-13)$$

The plant capacity factor of the first, second, and third year of operation were 0.5, 0.8, and 1.0, respectively. Depreciation credit was calculated using the 20-year straight line method. As a result, the discounted cash flow was determined by Eq. (7-14):

$$\text{Discounted cash flow}_i = \text{cash flow}_i \times (1 + \text{discount rate})^{(-2-i)} \quad (7-14)$$

The internal rate of return (*IRR*), payback period (*PBP*), and net present value (*NPV*) reflect the economic feasibility of each plant. The *PBP* describes the time required in years for the invested budget to be returned through the net cash outflow. It is applied to assess the risk of a suggested project.

$$PBP = \frac{FCI}{TPR - TOC} \quad (7-15)$$

where FCI is the fixed capital investment (\$), TPR represents the total plant revenue (\$/year) and TOC refers to the total operating cost (\$/year). The overall economic value of the plant is determined by NPV .

$$NPV = \sum_{i=0}^{30} \text{discounted cash flow}_i \quad (7-16)$$

IRR is the maximum discount rate (r) at which NPV of all cash flows equal to zero (Eq. 7-17).

$$NPV = \sum_{i=0}^{30} \frac{C_n}{(1+r)^n} = 0 \quad (7-17)$$

The difference between the present value of the cash inflow and outflow is defined as NPV . NPV is one of the economic indicators evaluating the profitability of plants as well as IRR .

$$NPV = (TPI - TOC) \times \frac{(1+i)^{Y-1}}{i \times (1+i)^Y} + TAC \times (1+i)^{-Y} - TCI \quad (7-18)$$

where TPI , TOC , TAC , TCI , and Y are total project investment (\$), total operating cost (\$/year), total annualized cost (\$), total capital investment (\$), and plant lifetime (years), respectively. The internal rate of return (IRR) or i was fixed at 10% when measuring the NPV . TAC can be calculated using Eq. (7-19).

$$TAC(\$/\text{year}) = \text{Depreciation} + TOC \quad (7-19)$$

7.3.7 Techno-economic analysis

The equipment was sized to produce 1 kg/h of ethylene based on the developed FTO flowsheet. An overview of the investment-dependent costs is presented in Table 7.3.

Table 7.3: Summary of economic assumptions.

Parameters for investment dependent costs	Unit	Scenario 1	Scenario 2	Scenario 3
Capacity	Lb/y	108440847	108440847	108440847
Expected lifetime	Years	20	20	20
Depreciation	Straight line method (US\$/year)	7.7E+06	5.1E+06	9.5E+06
Interest rate	%	14	14	14
Fixed capital investment	US\$	1.02E+07	6.74E+06	1.25E+07
Working capital	US\$	508450	336844	627139
Maintenance costs (average)	US\$	96097	108808	111766
Insurance and taxes	%	40	40	40
Syngas 4 MPa	US\$/h	4135	4135	4135
Electricity	US\$/h	179	179	181
Cooling water	MMG/h	3	3	3
Market prices of products (without taxes)				
Hydrocarbons	US\$/h	665	665	665
Gas	US\$/h	4310	4310	5399
Waste-water	US\$/h	37	37	37
Products sales	US\$/h	4.39E+07	5.35E+07	5.35E+07

The equipment prices undergoes fluctuation because of the change in materials, production method, and government policies. In this study, the equipment prices were provided by the vendors. The installation costs and facility parameters were presented in Tables 7.4 and 7.6. Considering the actual capacity required for equipment, the logarithmic relationship presented below was followed.

$$Cost_a = Cost_b \left(\frac{capac.a}{capac.b} \right)^n \quad (7-20)$$

where $Cost_a$ and $Cost_b$ represent the new price and the real price of equipment. $capac.a$ and $capac.b$ are the capacity of equipment a and b , with n referring to the amplification factor as presented in Table 7.4 (Wang et al., 2022).

Table 7.4: Equipment amplification factors and their percentages of the installation cost (Wang et al., 2022).

Type of Equipment	Installation cost (%)	Scaling Exponent
Compressor	30-60	0.69
Reactor	60-90	0.56
Heater	30-60	0.44
Pump	25-60	0.33
Condenser	30-60	0.44
Separator	20-60	0.49
Valve	10-30	0.30
Distillation Tower	60-90	0.57

Cost estimates in Table 7.5 provides major assumptions for estimating the balance of plant (*BOP*) costs and indirect costs owing to the guidelines in the references. Applying the chemical engineering plant cost index (CEPCI) for 2017 and 2021, the cost escalations associated with materials, equipment, engineering, and construction from 2017 to 2021 were calculated (Rafati et al., 2017). The CEPCI for 2017 and 2021 were reported 628.2 and 699.97, respectively (Junsittiwate et al., 2022). From Table 7.5, the levelized costs of FT liquid (FTL) production were measured based on the EPRI's TAG report (Rafati et al., 2017):

$$FTL \text{ production costs } (\$/GJ) = [(LACCR \times TCI) + (O \& M \text{ costs}) + (Feedstock \text{ costs}) - (Electricity \text{ sale price})] / (FT \text{ liquid production}) \quad (7-21)$$

where *LACCR* is the levelized annual capital charge rate represented as the annual percentage of *TCI* considering the annual sale of energy products. The *LACCR* was assumed 15.41%/y as measured and discussed by Kreutz et al. (Kreutz et al., 2008) with the debt/equity ratio of 55/45, plant lifetime of 20 years, and construction period of 3 years.

Other factors of the FTL production cost in Eq. (7-21) are depicted in Table 7.5. In this study, operating and maintenance (O&M) costs was not calculated in detail and it was considered as 4% of *TCI* (Kreutz et al., 2008).

Table 7.5: Important assumptions for measuring the overall production costs of FT liquids.

Parameter	Value	Source
Plant capacity factor	90%	Assumed
Total annual capital charges	15.41 %/y	(Kreutz et al., 2008)
Biomass cost	\$5/GJ, HHV	(Kreutz et al., 2008)
Natural gas cost	\$3.31/GJ, HHV	(Energy Information Administration, n.d.)
O&M ^a costs	4% of TCT^b	(Kreutz et al., 2008)
Electricity sale price	66.7 \$/MWh	(Energy Information Administration, n.d.)

^a Operating and maintenance costs^b Total capital investment**Table 7.6:** The cost of facilities.

Item	Material	Total Number	Unit cost (US\$)	Reference
Liquid heater	316 SS	3	1120	(Holger, 1954)
Liquid pump	316 SS	2	1414	(Browne, 1953)
Condenser	316 SS	2	1200	(Yancheng et al., 2017)
Vapor-liquid separator	CS	5	1360	(Qiang and Wang, 2020)
FT reactor	S31603	3	85,120	(Hsu et al., 2018)
Pressure relief valve	316 SS	3	751	(Merino et al., 2017)
Distillation tower	Q245R	2	61,800	(Wang et al., 2022)

Table 7.7: Fixed capital investments.

Scenario unit	Scenario 1	Scenario 2	Scenario 3
Multistage-compressors	2.51E+06	2.51E+06	2.51E+06
TEMA exchanger	13800	13800	13800, 12100
Liquid pumps	-	4400	4400
FT reactor	35700	35700	35700
Flash vessel	17600	17600, 17100	17600, 17100, 17600
Component mixer	-	-	33600
Distillation column	-	97600	97600
Total direct cost (US\$)	3074000	3.48E+06	3722600

7.3.8 Sensitivity analysis

Sensitivity analysis was used to ascertain which parameters are most critical to the operating costs (*OC*) for the FTO (Figure 7.6 (a-c)). It was observed that *OC* was highly sensitive to raw

materials, operating labor cost, and utilities for all scenarios. During the analysis, one parameter was increased or decreased by 12 or 11%, while all other parameters were kept fixed. When the cost of raw materials in scenario 1 was increased by 12%, the *OC* increased from \$25.3 M/y to \$72.1 M/y. However, a 12% rise in the cost of utilities decreased the *OC* to \$1.1 M/y. Similarly, in scenario 3, with 11% decrease in the maintenance cost, the *OC* decreased to \$70843/y. In scenario 2, increasing the maintenance cost from \$429745/y to \$1.19 M/y raised the *OC* by 11%. In scenario 3, the increase and decrease in operating labor cost by 11% resulted in 44% rise and 44% decline in *OC*, respectively.

Figure 7.6(d) shows the plant capital cost with respect to the feedstock rate (ranging from 2000 kg/h to 10000 kg/h) for production of olefins using different scenarios. The minimum selling price (*MSP*) of olefins at various syngas flow rate is plotted in Figure 7.7. For a lower *MSP*, the plant feedstock flow rates would need to increase. It can be observed that scenario 3 shows lower *MSP* (US\$ 0.85/kg) for a capacity of 7000 kg/h, which is not competitive with light olefin price using fossil fuel methods (US\$1600/MT) (C. Zhang et al., 2015). Considering *NPV* equaled to zero, the minimum olefin selling price were calculated as US\$ 0.93/kg and US\$ 0.95/kg for scenario 2 and scenario 1, respectively. It is worth noting that a plateau effect of the syngas flow rate on *MSP* is observed when the flow rate is over 7000 kg/h. This means 7000 kg/h is an ideal flow rate for syngas supply providing a cost-competitive production of olefins.

The annualized operating costs breakdown is shown in Figure 7.7. As it can be observed in all scenarios, raw materials cost accounts for 46-49 % of operating cost, followed by maintenance (20-30 %) and utility (11-13 %) costs. In addition, the maintenance cost of scenario 2 is more than that of scenario 1 and 3, which can be related to the higher flow rates in the water treatment section increasing the size of equipment and the corresponding costs.

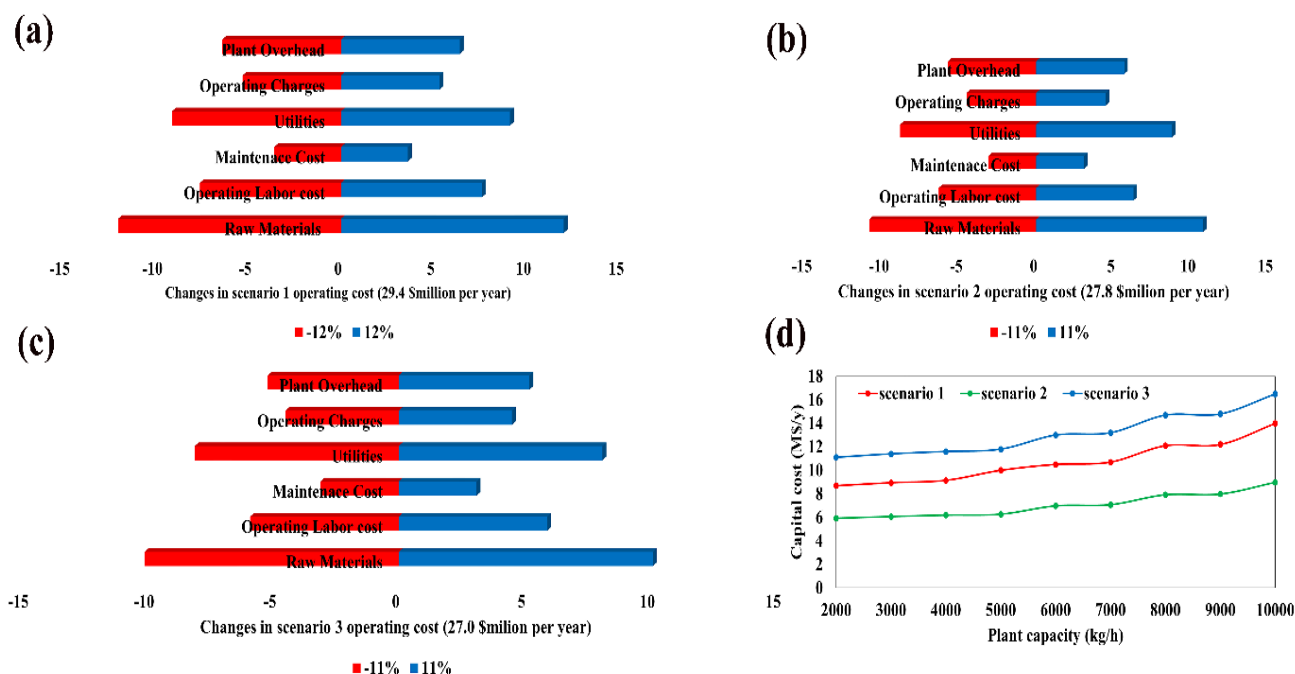


Figure 7.6: (a-c) Sensitivity of operating cost for the scenarios; (d) Effects of syngas flow rate on capital expenditure.

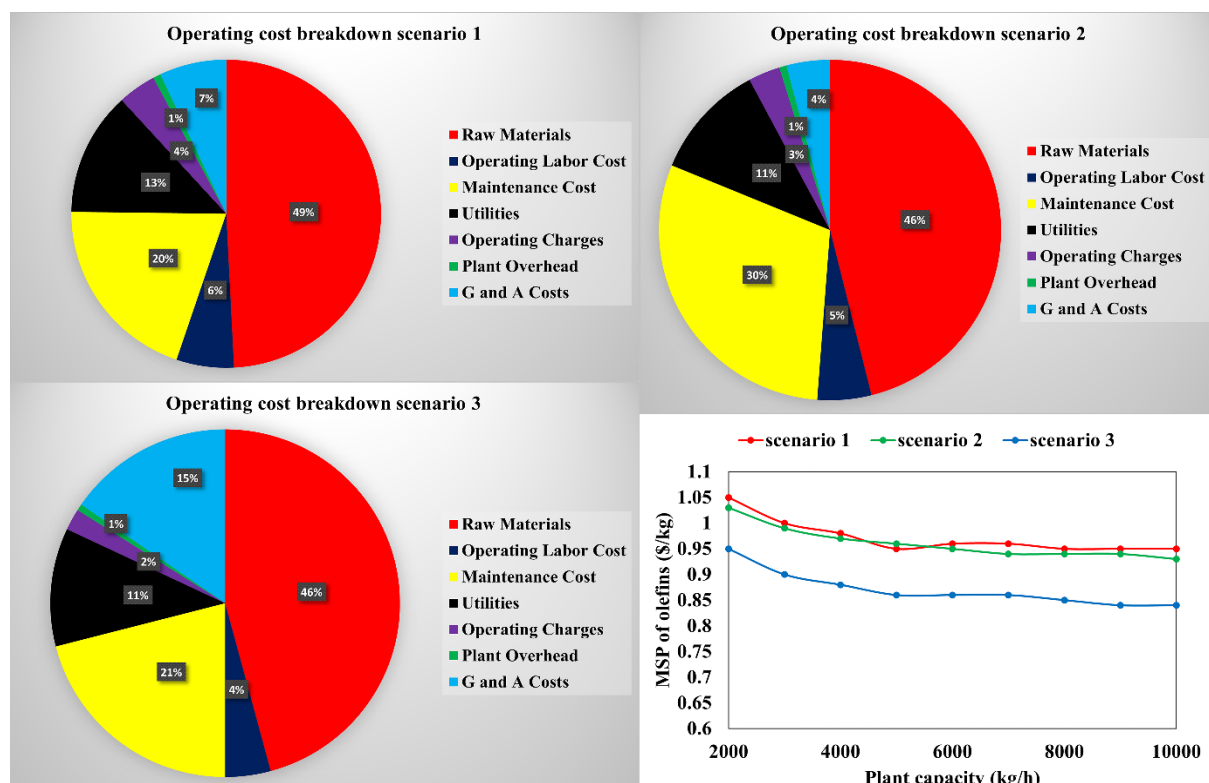


Figure 7.7: Cost break-down of the operating expenditure for different scenarios.

From Table 7.8, the number of operators required was determined according to guidelines obtained by Ulrich and Vasudevan (Ulrich and Vasudevan, 2004). The internal rate of return (*IRR*) was employed to determine the economic feasibility of scenarios 1-3 of the integrated FT plant. The profitability of plants is reflected by return on investment. From Table 10, the *IRR* of scenario 1 and 2 is 42.0% and 63.4%, respectively, which is less than that of scenario 3 with *IRR* of 154.7%. The higher *IRR* of scenario 3 is mainly due to the higher total capital investment of this scenario (C. Zhang et al., 2015). The *IRR* above 10% is acceptable for a feasible industrial plant and all scenarios (1-3) meet this criterion (Santos et al., 2021). The *IRR* reflects the profitability of a plant.

However, considering the modified internal rate of return (*MIRR*) would obtain a more reliable comparison. The value of *MIRR* is in the order of scenario 3 (21.9%) > scenario 2 (21.3%) > scenario 1 (20.7%), which is in a good agreement with the trend of profitability index (*PI*). The profitability index above 1 is economically favorable (Santos et al., 2021). Table 7.9 shows the *PI* for all scenarios in the FTS process, which is greater than 1 and confirmed the profitability of the plants. A positive value of net return rate (*NRR*) for different scenarios also indicates the profitability of the project. *NRR*, which combines *NPV* and discounted cash flow rate of return (*DCFR*) is affected by the project lifetime (Okolie et al., 2021).

Table 7.8: The number of operators required for the FTS.

Name of the equipment	No	Operators required	Number of operators required
Pumps	2	0	0
Splitters	2	0.2	0.4
Condenser	1	0.02	0.02
Compressors	2	0.1	0.2
Reactor	1	0.3	0.3
Column	1	0.3	0.3
Total No of operators required			1.22-2

Table 7.9: Summary of economic analysis.

Investment	Scenario 1	Scenario 2	Scenario 3
Total project capital investment (US\$)	10.68E+06	8.42E+06	1.39E+07
Working capital (US\$/y)	608450	436844	727139
Internal rate of return (<i>IRR</i> , %)	42.08	63.47	154.70
Net return rate (<i>NRR</i> , %)	5.67	7.48	18.21
Modified internal rate of return (<i>MIRR</i> , %)	20.79	21.35	21.94
Profitability index (<i>PI</i>)	1.24	1.27	1.38

The economic performance of FTO plants is influenced by the FT catalyst selectivity toward light olefins, providing a larger amount of products. The results also confirmed that as selectivity to light olefins rose, the *IRR* value increased remarkably. From Fig. 8a, once the selectivity to light olefins reached zero indicating all C₂–C₄ hydrocarbons as paraffins, the *IRR* of the FTO in scenario 3 was 28.6%. According to our previous study (Yahyazadeh et al., 2022b), the maximum light olefin selectivity of 0.5K5Mo10Fe/CNTs catalyst at H₂/CO of 1 was 49.6% at which the *MIRR* value increased to 21%. By increasing the syngas ratio from 1 to 2, the *MIRR* value of scenarios 1 and 2 improved slightly, which is required for an advanced technology to be attractive in capital markets (Zhang et al., 2013).

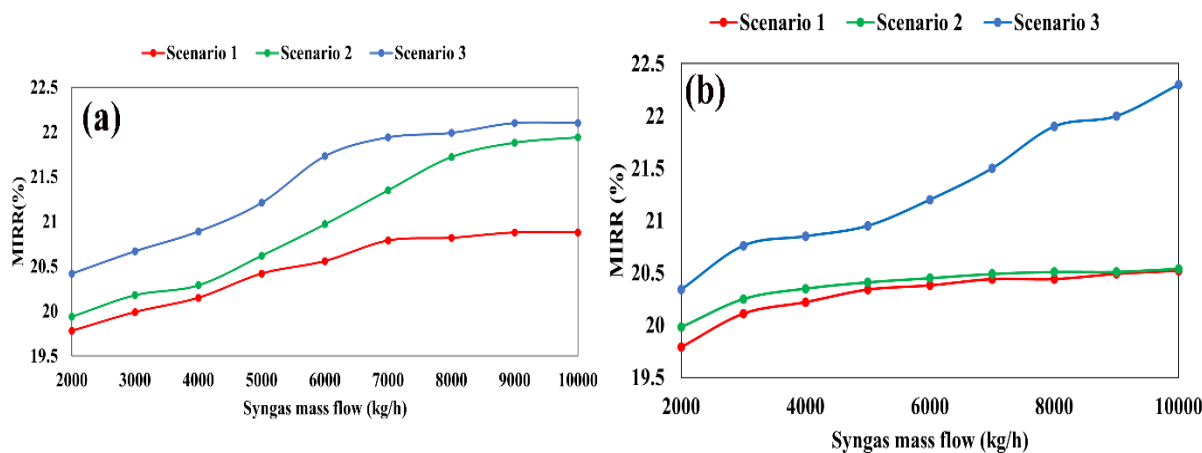


Figure 7.8: *MIRR* of FT process in different cases as a function of syngas rate for 0.5K5Mo10Fe/CNTs catalyst (a): H₂/CO = 1; (b): H₂/CO = 2.

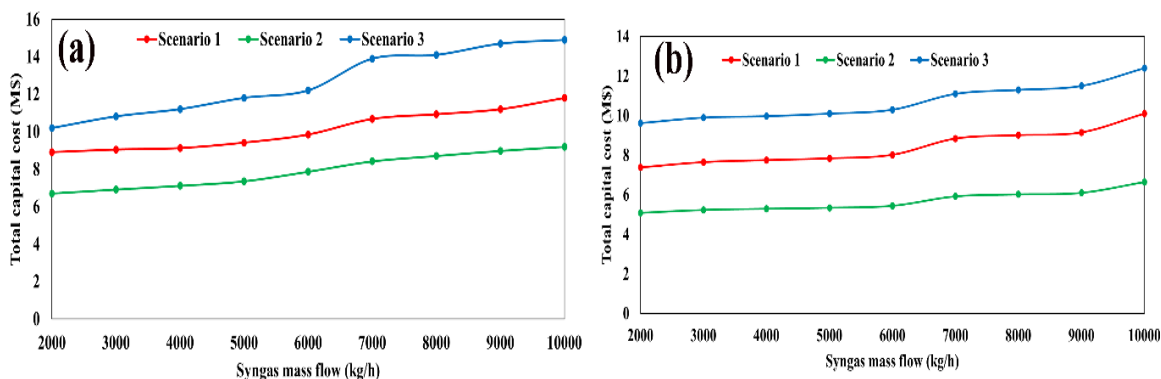


Figure 7.9: The FT plant costs in different cases as a function of syngas rate for 0.5K5Mo10Fe/CNTs catalyst (a): H₂/CO = 1; (b): H₂/CO = 2.

From Figure 7.9 the total capital cost is a function of the syngas feed ratio, the higher the syngas flow rate, the higher the total capital cost. The sensitivity analysis confirms that decreasing the feedstock rate is the most critical factor to the FTO plant economics (Figure 7.6). Furthermore, Figure 7.10 demonstrates the effects of plant capacity on the profitability index and depreciation cost. *PI* and depreciation cost of the FTO are sensitive to the scenarios, which is primarily due to the change in the total olefin cost. The results show that addition of separation unit in scenario 3 improved the profitability of the FTS plant compared with scenario 1 and 2. The economic profitability for olefin production also depends on process conditions and interest rate (Rahimi and Shafiei, 2019). Comparatively, scenario 3 shows that system integration causes the depreciation cost increase. Expanding the olefin production sale would compensate the higher depreciation cost of scenario 3 (Xiang et al., 2014).

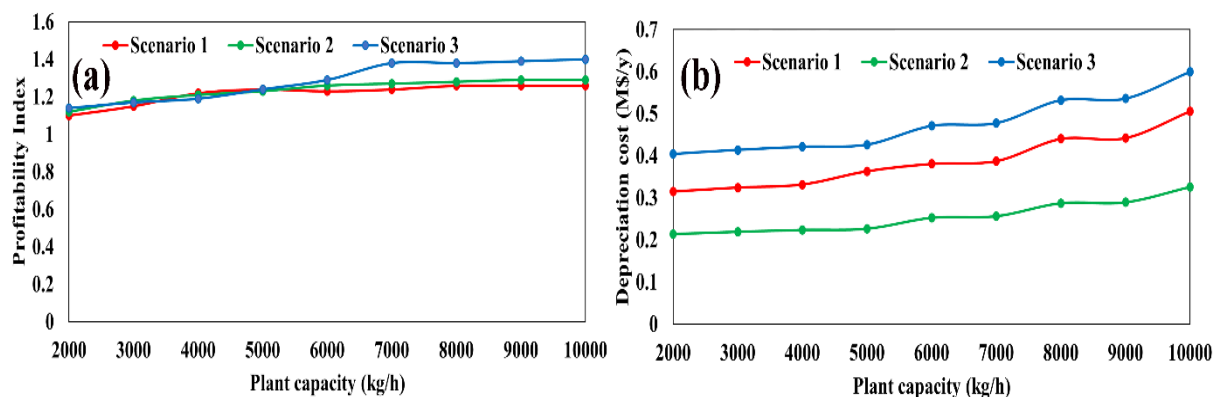


Figure 7.10: Impact of variations in plant capacity on (a) Profitability index; (b) Depreciation cost.

7.3.9 Life cycle assessment

The superiority of petroleum products obtained by FTS over fossil fuel-based products is related to lack of sulfur, nitrogen, and aromatics in FT products. Nevertheless, the global atmospheric and toxicological impacts associated with the proposed FT plant were estimated as potential environmental impact (PEI) including global warming, ozone layer depletion, acidification, eutrophication, human carcinogenic toxicity, human non-carcinogenic toxicity, resource depletion, respiratory effects, ecotoxicity, and photochemical ozone formation. 1 kg/hr ethylene production rate was considered for scenarios 1-3 as well as fossil fuel method, which is a common assumption in the literature. The PEIs were estimated based on the mass and energy balances considering the consumption of syngas, catalyst, and energy during FT process.

Table 7.10: LCA results for the FT plant located in Canada for a basis of 1 kg ethylene.

Impact category	Unit	Scenario 1	Scenario 2	Scenario 3	Fossil fuel
Global warming potential (GWP)	kg CO ₂ eq.	3.91	0.89E+01	2.10E+02	1.86E+02
Ozone depletion	kg CFC-11eq.	2.44E-07	2.44E-07	2.44E-07	3.09E-06
Acidification	kg SO ₂ eq.	4.55E-02	6.90E-02	6.10E-01	5.46E-01
Photochemical ozone formation	Kg O ₃ eq.	1.34	2.03	2.63E+01	7.24
Human health-carcinogenic	CTUh	1.44E-06	1.66E-7	4.74E-06	9.98E-06
Human health-noncarcinogenic	CTUh	3.48E-06	1.47E-06	4.10E-05	1.36E-05
Ecotoxicity	CTUe	6.34E+01	3.06	6.64E+02	3.76E+02
Resource depletion-fossil fuels	MJ surplus	4.51	4.51	4.51	9.66E+02
Respiratory effects	kg PM _{2.5} eq.	1.50E-03	3.20E-03	2.26E-01	4.80E-02
Eutrophication	kg N eq.	6.78E-02	1.78E-03	2.58E-02	2.14E-01

The potential environmental impact index across the system was evaluated for scenarios 1-3. A “cradle-to-gate” method was used to measure the GHG emissions for all scenarios through FTS process. The global warming potential (GWP) is estimated by kg of CO₂ equivalence which is one of the most important environmental impacts of plants. As shown in Table 7.10, the GWP in this study is in the order of scenario 3 (210 kg CO₂-eq) > scenario 2 (8.9 kg CO₂-eq) > scenario 1 (3.91 kg CO₂-eq). GHG emission for scenario 3 and fossil fuel method are much more than that of scenarios 1 and 2, indicating the higher risk of CO₂ emission by scenario 3.

Carcinogenic and non-carcinogenic effects for scenario 2 are 1.66×10^{-7} CTUh and 1.47×10^{-6} CTUh, respectively, which is lower than that of fossil fuel method (Table 7.10). Production of light olefins through scenario 1 exhibited a better performance compared to other scenarios (2,3) with respect to global warming potential, acidification, photochemical ozone formation, and respiratory effects.

Additionally, scenario 2 is found to be the best option in terms of eutrophication, carcinogenic and non-carcinogenic effects. It can be observed that the environmental impacts of scenarios 1 and 2 are mostly lower than those of scenario 3. As can be observed in Figure 7.11, scenario 3 demonstrates the worst performance in terms of GWP, acidification, photochemical ozone formation, ecotoxicity, non-carcinogenic, and respiratory effects. The greatest reductions of environmental impacts including eutrophication and ozone depletion can be achieved by scenario 3. Overall, the FT products were determined to be more environmentally benign compared to fossil fuel methods. In case the amount of fresh catalysts consumed can be decreased by enhancing the longevity of the catalyst, the ozone depletion potential can be reduced (Okeke et al., 2020b). Quantitatively, the amount of ozone depletion potential emission for all scenarios is too small (2.4×10^{-7} kg CFC-11_{eq}).

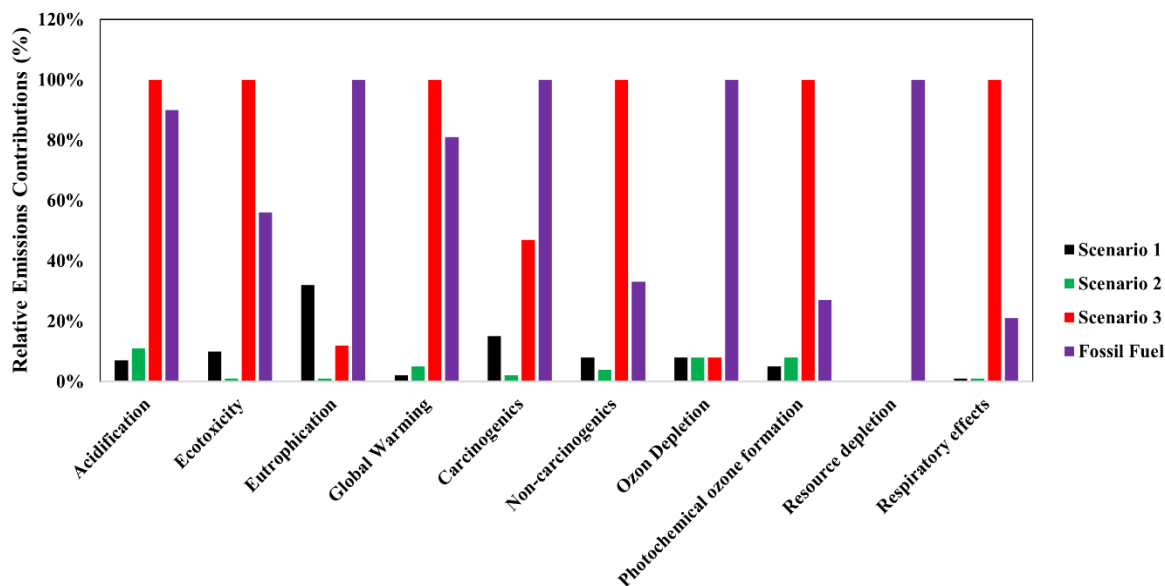


Figure 7.11: Comparison of the LCA results of light olefins' production in different scenarios using 0.5K5Mo10Fe/CNTs catalyst.

Regarding global warming potential, LCA provides a basis for comparison of bioenergy and biofuel production plants. As it can be seen in Table 7.11, six biofuel plants located in different countries including this study in Canada were evaluated in terms of CO₂ equivalence (g/MJ). A wide range of CO₂ emission (7.6-484.0 g CO_{2-eq}/MJ) were reported, among them the lowest level belongs to the non-FT biofuel production (7.6, 9.6, and 11.0 g CO_{2-eq}/MJ), while the FT fuel production resulted in a higher CO₂ emission. The CO₂ emission of FT process were in the range of 37.6-484.0 g CO_{2-eq}/MJ. The CO₂ emission from the light olefin production in our study is estimated to be about 77.5 g/MJ ethylene in base scenario 1 (3.91 kg CO_{2-eq} per 1 kg of ethylene) which is fairly acceptable.

Table 7.11: Comparison of LCA studies on biofuels, FT liquid fuels, and olefins.

Country	Scope	Feedstock	System boundaries	Indicator	CO _{2-eq} (g/MJ)	Reference
Tunisian	The life cycle sustainability performance of bioenergy system	Date palm waste	Cradle-to-gate	GWP	7.6	(Ben Hnich et al., 2021)
U.K.	LCA of jet fuel production from bagasse	Sugar Cane Residue	Cradle-to-grave	GWP	9.6	(Michailos, 2018)
U.K.	Environmental sustainability of different FT process designs	Sewage sludge	Cradle-to-grave	GWP	484.0	(Cuéllar-Franca et al., 2019)
U.S.	LCA of FT fuel production	Waste CO ₂ streams	Well-to-wheel	GWP	37.6	(Zang et al., 2021a)
Spain	LCA of bio-fuel production	Pine wood waste	Cradle-to-gate	GWP	11.0	(Gutiérrez Ortiz et al., 2020)
Switzerland	Environmental assessment of FT electro-diesel	Captured CO ₂ and electrolytic H ₂	Cradle-to-gate	GWP	150.0	(Medrano-García et al., 2022)
Canada	LCA of FT to light olefins	Syngas	Cradle-to-gate	GWP	77.5	This study

7.4 Conclusions

The feasibility of a designed FT process for direct production of light olefins along with its environmental impacts were evaluated by techno-economic analysis and life cycle assessment. Based on the performance of bimetallic promoted 0.5K5Mo10Fe/CNTs catalyst for production of light olefins at 280 °C and 4 MPa, the proposed FT design was found economically profitable.

By addition of wastewater treatment and separation units, three different scenarios were established. Scenario 3, including wastewater treatment and separation units was the most profitable olefin production process, and the profitability index increased by maximizing the plant capacity (10000 kg/h). Increasing the yield of light olefins is crucial to the economic performance of the designed FT process. In the sensitivity analysis, raw material followed by operating labor cost, and utilities were the major factors affecting the operating cost of the proposed designs. Compared to scenario 1 with the minimum selling price of 0.95 \$/kg, scenario 3 resulted in a lower MSP of 0.85 \$/kg at various plant capacities with the highest profitability index (1.38%). The potential environmental impact of the FT design was analyzed by a cradle-to-gate approach. The analysis showed that the greatest reductions of environmental impacts including eutrophication and ozone depletion can be achieved by scenario 3. However, significantly high GHG saving was achieved by production of light olefins through scenario 1 with 77.5 g CO_{2-eq} per MJ ethylene.

CHAPTER 8: Conclusions and Recommendations

8.1 Overall project overview and conclusions

Industries are concerned with production of light olefins via Fischer-Tropsch synthesis (FTS). Commercialization of FTS is limited by catalytic system development in terms of activity, selectivity, and stability to improve the feasibility of producing light olefins via Fischer-Tropsch to olefins (FTO) on an industrial scale. Fe was found as a promising active metal for light olefin production due to its tolerance for sulfur contaminants present in H₂-deficient syngas obtained from biomass, low cost, and high selective toward light olefins. Selection of support, promoter, catalyst synthesis methods, as well as process conditions can considerably influence the FTS productivity. In comparison with oxide supports, carbon nanotubes (CNTs) were found to be a promising catalyst support owing to their high surface area, excellent thermal conductivity, metal-support weak interaction, and modifiable surface chemistry. CNTs was synthesized by catalytic chemical vapor deposition and optimized to obtain maximum CNTs yield (47.4%) at 700 °C and minimum amorphous carbon structure ($I_D/I_G = 0.29$) at 800 °C.

FTS catalytic performance of Fe/CNTs-Syn supported catalyst was investigated under industrially relevant process conditions ($T = 280$ °C, $P = 2.0$ MPa, $H_2/CO = 1$, TOS = 24 h, GHSV = 2000 h⁻¹). The light olefins' selectivity and CO conversion over 20Fe/CNTs-Syn were 23.6% and 90.4%, respectively. 20Fe/CNTs-Syn shows a high and constant degree of CO conversion for a period of 120 h on stream.

Electronic structural promoters such as K and Mo improve light olefins' selectivity and catalytic activity. CNTs synthesized was used as support to obtain K and/or Mo-promoted Fe/CNTs catalysts for light olefins' production in FTS. In addition, FTS catalyst synthesis conditions including Mo/K promoter mass ratio (0.25-10 wt%/wt%), ultrasonic time (6-18 min), and iron loading (10-30 wt%) were optimized to obtain maximum light olefins' yield. 0.5K5Mo10Fe/CNTs prepared under the optimum synthesis conditions resulted in the highest olefins' yield (35.5%). It was found that the addition of potassium increases CO conversion, while molybdenum enhances the selectivity to light olefins.

The kinetic study of FTS was performed over 0.5K5Mo10Fe/CNTs catalyst in a fixed-bed reactor under operating conditions ($P = 0.7$ -4.1 MPa, $T = 270$ -290 °C, $H_2/CO = 1$, GHSV = 2000

h^{-1}). A total of twenty-two mechanisms describing the adsorption characteristics of carbon monoxide and hydrogen for monomer formation using the LHWW and ER adsorption theories were solved together with Arrhenius and Van't Hoff equations. Accordingly, kinetic parameters such as activation energy, CO adsorption enthalpy, and H_2 adsorption enthalpy were determined to be 65.0, -54.0, and -13.0 kJ/mol, respectively. Additionally, the kinetic model was further compared with the typical Anderson-Schulz-Flory model, suggesting the effects of water-gas-shift and the existence of additional formation pathway such as secondary re-adsorption of olefins for heavier hydrocarbons.

Finally, techno-economic analysis and life cycle assessment of light olefins' production through FTS were investigated in three scenarios. The net rate of return (*NRR*) calculated to be 5.6%, 7.4%, and 18.2% for the base scenario (scenario 1), scenario 2 with wastewater treatment, and scenario 3 with wastewater treatment-separation unit, respectively, which means the project is profitable from an economic perspective. From scenario 3, the minimum selling price of olefins is estimated to be 0.86 \$/kg, which was about 11% lower than that of scenario 1. Effects of syngas feedstock rate on the economic performance of the proposed scenarios were also evaluated in terms of the modified internal rate of return (*MIRR*) and total capital cost. A facility *MIRR* of 21.9% was obtained for scenario 3 and it was strongly influenced by syngas rate. Additionally, The GHG emissions of scenario 1 was measured 77.5 g $\text{CO}_2\text{-eq}$ per MJ ethylene confirming a significant drop in GHG emissions compared to petroleum-based FT fuel production.

8.2 Recommendations

Recommendations for future research in this field would be:

- The chemical vapor deposition reactor could be modelled and the CNTs growth would be investigated over a single metal catalyst. The potential results would benefit the reactor design on an industrial scale CNTs production.
- Other chemical and structural promoters, namely Mn, Bi, and Zr could be studied for their impacts on FTS iron catalyst supported on CNTs.
- The influence of preparation methods such as the sol-gel and precipitation techniques on catalytic performance of CNTs supported iron-based catalysts can be investigated.

REFERENCES

- A. Chernavskii, P., O. Kazak, V., V. Pankina, G., D. Perfiliev, Y., Tong Li, Mirella Virginie, Y. Khodakov, A., 2017. Influence of copper and potassium on the structure and carbidisation of supported iron catalysts for Fischer–Tropsch synthesis. *Catal. Sci. Technol.* 7, 2325–2334. <https://doi.org/10.1039/C6CY02676A>
- Abbasi, M., Mirzaei, A.A., Atashi, H., 2019. The mechanism and kinetics study of Fischer–Tropsch reaction over iron-nickel-cerium nano-structure catalyst. *Int. J. Hydrogen Energy* 44, 24667–24679.
- Abbaslou, R.M.M., Mohammadzadeh, J.S.S., Dalai, A.K., 2009a. Review on Fischer–Tropsch synthesis in supercritical media. *Fuel Process. Technol.* 90, 849–856.
- Abbaslou, R.M.M., Soltan, J., Dalai, A.K., 2011. Iron catalyst supported on carbon nanotubes for Fischer–Tropsch synthesis: Effects of Mo promotion. *Fuel* 90, 1139–1144.
- Abbaslou, R.M.M., Tavasoli, A., Dalai, A.K., 2009b. Effect of pre-treatment on physico-chemical properties and stability of carbon nanotubes supported iron Fischer–Tropsch catalysts. *Appl. Catal. A Gen.* 355, 33–41.
- Ail, S.S., Dasappa, S., 2016. Biomass to liquid transportation fuel via Fischer Tropsch synthesis – Technology review and current scenario. *Renew. Sustain. Energy Rev.* 58, 267–286. <https://doi.org/10.1016/J.RSER.2015.12.143>
- Alayat, A., Echeverria, E., McIlroy, D.N., McDonald, A.G., 2018. Enhancement of the catalytic performance of silica nanosprings (NS)-supported iron catalyst with copper, molybdenum, cobalt and ruthenium promoters for Fischer-Tropsch synthesis. *Fuel Process. Technol.* 177, 89–100. <https://doi.org/10.1016/J.FUPROC.2018.04.020>
- Aliyu, A., Kariim, I., Abdulkareem, S.A., 2017. Effects of aspect ratio of multi-walled carbon nanotubes on coal washery waste water treatment. *J. Environ. Manage.* 202, 84–93. <https://doi.org/10.1016/J.JENVMAN.2017.07.011>
- Alkathiri, R., Alshamrani, A., Wazeer, I., Boumaza, M., Hadj-Kali, M.K., 2022. Optimization of the Oxidative Coupling of Methane Process for Ethylene Production. *Processes* 10, 1085.
- Alotaibi, F.M., González-Cortés, S., Alotibi, M.F., Xiao, T., Al-Megren, H., Yang, G.,

- Edwards, P.P., 2018. Enhancing the production of light olefins from heavy crude oils: Turning challenges into opportunities. *Catal. Today* 317, 86–98. <https://doi.org/10.1016/J.CATTOD.2018.02.018>
- Amghizar, I., Vandewalle, L.A., Van Geem, K.M., Marin, G.B., 2017a. New trends in olefin production. *Engineering* 3, 171–178.
- Amghizar, I., Vandewalle, L.A., Van Geem, K.M., Marin, G.B., 2017b. New Trends in Olefin Production. *Engineering* 3, 171–178. <https://doi.org/10.1016/J.ENG.2017.02.006>
- Amiri, A., Shanbedi, M., Savari, M., Chew, B.T., Kazi, S.N., 2015. Cadmium ion sorption from aqueous solutions by high surface area ethylenediaminetetraacetic acid-and diethylene triamine pentaacetic acid-treated carbon nanotubes. *RSC Adv.* 5, 71144–71152.
- Anderson, R.B., Hall, W.K., Krieg, A., Seligman, B., 1949. Studies of the Fischer–Tropsch synthesis. v. Activities and surface areas of reduced and carburized cobalt catalysts. *J. Am. Chem. Soc.* 71, 183–188.
- Arsalanfar, M., Mirzaei, A.A., Atashi, H., Bozorgzadeh, H.R., Vahid, S., Zare, A., 2012. An investigation of the kinetics and mechanism of Fischer–Tropsch synthesis on Fe–Co–Mn supported catalyst. *Fuel Process. Technol.* 96, 150–159.
- Atashi, H., Siami, F., Mirzaei, A.A., Sarkari, M., 2010. Kinetic study of Fischer–Tropsch process on titania-supported cobalt–manganese catalyst. *J. Ind. Eng. Chem.* 16, 952–961. <https://doi.org/10.1016/J.JIEC.2010.04.005>
- Atchudan, R., Cha, B.G., Lone, N., Kim, J., Joo, J., 2019. Synthesis of high-quality carbon nanotubes by using monodisperse spherical mesoporous silica encapsulating iron oxide nanoparticles. *Korean J. Chem. Eng* 36, 157–165. <https://doi.org/10.1007/s11814-018-0200-z>
- Aziz, M., Chowdhury, I.R., Mazumder, M.A.J., Chowdhury, S., 2019. Highly porous carboxylated activated carbon from jute stick for removal of Pb²⁺ from aqueous solution. *Environ. Sci. Pollut. Res.* 26, 22656–22669.
- Badoga, S., Kamath, G., Dalai, A., 2020. Effects of promoters (Mn, Mg, Co and Ni) on the Fischer-Tropsch activity and selectivity of KCuFe/mesoporous-alumina catalyst. *Appl. Catal. A Gen.* 607, 117861. <https://doi.org/10.1016/J.APCATA.2020.117861>

- Badoga, S., Sohani, K., Zheng, Y., Dalai, A.K., 2017a. Mesoporous alumina and alumina-titania supported KCuFe catalyst for Fischer-Tropsch synthesis: Effects of CO₂ and CH₄ present in syngas. *Fuel Process. Technol.* 168, 140–151. <https://doi.org/10.1016/J.FUPROC.2017.08.033>
- Badoga, S., Vosoughi, V., Dalai, A.K., 2017b. Performance of Promoted Iron/CNT Catalyst for Fischer–Tropsch Synthesis: Influence of Pellet Shapes and Binder Loading. *Energy Fuels* 31, 12633–12644. <https://doi.org/10.1021/acs.energyfuels.7b01318>
- Bae, J.-S., Hong, S.Y., Park, J.C., Rhim, G.B., Youn, M.H., Jeong, H., Kang, S.W., Yang, J.-I., Jung, H., Chun, D.H., 2019. Eco-friendly prepared iron-ore-based catalysts for Fischer-Tropsch synthesis. *Appl. Catal. B Environ.* 244, 576–582.
- Bahome, M.C., Jewell, L.L., Padayachy, K., Hildebrandt, D., Glasser, D., Datye, A.K., Coville, N.J., 2007. Fe-Ru small particle bimetallic catalysts supported on carbon nanotubes for use in Fischer–Tröpsch synthesis. *Appl. Catal. A Gen.* 328, 243–251.
- Baliban, R.C., Elia, J.A., Floudas, C.A., 2013. Biomass and natural gas to liquid transportation fuels: process synthesis, global optimization, and topology analysis. *Ind. Eng. Chem. Res.* 52, 3381–3406.
- Bankole, M.T., Mohammed, I.A., Abdulkareem, A.S., Tijani, J.O., Ochigbo, S.S., Abubakre, O.K., Afolabi, A.S., 2018. Optimization of supported bimetallic (Fe-Co/CaCO₃) catalyst synthesis parameters for carbon nanotubes growth using factorial experimental design. *J. Alloys Compd.* 749, 85–102. <https://doi.org/10.1016/J.JALLCOM.2018.03.150>
- Barreca, D., Blau, W.J., Croke, G.M., Deeney, F.A., Dillon, F.C., Holmes, J.D., Kufazvinei, C., Morris, M.A., Spalding, T.R., Tondello, E., 2007. Iron oxide nanoparticle impregnated mesoporous silicas as platforms for the growth of carbon nanotubes. *Microporous Mesoporous Mater.* 103, 142–149. <https://doi.org/10.1016/J.MICROMESO.2007.01.041>
- Barrios, A.J., Gu, B., Luo, Y., Peron, D. V., Chernavskii, P.A., Virginie, M., Wojcieszak, R., Thybaut, J.W., Ordonsky, V. V., Khodakov, A.Y., 2020. Identification of efficient promoters and selectivity trends in high temperature Fischer-Tropsch synthesis over supported iron catalysts. *Appl. Catal. B Environ.* 273, 119028. <https://doi.org/10.1016/J.APCATB.2020.119028>

- Behbahani, R.M., Rostami, R.B., Lemraski, A.S., 2014. Methanol/dimethyl ether to light olefins over SAPO-34: Comprehensive comparison of the products distribution and catalyst performance. *J. Nat. Gas Sci. Eng.* 21, 532–539.
- Behnam, R., Roghani-Mamaqani, H., Salami-Kalajahi, M., 2019. Preparation of carbon nanotube and polyurethane-imide hybrid composites by sol–gel reaction. *Polym. Compos.* 40, E1903–E1909.
- Ben Hnich, K., Martín-Gamboa, M., Khila, Z., Hajjaji, N., Dufour, J., Iribarren, D., 2021. Life cycle sustainability assessment of synthetic fuels from date palm waste. *Sci. Total Environ.* 796, 148961. <https://doi.org/10.1016/J.SCITOTENV.2021.148961>
- Bertella, F., Lopes, C.W., Foucher, A.C., Agostini, G., Concepción, P., Stach, E.A., Martínez, A., 2020. Insights into the Promotion with Ru of Co/TiO₂ Fischer–Tropsch Catalysts: An In Situ Spectroscopic Study. *ACS Catal.* 10, 6042–6057. <https://doi.org/10.1021/acscatal.9b05359>
- Bhatelia, T., Li, C., Sun, Y., Hazewinkel, P., Burke, N., Sage, V., 2014. Chain length dependent olefin re-adsorption model for Fischer–Tropsch synthesis over Co-Al₂O₃ catalyst. *Fuel Process. Technol.* 125, 277–289. <https://doi.org/10.1016/J.FUPROC.2014.03.028>
- Biloen, P., Helle, J.N., Van den Berg, F.G.A., Sachtler, W.M.H., 1983. On the activity of Fischer-Tropsch and methanation catalysts: A study utilizing isotopic transients. *J. Catal.* 81, 450–463.
- Boahene, P.E., Vedachalam, S., Dalai, A.K., 2022. Catalytic oxidative desulfurization of light gas oil over Keggin-type phosphomolybdic acid supported on TUD-1 metallosilicates. *Fuel* 317, 123447. <https://doi.org/10.1016/J.FUEL.2022.123447>
- Bora Ye, Sun-I Kim, Minwoo Lee, Mohammadamin Ezazi, Hong-Dae Kim, Gibum Kwon, Hyun Lee, D., 2020. Synthesis of oxygen functionalized carbon nanotubes and their application for selective catalytic reduction of NO_x with NH₃. *RSC Adv.* 10, 16700–16708. <https://doi.org/10.1039/D0RA01665A>
- Borugadda, V.B., Kamath, G., Dalai, A.K., 2020. Techno-economic and life-cycle assessment of integrated Fischer-Tropsch process in ethanol industry for bio-diesel and bio-gasoline production. *Energy* 195, 116985. <https://doi.org/10.1016/J.ENERGY.2020.116985>

- Botes, F.G., Breman, B.B., 2006. Development and testing of a new macro kinetic expression for the iron-based low-temperature Fischer– Tropsch reaction. *Ind. Eng. Chem. Res.* 45, 7415–7426.
- Botes, G.F., Bromfield, T.C., Coetzer, R.L.J., Crous, R., Gibson, P., Ferreira, A.C., 2016. Development of a chemical selective iron Fischer Tropsch catalyst. *Catal. Today* 275, 40–48.
- Browne, L.H., 1953. Pump.
- Bukur, D.B., Lang, X., Akgerman, A., Feng, Z., 1997. Effect of process conditions on olefin selectivity during conventional and supercritical Fischer– Tropsch synthesis. *Ind. Eng. Chem. Res.* 36, 2580–2587.
- Campanario, F.J., Gutiérrez Ortiz, F.J., 2017. Techno-economic assessment of bio-oil aqueous phase-to-liquids via Fischer-Tropsch synthesis and based on supercritical water reforming. *Energy Convers. Manag.* 154, 591–602. <https://doi.org/10.1016/J.ENCONMAN.2017.10.096>
- Cao, R., Thapa, R., Kim, H., Xu, X., Kim, M.G., Li, Q., Park, N., Liu, M., Cho, J., 2013. Promotion of oxygen reduction by a bio-inspired tethered iron phthalocyanine carbon nanotube-based catalyst. *Nat. Commun.* 2013 41 4, 1–7. <https://doi.org/10.1038/ncomms3076>
- Chai, S.-H., Schwartz, V., Howe, J.Y., Wang, X., Kidder, M., Overbury, S.H., Dai, S., Jiang, D., 2013. Graphitic mesoporous carbon-supported molybdenum carbides for catalytic hydrogenation of carbon monoxide to mixed alcohols. *Microporous mesoporous Mater.* 170, 141–149.
- Chang, Q., Zhang, C., Liu, C., Wei, Y., Cheruvathur, A. V., Dugulan, A.I., Niemantsverdriet, J.W., Liu, X., He, Y., Qing, M., Zheng, L., Yun, Y., Yang, Y., Li, Y., 2018a. Relationship between Iron Carbide Phases (ϵ -Fe₂C, Fe₇C₃, and χ -Fe₅C₂) and Catalytic Performances of Fe/SiO₂ Fischer-Tropsch Catalysts. *ACS Catal.* 8, 3304–3316. https://doi.org/10.1021/ACSCATAL.7B04085/SUPPL_FILE/CS7B04085_SI_001.PDF
- Chang, Q., Zhang, C., Liu, C., Wei, Y., Cheruvathur, A. V., Dugulan, A.I., Niemantsverdriet, J.W., Liu, X., He, Y., Qing, M., 2018b. Relationship between iron carbide phases (ϵ -Fe₂C,

- Fe₇C₃, and χ -Fe₅C₂) and catalytic performances of Fe/SiO₂ Fischer–Tropsch catalysts. *ACS Catal.* 8, 3304–3316.
- Chen, B., Zhang, X., Chen, W., Wang, D., Song, N., Qian, G., Duan, X., Yang, J., Chen, D., Yuan, W., Zhou, X., 2018. Tailoring of Fe/MnK-CNTs composite catalysts for the fischer-tropsch synthesis of lower olefins from syngas. *Ind. Eng. Chem. Res.* 57, 11554–11560. https://doi.org/10.1021/ACS.IECR.8B01795/SUPPL_FILE/IE8B01795_SI_001.PDF
- Chen, W., Pan, X., Bao, X., 2007. Tuning of redox properties of iron and iron oxides via encapsulation within carbon nanotubes. *J. Am. Chem. Soc.* 129, 7421–7426.
- Chen, Y., Li, X., Nisa, M.U., Lv, J., Li, Z., 2019. ZIF-67 as precursor to prepare high loading and dispersion catalysts for Fischer-Tropsch synthesis: Particle size effect. *Fuel* 241, 802–812.
- Cheng, K., Kang, J., King, D.L., Subramanian, V., Zhou, C., Zhang, Q., Wang, Y., 2017. Chapter Three - Advances in Catalysis for Syngas Conversion to Hydrocarbons, in: Song, C.B.T.-A. in C. (Ed.), . Academic Press, pp. 125–208. <https://doi.org/https://doi.org/10.1016/bs.acat.2017.09.003>
- Cheng, K., Ordonsky, V. V., Legras, B., Virginie, M., Paul, S., Wang, Y., Khodakov, A.Y., 2015a. Sodium-promoted iron catalysts prepared on different supports for high temperature Fischer-Tropsch synthesis. *Appl. Catal. A Gen.* 502, 204–214. <https://doi.org/10.1016/j.apcata.2015.06.010>
- Cheng, K., Ordonsky, V. V., Legras, B., Virginie, M., Paul, S., Wang, Y., Khodakov, A.Y., 2015b. Sodium-promoted iron catalysts prepared on different supports for high temperature Fischer–Tropsch synthesis. *Appl. Catal. A Gen.* 502, 204–214. <https://doi.org/10.1016/J.APCATA.2015.06.010>
- Cheng, K., Ordonsky, V. V., Virginie, M., Legras, B., Chernavskii, P.A., Kazak, V.O., Cordier, C., Paul, S., Wang, Y., Khodakov, A.Y., 2014. Support effects in high temperature Fischer-Tropsch synthesis on iron catalysts. *Appl. Catal. A Gen.* 488, 66–77. <https://doi.org/10.1016/J.APCATA.2014.09.033>
- Cheng, K., Virginie, M., Ordonsky, V. V., Cordier, C., Chernavskii, P.A., Ivantsov, M.I., Paul, S., Wang, Y., Khodakov, A.Y., 2015c. Pore size effects in high-temperature Fischer–

- Tropsch synthesis over supported iron catalysts. *J. Catal.* 328, 139–150. <https://doi.org/10.1016/J.JCAT.2014.12.007>
- Cheng, Y., Lin, J., Xu, K., Wang, H., Yao, X., Pei, Y., Yan, S., Qiao, M., Zong, B., 2016. Fischer-Tropsch Synthesis to Lower Olefins over Potassium-Promoted Reduced Graphene Oxide Supported Iron Catalysts. *ACS Catal.* 6, 389–399. https://doi.org/10.1021/ACSCATAL.5B02024/SUPPL_FILE/CS5B02024_SI_001.PDF
- Cheng, Y., Qiao, M., Zong, B., 2017. Fischer–Tropsch Synthesis, in: Abraham, M.A.B.T.-E. of S.T. (Ed.), . Elsevier, Oxford, pp. 403–410. <https://doi.org/https://doi.org/10.1016/B978-0-12-409548-9.10107-1>
- Chernyak, S.A., Ivanov, A.S., Maksimov, S. V., Maslakov, K.I., Isaikina, O.Y., Chernavskii, P.A., Kazantsev, R. V., Eliseev, O.L., Savilov, S.S., 2020. Fischer-Tropsch synthesis over carbon-encapsulated cobalt and iron nanoparticles embedded in 3D-framework of carbon nanotubes. *J. Catal.* 389, 270–284. <https://doi.org/10.1016/J.JCAT.2020.06.011>
- Chernyak, S.A., Ivanov, A.S., Maslakov, K.I., Egorov, A. V, Shen, Z., Savilov, S.S., Lunin, V. V, 2017. Oxidation, defunctionalization and catalyst life cycle of carbon nanotubes: a Raman spectroscopy view. *Phys. Chem. Chem. Phys.* 19, 2276–2285.
- Chew, L.M., Xia, W., Düdder, H., Weide, P., Ruland, H., Muhler, M., 2016. On the role of the stability of functional groups in multi-walled carbon nanotubes applied as support in iron-based high-temperature Fischer–Tropsch synthesis. *Catal. Today* 270, 85–92. <https://doi.org/https://doi.org/10.1016/j.cattod.2015.09.023>
- Cho, J.M., Ahn, C. Il, Pang, C., Bae, J.W., 2015. Fischer–Tropsch synthesis on Co/AlSBA-15: effects of hydrophilicity of supports on cobalt dispersion and product distributions. *Catal. Sci. Technol.* 5, 3525–3535.
- Cuéllar-Franca, R., García-Gutiérrez, P., Dimitriou, I., Elder, R.H., Allen, R.W.K., Azapagic, A., 2019. Utilising carbon dioxide for transport fuels: The economic and environmental sustainability of different Fischer-Tropsch process designs. *Appl. Energy* 253, 113560.
- Dai, Y., Zhao, Y., Lin, T., Li, S., Yu, F., An, Y., Wang, X., Xiao, K., Sun, F., Jiang, Z., Lu, Y., Wang, H., Zhong, L., Sun, Y., 2019. Particle Size Effects of Cobalt Carbide for Fischer-Tropsch to Olefins. *ACS Catal.* 9, 798–809.

<https://doi.org/10.1021/ACSCATAL.8B03631>

- De La Osa, A.R., De Lucas, A., Romero, A., Valverde, J.L., Sánchez, P., 2011. Fischer–Tropsch diesel production over calcium-promoted Co/alumina catalyst: Effect of reaction conditions. *Fuel* 90, 1935–1945.
- De Menezes, B.R.C., Ferreira, F. V, Silva, B.C., Simonetti, E.A.N., Bastos, T.M., Cividanes, L.S., Thim, G.P., 2018. Effects of octadecylamine functionalization of carbon nanotubes on dispersion, polarity, and mechanical properties of CNT/HDPE nanocomposites. *J. Mater. Sci.* 53, 14311–14327.
- De Smit, E., Weckhuysen, B.M., 2008. The renaissance of iron -based Fischer–Tropsch synthesis: on the multifaceted catalyst deactivation behaviour. *Chem. Soc. Rev.* 37, 2758–2781. <https://doi.org/10.1039/B805427D>
- Di, Z., Zhao, T., Feng, X., Luo, M., 2019a. A Newly Designed Core-Shell-Like Zeolite Capsule Catalyst for Synthesis of Light Olefins from Syngas via Fischer–Tropsch Synthesis Reaction. *Catal. Letters* 149, 441–448. <https://doi.org/10.1007/S10562-018-2624-9/FIGURES/5>
- Di, Z., Zhao, T., Feng, X., Luo, M., 2019b. A Newly Designed Core-Shell-Like Zeolite Capsule Catalyst for Synthesis of Light Olefins from Syngas via Fischer–Tropsch Synthesis Reaction. *Catal. Letters* 149, 441–448.
- Diao, X., Ji, N., Li, X., Rong, Y., Zhao, Y., Lu, X., Song, C., Liu, C., Chen, G., Ma, L., Wang, S., Liu, Q., Li, C., 2022. Fabricating high temperature stable Mo-Co₉S₈/Al₂O₃ catalyst for selective hydrodeoxygenation of lignin to arenes. *Appl. Catal. B Environ.* 305, 121067. <https://doi.org/10.1016/J.APCATB.2022.121067>
- Díaz, J.A., Akhavan, H., Romero, A., Garcia-Minguillan, A.M., Romero, R., Giroir-Fendler, A., Valverde, J.L., 2014. Cobalt and iron supported on carbon nanofibers as catalysts for Fischer–Tropsch synthesis. *Fuel Process. Technol.* 128, 417–424. <https://doi.org/10.1016/J.FUPROC.2014.08.005>
- Dimian, A.C., Bildea, C.S., 2018. Energy efficient methanol-to-olefins process. *Chem. Eng. Res. Des.* 131, 41–54.
- Dimitriou, I., Goldingay, H., Bridgwater, A. V., 2018. Techno-economic and uncertainty

- analysis of Biomass to Liquid (BTL) systems for transport fuel production. *Renew. Sustain. Energy Rev.* 88, 160–175. <https://doi.org/10.1016/J.RSER.2018.02.023>
- Do, T.N., Kim, J., 2020. Green C2-C4 hydrocarbon production through direct CO₂ hydrogenation with renewable hydrogen: Process development and techno-economic analysis. *Energy Convers. Manag.* 214, 112866. <https://doi.org/10.1016/J.ENCONMAN.2020.112866>
- Duan, X., Wang, D., Qian, G., Walmsley, J.C., Holmen, A., Chen, D., Zhou, X., 2016. Fabrication of K-promoted iron/carbon nanotubes composite catalysts for the Fischer–Tropsch synthesis of lower olefins. *J. Energy Chem.* 25, 311–317. <https://doi.org/10.1016/J.JECHEM.2016.01.003>
- El-Ahwany, O.M., Awadallah, A.E., Aboul-Enein, A.A., Abdel-Azim, S.M., Aboul-Gheit, N.A.K., Abo-EL-Enein, S.A., 2020. Dual growth of graphene nanoplatelets and carbon nanotubes hybrid structure via chemical vapor deposition of methane over Fe–MgO catalysts. *Fullerenes, Nanotub. Carbon Nanostructures* 28, 435–445.
- Energy Information Administration, U., n.d. AEO2022 Narrative.
- Eshraghi, A., Mirzaei, A.A., Rahimi, R., Atashi, H., 2020. Fischer-Tropsch Synthesis on Fe-Co-Pt/□-Al₂O₃ catalyst: A mass transfer, kinetic and mechanistic study. *Korean J. Chem. Eng* 37, 1699–1708. <https://doi.org/10.1007/s11814-020-0590-6>
- Farghali, A.A., Abdel Tawab, H.A., Abdel Moaty, S.A., Khaled, R., 2017. Functionalization of acidified multi-walled carbon nanotubes for removal of heavy metals in aqueous solutions. *J. Nanostructure Chem.* 2017 72 7, 101–111. <https://doi.org/10.1007/S40097-017-0227-4>
- Fellenberg, A.K., Addad, A., Hong, J., Simon, P., Kosto, Y., Šmíd, B., Ji, G., Khodakov, A.Y., 2021. Iron and copper nanoparticles inside and outside carbon nanotubes: Nanoconfinement, migration, interaction and catalytic performance in Fischer-Tropsch synthesis. *J. Catal.* 404, 306–323. <https://doi.org/10.1016/J.JCAT.2021.09.034>
- Feng Jiang, Min Zhang, Bing Liu, Yuebing Xu, Xiaohao Liu, 2017. Insights into the influence of support and potassium or sulfur promoter on iron-based Fischer–Tropsch synthesis: understanding the control of catalytic activity, selectivity to lower olefins, and catalyst

- deactivation. *Catal. Sci. Technol.* 7, 1245–1265. <https://doi.org/10.1039/C7CY00048K>
- Feng, Y., Wang, J., Hu, Y., Lu, J., Zhang, M., Mi, J., 2020. Microwave heating motivated performance promotion and kinetic study of iron oxide sorbent for coal gas desulfurization. *Fuel* 267, 117215. <https://doi.org/10.1016/J.FUEL.2020.117215>
- Feyzi, M., Khodaei, M.M., Shahmoradi, J., 2014. Effect of sulfur on the catalytic performance of Fe–Ni/Al₂O₃ catalysts for light olefins production. *J. Taiwan Inst. Chem. Eng.* 45, 452–460.
- Filot, I.A.W., Broos, R.J.P., van Rijn, J.P.M., van Heugten, G.J.H.A., van Santen, R.A., Hensen, E.J.M., 2015. First-principles-based microkinetics simulations of synthesis gas conversion on a stepped rhodium surface. *ACS Catal.* 5, 5453–5467.
- Fleming, E., Du, F., Ou, E., Dai, L., Shi, L., 2019. Thermal conductivity of carbon nanotubes grown by catalyst-free chemical vapor deposition in nanopores. *Carbon N. Y.* 145, 195–200. <https://doi.org/10.1016/J.CARBON.2019.01.023>
- Förtsch, D., Pabst, K., Groß-Hardt, E., 2015. The product distribution in Fischer–Tropsch synthesis: An extension of the ASF model to describe common deviations. *Chem. Eng. Sci.* 138, 333–346.
- Fu, T., Li, Z., 2015. Review of recent development in Co-based catalysts supported on carbon materials for Fischer–Tropsch synthesis. *Chem. Eng. Sci.* 135, 3–20. <https://doi.org/10.1016/J.CES.2015.03.007>
- Fusco, R., Sansone, M., Petrillo, A., 2015. The use of the Levenberg–Marquardt and variable projection curve-fitting algorithm in intravoxel incoherent motion method for DW-MRI data analysis. *Appl. Magn. Reson.* 46, 551–558.
- Gabriel, K.J., Linke, P., Jiménez-Gutiérrez, A., Martínez, D.Y., Noureldin, M., El-Halwagi, M.M., 2014. Targeting of the water-energy nexus in gas-to-liquid processes: A comparison of syngas technologies. *Ind. Eng. Chem. Res.* 53, 7087–7102. https://doi.org/10.1021/IE4042998/ASSET/IMAGES/IE-2013-042998_M021.GIF
- Galvis, H.M.T., Koeken, A.C.J., Bitter, J.H., Davidian, T., Ruitenbeek, M., Dugulan, A.I., de Jong, K.P., 2013. Effects of sodium and sulfur on catalytic performance of supported iron catalysts for the Fischer–Tropsch synthesis of lower olefins. *J. Catal.* 303, 22–30.

- Gao, X., Zhang, J., Chen, N., Ma, Q., Fan, S., Zhao, T., Tsubaki, N., 2016. Effects of zinc on Fe-based catalysts during the synthesis of light olefins from the Fischer-Tropsch process. *Chinese J. Catal.* 37, 510–516. [https://doi.org/10.1016/S1872-2067\(15\)61051-8](https://doi.org/10.1016/S1872-2067(15)61051-8)
- Garona, H.A., Cavalcanti, F.M., de Abreu, T.F., Schmal, M., Alves, R.M.B., 2021. Evaluation of Fischer-Tropsch synthesis to light olefins over Co- and Fe-based catalysts using artificial neural network. *J. Clean. Prod.* 321, 129003. <https://doi.org/10.1016/J.JCLEPRO.2021.129003>
- Gavrilović, L., Jørgensen, E.A., Pandey, U., Putta, K.R., Rout, K.R., Rytter, E., Hillestad, M., Blekkan, E.A., 2021. Fischer-Tropsch synthesis over an alumina-supported cobalt catalyst in a fixed bed reactor—Effect of process parameters. *Catal. Today* 369, 150–157.
- Ghofran Pakdel, M., Atashi, H., Zohdi-Fasaei, H., Mirzaei, A.A., 2019. Effect of temperature on deactivation models of alumina supported iron catalyst during Fischer-Tropsch synthesis. *Pet. Sci. Technol.* 37, 500–505.
- Gholami, Z., Gholami, F., Tišler, Z., Vakili, M., 2021. A Review on the Production of Light Olefins Using Steam Cracking of Hydrocarbons. <https://doi.org/10.3390/en14238190>
- Gong, W., Ye, R.P., Ding, J., Wang, T., Shi, X., Russell, C.K., Tang, J., Eddings, E.G., Zhang, Y., Fan, M., 2020. Effect of copper on highly effective Fe-Mn based catalysts during production of light olefins via Fischer-Tropsch process with low CO₂ emission. *Appl. Catal. B Environ.* 278, 119302. <https://doi.org/10.1016/J.APCATB.2020.119302>
- Gu, B., He, S., Peron, D. V., Strossi Pedrolo, D.R., Moldovan, S., Ribeiro, M.C., Lobato, B., Chernavskii, P.A., Ordonsky, V. V., Khodakov, A.Y., 2019a. Synergy of nanoconfinement and promotion in the design of efficient supported iron catalysts for direct olefin synthesis from syngas. *J. Catal.* 376, 1–16. <https://doi.org/10.1016/J.JCAT.2019.06.035>
- Gu, B., He, S., Peron, D. V., Strossi Pedrolo, D.R., Moldovan, S., Ribeiro, M.C., Lobato, B., Chernavskii, P.A., Ordonsky, V. V., Khodakov, A.Y., 2019b. Synergy of nanoconfinement and promotion in the design of efficient supported iron catalysts for direct olefin synthesis from syngas. *J. Catal.* 376, 1–16.

<https://doi.org/10.1016/j.jcat.2019.06.035>

- Gu, B., He, S., Zhou, W., Kang, J., Cheng, K., Zhang, Q., Wang, Y., 2017. Polyaniline-supported iron catalyst for selective synthesis of lower olefins from syngas. *J. Energy Chem.* 26, 608–615. <https://doi.org/10.1016/J.JECHEM.2017.04.009>
- Gu, B., Ordonsky, V. V., Bahri, M., Ersen, O., Chernavskii, P.A., Filimonov, D., Khodakov, A.Y., 2018a. Effects of the promotion with bismuth and lead on direct synthesis of light olefins from syngas over carbon nanotube supported iron catalysts. *Appl. Catal. B Environ.* 234, 153–166. <https://doi.org/10.1016/J.APCATB.2018.04.025>
- Gu, B., Ordonsky, V. V., Bahri, M., Ersen, O., Chernavskii, P.A., Filimonov, D., Khodakov, A.Y., 2018b. Effects of the promotion with bismuth and lead on direct synthesis of light olefins from syngas over carbon nanotube supported iron catalysts. *Appl. Catal. B Environ.* 234, 153–166. <https://doi.org/10.1016/j.apcatb.2018.04.025>
- Gu, B., Ordonsky, V. V., Bahri, M., Ersen, O., Chernavskii, P.A., Filimonov, D., Khodakov, A.Y., 2018c. Effects of the promotion with bismuth and lead on direct synthesis of light olefins from syngas over carbon nanotube supported iron catalysts. *Appl. Catal. B Environ.* 234, 153–166. <https://doi.org/10.1016/j.apcatb.2018.04.025>
- Gu, B., Peron, D. V., Barrios, A.J., Virginie, M., La Fontaine, C., Briois, V., Vorokhta, M., Šmíd, B., Moldovan, S., Koneti, S., Gambu, T.G., Saeys, M., Ordonsky, V. V., Khodakov, A.Y., 2021. Bismuth mobile promoter and cobalt-bismuth nanoparticles in carbon nanotube supported Fischer-Tropsch catalysts with enhanced stability. *J. Catal.* 401, 102–114. <https://doi.org/10.1016/J.JCAT.2021.07.011>
- Gu, B., Zhou, C., He, S., Moldovan, S., Chernavskii, P.A., Ordonsky, V. V., Khodakov, A.Y., 2020a. Size and promoter effects on iron nanoparticles confined in carbon nanotubes and their catalytic performance in light olefin synthesis from syngas. *Catal. Today* 357, 203–213. <https://doi.org/10.1016/J.CATTOD.2019.05.054>
- Gu, B., Zhou, C., He, S., Moldovan, S., Chernavskii, P.A., Ordonsky, V. V., Khodakov, A.Y., 2020b. Size and promoter effects on iron nanoparticles confined in carbon nanotubes and their catalytic performance in light olefin synthesis from syngas. *Catal. Today* 357, 203–213. <https://doi.org/10.1016/j.cattod.2019.05.054>

- Guo, S., Li, C., You, L., Yang, W., Li, J., Zhou, K., 2021. Facile Synthesis of AgFeO₂-Decorated CaCO₃ with Enhanced Catalytic Activity in Activation of Peroxymonosulfate for Efficient Degradation of Organic Pollutants. *Adv. Energy Sustain. Res.* 2, 2100038.
- Gutiérrez Ortiz, F.J., Alonso-Fariñas, B., Campanario, F.J., Kruse, A., 2020. Life cycle assessment of the Fischer-Tropsch biofuels production by supercritical water reforming of the bio-oil aqueous phase. *Energy* 210, 118648. <https://doi.org/10.1016/J.ENERGY.2020.118648>
- Hassankiadeh, M.N., Khajehfard, A., Golmohammadi, M., 2012. Kinetic and product distribution modeling of Fischer-Tropsch synthesis in a fluidized bed reactor. *Int. J. Chem. Eng. Appl.* 3, 400.
- Hazemann, P., Decottignies, D., Maury, S., Humbert, S., Berliet, A., Daniel, C., Schuurman, Y., 2020. Kinetic data acquisition in high-throughput Fischer–Tropsch experimentation. *Catal. Sci. Technol.* 10, 7331–7343.
- Herz, G., Reichelt, E., Jahn, M., 2018. Techno-economic analysis of a co-electrolysis-based synthesis process for the production of hydrocarbons. *Appl. Energy* 215, 309–320.
- Holger, P.L.K., 1954. Liquid heater.
- Hong, J., Du, J., Wang, B., Zhang, Y., Liu, C., Xiong, H., Sun, F., Chen, S., Li, J., 2018. Plasma-assisted preparation of highly dispersed cobalt catalysts for enhanced Fischer–Tropsch synthesis performance. *ACS Catal.* 8, 6177–6185.
- Hsu, K.-H., Wang, W.-C., Liu, Y.-C., 2018. Experimental studies and techno-economic analysis of hydro-processed renewable diesel production in Taiwan. *Energy* 164, 99–111.
- Huang, S., Liu, C., Chen, Y., Hong, J., Zhao, Y., Zhang, Y., Li, J., 2020. The effect of Mn on the performance of MCF-supported highly dispersed iron catalysts for Fischer–Tropsch synthesis. *Catal. Sci. Technol.* 10, 502–509.
- Huang, Y., Yi, Q., Wei, G. qiang, Kang, J. xian, Li, W. ying, Feng, J., Xie, K. chang, 2018. Energy use, greenhouse gases emission and cost effectiveness of an integrated high– and low–temperature Fisher–Tropsch synthesis plant from a lifecycle viewpoint. *Appl. Energy* 228, 1009–1019. <https://doi.org/10.1016/J.APENERGY.2018.07.007>

- Hwang, S.M., Zhang, C., Han, S.J., Park, H.G., Kim, Y.T., Yang, S., Jun, K.W., Kim, S.K., 2020. Mesoporous carbon as an effective support for Fe catalyst for CO₂ hydrogenation to liquid hydrocarbons. *J. CO₂ Util.* 37, 65–73. <https://doi.org/10.1016/J.JCOU.2019.11.025>
- Iablokov, V., Kruse, N., 2019. Discovery of a Fischer-Tropsch Hybrid Reaction: Hydrogenation of Methylformate to Long-Chain Hydrocarbons with Anderson-Schulz-Flory Chain Length Distribution. *ChemCatChem* 11, 1200–1204.
- Jahangiri, H., Bennett, J., Mahjoubi, P., Wilson, K., Gu, S., 2014. A review of advanced catalyst development for Fischer–Tropsch synthesis of hydrocarbons from biomass derived syngas. *Catal. Sci. Technol.* 4, 2210–2229.
- Jiang, F., Zhang, M., Liu, B., Xu, Y., Liu, X., 2017. Insights into the influence of support and potassium or sulfur promoter on iron-based Fischer–Tropsch synthesis: understanding the control of catalytic activity, selectivity to lower olefins, and catalyst deactivation. *Catal. Sci. Technol.* 7, 1245–1265. <https://doi.org/10.1039/C7CY00048K>
- Jiang, H., Yao, Y., Zhu, Y., Liu, Y., Su, Y., Yang, X., Li, C., 2015. Iron Carbide Nanoparticles Encapsulated in Mesoporous Fe–N-Doped Graphene-Like Carbon Hybrids as Efficient Bifunctional Oxygen Electrocatalysts. *ACS Appl. Mater. Interfaces* 7, 21511–21520. <https://doi.org/10.1021/acsami.5b06708>
- Jiao, F., Li, J., Pan, X., Xiao, J., Li, H., Ma, H., Wei, M., Pan, Y., Zhou, Z., Li, M., 2016. Selective conversion of syngas to light olefins. *Science* (80-.). 351, 1065–1068.
- Johnson, G.R., Werner, S., Bell, A.T., 2015. An investigation into the effects of Mn promotion on the activity and selectivity of Co/SiO₂ for Fischer–Tropsch synthesis: evidence for enhanced CO adsorption and dissociation. *ACS Catal.* 5, 5888–5903.
- Junsittiwate, R., Srinophakun, T.R., Sukpancharoen, S., 2022. Techno-economic, environmental, and heat integration of palm empty fruit bunch upgrading for power generation. *Energy Sustain. Dev.* 66, 140–150. <https://doi.org/10.1016/J.ESD.2021.12.001>
- Karimifard, S., Alavi Moghaddam, M.R., 2016. Enhancing the adsorption performance of carbon nanotubes with a multistep functionalization method: Optimization of Reactive

- Blue 19 removal through response surface methodology. *Process Saf. Environ. Prot.* 99, 20–29. <https://doi.org/10.1016/J.PSEP.2015.10.007>
- Kazakov, M.O., Kazakova, M.A., Vatutina, Y. V., Larina, T. V., Chesalov, Y.A., Gerasimov, E.Y., Prosvirin, I.P., Klimov, O. V., Noskov, A.S., 2020. Comparative study of MWCNT and alumina supported CoMo hydrotreating catalysts prepared with citric acid as chelating agent. *Catal. Today* 357, 221–230. <https://doi.org/10.1016/J.CATTOD.2019.03.051>
- Kazakova, M.A., Andreev, A.S., Selyutin, A.G., Ishchenko, A. V., Shuvaev, A. V., Kuznetsov, V.L., Lapina, O.B., d’Espinose de Lacaillerie, J.B., 2018. Co metal nanoparticles deposition inside or outside multi-walled carbon nanotubes via facile support pretreatment. *Appl. Surf. Sci.* 456, 657–665. <https://doi.org/10.1016/J.APSUSC.2018.06.124>
- Kitakami, O., Sato, H., Shimada, Y., Sato, F., Tanaka, M., 1997. Size effect on the crystal phase of cobalt fine particles. *Phys. Rev. B* 56, 13849.
- Kreutz, T.G., Larson, E.D., Elsidio, C., Martelli, E., Greig, C., Williams, R.H., 2020. Techno-economic prospects for producing Fischer-Tropsch jet fuel and electricity from lignite and woody biomass with CO₂ capture for EOR. *Appl. Energy* 279, 115841.
- Kreutz, T.G., Larson, E.D., Liu, G., Williams, R.H., 2008. Fischer-Tropsch fuels from coal and biomass, in: 25th Annual International Pittsburgh Coal Conference. International Pittsburgh Coal Conference Pittsburgh, Pennsylvania.
- Kumar, A., Yasin, G., Vashistha, V.K., Das, D.K., Rehman, M.U., Iqbal, R., Mo, Z., Nguyen, T.A., Slimani, Y., Nazir, M.T., 2021. Enhancing oxygen reduction reaction performance via CNTs/graphene supported iron protoporphyrin IX: A hybrid nanoarchitecture electrocatalyst. *Diam. Relat. Mater.* 113, 108272.
- Lai, L., Ji, H., Zhang, H., Liu, R., Zhou, C., Liu, W., Ao, Z., Li, N., Liu, C., Yao, G., Lai, B., 2021. Activation of peroxydisulfate by V-Fe concentrate ore for enhanced degradation of carbamazepine: Surface $\equiv\text{V(III)}$ and $\equiv\text{V(IV)}$ as electron donors promoted the regeneration of $\equiv\text{Fe(II)}$. *Appl. Catal. B Environ.* 282, 119559. <https://doi.org/10.1016/J.APCATB.2020.119559>
- Lama, S.M.G., Weber, J.L., Heil, T., Hofmann, J.P., Yan, R., de Jong, K.P., Oschatz, M., 2018.

- Tandem promotion of iron catalysts by sodium-sulfur and nitrogen-doped carbon layers on carbon nanotube supports for the Fischer-Tropsch to olefins synthesis. *Appl. Catal. A Gen.* 568, 213–220. <https://doi.org/10.1016/J.APCATA.2018.09.016>
- Lee, J.H., Lee, H.K., Chun, D.H., Choi, H., Rhim, G.B., Youn, M.H., Jeong, H., Kang, S.W., Yang, J. Il, Jung, H., Kim, C.S., Park, J.C., 2019. Phase-controlled synthesis of thermally stable nitrogen-doped carbon supported iron catalysts for highly efficient Fischer-Tropsch synthesis. *Nano Res.* 2019 1210 12, 2568–2575. <https://doi.org/10.1007/S12274-019-2487-4>
- Lee, S., Seo, J.C., Chun, H.J., Yang, S., Sim, E.H., Lee, J., Kim, Y.T., 2022. Selective olefin production on silica based iron catalysts in Fischer–Tropsch synthesis. *Catal. Sci. Technol.* <https://doi.org/10.1039/D2CY00988A>
- Lewis, P.E., 2013. Gas to Liquids: Beyond Fischer Tropsch, in: SPE Asia Pacific Oil and Gas Conference and Exhibition. OnePetro.
- Li, C., Sayaka, I., Chisato, F., Fujimoto, K., 2016. Development of high performance graphite-supported iron catalyst for Fischer–Tropsch synthesis. *Appl. Catal. A Gen.* 509, 123–129.
- Li, J., Cheng, X., Zhang, C., Chang, Q., Wang, J., Wang, X., Lv, Z., Dong, W., Yang, Y., Li, Y., 2016. Effect of alkalis on iron-based Fischer-Tropsch synthesis catalysts: Alkali-FeOx interaction, reduction, and catalytic performance. *Appl. Catal. A Gen.* 528, 131–141.
- Li, J., Cheng, X., Zhang, C., Wang, J., Dong, W., Yang, Y., Li, Y., 2017. Alkalis in iron-based Fischer–Tropsch synthesis catalysts: distribution, migration and promotion. *J. Chem. Technol. Biotechnol.* 92, 1472–1480. <https://doi.org/10.1002/JCTB.5152>
- Li, L., Hu, C., Liu, W., Fei, P., Cui, X., Li, Y., Xu, J., 2017. The origin of Mo promotion during H₂ pretreatment on an Fe catalyst for Fischer–Tropsch synthesis. *RSC Adv.* 7, 44474–44481. <https://doi.org/10.1039/C7RA07338K>
- Li, M., Zhao, W., Xu, Y., Zhao, Y., Yang, K., Tao, W., Xiao, J., 2019. Comprehensive Life Cycle Evaluation of Jet Fuel from Biomass Gasification and Fischer-Tropsch Synthesis Based on Environmental and Economic Performances. *Ind. Eng. Chem. Res.* 58, 19179–19188. <https://doi.org/10.1021/acs.iecr.9b03468>
- LI, S., Shuai, L.Ü., ZHANG, Y., LI, J., LIU, Z., Li, W., 2018. Syngas-derived olefins over iron-

- based catalysts: Effects of basic properties of MgO nanocrystals. *J. Fuel Chem. Technol.* 46, 1342–1351.
- Li, T., Virginie, M., Khodakov, A.Y., 2017. Effect of potassium promotion on the structure and performance of alumina supported carburized molybdenum catalysts for Fischer-Tropsch synthesis. *Appl. Catal. A Gen.* 542, 154–162. <https://doi.org/10.1016/J.APCATA.2017.05.018>
- Li, Z., Lin, T., Yu, F., An, Y., Dai, Y., Li, S., Zhong, L., Wang, H., Gao, P., Sun, Y., 2017. Mechanism of the Mn promoter via CoMn spinel for morphology control: formation of Co₂C nanoprisms for Fischer–Tropsch to olefins reaction. *Acs Catal.* 7, 8023–8032.
- Li, Z., Liu, R., Xu, Y., Ma, X., 2015. Enhanced Fischer–Tropsch synthesis performance of iron-based catalysts supported on nitric acid treated N-doped CNTs. *Appl. Surf. Sci.* 347, 643–650.
- Li, Z., Sellaoui, L., Franco, D., Netto, M.S., Georgin, J., Dotto, G.L., Bajahzar, A., Belmabrouk, H., Bonilla-Petriciolet, A., Li, Q., 2020. Adsorption of hazardous dyes on functionalized multiwalled carbon nanotubes in single and binary systems: Experimental study and physicochemical interpretation of the adsorption mechanism. *Chem. Eng. J.* 389, 124467. <https://doi.org/10.1016/J.CEJ.2020.124467>
- Liang, P., Gao, H., Yao, Z., Jia, R., Shi, Y., Sun, Y., Fan, Q., Wang, H., 2017. Simple synthesis of ultrasmall β -Mo₂C and α -MoC_{1-x} nanoparticles and new insights into their catalytic mechanisms for dry reforming of methane. *Catal. Sci. Technol.* 7, 3312–3324.
- Lin, T., Gong, K., Wang, C., An, Y., Wang, X., Qi, X., Li, S., Lu, Y., Zhong, L., Sun, Y., 2019. Fischer–Tropsch synthesis to olefins: catalytic performance and structure evolution of Co₂C-based catalysts under a CO₂ environment. *ACS Catal.* 9, 9554–9567.
- Liu, B., Li, W., Xu, Y., Lin, Q., Jiang, F., Liu, X., 2019. Insight into the Intrinsic Active Site for Selective Production of Light Olefins in Cobalt-Catalyzed Fischer–Tropsch Synthesis. *ACS Catal.* 9, 7073–7089. <https://doi.org/10.1021/ACSCATAL.9B00352>
- Liu, C.M., Sandhu, N.K., McCoy, S.T., Bergerson, J.A., 2020. A life cycle assessment of greenhouse gas emissions from direct air capture and Fischer-Tropsch fuel production. *Sustain. Energy Fuels* 4, 3129–3142. <https://doi.org/10.1039/c9se00479c>

- Liu, G., Chen, Q., Oyunkhand, E., Ding, S., Yamane, N., Yang, G., Yoneyama, Y., Tsubaki, N., 2018. Nitrogen-rich mesoporous carbon supported iron catalyst with superior activity for Fischer-Tropsch synthesis. *Carbon* N. Y. 130, 304–314. <https://doi.org/10.1016/j.carbon.2018.01.015>
- Liu, J.X., Wang, P., Xu, W., Hensen, E.J.M., 2017. Particle Size and Crystal Phase Effects in Fischer-Tropsch Catalysts. *Engineering* 3, 467–476. <https://doi.org/10.1016/J.ENG.2017.04.012>
- Liu, W.-W., Aziz, A., Chai, S.-P., Rahman Mohamed, A., Hashim, U., 2013. Synthesis of Single-Walled Carbon Nanotubes: Effects of Active Metals, Catalyst Supports, and Metal Loading Percentage. *J. Nanomater.* 2013. <https://doi.org/10.1155/2013/592464>
- Liu, Y., Chen, J.-F., Zhang, Y., 2015a. The effect of pore size or iron particle size on the formation of light olefins in Fischer–Tropsch synthesis. *RSC Adv.* 5, 29002–29007.
- Liu, Y., Chen, J.F., Zhang, Y., 2015b. The effect of pore size or iron particle size on the formation of light olefins in Fischer–Tropsch synthesis. *RSC Adv.* 5, 29002–29007. <https://doi.org/10.1039/C5RA02319J>
- Liu, Y., Kamata, H., Ohara, H., Izumi, Y., Sze Wei Ong, D., Chang, J., Kok Poh, C., Chen, L., Borgna, A., 2020. Low-Olefin Production Process Based on Fischer–Tropsch Synthesis: Process Synthesis, Optimization, and Techno-Economic Analysis. <https://doi.org/10.1021/acs.iecr.0c00542>
- Liu, Y., Li, Z., Zhang, Y., 2016. Selectively forming light olefins via macroporous iron-based Fischer–Tropsch catalysts. *React. Kinet. Mech. Catal.* 119, 457–468.
- Liu, Z., Jia, G., Zhao, C., Xing, Y., 2021. Efficient Fischer-Tropsch to light olefins over iron-based catalyst with low methane selectivity and high olefin/paraffin ratio. *Fuel* 288, 119572. <https://doi.org/10.1016/J.FUEL.2020.119572>
- Lødeng, R., Lunder, O., Lein, J.-E., Dahl, P.I., Svenum, I.-H., 2018. Synthesis of light olefins and alkanes on supported iron oxide catalysts. *Catal. Today* 299, 47–59.
- Lu, J., Yang, L., Xu, B., Wu, Q., Zhang, D., Yuan, S., Zhai, Y., Wang, X., Fan, Y., Hu, Z., 2014a. Promotion effects of nitrogen doping into carbon nanotubes on supported iron fischer-tropsch catalysts for lower olefins. *ACS Catal.* 4, 613–621.

https://doi.org/10.1021/CS400931Z/SUPPL_FILE/CS400931Z_SI_001.PDF

- Lu, J., Yang, L., Xu, B., Wu, Q., Zhang, D., Yuan, S., Zhai, Y., Wang, X., Fan, Y., Hu, Z., 2014b. Promotion effects of nitrogen doping into carbon nanotubes on supported iron fischer-tropsch catalysts for lower olefins. *ACS Catal.* 4, 613–621. https://doi.org/10.1021/CS400931Z/SUPPL_FILE/CS400931Z_SI_001.PDF
- Lu, J., Yang, L., Xu, B., Wu, Q., Zhang, D., Yuan, S., Zhai, Y., Wang, X., Fan, Y., Hu, Z., 2014c. Promotion effects of nitrogen doping into carbon nanotubes on supported iron fischer-tropsch catalysts for lower olefins. *ACS Catal.* 4, 613–621. https://doi.org/10.1021/CS400931Z/SUPPL_FILE/CS400931Z_SI_001.PDF
- Luo, M., Li, S., Di, Z., Yang, Z., Chou, W., Shi, B., 2020. Fischer-Tropsch synthesis: Effect of nitric acid pretreatment on graphene-supported cobalt catalyst. *Appl. Catal. A Gen.* 599, 117608. <https://doi.org/10.1016/J.APCATA.2020.117608>
- Ma, W., Jacobs, G., Das, T.K., Masuku, C.M., Kang, J., Pendyala, V.R.R., Davis, B.H., Klettlinger, J.L.S., Yen, C.H., 2014. Fischer–Tropsch Synthesis: Kinetics and Water Effect on Methane Formation over 25%Co/ γ -Al₂O₃ Catalyst. *Ind. Eng. Chem. Res.* 53, 2157–2166. <https://doi.org/10.1021/ie402094b>
- Ma, W., Kugler, E.L., Dadyburjor, D.B., 2007. Effect of Mo loading and support type on hydrocarbons and oxygenates produced over Fe-Mo-Cu-K catalysts supported on activated carbons. *Stud. Surf. Sci. Catal.* 163, 125–140.
- Ma, W., Kugler, E.L., Wright, J., Dadyburjor, D.B., 2006. Mo-Fe Catalysts Supported on Activated Carbon for Synthesis of Liquid Fuels by the Fischer-Tropsch Process: Effect of Mo Addition on Reducibility, Activity, and Hydrocarbon Selectivity. *Energy Fuels* 20, 2299–2307. <https://doi.org/10.1021/ef0602372>
- Ma, W., Mao, J., Yang, X., Pan, C., Chen, W., Wang, M., Yu, P., Mao, L., Li, Y., 2019. A single-atom Fe–N₄ catalytic site mimicking bifunctional antioxidative enzymes for oxidative stress cytoprotection. *Chem. Commun.* 55, 159–162.
- Mahmoudi, H., Mahmoudi, M., Doustdar, O., Jahangiri, H., Tsolakis, A., Gu, S., LechWyszynski, M., 2017. A review of Fischer Tropsch synthesis process, mechanism, surface chemistry and catalyst formulation. *Biofuels Eng.* 2, 11–31.

<https://doi.org/10.1515/BFUEL-2017-0002>

- Malek Abbaslou, R.M., Soltan, J., Dalai, A.K., 2011. Iron catalyst supported on carbon nanotubes for Fischer-Tropsch synthesis: Effects of Mo promotion. *Fuel* 90, 1139–1144. <https://doi.org/10.1016/j.fuel.2010.10.044>
- Malek Abbaslou, R.M., Tavasoli, A., Dalai, A.K., 2009. Effect of pre-treatment on physico-chemical properties and stability of carbon nanotubes supported iron Fischer–Tropsch catalysts. *Appl. Catal. A Gen.* 355, 33–41. <https://doi.org/10.1016/J.APCATA.2008.11.023>
- Mansouri, M., Atashi, H., Tabrizi, F.F., Mirzaei, A.A., mansouri, G., 2013. Kinetics studies of nano-structured cobalt–manganese oxide catalysts in Fischer–Tropsch synthesis. *J. Ind. Eng. Chem.* 19, 1177–1183. <https://doi.org/10.1016/J.JIEC.2012.12.015>
- Martinelli, M., Gnanamani, M.K., LeViness, S., Jacobs, G., Shafer, W.D., 2020. An overview of Fischer-Tropsch Synthesis: XtL processes, catalysts and reactors. *Appl. Catal. A Gen.* 608, 117740. <https://doi.org/10.1016/J.APCATA.2020.117740>
- Martínez del Monte, D., Vizcaíno, A.J., Dufour, J., Martos, C., 2019. Effect of K, Co and Mo addition in Fe-based catalysts for aviation biofuels production by Fischer-Tropsch synthesis. *Fuel Process. Technol.* 194, 106102. <https://doi.org/10.1016/J.FUPROC.2019.05.025>
- Matandabuzo, M., Ajibade, P.A., 2018. Synthesis and surface functionalization of multi-walled carbon nanotubes with imidazolium and pyridinium-based ionic liquids: Thermal stability, dispersibility and hydrophobicity characteristics. *J. Mol. Liq.* 268, 284–293. <https://doi.org/10.1016/J.MOLLIQ.2018.07.028>
- Medrano-García, J.D., Charalambous, M.A., Guillén-Gosálbez, G., 2022. Economic and Environmental Barriers of CO₂-Based Fischer–Tropsch Electro-Diesel. *ACS Sustain. Chem. Eng.* 10, 11751–11759. <https://doi.org/10.1021/acssuschemeng.2c01983>
- Méndez, C.I., Ancheyta, J., 2020. Kinetic models for Fischer-Tropsch synthesis for the production of clean fuels. *Catal. Today* 353, 3–16. <https://doi.org/10.1016/J.CATTOD.2020.02.012>
- Merino, O., Almazán, V., Martínez-Palou, R., Aburto, J., 2017. Screening of ionic liquids for

- pretreatment of Taiwan grass in Q-Tube minireactors for improving bioethanol production. *Waste and biomass valorization* 8, 733–742.
- Michailos, S., 2018. Process design, economic evaluation and life cycle assessment of jet fuel production from sugar cane residue. *Environ. Prog. Sustain. Energy* 37, 1227–1235. <https://doi.org/10.1002/EP.12840>
- Minett, D.R., O’Byrne, J.P., Pascu, S.I., Plucinski, P.K., Owen, R.E., Jones, M.D., Mattia, D., 2014. Fe@ CNT-monoliths for the conversion of carbon dioxide to hydrocarbons: structural characterisation and Fischer–Tropsch reactivity investigations. *Catal. Sci. Technol.* 4, 3351–3358.
- Miroliaei, A.R., Shahraki, F., Atashi, H., Karimzadeh, R., 2012. Comparison of CFD results and experimental data in a fixed bed Fischer–Tropsch synthesis reactor. *J. Ind. Eng. Chem.* 18, 1912–1920. <https://doi.org/https://doi.org/10.1016/j.jiec.2012.05.003>
- Mitchell, R.W., Lloyd, D.C., van de Water, L.G.A., Ellis, P.R., Metcalfe, K.A., Sibbald, C., Davies, L.H., Enache, D.I., Kelly, G.J., Boyes, E.D., Gai, P.L., 2018. Effect of Pretreatment Method on the Nanostructure and Performance of Supported Co Catalysts in Fischer–Tropsch Synthesis. *ACS Catal.* 8, 8816–8829. <https://doi.org/10.1021/acscatal.8b02320>
- Mohammadian, N., Ghoreishi, S.M., Hafeziyeh, S., Saeidi, S., Dionysiou, D.D., 2018. Optimization of Synthesis Conditions of Carbon Nanotubes via Ultrasonic-Assisted Floating Catalyst Deposition Using Response Surface Methodology. *Nanomaterials* 8. <https://doi.org/10.3390/NANO8050316>
- Mohammed, I.A., Bankole, M.T., Abdulkareem, A.S., Ochigbo, S.S., Afolabi, A.S., Abubakre, O.K., 2017. Full factorial design approach to carbon nanotubes synthesis by CVD method in argon environment. *South African J. Chem. Eng.* 24, 17–42. <https://doi.org/10.1016/j.sajce.2017.06.001>
- Nabaho, D., Niemantsverdriet, J.W.H., Claeys, M., van Steen, E., 2016. Hydrogen spillover in the Fischer–Tropsch synthesis: An analysis of platinum as a promoter for cobalt–alumina catalysts. *Catal. Today* 261, 17–27.
- Nakhaei Pour, A., Karimi, J., Taghipoor, S., Gholizadeh, M., Hashemian, M., 2017. Fischer–

- Tropsch synthesis over CNT-supported cobalt catalyst: effect of magnetic field. *J. Iran. Chem. Soc.* 14, 1477–1488.
- Nakhaei Pour, A., Khodabandeh, H., Izadyar, M., Housaindokht, M.R., 2013. Mechanistic double ASF product distribution study of Fischer–Tropsch synthesis on precipitated iron catalyst. *J. Nat. Gas Sci. Eng.* 15, 53–58. <https://doi.org/10.1016/J.JNGSE.2013.09.005>
- Navas-Anguila, Z., Cruz, P.L., Martín-Gamboa, M., Iribarren, D., Dufour, J., 2019. Simulation and life cycle assessment of synthetic fuels produced via biogas dry reforming and Fischer-Tropsch synthesis. *Fuel* 235, 1492–1500. <https://doi.org/10.1016/J.FUEL.2018.08.147>
- Ni, Z., Qin, H., Kang, S., Bai, J., Wang, Z., Li, Y., Zheng, Z., Li, X., 2018. Effect of graphitic carbon modification on the catalytic performance of Fe@ SiO₂-GC catalysts for forming lower olefins via Fischer-Tropsch synthesis. *J. Colloid Interface Sci.* 516, 16–22.
- Nielsen, M.R., Moss, A.B., Bjørnlund, A.S., Liu, X., Knop-Gericke, A., Klyushin, A.Y., Grunwaldt, J.-D., Sheppard, T.L., Doronkin, D.E., Zimina, A., Smits huysen, T.E.L., Damsgaard, C.D., Wagner, J.B., Hansen, T.W., 2020. Reduction and carburization of iron oxides for Fischer–Tropsch synthesis. *J. Energy Chem.* 51, 48–61. <https://doi.org/https://doi.org/10.1016/j.jechem.2020.03.026>
- Nikparsa, P., Mirzaei, A.A., Atashi, H., 2015. How do the preparation methods impact the kinetic parameters of the two Co/Ni/Al₂O₃ nanocatalysts in Fischer-Tropsch process? *Monatshefte fur Chemie* 146, 1935–1947. <https://doi.org/10.1007/S00706-015-1506-8/TABLES/5>
- Nikparsaa, P., Mirzaeia, A.A., Atashib, H., 2014. Effect of reaction conditions and Kinetic study on the Fischer-Tropsch synthesis over fused Co-Ni/Al₂O₃ catalyst. *J. Fuel Chem. Technol.* 42, 710–718.
- Niu, L., Liu, X., Wen, X., Yang, Y., Xu, J., Li, Y., 2020. Effect of potassium promoter on phase transformation during H₂ pretreatment of α -Fe₂O₃ Fischer Tropsch synthesis catalyst precursor. *Catal. Today* 343, 101–111.
- Okeke, I.J., Mani, S., 2017. Techno-economic assessment of biogas to liquid fuels conversion technology via Fischer-Tropsch synthesis. *Biofuels, Bioprod. Biorefining* 11, 472–487.

- Okeke, I.J., Sahoo, K., Kaliyan, N., Mani, S., 2020a. Life cycle assessment of renewable diesel production via anaerobic digestion and Fischer-Tropsch synthesis from miscanthus grown in strip-mined soils. *J. Clean. Prod.* 249, 119358. <https://doi.org/10.1016/J.JCLEPRO.2019.119358>
- Okeke, I.J., Sahoo, K., Kaliyan, N., Mani, S., 2020b. Life cycle assessment of renewable diesel production via anaerobic digestion and Fischer-Tropsch synthesis from miscanthus grown in strip-mined soils. *J. Clean. Prod.* 249, 119358. <https://doi.org/10.1016/j.jclepro.2019.119358>
- Okolie, J.A., Nanda, S., Dalai, A.K., Kozinski, J.A., 2021. Techno-economic evaluation and sensitivity analysis of a conceptual design for supercritical water gasification of soybean straw to produce hydrogen. *Bioresour. Technol.* 331, 125005. <https://doi.org/10.1016/J.BIORTECH.2021.125005>
- Okoye-Chine, C.G., Mbuya, C.O.L., Ntelane, T.S., Moyo, M., Hildebrandt, D., 2020. The effect of silanol groups on the metal-support interactions in silica-supported cobalt Fischer-Tropsch catalysts. A temperature programmed surface reaction. *J. Catal.* 381, 121–129.
- Oliaei Torshizi, H., Mirzaei, A.A., Hossein Bayat, M., Sarani, R., Azizi, H.R., Vahid, S., Golzarpour, H.R., 2015. Kinetics studies of fused Fe–Co–Mn (ternary) catalyst in Fischer–Tropsch synthesis. *J. Environ. Chem. Eng.* 3, 2243–2252. <https://doi.org/https://doi.org/10.1016/j.jece.2015.07.027>
- Ordonsky, V. V., Luo, Y., Gu, B., Carvalho, A., Chernavskii, P.A., Cheng, K., Khodakov, A.Y., 2017. Soldering of Iron Catalysts for Direct Synthesis of Light Olefins from Syngas under Mild Reaction Conditions. *ACS Catal.* 7, 6445–6452. <https://doi.org/10.1021/ACSCATAL.7B01307>
- Ordonsky, V. V., Luo, Y., Gu, B., Carvalho, A., Chernavskii, P.A., Cheng, K., Khodakov, A.Y., 2017. Soldering of iron catalysts for direct synthesis of light olefins from syngas under mild reaction conditions. *ACS Catal.* 7, 6445–6452.
- Oschatz, M., Hofmann, J.P., van Deelen, T.W., Lamme, W.S., Krans, N.A., Hensen, E.J.M., de Jong, K.P., 2017. Effects of the functionalization of the ordered mesoporous carbon

- support surface on iron catalysts for the Fischer–Tropsch synthesis of lower olefins. *ChemCatChem* 9, 620–628.
- Øyen, S.B., Jakobsen, H.A., Haug-Warberg, T., Solsvik, J., 2022. Mass transfer modeling and sensitivity study of low-temperature Fischer-Tropsch synthesis. *Chem. Eng. Sci.* 259, 117774. <https://doi.org/10.1016/J.CES.2022.117774>
- Pan, X., Fan, Z., Chen, W., Ding, Y., Luo, H., Bao, X., 2007. Enhanced ethanol production inside carbon-nanotube reactors containing catalytic particles. *Nat. Mater.* 6, 507–511.
- Panzone, C., Philippe, R., Chappaz, A., Fongarland, P., Bengaouer, A., 2020. Power-to-Liquid catalytic CO₂ valorization into fuels and chemicals: focus on the Fischer-Tropsch route. *J. CO₂ Util.* 38, 314–347. <https://doi.org/https://doi.org/10.1016/j.jcou.2020.02.009>
- Park, J.Y., Lee, Y.J., Khanna, P.K., Jun, K.W., Bae, J.W., Kim, Y.H., 2010. Alumina-supported iron oxide nanoparticles as Fischer-Tropsch catalysts: Effect of particle size of iron oxide. *J. Mol. Catal. A Chem.* 323, 84–90. <https://doi.org/10.1016/j.molcata.2010.03.025>
- Park, N., Kim, J.-R., Yoo, Y., Lee, J., Park, M.-J., 2014. Modeling of a pilot-scale fixed-bed reactor for iron-based Fischer–Tropsch synthesis: Two-dimensional approach for optimal tube diameter. *Fuel* 122, 229–235.
- Pedersen, E.Ø., Svenum, I.H., Blekkan, E.A., 2018. Mn promoted Co catalysts for Fischer-Tropsch production of light olefins – An experimental and theoretical study. *J. Catal.* 361, 23–32. <https://doi.org/10.1016/J.JCAT.2018.02.011>
- Peña, D., Cognigni, A., Neumayer, T., van Beek, W., Jones, D.S., Quijada, M., Rønning, M., 2018. Identification of carbon species on iron-based catalysts during Fischer-Tropsch synthesis. *Appl. Catal. A Gen.* 554, 10–23. <https://doi.org/10.1016/J.APCATA.2018.01.019>
- Pendyala, V.R.R., Graham, U.M., Jacobs, G., Hamdeh, H.H., Davis, B.H., 2014. Fischer-Tropsch synthesis: Deactivation as a function of potassium promoter loading for precipitated iron catalyst. *Catal. Letters* 144, 1704–1716. <https://doi.org/10.1007/S10562-014-1336-Z/FIGURES/9>
- Peng, Z., Zou, Y., Xu, S., Zhong, W., Yang, W., 2018. High-performance biomass-based flexible solid-state supercapacitor constructed of pressure-sensitive lignin-based and

- cellulose hydrogels. *ACS Appl. Mater. Interfaces* 10, 22190–22200.
- Peron, D. V., Barrios, A.J., Taschin, A., Dugulan, I., Marini, C., Gorni, G., Moldovan, S., Koneti, S., Wojcieszak, R., Thybaut, J.W., Virginie, M., Khodakov, A.Y., 2021. Active phases for high temperature Fischer-Tropsch synthesis in the silica supported iron catalysts promoted with antimony and tin. *Appl. Catal. B Environ.* 292, 120141. <https://doi.org/10.1016/J.APCATB.2021.120141>
- Phaahlamohlaka, T.N., Dlamini, M.W., Mogodi, M.W., Kumi, D.O., Jewell, L.L., Billing, D.G., Coville, N.J., 2018. A sinter resistant Co Fischer-Tropsch catalyst promoted with Ru and supported on titania encapsulated by mesoporous silica. *Appl. Catal. A Gen.* 552, 129–137.
- Ponec, V., 1979. Surface composition and catalysis on alloys. *Surf. Sci.* 80, 352–366.
- Pour, A.N., Housaindokht, M.R., Tayyari, S.F., Zarkesh, J., 2010. Deactivation studies of nano-structured iron catalyst in Fischer-Tropsch synthesis. *J. Nat. Gas Chem.* 19, 333–340. [https://doi.org/10.1016/S1003-9953\(09\)60061-X](https://doi.org/10.1016/S1003-9953(09)60061-X)
- Qian, W., Zhang, H., Ying, W., Fang, D., 2011. Product distributions of Fischer-Tropsch synthesis over Co/AC catalyst. *J. Nat. Gas Chem.* 20, 389–396. [https://doi.org/https://doi.org/10.1016/S1003-9953\(10\)60203-4](https://doi.org/https://doi.org/10.1016/S1003-9953(10)60203-4)
- Qiang, S.S., Wang, W.-C., 2020. Experimental and techno-economic studies of upgrading heavy pyrolytic oils from wood chips into valuable fuels. *J. Clean. Prod.* 277, 124136.
- Qin, S., Zhang, C., Xu, J., Yang, Y., Xiang, H., Li, Y., 2011. Fe–Mo interactions and their influence on Fischer–Tropsch synthesis performance. *Appl. Catal. A Gen.* 392, 118–126. <https://doi.org/10.1016/J.APCATA.2010.10.032>
- Qiu, C., Odarchenko, Y., Meng, Q., Xu, S., Lezcano-Gonzalez, I., Olalde-Velasco, P., Maccherozzi, F., Zanetti-Domingues, L., Martin-Fernandez, M., Beale, A.M., 2022. Resolving the Effect of Oxygen Vacancies on Co Nanostructures Using Soft XAS/X-PEEM. *ACS Catal.* 9125–9134. <https://doi.org/10.1021/acscatal.2c00611>
- Qu, Z., Miao, L., Wang, H., Fu, Q., 2014. Highly dispersed Fe₂O₃ on carbon nanotubes for low-temperature selective catalytic reduction of NO with NH₃. *Chem. Commun.* 51, 956–958. <https://doi.org/10.1039/C4CC06941B>

- Ra, H.W., Mun, T.Y., Hong, S.J., Chun, D.H., Lee, H.T., Yoon, S.M., Moon, J.H., Park, S.J., Lee, S.H., Yang, J.H., Kim, J.K., Jung, H., Seo, M.W., 2021. Indirect coal liquefaction by integrated entrained flow gasification and Rectisol/Fischer–Tropsch processes for producing automobile diesel substitutes. *Energy* 219, 119597. <https://doi.org/10.1016/J.ENERGY.2020.119597>
- Rafati, M., Wang, L., Dayton, D.C., Schimmel, K., Kabadi, V., Shahbazi, A., 2017. Techno-economic analysis of production of Fischer-Tropsch liquids via biomass gasification: The effects of Fischer-Tropsch catalysts and natural gas co-feeding. *Energy Convers. Manag.* 133, 153–166. <https://doi.org/10.1016/J.ENCONMAN.2016.11.051>
- Rahimi, V., Shafiei, M., 2019. Techno-economic assessment of a biorefinery based on low-impact energy crops: A step towards commercial production of biodiesel, biogas, and heat. *Energy Convers. Manag.* 183, 698–707. <https://doi.org/10.1016/J.ENCONMAN.2019.01.020>
- Ribeiro, M.C., Jacobs, G., Davis, B.H., Cronauer, D.C., Kropf, A.J., Marshall, C.L., 2010. Fischer-tropsch synthesis: An in-situ TPR-EXAFS/XANES investigation of the influence of group i alkali promoters on the local atomic and electronic structure of carburized iron/silica catalysts. *J. Phys. Chem. C* 114, 7895–7903. https://doi.org/10.1021/JP911856Q/ASSET/IMAGES/MEDIUM/JP-2009-11856Q_0009.GIF
- Rinaldi, A., Zhang, J., Frank, B., Su, D.S., Hamid, S.B.A., Schlögl, R., 2010. Oxidative Purification of Carbon Nanotubes and Its Impact on Catalytic Performance in Oxidative Dehydrogenation Reactions. *ChemSusChem* 3, 254–260. <https://doi.org/10.1002/CSSC.200900179>
- Riyahin, M., Atashi, H., Mohebbi-Kalhari, D., 2016. Effect of process conditions on Fischer–Tropsch synthesis product selectivity over an industrial iron-based catalyst in slurry reactor. *Pet. Sci. Technol.* 34, 1211–1218. <https://doi.org/10.1080/10916466.2016.1193521>
- Roe, D.P., Xu, R., Roberts, C.B., 2017. Influence of a carbon nanotube support and supercritical fluid reaction medium on Fe-catalyzed Fischer-Tropsch synthesis. *Appl. Catal. A Gen.* 543, 141–149.

- Ryu, J.-H., Kang, S.-H., Kim, J.-H., Lee, Y.-J., Jun, K.-W., 2015. Fischer-Tropsch synthesis on Co-Al₂O₃-(promoter)/ZSM5 hybrid catalysts for the production of gasoline range hydrocarbons. *Korean J. Chem. Eng.* 32, 1993–1998.
- Sachtler, W.M.H., 1981. The second rideal lecture. What makes a catalyst selective? *Faraday Discuss. Chem. Soc.* 72, 7–31.
- Sadrameli, S.M., 2015. Thermal/catalytic cracking of hydrocarbons for the production of olefins: A state-of-the-art review I: Thermal cracking review. *Fuel* 140, 102–115. <https://doi.org/10.1016/J.FUEL.2014.09.034>
- Sadykov, I.I., Zabilskiy, M., Clark, A.H., Krumeich, F., Sushkevich, V., van Bokhoven, J.A., Nachtegaal, M., Safonova, O. V., 2021. Time-Resolved XAS Provides Direct Evidence for Oxygen Activation on Cationic Iron in a Bimetallic Pt-FeO_x/Al₂O₃Catalyst. *ACS Catal.* 11, 11793–11805. https://doi.org/10.1021/ACSCATAL.1C02795/SUPPL_FILE/CS1C02795_SI_001.PDF
- Sage, V., Sun, Y., Hazewinkel, P., Bhatelia, T., Braconnier, L., Tang, L., Chiang, K., Batten, M., Burke, N., 2017. Modified product selectivity in Fischer-Tropsch synthesis by catalyst pre-treatment. *Fuel Process. Technol.* 167, 183–192.
- Saheli, S., Rezvani, A.R., Arabshahi, A., Dusek, M., Samolova, E., Jarosova, M., 2021. Synthesis new Co–Mn mixed oxide catalyst for the production of light olefins by tuning the catalyst structure. *Appl. Organomet. Chem.* 35. <https://doi.org/10.1002/AOC.6038>
- Sahir, A.H., Zhang, Y., Tan, E.C.D., Tao, L., 2019a. Understanding the role of Fischer–Tropsch reaction kinetics in techno-economic analysis for co-conversion of natural gas and biomass to liquid transportation fuels. *Biofuels, Bioprod. Biorefining* 13, 1306–1320. <https://doi.org/10.1002/BBB.2035>
- Sahir, A.H., Zhang, Y., Tan, E.C.D., Tao, L., 2019b. Understanding the role of Fischer–Tropsch reaction kinetics in techno-economic analysis for co-conversion of natural gas and biomass to liquid transportation fuels. *Biofuels, Bioprod. Biorefining* 13, 1306–1320. <https://doi.org/10.1002/BBB.2035>
- Santos, G.R.S., Basha, O.M., Wang, R., Ashkanani, H., Morsi, B., 2021. Techno-economic assessment of Fischer-Tropsch synthesis and direct methane-to-methanol processes in

- modular GTL reactors. *Catal. Today* 371, 93–112. <https://doi.org/10.1016/J.CATTOD.2020.07.012>
- Sari, A., Zamani, Y., Taheri, S.A., 2009. Intrinsic kinetics of Fischer–Tropsch reactions over an industrial Co–Ru/ γ -Al₂O₃ catalyst in slurry phase reactor. *Fuel Process. Technol.* 90, 1305–1313.
- Sarkari, M., Fazlollahi, F., Ajamein, H., Atashi, H., Hecker, W.C., Baxter, L.L., 2014. Catalytic performance of an iron-based catalyst in Fischer–Tropsch synthesis. *Fuel Process. Technol.* 127, 163–170. <https://doi.org/10.1016/J.FUPROC.2014.05.003>
- Sarkari, M., Fazlollahi, F., Atashi, H., Mirzaei, A.A., Hosseinpour, V., 2012. Fischer–Tropsch synthesis: Development of kinetic expression for a sol–gel Fe–Ni/Al₂O₃ catalyst. *Fuel Process. Technol.* 97, 130–139. <https://doi.org/10.1016/J.FUPROC.2012.01.008>
- Schulz, H., 2014. Selforganization in Fischer–Tropsch synthesis with iron- and cobalt catalysts. *Catal. Today* 228, 113–122. <https://doi.org/10.1016/J.CATTOD.2013.11.060>
- Serp, P., Corrias, M., Kalck, P., 2003. Carbon nanotubes and nanofibers in catalysis. *Appl. Catal. A Gen.* 253, 337–358.
- Setiabudi, H.D., Chong, C.C., Abed, S.M., Teh, L.P., Chin, S.Y., 2018. Comparative study of Ni–Ce loading method: Beneficial effect of ultrasonic-assisted impregnation method in CO₂ reforming of CH₄ over Ni–Ce/SBA-15. *J. Environ. Chem. Eng.* 6, 745–753. <https://doi.org/10.1016/J.JECE.2018.01.001>
- Sezer, N., Koç, M., 2019. Oxidative acid treatment of carbon nanotubes. *Surfaces and Interfaces* 14, 1–8. <https://doi.org/10.1016/J.SURFIN.2018.11.001>
- Shen, S., Tan, S., Wu, S., Guo, C., Liang, J., Yang, Q., Xu, G., Deng, J., 2018. The effects of modified carbon nanotubes on the thermal properties of erythritol as phase change materials. *Energy Convers. Manag.* 157, 41–48.
- Shipilin, M., Degerman, D., Lömker, P., Goodwin, C.M., Rodrigues, G.L.S., Wagstaffe, M., Gladh, J., Wang, H.-Y., Stierle, A., Schlueter, C., Pettersson, L.G.M., Nilsson, A., Amann, P., 2022. In Situ Surface-Sensitive Investigation of Multiple Carbon Phases on Fe(110) in the Fischer–Tropsch Synthesis. *ACS Catal.* 12, 7609–7621. <https://doi.org/10.1021/acscatal.2c00905>

- Simonetti, D.A., Rass-Hansen, J., Kunkes, E.L., Soares, R.R., Dumesic, J.A., 2007. Coupling of glycerol processing with Fischer–Tropsch synthesis for production of liquid fuels. *Green Chem.* 9, 1073–1083. <https://doi.org/10.1039/B704476C>
- Snehesh, A.S., Mukunda, H.S., Mahapatra, S., Dasappa, S., 2017. Fischer-Tropsch route for the conversion of biomass to liquid fuels-Technical and economic analysis. *Energy* 130, 182–191.
- Sonal, Kondamudi, K., Pant, K.K., Upadhyayula, S., 2017. Synergistic Effect of Fe-Co Bimetallic Catalyst on FTS and WGS Activity in the Fischer-Tropsch Process: A Kinetic Study. *Ind. Eng. Chem. Res.* 56, 4659–4671. https://doi.org/10.1021/ACS.IECR.6B04517/SUPPL_FILE/IE6B04517_SI_001.PDF
- Spallina, V., Velarde, I.C., Jimenez, J.A.M., Godini, H.R., Gallucci, F., Annaland, M.V.S., 2017. Techno-economic assessment of different routes for olefins production through the oxidative coupling of methane (OCM): Advances in benchmark technologies. *Energy Convers. Manag.* 154, 244–261.
- Stalin, B., Sudha, · G T, Ravichandran, · M, 2018. Investigations on Characterization and Properties of Al-MoO₃ Composites Synthesized Using Powder Metallurgy Technique. *Silicon* 10, 2663–2670. <https://doi.org/10.1007/s12633-018-9803-6>
- Stehle, M., Gaur, A., Weber, S., Sheppard, T.L., Thomann, M., Fischer, A., Grunwaldt, J.D., 2021. Complementary operando insights into the activation of multicomponent selective propylene oxidation catalysts. *J. Catal.* <https://doi.org/10.1016/J.JCAT.2021.08.053>
- Su, H.-Y., Zhao, Y., Liu, J.-X., Sun, K., Li, W.-X., 2017. First-principles study of structure sensitivity of chain growth and selectivity in Fischer–Tropsch synthesis using HCP cobalt catalysts. *Catal. Sci. Technol.* 7, 2967–2977.
- Sun, Y., Jia, Z., Yang, G., Zhang, L., Sun, Z., 2017a. Fischer-Tropsch synthesis using iron based catalyst in a microchannel reactor: Performance evaluation and kinetic modeling. *Int. J. Hydrogen Energy* 42, 29222–29235. <https://doi.org/10.1016/J.IJHYDENE.2017.10.022>
- Sun, Y., Jia, Z., Yang, G., Zhang, L., Sun, Z., 2017b. Fischer-Tropsch synthesis using iron based catalyst in a microchannel reactor: Performance evaluation and kinetic modeling.

- Int. J. Hydrogen Energy 42, 29222–29235.
<https://doi.org/https://doi.org/10.1016/j.ijhydene.2017.10.022>
- Sun, Y., Wei, J., Zhang, J.P., Yang, G., 2016. Optimization using response surface methodology and kinetic study of Fischer–Tropsch synthesis using SiO₂ supported bimetallic Co–Ni catalyst. J. Nat. Gas Sci. Eng. 28, 173–183.
<https://doi.org/10.1016/J.JNGSE.2015.11.008>
- Sun, Y., Yang, G., Zhang, L., Sun, Z., 2017c. Fischer-Tropsch synthesis in a microchannel reactor using mesoporous silica supported bimetallic Co-Ni catalyst: Process optimization and kinetic modeling. Chem. Eng. Process. Process Intensif. 119, 44–61.
- Tan, K.F., Xu, J., Chang, J., Borgna, A., Saeys, M., 2010. Carbon deposition on Co catalysts during Fischer–Tropsch synthesis: A computational and experimental study. J. Catal. 274, 121–129.
- Tavakoli, A., Sohrabi, M., Kargari, A., 2008. Application of Anderson–Schulz–Flory (ASF) equation in the product distribution of slurry phase FT synthesis with nanosized iron catalysts. Chem. Eng. J. 136, 358–363.
- Tavasoli, A., Trépanier, M., Malek Abbaslou, R.M., Dalai, A.K., Abatzoglou, N., 2009. Fischer–Tropsch synthesis on mono- and bimetallic Co and Fe catalysts supported on carbon nanotubes. Fuel Process. Technol. 90, 1486–1494.
<https://doi.org/10.1016/J.FUPROC.2009.07.007>
- Teimouri, Z., Abatzoglou, N., Dalai, A.K., 2021. Kinetics and Selectivity Study of Fischer–Tropsch Synthesis to C₅₊ Hydrocarbons: A Review. Catal. 2021, Vol. 11, Page 330 11, 330. <https://doi.org/10.3390/CATAL11030330>
- Thüne, P., Moodley, P., Scheijen, F., Fredriksson, H., Lancee, R., Kropf, J., Miller, J., Niemantsverdriet, J.W.H., 2012. The effect of water on the stability of iron oxide and iron carbide nanoparticles in hydrogen and syngas followed by in situ X-ray absorption spectroscopy. J. Phys. Chem. C 116, 7367–7373.
https://doi.org/10.1021/JP210754K/SUPPL_FILE/JP210754K_SI_001.PDF
- Tian, Z., Wang, C., Si, Z., Ma, L., Chen, L., Liu, Q., Zhang, Q., Huang, H., 2017. Fischer-Tropsch synthesis to light olefins over iron-based catalysts supported on KMnO₄ modified

- activated carbon by a facile method. *Appl. Catal. A Gen.* 541, 50–59. <https://doi.org/10.1016/J.APCATA.2017.05.001>
- Tian, Z., Wang, C., Yue, J., Zhang, X., Ma, L., 2019a. Effect of a potassium promoter on the Fischer–Tropsch synthesis of light olefins over iron carbide catalysts encapsulated in graphene-like carbon. *Catal. Sci. Technol.* 9, 2728–2741. <https://doi.org/10.1039/C9CY00403C>
- Tian, Z., Wang, C., Yue, J., Zhang, X., Ma, L., 2019b. Effect of a potassium promoter on the Fischer–Tropsch synthesis of light olefins over iron carbide catalysts encapsulated in graphene-like carbon. *Catal. Sci. Technol.* 9, 2728–2741. <https://doi.org/10.1039/c9cy00403c>
- Todic, B., Bhatelia, T., Froment, G.F., Ma, W., Jacobs, G., Davis, B.H., Bukur, D.B., 2013. Kinetic model of Fischer–Tropsch synthesis in a slurry reactor on Co–Re/Al₂O₃ catalyst. *Ind. Eng. Chem. Res.* 52, 669–679.
- Todic, B., Ma, W., Jacobs, G., Davis, B.H., Bukur, D.B., 2014. Effect of process conditions on the product distribution of Fischer–Tropsch synthesis over a Re-promoted cobalt-alumina catalyst using a stirred tank slurry reactor. *J. Catal.* 311, 325–338. <https://doi.org/https://doi.org/10.1016/j.jcat.2013.12.009>
- Todic, B., Ma, W., Jacobs, G., Nikacevic, N., Davis, B.H., Bukur, D.B., 2017. Kinetic Modeling of Secondary Methane Formation and 1-Olefin Hydrogenation in Fischer–Tropsch Synthesis over a Cobalt Catalyst. *Int. J. Chem. Kinet.* 49, 859–874.
- Todic, B., Nowicki, L., Nikacevic, N., Bukur, D.B., 2016. Fischer–Tropsch synthesis product selectivity over an industrial iron-based catalyst: Effect of process conditions. *Catal. Today* 261, 28–39. <https://doi.org/10.1016/J.CATTOD.2015.09.005>
- Torang, H.Z., Atashi, H., Zohdi-Fasaei, H., Meshkani, F., 2021. Investigating catalytic performance of Ag/Ce promoted Fe/Al₂O₃ catalyst in the CO hydrogenation process: Selectivity modeling and optimization using response surface methodology. *Int. J. Energy Res.* 45, 14518–14529. <https://doi.org/10.1002/ER.6667>
- Torres Galvis, H.M., Bitter, J.H., Davidian, T., Ruitenbeek, M., Dugulan, A.I., De Jong, K.P., Benelux, D., 2012. Iron Particle Size Effects for Direct Production of Lower Olefins from

- Synthesis Gas. *J. Am. Chem. Soc.* 134, 16207–16215. <https://doi.org/10.1021/ja304958u>
- Torres Galvis, H.M., de Jong, K.P., 2013. Catalysts for production of lower olefins from synthesis gas: a review. *ACS Catal.* 3, 2130–2149.
- Torshizi, H.O., Nakhaei Pour, A., Mohammadi, A., Zamani, Y., Mehdi, S., Shahri, K., 2021. Fischer-Tropsch synthesis by reduced graphene oxide nanosheets supported cobalt catalysts: role of support and metal nanoparticle size on catalyst activity and products selectivity. *Front. Chem. Sci. Eng.* 15, 299–309. <https://doi.org/10.1007/s11705-020-1925-x>
- Toyoshima, R., Kawai, J., Isegawa, K., Kondoh, H., Junkaew, A., Nakayama, A., Asano, T., Tamura, M., Nakagawa, Y., Yabushita, M., Tomishige, K., 2021. Detailed Characterization of MoO_x-Modified Rh Metal Particles by Ambient-Pressure XPS and DFT Calculations. *J. Phys. Chem. C* 125, 4540–4549. <https://doi.org/10.1021/ACS.JPCC.0C10380>
- Trippe, F., Fröhling, M., Schultmann, F., Stahl, R., Henrich, E., Dalai, A., 2013. Comprehensive techno-economic assessment of dimethyl ether (DME) synthesis and Fischer–Tropsch synthesis as alternative process steps within biomass-to-liquid production. *Fuel Process. Technol.* 106, 577–586. <https://doi.org/10.1016/J.FUPROC.2012.09.029>
- Tsakoumis, N.E., Patanou, E., Lögdberg, S., Johnsen, R.E., Myrstad, R., van Beek, W., Rytter, E., Blekkan, E.A., 2019. Structure–Performance Relationships on Co-Based Fischer–Tropsch Synthesis Catalysts: The More Defect-Free, the Better. *ACS Catal.* 9, 511–520. <https://doi.org/10.1021/acscatal.8b03549>
- Tsakoumis, N.E., Voronov, A., Ronning, M., Beek, W. Van, Borg, O., Rytter, E., Holmen, A., 2012. Fischer–Tropsch synthesis: An XAS/XRPD combined in situ study from catalyst activation to deactivation. *J. Catal.* 291, 138–148. <https://doi.org/10.1016/J.JCAT.2012.04.018>
- Tu, W., Sun, C., Zhang, Z., Liu, W., Malhi, H.S., Ma, W., Zhu, M., Han, Y.-F., 2021. Chemical and structural properties of Na decorated Fe₅C₂-ZnO catalysts during hydrogenation of CO₂ to linear α -olefins. *Appl. Catal. B Environ.* 298, 120567.

- Turan, A.Z., Ataç, Ö., Kurucu, O.A., Ersöz, A., Sarioğlu, A., Okutan, H., 2022. Kinetic modeling of Fischer–Tropsch-to-olefins process via advanced optimization. *Int. J. Chem. Kinet.* 54, 3–15. <https://doi.org/10.1002/KIN.21536>
- Ulrich, G.D., Vasudevan, P.T., 2004. Chemical engineering process design and economics: a practical guide. Process Publishing.
- van der Laan, G.P., Beenackers, A.A.C.M., 1999. Hydrocarbon selectivity model for the gas–solid Fischer–Tropsch synthesis on precipitated iron catalysts. *Ind. Eng. Chem. Res.* 38, 1277–1290.
- Van Der Laan, G.P., Beenackers, A.A.C.M., 1999. Kinetics and Selectivity of the Fischer–Tropsch Synthesis: A Literature Review. *Catal. Rev. - Sci. Eng.* 41, 255–318. <https://doi.org/10.1081/CR-100101170>
- Van Ravenhorst, I.K., Hoffman, A.S., Vogt, C., Boubnov, A., Patra, N., Oord, R., Akatay, C., Meirer, F., Bare, S.R., Weckhuysen, B.M., 2021. On the Cobalt Carbide Formation in a Co/TiO₂Fischer-Tropsch Synthesis Catalyst as Studied by High-Pressure, Long-Term Operando X-ray Absorption and Diffraction. *ACS Catal.* 11, 2956–2967. https://doi.org/10.1021/ACSCATAL.0C04695/ASSET/IMAGES/LARGE/CS0C04695_0010.JPEG
- Van Santen, R.A., Ghouri, M.M., Shetty, S., Hensen, E.M.H., 2011. Structure sensitivity of the Fischer–Tropsch reaction; molecular kinetics simulations. *Catal. Sci. Technol.* 1, 891–911. <https://doi.org/10.1039/C1CY00118C>
- Van Vliet, O.P.R., Faaij, A.P.C., Turkenburg, W.C., 2009. Fischer–Tropsch diesel production in a well-to-wheel perspective: A carbon, energy flow and cost analysis. *Energy Convers. Manag.* 50, 855–876.
- Vannice, M.A., 1975. The catalytic synthesis of hydrocarbons from H₂CO mixtures over the group VIII metals: II. The kinetics of the methanation reaction over supported metals. *J. Catal.* 37, 462–473. [https://doi.org/https://doi.org/10.1016/0021-9517\(75\)90182-7](https://doi.org/https://doi.org/10.1016/0021-9517(75)90182-7)
- Venugopalan, A.T., Kandasamy, P., Gupta, N.N., Thirumalaiswamy, R., 2021. Promoted mesoporous Fe-alumina catalysts for the non-oxidative dehydrogenation of isobutane. *Catal. Commun.* 150, 106263. <https://doi.org/10.1016/J.CATCOM.2020.106263>

- Vo, D.V.N., Arcotumapathy, V., Abdullah, B., Adesina, A.A., 2013. Evaluation of Ba-promoted Mo carbide catalyst for Fischer–Tropsch synthesis. *J. Chem. Technol. Biotechnol.* 88, 1358–1363. <https://doi.org/10.1002/JCTB.3984>
- Wan, H., Wu, B., Zhang, C., Xiang, H., Li, Y., 2008. Promotional effects of Cu and K on precipitated iron-based catalysts for Fischer–Tropsch synthesis. *J. Mol. Catal. A Chem.* 283, 33–42. <https://doi.org/10.1016/J.MOLCATA.2007.12.013>
- Wang, D., Chen, B., Duan, X., Chen, D., Zhou, X., 2016. Iron-based Fischer–Tropsch synthesis of lower olefins: The nature of χ -Fe₅C₂ catalyst and why and how to introduce promoters. *J. Energy Chem.* 25, 911–916.
- Wang, D., Zhou, Xiangping, Ji, J., Duan, X., Qian, G., Zhou, Xinggui, Chen, D., Yuan, W., 2015. Modified carbon nanotubes by KMnO₄ supported iron Fischer–Tropsch catalyst for the direct conversion of syngas to lower olefins. *J. Mater. Chem. A* 3, 4560–4567. <https://doi.org/10.1039/C4TA05202A>
- Wang, H., Li, G., Ma, J., Zhao, D., 2017. The effect of methane decomposition on the formation and magnetic properties of iron carbide prepared from oolitic hematite. *RSC Adv.* 7, 3921–3927. <https://doi.org/10.1039/C6RA26166C>
- Wang, W.C., Liu, Y.C., Nugroho, R.A.A., 2022. Techno-economic analysis of renewable jet fuel production: The comparison between Fischer-Tropsch synthesis and pyrolysis. *Energy* 239, 121970. <https://doi.org/10.1016/J.ENERGY.2021.121970>
- Wang, Z.J., Skiles, S., Yang, F., Yan, Z., Goodman, D.W., 2012. Particle size effects in Fischer–Tropsch synthesis by cobalt. *Catal. Today* 181, 75–81. <https://doi.org/10.1016/j.cattod.2011.06.021>
- Wei, Y., Yan, L., Ma, C., Zhang, C., Sun, S., Wen, X., Yang, Y., Li, Y., 2020. Mesoporous Iron Oxide Nanoparticle-Decorated Graphene Oxide Catalysts for Fischer–Tropsch Synthesis. *ACS Appl. Nano Mater.* 3, 7182–7191. <https://doi.org/10.1021/ACSANM.0C01522>
- Wu, X., Ma, H., Zhang, H., Qian, W., Liu, D., Sun, Q., Ying, W., 2019. High-Temperature Fischer–Tropsch Synthesis of Light Olefins over Nano-Fe₃O₄@MnO₂ Core–Shell Catalysts. *Ind. Eng. Chem. Res.* 58, 21350–21362.

<https://doi.org/10.1021/acs.iecr.9b04221>

- Xiang, D., Qian, Y., Man, Y., Yang, S., 2014. Techno-economic analysis of the coal-to-olefins process in comparison with the oil-to-olefins process. *Appl. Energy* 113, 639–647. <https://doi.org/https://doi.org/10.1016/j.apenergy.2013.08.013>
- Xie, J., Torres Galvis, H.M., Koeken, A.C.J., Kirilin, A., Dugulan, A.I., Ruitenbeek, M., De Jong, K.P., 2016a. Size and promoter effects on stability of carbon-nanofiber-supported iron-based Fischer-Tropsch catalysts. *ACS Catal.* 6, 4017–4024. https://doi.org/10.1021/ACSCATAL.6B00321/SUPPL_FILE/CS6B00321_SI_001.PDF
- Xie, J., Yang, J., Dugulan, A.I., Holmen, A., Chen, D., De Jong, K.P., Louwerse, M.J., 2016b. Size and promoter effects in supported iron Fischer–Tropsch catalysts: Insights from experiment and theory. *ACS Catal.* 6, 3147–3157.
- Xie, T., Wang, J., Ding, F., Zhang, A., Li, W., Guo, X., Song, C., 2017. CO₂ hydrogenation to hydrocarbons over alumina-supported iron catalyst: Effect of support pore size. *J. CO₂ Util.* 19, 202–208. <https://doi.org/10.1016/J.JCOU.2017.03.022>
- Xing, C., Sun, J., Yang, G., Shen, W., Tan, L., Zhu, P., Wei, Q., Li, J., Kyodo, M., Yang, R., 2015. Tunable isoparaffin and olefin synthesis in Fischer–Tropsch synthesis achieved by composite catalyst. *Fuel Process. Technol.* 136, 68–72.
- Xiong, H., Motchelaho, M.A., Moyo, M., Jewell, L.L., Coville, N.J., 2015. Effect of Group I alkali metal promoters on Fe/CNT catalysts in Fischer–Tropsch synthesis. *Fuel* 150, 687–696. <https://doi.org/10.1016/J.FUEL.2015.02.099>
- Xu, Y., Jia, X., Liu, X., 2018. Supported Fe/MnO_x catalyst with Ag doping for remarkably enhanced catalytic activity in Fischer–Tropsch synthesis. *Catal. Sci. Technol.* 8, 1953–1970.
- Yahyazadeh, A., Borugadda, V.B., Dalai, A.K., Zhang, L., 2022a. Optimization of carbon nanotube growth via response surface methodology for Fischer-Tropsch synthesis over Fe/CNT catalyst. *Catal. Today*. <https://doi.org/10.1016/J.CATTOD.2022.05.006>
- Yahyazadeh, A., Borugadda, V.B., Dalai, A.K., Zhang, L., 2022b. Optimization of olefins' yield in Fischer-Tropsch synthesis using carbon nanotubes supported iron catalyst with potassium and molybdenum promoters. *Appl. Catal. A Gen.* 643, 118759.

<https://doi.org/10.1016/J.APCATA.2022.118759>

- Yahyazadeh, A., Dalai, A.K., Ma, W., Zhang, L., Murzin, D.Y., 2021. Fischer–Tropsch Synthesis for Light Olefins from Syngas: A Review of Catalyst Development. *React. 2021*, Vol. 2, Pages 227-257 2, 227–257. <https://doi.org/10.3390/REACTIONS2030015>
- Yahyazadeh, A., Khoshandam, B., 2017. Carbon nanotube synthesis via the catalytic chemical vapor deposition of methane in the presence of iron, molybdenum, and iron–molybdenum alloy thin layer catalysts. *Results Phys.* 7, 3826–3837. <https://doi.org/10.1016/J.RINP.2017.10.001>
- Yancheng, L.I.U., Xianbo, L.U.O., Kai, K., Tingli, L.I., JIANG, S., ZHANG, J., Zhang, Z., Yunting, L.I., 2017. Permeability characterization and directional wells initial productivity prediction in the continental multilayer sandstone reservoirs: A case from Penglai 19-3 oil field, Bohai Bay Basin. *Pet. Explor. Dev.* 44, 97–104.
- Yang, J., Ma, W., Chen, D., Holmen, A., Davis, B.H., 2014. Fischer–Tropsch synthesis: A review of the effect of CO conversion on methane selectivity. *Appl. Catal. A Gen.* 470, 250–260.
- Yang, X., Yang, J., Wang, Y., Zhao, T., Ben, H., Li, X., Holmen, A., Huang, Y., Chen, D., 2022. Promotional effects of sodium and sulfur on light olefins synthesis from syngas over iron-manganese catalyst. *Appl. Catal. B Environ.* 300, 120716. <https://doi.org/10.1016/J.APCATB.2021.120716>
- Yao, S., Xiao, D., Ma, D., 2018. Observing How Fischer-Tropsch Synthesis Catalysts Work at the Nanoscale via Operando STXM. *Chem* 4, 2493–2495. <https://doi.org/https://doi.org/10.1016/j.chempr.2018.10.012>
- Yoo, S.C., Kang, B., Van Trinh, P., Phuong, D.D., Hong, S.H., 2020. Enhanced mechanical and wear properties of Al6061 alloy nanocomposite reinforced by CNT-template-grown core–shell CNT/SiC nanotubes. *Sci. Rep.* 10, 1–11.
- Yoon, H.J., Lee, C.H., Lee, K.B., 2021. Mass transfer enhanced CaO pellets for CO₂ sorption: Utilization of CO₂ emitted from CaCO₃ pellets during calcination. *Chem. Eng. J.* 421, 129584. <https://doi.org/10.1016/J.CEJ.2021.129584>
- Zafari, R., Abdouss, M., Zamani, Y., 2020. Effect of Mn and reduced graphene oxide for the

- Fischer–Tropsch reaction: an efficient catalyst for the production of light olefins from syngas. *React. Kinet. Mech. Catal.* 129, 707–724.
- Zafari, R., Abdouss, M., Zamani, Y., 2019. Application of response surface methodology for the optimization of light olefins production from CO hydrogenation using an efficient catalyst. *Fuel* 237, 1262–1273.
- Zafari, R., Abdouss, M., Zamani, Y., Tavasoli, A., 2017. An efficient catalyst for light olefins production from CO hydrogenation: synergistic effect of Zn and Ce promoters on performance of Co–Mn/SiO₂ catalyst. *Catal. Letters* 147, 2475–2486.
- Zang, G., Sun, P., Elgowainy, A., Bafana, A., Wang, M., 2021a. Life Cycle Analysis of Electrofuels: Fischer-Tropsch Fuel Production from Hydrogen and Corn Ethanol Byproduct CO₂. *Environ. Sci. Technol.* 2–11. <https://doi.org/10.1021/acs.est.0c05893>
- Zang, G., Sun, P., Elgowainy, A.A., Bafana, A., Wang, M., 2021b. Performance and cost analysis of liquid fuel production from H₂ and CO₂ based on the Fischer-Tropsch process. *J. CO₂ Util.* 46, 101459. <https://doi.org/10.1016/J.JCOU.2021.101459>
- Zhang, C., Jun, K.W., Gao, R., Lee, Y.J., Kang, S.C., 2015. Efficient utilization of carbon dioxide in gas-to-liquids process: Process simulation and techno-economic analysis. *Fuel* 157, 285–291. <https://doi.org/10.1016/J.FUEL.2015.04.051>
- Zhang, J., Chen, J., Ren, J., Li, Y., Sun, Y., 2003. Support effect of Co/Al₂O₃ catalysts for Fischer–Tropsch synthesis☆. *Fuel* 82, 581–586.
- Zhang, K., Yang, W., Ma, C., Wang, Y., Sun, C., Chen, Y., Duchesne, P., Zhou, J., Wang, J., Hu, Y., Banis, M.N., Zhang, P., Li, F., Li, J., Chen, L., 2015. A highly active, stable and synergistic Pt nanoparticles/Mo₂C nanotube catalyst for methanol electro-oxidation. *NPG Asia Mater.* 2015 71 7, e153–e153. <https://doi.org/10.1038/am.2014.122>
- Zhang, Q., Kang, J., Wang, Y., 2010a. Development of Novel Catalysts for Fischer-Tropsch Synthesis: Tuning the Product Selectivity. *ChemCatChem* 2, 1030–1058. <https://doi.org/10.1002/cctc.201000071>
- Zhang, Q., Kang, J., Wang, Y., 2010b. Development of Novel Catalysts for Fischer–Tropsch Synthesis: Tuning the Product Selectivity. *ChemCatChem* 2, 1030–1058.

<https://doi.org/10.1002/CCTC.201000071>

- Zhang, R., Kang, L., Liu, H., Wang, B., Li, D., Fan, M., 2020. Crystal facet dependence of carbon chain growth mechanism over the Hcp and Fcc Co catalysts in the Fischer-Tropsch synthesis. *Appl. Catal. B Environ.* 269, 118847. <https://doi.org/10.1016/j.apcatb.2020.118847>
- Zhang, S., Li, D., Liu, Y., Zhang, Y., Wu, Q., 2019. Zirconium Doped Precipitated Fe-Based Catalyst for Fischer-Tropsch Synthesis to Light Olefins at Industrially Relevant Conditions. *Catal. Lett.* 2019 1496 149, 1486–1495. <https://doi.org/10.1007/S10562-019-02775-X>
- Zhang, T., Gu, B., Qiu, F., Peng, X., Yue, X., Yang, D., 2018. Preparation of carbon nanotubes/polyurethane hybrids as a synergistic absorbent for efficient oil/water separation. *Fibers Polym.* 19, 2195–2202.
- Zhang, Y., Brown, T.R., Hu, G., Brown, R.C., 2013. Techno-economic analysis of monosaccharide production via fast pyrolysis of lignocellulose. *Bioresour. Technol.* 127, 358–365. <https://doi.org/10.1016/J.BIORTECH.2012.09.070>
- Zhang, Y., Ma, L., Tu, J., Wang, T., Li, X., 2015. One-pot synthesis of promoted porous iron-based microspheres and its Fischer-Tropsch performance. *Appl. Catal. A Gen.* 499, 139–145.
- Zhang, Y.X., Jia, Y., 2013. Synthesis of high-quality double-walled carbon nanotubes using porous MgO nanowire supported iron oxide as catalyst. *Mater. Lett.* 107, 46–49. <https://doi.org/10.1016/J.MATLET.2013.05.120>
- Zhang, Z., Zhang, J., Wang, X., Si, R., Xu, J., Han, Y.F., 2018a. Promotional effects of multiwalled carbon nanotubes on iron catalysts for Fischer-Tropsch to olefins. *J. Catal.* 365, 71–85. <https://doi.org/10.1016/j.jcat.2018.05.021>
- Zhang, Z., Zhang, J., Wang, X., Si, R., Xu, J., Han, Y.F., 2018b. Promotional effects of multiwalled carbon nanotubes on iron catalysts for Fischer-Tropsch to olefins. *J. Catal.* 365, 71–85. <https://doi.org/10.1016/J.JCAT.2018.05.021>
- Zhao, M., Yan, C., Jinchang, S., Qianwen, Z., 2018a. Modified iron catalyst for direct synthesis of light olefin from syngas. *Catal. Today* 316, 142–148.

- Zhao, M., Yan, C., Jinchang, S., Qianwen, Z., 2018b. Modified iron catalyst for direct synthesis of light olefin from syngas. *Catal. Today* 316, 142–148. <https://doi.org/10.1016/J.CATTOD.2018.05.018>
- Zhao, X., Lv, S., Wang, L., Li, L., Wang, G., Zhang, Y., Li, J., 2018. Comparison of preparation methods of iron-based catalysts for enhancing Fischer-Tropsch synthesis performance. *Mol. Catal.* 449, 99–105. <https://doi.org/10.1016/J.MCAT.2018.02.022>
- Zhao, Z., Jiang, J., Wang, F., 2021. An economic analysis of twenty light olefin production pathways. *J. Energy Chem.* 56, 193–202. <https://doi.org/10.1016/J.JECHEM.2020.04.021>
- Zhao, Z., Liu, Y., Wang, F., Li, X., Deng, S., Xu, J., Wei, W., 2017. Life cycle assessment of primary energy demand and greenhouse gas (GHG) emissions of four propylene production pathways in China. *J. Clean. Prod.* 163, 285–292.
- Zhipeng Tian, Chenguang Wang, Jun Yue, Xinghua Zhang, Longlong Ma, 2019a. Effect of a potassium promoter on the Fischer–Tropsch synthesis of light olefins over iron carbide catalysts encapsulated in graphene-like carbon. *Catal. Sci. Technol.* 9, 2728–2741. <https://doi.org/10.1039/C9CY00403C>
- Zhipeng Tian, Chenguang Wang, Jun Yue, Xinghua Zhang, Longlong Ma, 2019b. Effect of a potassium promoter on the Fischer–Tropsch synthesis of light olefins over iron carbide catalysts encapsulated in graphene-like carbon. *Catal. Sci. Technol.* 9, 2728–2741. <https://doi.org/10.1039/C9CY00403C>
- Zhou, F., Pan, N., Chen, H., Xu, X., Wang, C., Du, Y., Guo, Y., Zeng, Z., Li, L., 2019. Hydrogen production through steam reforming of toluene over Ce, Zr or Fe promoted Ni-Mg-Al hydrotalcite-derived catalysts at low temperature. *Energy Convers. Manag.* 196, 677–687. <https://doi.org/10.1016/J.ENCONMAN.2019.06.047>
- Zhou, H., Li, K., Zhao, B., Deng, W., Su, Y., Zhong, F., 2017. Surface properties and reactivity of Fe/Al₂O₃/cordierite catalysts for NO reduction by C₂H₆: Effects of calcination temperature. *Chem. Eng. J.* 326, 737–744.
- Zhou, W.-G., Liu, J.-Y., Wu, X., Chen, J.-F., Zhang, Y., 2015. An effective Co/MnO_x catalyst for forming light olefins via Fischer–Tropsch synthesis. *Catal. Commun.* 60, 76–81. <https://doi.org/https://doi.org/10.1016/j.catcom.2014.10.027>

- Zhou, X., Ji, J., Wang, D., Duan, X., Qian, G., Chen, D., Zhou, Xinggui, 2015. Hierarchical structured α -Al₂O₃ supported S-promoted Fe catalysts for direct conversion of syngas to lower olefins. Chem. Commun. 51, 8853–8856. <https://doi.org/10.1039/C5CC00786K>
- Zhu, J., Holmen, A., Chen, D., 2013. Carbon nanomaterials in catalysis: proton affinity, chemical and electronic properties, and their catalytic consequences. ChemCatChem 5, 378–401.
- Zohdi-Fasaei, H., Atashi, H., Farshchi Tabrizi, F., Mirzaei, A.A., 2017. Modeling and optimization of Fischer-Tropsch synthesis over Co-Mn-Ce/SiO₂ catalyst using hybrid RSM/LHHW approaches. Energy 128, 496–508. <https://doi.org/10.1016/J.ENERGY.2017.03.122>

APPENDIX A: Experimental Calibrations

A.1. Reactor temperature calibration

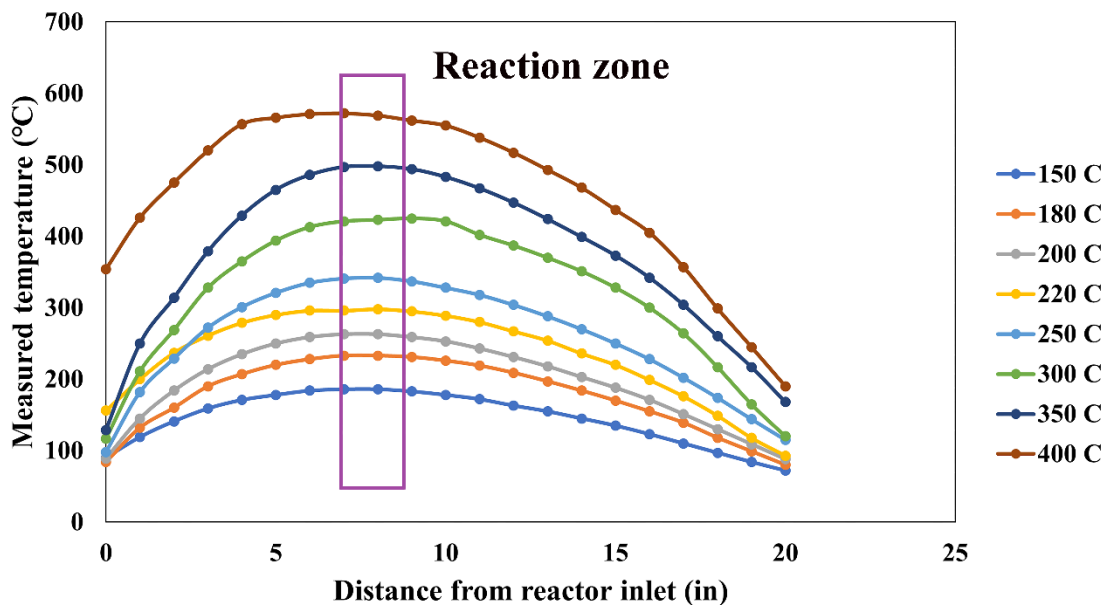


Figure A.1. 1: Temperature profile along the fixed-bed FT reactor.

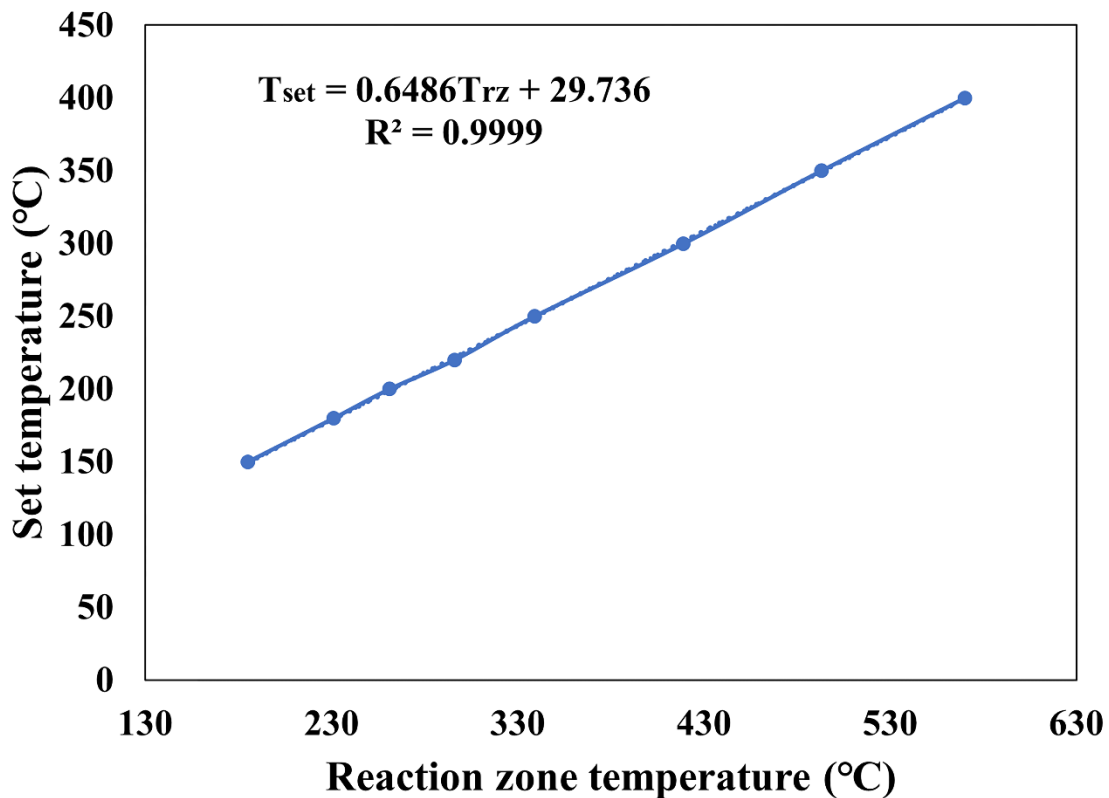


Figure A.1. 2: Temperature calibration curve for reaction zone in FTS reactor.

A.2. Mass flow controller calibration

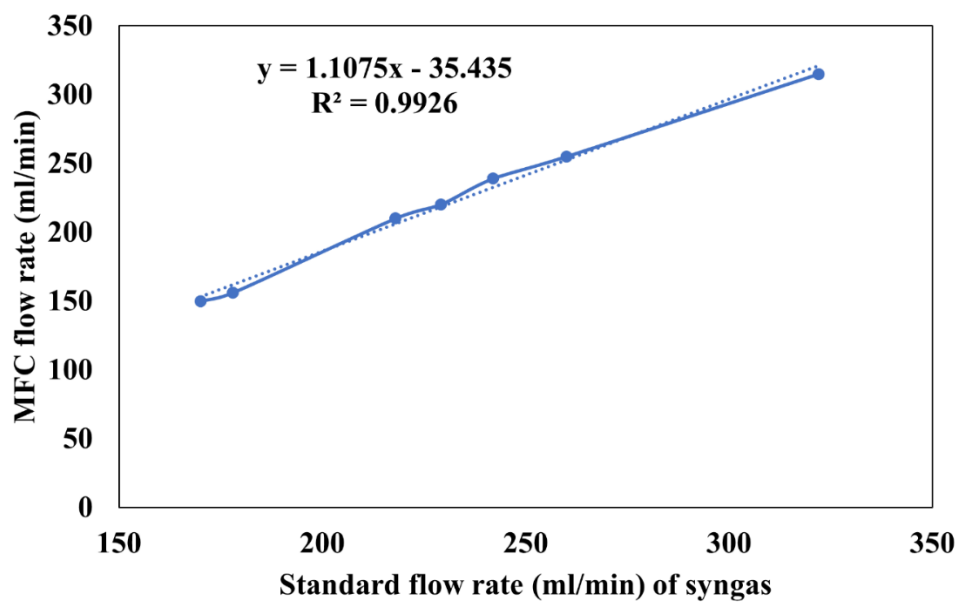


Figure A.2. 1: Mass flow controller (MFC) calibration for syngas flow into FT reactor.

APPENDIX B: Permissions from Publishers

The data used in this thesis were published in MDPI Journal of Reactions and Elsevier Journals of Catalysis Today and Applied Catalysis A: General. Based on the MDPI and Elsevier copy rights: as the author of the articles, I have got permission to include them in my thesis.

MDPI Open Access Information and Policy

All articles published by MDPI are made immediately available worldwide under an open access license. This means:

- everyone has free and unlimited access to the full-text of *all* articles published in MDPI journals;
- everyone is free to re-use the published material if proper accreditation/citation of the original publication is given;
- open access publication is supported by the authors' institutes or research funding agencies by payment of a comparatively low **Article Processing Charge (APC)** for accepted articles.

Permissions

No special permission is required to reuse all or part of article published by MDPI, including figures and tables. For articles published under an open access Creative Common CC BY license, any part of the article may be reused without permission provided that the original article is clearly cited. Reuse of an article does not imply endorsement by the authors or MDPI.

Figure B. 1: Permission to use the published paper “Fischer–Tropsch Synthesis for Light Olefins from Syngas: A Review of Catalyst Development”.

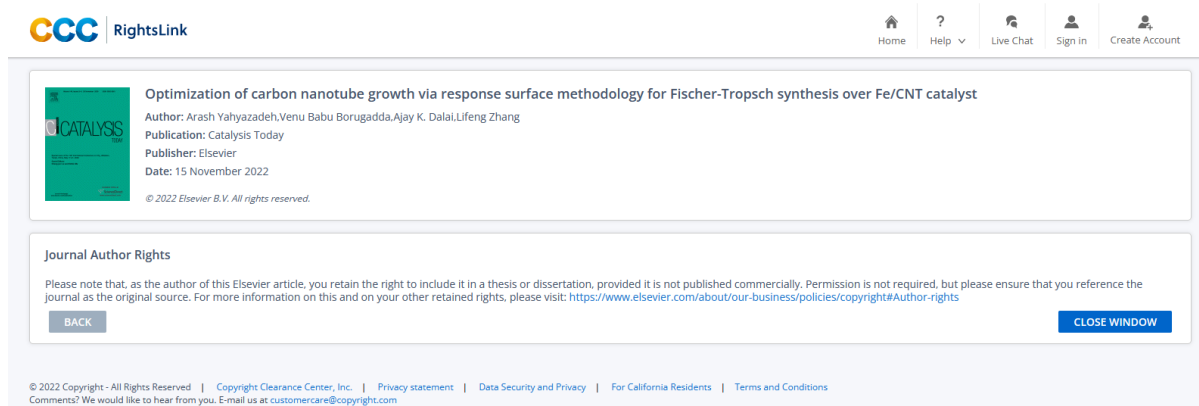



Figure B. 2: Permission to use the published paper “Optimization of Carbon Nanotube Growth via Response Surface Methodology for Fischer-Tropsch Synthesis over Fe/CNT Catalyst”.

CCC RightsLink

Home ? Help Live Chat Sign in Create Account

 Optimization of olefins' yield in Fischer-Tropsch synthesis using carbon nanotubes supported iron catalyst with potassium and molybdenum promoters

Author: Arash Yahyazadeh, Venu Babu Borugadda, Ajay K. Dalai, Lifeng Zhang
Publication: Applied Catalysis A: General
Publisher: Elsevier
Date: 5 August 2022
© 2022 Elsevier B.V. All rights reserved.

Journal Author Rights

Please note that, as the author of this Elsevier article, you retain the right to include it in a thesis or dissertation, provided it is not published commercially. Permission is not required, but please ensure that you reference the journal as the original source. For more information on this and on your other retained rights, please visit: <https://www.elsevier.com/about/our-business/policies/copyright#Author-rights>

BACK CLOSE WINDOW

© 2022 Copyright - All Rights Reserved | Copyright Clearance Center, Inc. | Privacy statement | Data Security and Privacy | For California Residents | Terms and Conditions
Comments? We would like to hear from you. E-mail us at customer-care@copyright.com

Figure B. 3: Permission to use the published paper “Optimization of olefins' yield in Fischer-Tropsch synthesis using carbon nanotubes supported iron catalyst with potassium and molybdenum promoters”.